Faculty of Science and Engineering
Department of Exploration Geophysics

Analysis of Seismic Anisotropy at the CO2CRC Otway Project Site

Mehdi Asgharzadeh

This thesis is presented for the Degree of
Doctor of Philosophy
of
Curtin University

March 2014

Declaration

To the best of my knowledge and belief this thesis contains no material previously published by any other person except where due acknowledgment has been made. This thesis contains no material which has been accepted for the award of any other degree or diploma in any university.

Signature: .....

Date: ....15/08/2014....

Abstract

This work evaluates the reliability of VSP related slowness and slowness-polarization methods for local (to the receiver) VTI and orthorhombic anisotropy parameter estimation that can be ultimately utilized as a time-lapse tool for monitoring the changes in the state of underground stress as a result of CO_2 injection into geological formations. This is particularly important in cases when time-lapse signal is small or beyond the recording threshold of the conventional methodologies such as 4D reflection seismic.

This is indeed the case at the CO2CRC Otway project for CO_2 geosequestration in Victoria, Australia where conventional acoustic impedance inversion of 3D surface seismic data acquired in 2008, 2009 and 2010 showed subtle changes for both the acoustic impedance and amplitudes of top Waarre C reservoir formation after injection of 33000 tonnes of CO_2/CH_4 (80/20%) mixture in 2007 and another 32000 tonnes in 2009, respectively. The time lapse signal is weak (at close to the level of background noise) and cannot be reliably used to monitor CO_2 migration inside the reservoir or CO_2 leakage into the overburden rock. However, CO_2 injection has increased pore pressure in the reservoir by over 6 Mp and may have caused seismic anisotropy changes in the overburden that potentially could be studied by borehole seismic measurements.

To apply time lapse anisotropy analysis it was first necessary to quantify the uncertainties related to the estimation of VTI anisotropy parameters using P-wave slowness and slowness-polarization data that are measureable in a conventional VSP survey. I have shown that the selection of a proper methodology for VTI parameter estimation is largely dependent on our ability to accurately measure horizontal components of P-wave slowness vector or polarization vector. Methods that include horizontal components of the slowness vector show greater accuracy than the methods that replace this data with polarization vector. In the absence of horizontal slownesses (a heterogeneous overburden), methods that are based on using exact relationship between P-wave polarization dip (with vertical) and the vertical component of the slowness vector can be used for accurate estimation of VTI parameters δ and ε.

I have also presented a workflow to quantify the reliability of VSP methods for estimation of local orthorhombic anisotropy parameters by using numerical P-wave

slownesses only. For that purpose I have modelled the orthorhombic medium by embedding a set of vertical, dry and rotationally invariant fractures in a VTI background. If sufficient phase (dip) angle coverage is provided, the method based on using the exact relationship for P-wave phase velocity in orthorhombic media is capable of estimating anisotropy parameters $\delta^{(1)}$, $\delta^{(2)}$, $\delta^{(3)}$, $\varepsilon^{(1)}$ and $\varepsilon^{(2)}$ for a wide range of VTI anisotropy in the background medium, large fracture intensity and high level of measurement noise (up to 3%). Anisotropy parameters defined in the symmetry plane perpendicular to the fracture plane $\delta^{(2)}$ and $\varepsilon^{(2)}$ are more reliably estimated than the parameters defined in the fracture plane $\delta^{(1)}$ and $\varepsilon^{(1)}$.

The effectiveness and accuracy of both slownesses only and slowness-polarization methods were investigated using both synthetic and real VSP measurements conducted at the CO2CRC Otway project geosequestration site.

Application of slownesses only and slowness-polarization methods to invert CRC-1 synthetic walkaway VSP data shows that the methods are capable of recovering Thomsen's VTI parameters ε and δ for greater depths (1000 m and deeper). In the shallow section, for (approximately 600 to 1000 m depth) slowness and polarization measurements are contaminated by the arrival of head waves yielding less reliable estimates. The synthetic exercise shows that the geometry of the existing 3D VSP survey allows reasonable estimate of VTI anisotropy parameters. Interestingly, P-wave slownesses computed from 3D VSP travel times at CRC-1 well confirm that the anisotropy of the shale formation (the measurement interval) is changing with azimuth and indicates the presence of lower symmetry than VTI, as commonly assumed for a shale rock.

Finally, orthorhombic symmetry was inferred from the slowness measurements that are computed from P-wave travel times of 2010 3D VSP survey at well CRC-1. Minimizing the error between the velocities predicted by this model and the measured VSP velocities results in the orthorhombic parameters: $\delta^{(1)} \approx -0.02$, $\delta^{(2)} \approx -0.01$, $\varepsilon^{(1)} \approx 0.14$ and $\varepsilon^{(2)} \approx 0.1$ and two azimuthal directions of 150^o and 60^o for symmetry planes of the orthorhombic model that match closely to the direction of fast and slow shear wave

measurements at well CRC-1, respectively. Symmetry axis, x_3 of the best fitted orthorhombic model at well CRC-1 is deviating from vertical direction by about 8^o.

The methodology presented in this study can be used to analyse low intensity time lapse signals caused by changes in the medium anisotropy as a result of CO_2 injection in an underground reservoir rock.

Acknowledgement

Foremost, I would like to express my deepest gratitude to my supervisory panel, associate Prof. Dr. Milovan Urosevic (supervisor), associate Prof. Dr. Andrej Bóna (co-supervisor), associate Prof. Dr. Roman Pevzner (co-supervisor) and Prof. Buris Gurevich (co-supervisor and chair) for their caring and continuous support of my Ph.D study, their guidances through every step of this research work, their encouragement, patience, insightful comments, enthusiasm, and for generously sharing their immense knowledge about the research subject without which this PhD work would not have been possible.

Besides my supervisory panel, I would like to thank Dr. Dariush Nadri and Dr. Mahyar Madadi for kindly sharing their knowledge about my research subject through the in-depth discussions and their informative comments and the inspirations.

I would also like to express my sincere appreciation to the administrative and technical staff of the department of exploration geophysics, Ms. Deirdre Hollingsworth, Mr. Dominic Howman, Ms. Jennifer Mcpherson, Ms. Judith Tournay and Mr. Robert Verstandig for their wonderful work to keep the department up and running.

I am particularly indebted to the Australian Commonwealth Government for their financial support through the Australian Postgraduate Award (APA) and Cooperative Research Centre for Greenhouse Gas Technologies (CO2CRC) for their financial support and allowing me to use data from the CO2CRC Otway project and publication of the results.

I wish to acknowledge CGG-Veritas for using Hampson-Russell, Schlumberger for using Petrel, Tesseral technologies for using Tesseral 2D, RadExPro for using their processing software, Landmark for using Promax and MathWorks for using MATLAB in this PhD study.

I will always remember the wonderful time I spent with my friends and office-mates Mr. Majed Almalki, Mr. Faisal Alonaizi, Mr. Mamdoh Alajami, Mr. Yousuf Y. Aljabri, Ms. Eva Caspari, Ms. Olivia Collet, Ms. Sofia Correia Lopes, Mr. Aleksander Dzunic, Mr Jamal Esttaifan, Mr. Mohammad Javad Khoshnavaz, Mr. Vassili Mikhaltsevitch, Mr.

Andrew Pethick, Mr. Elmar Strobach, Mr Konstantin Tertyshnikov, Ms. Sinem Yavuz, Dr. Brett Harris, Dr. Maxim Lebedev and Mr. Andrew Greenwood.

Finally, I dedicate this thesis work to the most wonderful people in my life, my beloved parents, Ms. Manijeh Gharibi and Mr. Ali Asgharzadeh and my lovely wife Ms. Shohreh Razmi for their support, love and encouragement during the course of this PhD work.

Table of Contents

List of Figures

Chapter 1

Chapter 2

Figure 8, top, inversion analysis at well Naylor-1, 2008 survey. Bottom, three statistical wavelets extracted from seismic data for 2008 to 2010 surveys.

Figure 9, an arbitrary line through wells CRC-1 and Nalylor-1 extracted from AI inversion on pre injection seismic survey 2008.

Figure 10, result of 2008 inversion versus acoustic impedance computed for the well CRC-2 in Otway geosequestration site.

Figure 11, inversion results and amplitude maps at top Waarre C formation for 3 seismic surveys. Left, top Waarre C amplitude maps, top, 2008, middle, 2009 and bottom, 2010. In the middle, results of inversion at Waarre C interval, top, 2008, middle, 2009 and bottom, 2010. In the right, relative AI change and AI distribution of Waarre C formation, top, $AI_{2008} - AI_{2009}/AI_{2008}$ **, middle,** $AI_{2008} - AI_{2010}/AI_{2008}$ **, bottom,** $AI_{2009} - AI_{2010}/AI_{2009}$ **.**

Chapter 3

Figure 1, a single system of vertical and parallel fractures embedded in an isotropic background rock will form an HTI medium.

Figure 2, a single system of vertical and parallel fractures embedded in a VTI background rock will form an orthorhombic medium.

Figure 3, phase velocity $V(\theta)$ **(measured in the direction normal to the wavefront) is different than the group velocity** $V_G(\psi)$ **(measured in the ray direction) for anisotropic media. Both of the velocities will have no component outside the wave propagation plane in a TI media.**

Figure 4, top, polarization angle, red dots (weak anisotropy approximation, red curve) and group angle, blue dots (weak anisotropy approximation, blue curve) are plotted versus the phase angle (black dash dots) for a P-wave traveling in a VTI medium with anisotropy parameters defined as: $V_{P0} = 3000$ **m/s,** $V_{S0} = 1500$ **m/s,** $\delta = -0.2$ **and** $\varepsilon = -0.1$ **. Bottom, P-wave's phase velocity (red dots) is plotted**

versus group velocity (blue dots) in the same VTI medium as in top. The angle is phase angle for phase velocity curve and group angle for the group velocity curve.

Figure 5, top, polarization angle, red dots (weak anisotropy approximation, red curve) and group angle, blue dots (weak anisotropy approximation, blue curve) are plotted versus the phase angle(black dash dots) for a P-wave traveling in a VTI medium with anisotropy parameters defined as: $V_{P0} = 3000$ **m/s,** $V_{S0} = 1500$ **m/s,** $\delta = 0.15$ **and** $\varepsilon = 0.4$**. Bottom, P-wave's phase velocity (red dots) is plotted versus group velocity (blue dots) in the same VTI medium as in top. The angle is phase angle for phase velocity curve and group angle for the group velocity curve. This medium can represent a shale formation in sedimentary basins.**

Figure 6, top, polarization angle, red dots (weak anisotropy approximation, red curve) and group angle, blue dots (weak anisotropy approximation, blue curve) are plotted versus the phase angle(black dash dots) for a P-wave traveling in a VTI medium with anisotropy parameters defined as: $V_{P0} = 3000$ **m/s,** $V_{S0} = 1500$ **m/s,** $\delta = -0.1$ **and** $\varepsilon = 0.3$**. Bottom, P-wave's phase velocity (red dots) is plotted versus group velocity (blue dots) in the same VTI medium as in top. The angle is phase angle for phase velocity curve and group angle for the group velocity curve. This medium can represent anisotropy caused by interbedding of thin isotropic layers in sedimentary basins.**

Figure 7, top, polarization angle, red dots (weak anisotropy approximation, red curve) and group angle, blue dots (weak anisotropy approximation, blue curve) are plotted versus the phase angle(black dash dots) for a P-wave traveling in a VTI medium with anisotropy parameters defined as: $V_{P0} = 3000$ **m/s,** $V_{S0} = 1500$ **m/s,** $\delta = 0.3$ **and** $\varepsilon = -0.1$**. Bottom, P-wave's phase velocity (red dots) is plotted versus group velocity (blue dots) in the same VTI medium as in top. The angle is phase angle for phase velocity curve and group angle for the group velocity curve.**

Figure 8, P-wave phase velocity (top left), group velocity (top right), deviation of polarization and group velocity vectors from the slowness vector (middle and bottom, respectively) for the orthorhombic medium that is generated by combining

a VTI background ($\delta = -0.2$ and $\varepsilon = -0.1$) and a dry vertical fracture set ($\delta_N = 0.4$) with fracture normals in the x_1 direction.

Figure 9, P-wave phase velocity (top left), group velocity (top right), deviation of polarization and group velocity vectors from the slowness vector (middle and bottom, respectively) for the orthorhombic medium that is generated by combining a VTI background ($\delta = 0.2$ and $\varepsilon = 0.1$) and a dry vertical fracture set ($\delta_N = 0.4$) with fracture normals in the x_1 direction.

Figure 10, P-wave phase velocity (top left), group velocity (top right), deviation of polarization and group velocity vectors from the slowness vector (middle and bottom, respectively) for the orthorhombic medium that is generated by combining a VTI background ($\delta = -0.1$ and $\varepsilon = 0.3$) and a dry vertical fracture set ($\delta_N = 0.4$) with fracture normals in the x_1 direction.

Figure 11, P-wave slowness vectors (black solid arrow in 9 phase directions) are contaminated by normally distributed random noise vectors (red arrow) to generate new slowness vectors (black dot-dash arrows) for the error analysis.

Figure 12, construction of the reflection point in the simplex method.

Chapter 4

Figure 1, P-wave's vertical component of the slowness vector is measured in the borehole (left) and is local to the receiver location. Horizontal component of the P-wave's slowness vector is measured on the surface (right) and can be transferred to the receiver location if the overburden is laterally homogeneous.

Figure 2, VSP measurements can be used to estimate both vertical and horizontal components of P-wave's slowness vector. Vertical component of the slowness vector is measured in the shot domain (top). In this example, vertical component of the slowness vector is measured for a source located at offset=2000 m and a receiver located at depth=1250 m. Horizontal component is measured in the receiver domain (bottom). In this example, horizontal component of the slowness

vector is measured for a source located at offset=4980 m and a receiver at depth=1250 m.

Figure 3, schematic illustration of the methodology that uses numerical data to analyse the uncertainty of VTI parameter estimation based on P-wave slowness measurements.

Figure 4, maps of errors associated with the inversion of synthetic P-wave slownesses using Equation 1 as functions of the true anisotropy parameters ε and δ . 1% random noise has been added to the slowness vector.

Figure 5, standard deviations for the corresponding quantities shown in Figure 4.

Figure 6, maps of errors associated with the inversion of synthetic P-wave slownesses using Equation 1 as functions of the true anisotropy parameters ε and δ . 3% random noise has been added to the slowness vector.

Figure 7, standard deviations for the corresponding quantities shown in Figure 6.

Figure 8, errors inherent in the approximate Equation 2 used in the inversion of error-free synthetic phase velocities to VTI parameters ε and δ . $\theta_{\max}$ reaches 30^o (top) and 80^o (bottom).

Figure 9, error maps, associated with the inversion of synthetic P-wave velocities using Equation 2 as functions of the true anisotropy parameters ε and δ . Maximum phase angle reaches 30^o (top) and 80^o (bottom). 1% random noise is added to the slowness vectors where the velocities are derived from.

Figure 10, standard deviations for the corresponding quantities shown in Figure 9.

Figure 11, geometry of the earth model used to generate synthetic walkaway VSP data. 3C Receivers are located at every 10 m interval from the surface of the

model to 2 km depth. Sources are symmetrically distributed around the wellhead at every 20 m distances.

Figure 12, left, a sample common receiver domain data which shows vertical component of the wavefield generated by all the VSP sources and recorded by the receiver at depth 1250 m. First arrival times of the P-wave are picked in this domain and used to compute horizontal component of the slowness vector. In the middle top, travel times corresponding to a window of sources are displayed where the example source (X=5000m) is located in the middle. The graph on the right shows how a straight line is fitted to travel times of the window where the slope of this line is regarded as horizontal slowness of the P-wave generated by the example source.

Figure 13, vertical component of the wavefield generated by an example source at X=5000 m, top right. Bottom, first arrivals of P-wave generated by the same source and recorded by an array of 9 geophones centered at depth 1250 m. Top, a regression line is fitted to first break times of P-wave generated by the example source where the slope of this line is regarded as horizontal slowness of this wave.

Figure 14, P-wave phase angles computed from the slowness measurements in the borehole for the model depicted in Figure 11. Notice how P-wave maximum propagation angle decreases with depth.

Figure 15, P-wave slownesses at various maximum phase angles plotted for the receiver located at the depth 1250 m.

Figure 16, VTI parameter estimation from synthetic VSP data measured in the earth model displayed in Figure11. Maximum phase angle is limited to less than 30^o**.**

Figure 17, VTI parameter estimation from synthetic VSP data measured in the earth model displayed in Figure11. Maximum phase angle is limited to less than 45^o**.**

Figure 18, VTI parameter estimation from synthetic VSP data measured in the earth model displayed in Figure11. Maximum phase angle is limited to less than 60^o.

Figure 19, VTI parameter estimation from synthetic VSP data measured in the earth model displayed in Figure11. Maximum phase angle is limited to less than 80^o. Notice the head wave effect in the estimations at depth 600 m.

Figure 20, top, P-wave vertical slowness plotted against horizontal slowness for the receiver located at depth of 600 m. Slowness measurements for the sources at large offsets are noisy and inaccurate. At this depth, head waves precede the P-waves generated by the sources located at large offsets (bottom, SOU_X =1020 m) and can be wrongly picked as P-wave first arrivals.

Figure 21, P-wave phase velocity estimated from 3D VSP measurements at well CRC-1.

Figure 22, top, P-wave phase angles calculated from 3D VSP measurements at well CRC-1 and bottom, values corresponding to source offsets. For VTI anisotropy, this range of slowness data is wide enough to constrain elastic parameters (see also Figure 18).

Figure 23, P-wave phase angle as a function of source offset derived from 3D VSP measurements at well CRC-1.

Figure 24, P-wave vertical component of the slowness vector plotted against the horizontal component derived from 3D VSP measurements at well CRC-1. Deviation from a hyperbolic curve is an indication of azimuthal anisotropy.

Chapter 5

Figure 1, absolute errors associated with the inversion of synthetic P-wave slowness and polarization using approximate slowness-polarization relationship, Equation 1, with $\theta_{\max} = 30^o$ (top) and $\theta_{\max} = 80^o$ (bottom). Since the data was not

contaminated with errors, this Figure illustrates the errors inherent in the approximation used by the method.

Figure 2, errors of 1000 inversions of synthetic P-wave slowness and polarization using the exact slowness-polarization relationship, Equations 2 to 4, as functions of true anisotropy parameters ε and δ . In the top, $\theta_{\max} = 30^o$ and $\theta_{\max} = 80^o$ in the bottom. Slowness and polarization vectors are contaminated with 1 and 5 % random noises, respectively.

Figure 3, Standard deviations for the corresponding quantities shown in Figure 2.

Figure 4, errors of the inversion of synthetic P-wave slowness and polarization using the exact slowness-polarization relationship, Equations 2 to 4, as functions of true anisotropy parameters ε and δ . In the top, $\theta_{\max} = 30^o$ and $\theta_{\max} = 80^o$ in the bottom. Here, the error on polarization vector has been reduced to 2% while the error on slowness vectors remains 1%.

Figure 5, Standard deviations for the corresponding quantities shown in Figure 4.

Figure 6, P-wave vertical component of particle displacement recorded in a synthetic offset VSP experiment with source positioned at offset=1520 m. P-wave polarizations become distorted near to the elastic boundary at depth=800 m.

Figure 7, Synthetic VSP recordings acquired over a two-layer model used to investigate wave interference effect on P-wave polarization measurements. Receivers are positioned in the borehole at every 10 m intervals from 200 m to 2000 m. Sources are located on the surface at every 20 m intervals.

Figure 8, (top) illustrates a snapshot at time= 0.47 s of the wavefield generated by zero offset source. Vertical component of the recorded wavefield is

displayed in the middle. The linearity factor L and plots of particle motion hodograms at some selected receivers are shown in the bottom.

Figure 9, (top) illustrates a snapshot at time= 0.56 s of the vertical component of the particle velocity vector from the wavefield generated by source at offset =1000 m. Vertical component of the recorded wavefield is displayed in the middle. The linearity factor L and plots of particle motion hodograms at some selected receivers are shown in the bottom of the figure.

Figure 10 (top) illustrates a snapshot at time= 0.86 s of the vertical component of the particle velocity vector from the wavefield generated by source at offset =2000 m. Vertical component of the recorded wavefield is displayed in the middle. The linearity factor L and plots of particle motion hodograms at some selected receivers are shown in the bottom of the figure.

Figure 11 (top) illustrates a snapshot at time= 1.18 s of the vertical component of the particle velocity vector from the wavefield generated by source at offset =3000 m. Vertical component of the recorded wavefield is displayed in the middle. The linearity factor L and plots of particle motion hodograms at some selected receivers are shown in the bottom of the figure.

Figure 12 (top) illustrates a snapshot at time= 1.5 s of the vertical component of the particle velocity vector from the wavefield generated by source at offset =4000 m. Vertical component of the recorded wavefield is displayed in the middle. The linearity factor L and plots of particle motion hodograms at some selected receivers are shown in the bottom of the Figure.

Figure 13, bottom, vertical component of the wavefield generated by all the sources in Figure 7 and recorded by the receiver located at depth=900 m. P-wave first arrivals are picked and displayed with yellow curve in this figure. Top right, is a display of data recorded from sources at large offsets (>5000 m) where head waves have preceded P-waves.

Figure 14, first arrival times of the P-wave generated by all the sources in Figure 7 and recorded by all the receivers in the borehole.

Figure 15, P-wave phase angles as a function of source offset and receiver depth for the model displayed in Figure 7. Notice the noise caused by head wave interference near the interface. Phase angles lower than 30^o is restricted within the trapezoid.

Figure 16, P-wave polarization dip angles as a function of source offset and receiver depth for the model displayed in Figure 7. Head wave interference effect introduce noise in polarization measurements near the interface.

Figure 17, difference between P-wave polarization dip and phase angle as a function of source offset and receiver depth for the model displayed in Figure 7. The deviation is small for propagation angles up to 30^o but increases up to 13^o for larger phase angles.

Figures 18, synthetic slowness-polarization data (black dots) selected for the inversion at depths=900 m. Black curve, is the best fit function to the data. Green dots are the slowness and polarization data which are generated by the application of Christoffell equation with elastic properties taken from the first layer in the model. The green curve (overlapped by red curve here) is the same data derived by using exact VTI slowness-polarization relationship (Equations 2 to 4). Red curve is Grechka and Mateeva (2007) approximation.

Figures 19, synthetic slowness-polarization data (black dots) selected for the inversion at depths=1100 m. Black curve, is the best fit function to the data. Green dots are the slowness and polarization data which are generated by the application of Christoffell equation with elastic properties taken from the second layer in the model. The green curve is the same data derived by using exact VTI slowness-polarization relationship (Equations 2 to 4). Red curve is Grechka and Mateeva (2007) approximation.

Figures 20, the results of VTI inversion using exact slowness-polarization relationship for the data acquired in two-layer model shown in Figure 7.

Figures 21, P-wave polarization dip, ν computed from 3C receiver measurements of the synthetic VSP acquired on CRC-1 model.

Figure 22, results of the inversion using slowness-polarization data derived from the synthetic walkaway VSP at well CRC-1 and using exact relationship given by Equations 2-4.

Chapter 6

Figure 1, orientation of the most general fracture set is defined the azimuth α and dip β of the unit vector n that is orthogonal to the fracture plane.

Figure 2, anisotropy parameters of the orthorhombic medium that is generated by inserting a single set of vertical fractures in a VTI background. Fractures are assumed to be rotationally invariant, filled with gas (dry) and oriented along x_2 direction. Intensity of the fracturing in the medium (defined with fracture weaknesses) is minor in the left column ($\delta_N = 0.1$) and increases to moderately fractured in the middle column ($\delta_N = 0.3$) and intensely fractured in the right column ($\delta_N = 0.5$). Background VTI medium is represented by δ and ε values on horizontal and vertical axes, respectively.

Figure 3, Estimation of the valid range for the approximate relationship of P-wave velocity in orthorhombic media. Numerical velocities are generated by using Christoffel equation. To estimate the validity of the approximation, no error is added to the velocities. Orthorhombic medium, described in the right side of the Figure, is created by inserting a single set of vertical fractures ($\delta_N = 0.1$) into a VTI background medium (ε and δ) where fractures are parallel to x_2 direction.

Figure 4, estimation of the valid range for the approximate relationship of P-wave velocity in orthorhombic media. Numerical velocities are generated by using Christoffel equation. To estimate the validity of the approximation, no error is

added to the velocities. Orthorhombic medium, described in the right side of the Figure, is created by inserting a single set of vertical fractures ($\delta_N = 0.3$) into a VTI background medium (ε and δ) where fractures are parallel to x_2 direction.

Figure 5, the errors related to the inversion of the exact velocity relationship in orthorhombic medium for the anisotropy parameter $\delta^{(1)}$ where 1% random noise has been added to the slowness vectors. $\theta_{\max}$ decreases from 80^o (top) to 30^o (bottom) and fracture weakness increases from left to right ($\delta_N = 0.1$, $\delta_N = 0.3$ and $\delta_N = 0.5$). Vertical and horizontal axes represent anisotropy parameters of the background VTI medium.

Figure 6, the errors related to the inversion of the exact velocity relationship in orthorhombic medium for the anisotropy parameter $\delta^{(2)}$ where 1% random noise has been added to the slowness vectors. $\theta_{\max}$ decreases from 80^o (top) to 30^o (bottom) and fracture weakness increases from left to right ($\delta_N = 0.1$, $\delta_N = 0.3$ and $\delta_N = 0.5$). Vertical and horizontal axes represent anisotropy parameters of the background VTI medium.

Figure 7, the errors related to the inversion of the exact velocity relationship in orthorhombic medium for the anisotropy parameter $\delta^{(3)}$ where 1% random noise has been added to the slowness vectors. $\theta_{\max}$ decreases from 80^o (top) to 30^o (bottom) and fracture weakness increases from left to right ($\delta_N = 0.1$, $\delta_N = 0.3$ and $\delta_N = 0.5$). Vertical and horizontal axes represent anisotropy parameters of the background VTI medium.

Figure 8, the errors related to the inversion of the exact velocity relationship in orthorhombic medium for the anisotropy parameter $\varepsilon^{(1)}$ where 1% random noise has been added to the slowness vectors. $\theta_{\max}$ decreases from 80^o (top) to 30^o (bottom) and fracture weakness increases from left to right ($\delta_N = 0.1$, $\delta_N = 0.3$

and $\delta_N = 0.5$). Vertical and horizontal axes represent anisotropy parameters of the background VTI medium.

Figure 9, the errors related to the inversion of the exact velocity relationship in orthorhombic medium for the anisotropy parameter $\varepsilon^{(2)}$ where 1% random noise has been added to the slowness vectors. $\theta_{\max}$ decreases from 80^o (top) to 30^o (bottom) and fracture weakness increases from left to right ($\delta_N = 0.1$, $\delta_N = 0.3$ and $\delta_N = 0.5$). Vertical and horizontal axes represent anisotropy parameters of the background VTI medium.

Figure 10, the errors related to the inversion of the exact velocity relationship in orthorhombic medium for the anisotropy parameter $\delta^{(1)}$ where 3% random noise has been added to the slowness vectors. $\theta_{\max}$ decreases from 80^o (top) to 30^o (bottom) and fracture weakness increases from left to right ($\delta_N = 0.1$, $\delta_N = 0.3$ and $\delta_N = 0.5$). Vertical and horizontal axes represent anisotropy parameters of the background VTI medium.

Figure 11, the errors related to the inversion of the exact velocity relationship in orthorhombic medium for the anisotropy parameter $\delta^{(2)}$ where 3% random noise has been added to the slowness vectors. $\theta_{\max}$ decreases from 80^o (top) to 30^o (bottom) and fracture weakness increases from left to right ($\delta_N = 0.1$, $\delta_N = 0.3$ and $\delta_N = 0.5$). Vertical and horizontal axes represent anisotropy parameters of the background VTI medium.

Figure 12, the errors related to the inversion of the exact velocity relationship in orthorhombic medium for the anisotropy parameter $\delta^{(3)}$ where 3% random noise has been added to the slowness vectors. $\theta_{\max}$ decreases from 80^o (top) to 30^o (bottom) and fracture weakness increases from left to right ($\delta_N = 0.1$, $\delta_N = 0.3$ and $\delta_N = 0.5$). Vertical and horizontal axes represent anisotropy parameters of the background VTI medium.

Figure 13, the errors related to the inversion of the exact velocity relationship in orthorhombic medium for the anisotropy parameter $\varepsilon^{(1)}$ where 3% random noise has been added to the slowness vectors. $\theta_{\max}$ decreases from 80^o (top) to 30^o (bottom) and fracture weakness increases from left to right ($\delta_N = 0.1$, $\delta_N = 0.3$ and $\delta_N = 0.5$). Vertical and horizontal axes represent anisotropy parameters of the background VTI medium.

Figure 14, the errors related to the inversion of the exact velocity relationship in orthorhombic medium for the anisotropy parameter $\varepsilon^{(2)}$ where 3% random noise has been added to the slowness vectors. $\theta_{\max}$ decreases from 80^o (top) to 30^o (bottom) and fracture weakness increases from left to right ($\delta_N = 0.1$, $\delta_N = 0.3$ and $\delta_N = 0.5$). Vertical and horizontal axes represent anisotropy parameters of the background VTI medium.

Figure 15, the geometry of the 2D model and parameters of the synthetic walkaway VSP survey.

Figure 16, values of $\delta(\phi)$ computed for the orthorhombic layer number 11 using Equations 62 and 63 of Chapter 3.

Figure 17, values of $\varepsilon(\phi)$ computed for the orthorhombic layer number 11 using Equations 62 and 63 of Chapter 3.

Figure 18, an example of P-wave travel times recorded by the receiver positioned at depth 1500 m within the orthorhombic layer.

Figure 19, displays the values of the 3 components of the slowness vector computed from the travel times recorded by the receiver located at depth 1500 m within the orthorhombic layer.

Figure 20, top left, magnitude of the P-wave slowness vector $|P|$ and top right, normal vectors to P-wave wavefront computed for the receiver located at depth

List of Tables

Chapter 2

Chapter 4

Chapter 6

Chapter 1, Introduction

"The time has come when seismic anisotropy should be a part of every geophysicist's expertise" ***Leon Thomsen***

A few years back in time, late 70's and 80's, the ultimate goal of seismic data processing was to generate a reasonable image of the subsurface based on 2D seismic data where prospectus geometries could be mapped, depth converted and put forward for drilling campaign. Simple forms of quantitative interpretation had been noticed and practiced by the interpreters in the form of relating seismic amplitude brightening or dimming to subsurface gas accumulations. In recent years however, more quantitative information have been extracted from seismic data to meet the growing challenges in hydrocarbon exploration and production industry. It is now a realistic expectation to acquire clear images from 3D long-offset/wide-azimuth seismic surveys and to obtain more information about the properties of the subsurface rocks and fluids (rock characterization) and use this information to monitor production/injection related changes with time (4D). To meet these expectations, more realistic models (equations) and less simplified geological concepts have to be incorporated in our analysis. It is along this new working attitude that building anisotropic earth models have recently become the centre of attention for geophysicists involved in the exploration seismology. One good reason of reluctance in using anisotropic models in the past was the complexity of the anisotropic workflows which requires high speed computers to decrease computation time for anisotropic algorithms. The concept of anisotropic earth represents a more realistic picture of the subsurface in the sense that the effect of geological layering, fractures and the stress on seismic velocities are incorporated into calculations rather than ignoring it in a simple isotropic earth model. There is a downside however; their usage includes estimation of several parameters that can be sometimes non-unique and poorly constrained. Nevertheless, abundant of data recorded over wider source-receiver offsets and azimuths (especially for marine acquisition) and the worth of extra subsurface information that can be extracted through the usage of a

more realistic earth model make the analysis of the angle/azimuth dependency of seismic velocities an interesting subject for the purposes of the subsurface characterization.

In the exploration context, as bigger and shallower hydrocarbon prospects are discovered in earth sedimentary basins, exploration of new reserves becomes more challenging in the sense that new explorations would naturally occur in deeper strata than before and of a smaller size. Looking for a smaller target in a deeper interval with seismic tools would not be an easy task as seismic waves would have to travel a larger distance for which stronger sources have to be employed for extra cost. In addition, a larger travel distance means that a greater portion of wave components with higher frequency will be attenuated along the way down and back to the surface. The loss of higher frequency content of the wave spectrum means larger resolution and less accuracy in both the vertical and lateral directions. Another issue would be the risk associated with the drilling of deep targets. Larger depths are usually harder to drill and usually require incorporating multi-parameter geomechanical earth models to identify and avoid drilling hazards such as over-pressured gas pockets and fracture swarms that leads to lost circulation, washouts, stuck pipe, loss of tools and equipment, additional casing strings, and unplanned sidetracks. This makes the job costly and most of the times uneconomic if not properly foreseen by the drillers.

To overcome these problems, exploration seismology has chosen to apply more advanced technology in acquisition, processing and interpretation of seismic data. Seismic vessels are now capable of towing a dozen of streamers which are hundreds of meters apart and cover very long offsets. Acquisition of long-offset seismic data has revealed an important manifestation of anisotropy, non-hyperbolic move out on large spreads that cannot be reproduced with isotropic velocity models. On the other hand, acquisition of long offset data has made it possible to analyse seismic amplitudes as a function of source-receiver offset (AVO). Seismic amplitudes were first used for quantitative characterization of the subsurface in the 70’s when “bright spots” on stacked sections were used to delineate gas reservoirs. If properly processed, P-wave amplitudes may be inverted (isotropic) to obtain both P- and S-wave velocities and

density of the subsurface formations. The amplitudes have to be corrected for a large number of angle-dependent effects, namely: source and receiver directivity, transmission coefficient, geometrical spreading, reflector curvature and thin-bed tuning before using them as a rough estimate for the earth reflectivity. The velocity information can then be used to separate different lithologies and fluid contents in a hydrocarbon bearing rock. However, results of isotropic AVO inversion would be uncertain if the effect of velocity anisotropy (along with all the other effects) has not been accounted for during the processing stage. The anisotropy effects can be large in some cases and usually influence data in three ways (Thomsen, 2002): a dynamic effect on P-wave reflection amplitudes (Banik, 1987 and Rueger 1996), a kinematic effect on AVO (ray angle cannot be used as incident angle and phase angle has to be computed) and an effect on incident-wave amplitude (source radiation amplitude varies with angle in anisotropic media).

In a flat-lying geology, azimuthal variation in P-wave travel-times and reflection amplitudes can also be present mainly as a result of the asymmetric stress field in the earth subsurface (stress deformed pore space or grain shape of micro-cracks and fractures). Azimuthally dependent reflection coefficients have been traditionally used for anisotropic parameter estimation and fracture characterization. In fact, pre-stack seismic amplitude variation with offset and azimuth (AVAZ) is an important tool in the analysis of earth fractures and estimation of in situ stress (Mallick et al., 1998, Lynn et al., 1999, Bakulin et al., 2000 b,c). Production related stress changes in a hydrocarbon reservoir will cause anisotropic velocity changes both in the reservoir and also in the surrounding rocks that can be detected by 4D travel-time observations (Sayers, 2004, Herwanger and Horne, 2005, Fuck et al., 2009). Herwanger and Horne (2009) establish a link between reservoir geomechanics and anisotropic velocity changes using a synthetic model of an oil reservoir that is undergoing depletion.

Another common example of anisotropy-related phenomena that worth mentioning here is the mis-tie observed in time to depth conversion of horizon interpretations using isotropic velocity models. This distortion appears as depth over-estimation up to 10%

for a typical value of 0.1 for Thomsen parameter δ (will be defined in Chapter 3) which is not accounted for in a standard (isotropic) processing workflow.

1.1 Anisotropy versus heterogeneity

So, what is the anisotropy? A medium is regarded as anisotropic with respect to a physical parameter if the magnitude of this parameter changes with the direction of the measurement. Heterogeneity is defined to be the dependence of the parameter upon position. How heterogeneity and anisotropy are related? It is believed that an ordered heterogeneity or a fabric on the small scale, e. g. flat lying of shale grains in microscopic scale, appears as anisotropy on the large scale (seismic wavelength). It has been known from field and laboratory measurements (Wang, 2002) that seismic velocities exhibit directional dependence or anisotropy. Velocity anisotropy in sedimentary basins can be caused by the intrinsic structure of the rocks (clay particles in the shale example), thin layering, natural fracture systems and non-hydrostatic stress. Heterogeneity and anisotropy are wavelength-dependent. For example, a stack of thin geological layers will appear heterogeneous with respect to P-wave velocity if measured by short wavelength well logs whereas the same medium's response is homogenous (but anisotropic) to long wavelength seismic waves. Velocity variation with direction in a two dimensional plane can be symmetrical with respect to vertical (or horizontal) axis of the plane (Figure 1). The plane with symmetrical velocity behaviour is called a symmetry plane and the corresponding axis is the symmetry axis of this plane.

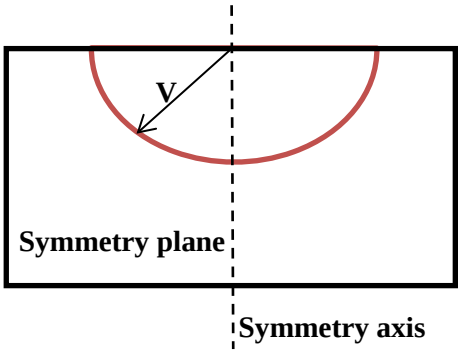

Figure 1, velocity varies symmetrically with respect to the symmetry axis in the symmetry plane of an anisotropic medium.

1.2 Why do we need to consider seismic anisotropy?

Anisotropy is widespread: geological layering and the abundant shale formations in sedimentary basins give rise to seismic anisotropy as a scale dependent phenomenon. Similarly asymmetric stress field produce fracture systems which also, yet in a different way result in the seismic anisotropy.

Theoretical foundation of seismic anisotropy has been well established and mathematically formulated, Rudzki (1898), Postma (1955), Helbig (1956), Backus (1962), Crampin (1981, 1985), Lynn and Thomsen (1986), Willis et al. (1986), Martin and Davis (1987) have shown that the anisotropy has a first-order effect on shear wave propagation by splitting a shear wave into the fast and slow modes with orthogonal polarizations. Tsvankin et al., (2010) believe that the progress in anisotropic P-wave processing is largely dedicated to the parameterization of the transverse isotropic models by Thomsen (1986) and formulation of the P-wave time-processing parameter η by Alkhalifah and Tsvankin (1995). Transverse isotropy (hexagonal or polar anisotropy) has a single axis of rotational symmetry and seismic velocity in such a model depends just on the angle between the propagation direction and the symmetry axis. There is also one more symmetry plane, that is isotropic and is perpendicular (transverse) to the symmetry axis. A historical review of developments in seismic anisotropy can be found in Helbig and Thomsen (2005). Advances in parameter estimation and acquisition of wide offset/azimuth multi-component 3D surveys has made it possible to incorporate the effect of anisotropy in seismic exploration and monitoring. On the other hand, ignoring anisotropy in for example, seismic data processing, may result in blurred migrated images, mis-positioning of the reflectors laterally and in depth and incorrect analysis of reflection amplitudes (Tsvankin et al., 2010). Inadequacy of isotropic velocity models is well exposed in pre-stack depth migration algorithms with high sensitivity to the accuracy of the velocity field (Tsvankin et al., 2010). Interpretation of seismic amplitudes without accounting for the effect of seismic anisotropy can also be incorrect. Instead, application of anisotropic models can significantly improve well ties, focusing and positioning of steeply dipping reflectors, fault imaging and geomechanical earth models.

1.3 Notation for anisotropic media

Because anisotropy adds complexity to seismic data processing and analysis it is important to have standard parameterization of the anisotropic models (see Chapter 3) to avoid confusion and misuse of various terms. Thomsen (1986) suggested to describe a transverse isotropy (TI) medium by the symmetry-direction velocities of P- and S-waves and three dimensionless parameters ε , δ and γ to characterize the anisotropy. Alkhalifah and Tsvankin (1995) proposed a single parameter η for anisotropic time processing of P-wave reflection data for VTI media. These have been regarded as a breakthrough in the progress of anisotropic P-wave processing and inversion by solving the problem of anisotropic notation. Principles of Thomsen (1986) notation for TI models have been generalized by later researchers to incorporate lower symmetry orthorhombic (Tsvankin, 1997), monoclinic (Grechka et al., 2000) and triclinic models (Mensch and Rosolofosaon, 1997).

1.4 Local anisotropic parameter estimation from VSP measurements

Incorporating the effect of anisotropy in seismic interpretation and processing is not overly hard. However recovering or estimating anisotropic parameters of a multi-layered medium is challenging. In seismic processing, it is in general necessary to supplement surface P-wave reflection data with borehole measurements even for isotropic flows and it is a must for anisotropic processing and recovery of elastic parameters. Of particular importance for this process is the use of vertical seismic profiling (VSP). This type of survey utilizes surface sources and borehole receivers to enable recording of both transmitted and reflected wavefields. VSP data can be acquired by using only one single source that is located near the well head (zero offset VSP or ZVSP) or at a distance to well (offset VSP or OVSP). A walkaway VSP (WVSP) geometry is when successive sources are positioned along a single traverse that crosses the well head. 3D VSP data are commonly recorded for a certain depth interval in the borehole by synchronous recording with 3D surface seismic data.

Typical VSP set-up utilizes three components receivers which are oriented as three orthogonal elements or in less common using Galperin (1974) system (oriented at 54.7^o to vertical) from which the polarizations of each wave type can be estimated. A string of

geophones in the borehole can be used to record P-wave first arrival times as a function of geophone depth to estimate P-wave vertical (phase) slowness that is local to the recording interval. For horizontally layered strata, P-waves horizontal (phase) slowness is preserved along the ray and can be measured on the earth surface and be transferred to the receiver level. In the receiver domain, P-wave horizontal slowness can be regarded as the rate of change in first arrival times as a function of distance between the sources on the surface.

In the next part, I will briefly explain how P-wave slownesses and polarizations derived from a VSP experiment can be used to estimate anisotropy parameters of the medium that is local (size of a typical seismic wavelength) to the receiver in the survey borehole. The accuracy of the slowness and polarization measurements will have a significant influence on anisotropy parameter estimation based on VSP data.

1.4.1 Local anisotropy parameter estimation using P-wave slownesses only

Estimation of P-wave slowness surfaces is very dependent on the overburden conditions. If the overburden composed of horizontal, laterally homogeneous layers, the horizontal components of the slowness vector can be measured on the earth surface and transferred to the receiver location in the borehole. This technique is known as slowness method. In the slowness technique, vertical component of the P-wave slowness vector is measured in the borehole that is vertical. Travel times of the wave excited on the surface are recorded by a string of geophones in the vertical borehole. Vertical slowness is then regarded as travel time gradient when VSP data are sorted in common-shot gather. Horizontal slowness is usually measured on the earth surface. In the common-receiver domain, the gradient of the travel times with respect to the distance between the sources on the surface are regarded as the horizontal component of the slowness vector. Assumption of lateral homogeneity in the overburden enables us to use Snell's law to transfer the measured slownesses to the receiver depth. The stiffness tensor C can then be estimated by solving Christoffel equation. However, for a given anisotropy model, only certain elements of the stiffness tensor C can be reliably estimated from P-wave measurements. For example, stiffness coefficient that describes SH-wave velocity in an anisotropy medium can never be constrained by inverting P-wave slownesses.

1.4.2 Local anisotropy parameter estimation using P-wave slowness and polarization

Polarization vector is defined as the direction of particle motion as a result of wave's medium excitation. If the medium in the vicinity of the borehole is homogeneous and the interference effect of various waves can be separated on VSP seismogram, polarization vector *U* of the direct arrivals of the P-wave can be measured with 3C geophones in the borehole (Figure 2). Polarization information together with the slowness measurements can then be used in the Christoffel equation to estimate the some components of the stiffness tensor.

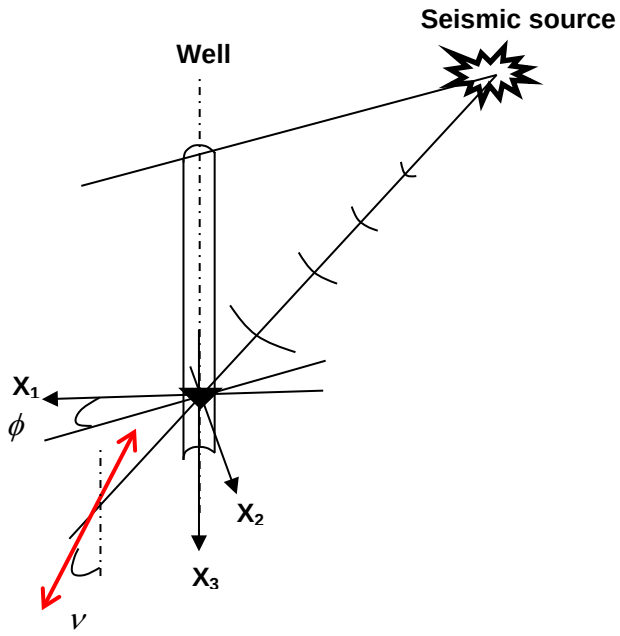

Figure 2, schematic view of estimating wave polarization in the receiver locality in a 3C VSP experiment. Polarization dip, ν is the angle between polarization direction and the vertical axis.

A three component multi-offset multi-azimuth VSP offers the best dataset for determination of anisotropy parameters as it enables wide azimuth/phase angle information to be collected. Phase angle range depends on the ratio between the receiver depth and the source offset. Also, VSP estimates are made at seismic frequencies and as so they have advantage to well log estimates that are made at higher frequency range ($10^3 - 10^4$ Hz) so that up scaling of the results may be needed.

Miller and Spencer (1994) introduced a workflow to invert a walkaway VSP arrival times recorded in a vertical borehole for elasticity parameters of a TI medium assuming a horizontally layered medium and lateral homogeneity. In their methodology, horizontal slowness is given by the change in arrival time with horizontal source offset and the vertical slowness is given by the change in arrival time with vertical receiver depth. Grechka and Mateeva (2007) introduce a method that utilizes P-wave vertical slowness and polarization dip measured in a walkaway VSP experiment to estimate elastic anisotropic parameters of the TI medium. Their method does not require horizontal components of the slowness vector and can be applied in the case of lateral heterogeneity in the overburden.

A wide azimuth, multi-level, multi-component VSP survey comprises a favourable geometry for estimation of a complete triclinic local stiffness tensor beneath a laterally homogeneous overburden (Bóna and Slawinski, 2008). Dewangan and Grechka (2003) go beyond the standard VTI symmetry and use P- and S-wave slownesses (derived from travel times) and polarization directions measured in a 3D 3C VSP survey (Vacuum Field, New Mexico, USA) to estimate anisotropy parameters of an orthorhombic model that best fits the data. Kochetov and Slawinski (2009) examine all the orientations of the orthorhombic tensor and confirm the results derived by Dewangan and Grechka (2003). Grechka et al. (2007) is another example of anisotropy parameter estimation for lower symmetry media, they invert wide-azimuth VSP data acquired at Rulison Field (Colorado, USA) for Tsvankin's (1997) parameters of an orthorhombic media and show that the estimated anisotropic model is consistent with the presence of gas in vertical fractures embedded in a VTI background.

We can categorize VSP methods for recovery of elastic parameters into: a) one that uses slownesses, and b) methods that use both slowness and polarizations. I termed them slowness and slowness-polarization methods, respectively.

For the purposes of the recovery of a medium parameters one can utilize P-wave information or both P-wave and the S-wave measurements. The choice is influenced by the overburden properties which may limit data that are required for the inversion. Beneath a laterally homogeneous overburden, slowness only methods for which no

polarization information is required can be applied (Gaiser, 1990; White et al., 1993; Miller and Spencer, 1994; Williamson and Maocec, 2000; Jílek et al., 2003; Grechka et al., 2006; Owusu et al., 2011). In this method, vertical component of the slowness vector is measured locally at the geophone depth assuming the borehole is vertically oriented whereas the horizontal components are measured on the earth surface and transferred to the receiver level using Snell's law.

Use of polarization information to estimate parameters of local vertical transverse isotropy (VTI) beneath a laterally heterogeneous overburden was first proposed by White et al. (1983) and further developed by de Parscau (1991) and Hsu et al. (1991). In the slowness-polarization method, anisotropy is estimated from the slowness vectors and polarization directions of P- and SV-waves (Horne and Leaney, 2000; Dewangan and Grechka, 2003). For a laterally heterogeneous overburden two major issues arise:

1. Two shear modes (slow and fast) may be difficult to separate. This should be particularly noticed where there is no independent azimuth measurement for the geophones in the borehole. However, this would not be a problem if the velocity structure of the overburden is 2D and SH-waves are absent (Grechka and Mateeva, 2007). Esmersoy (1990) reviews the short comings of the existing methods for shear wave separation such as hodogram analysis (Crampin, 1985), Alford's (1986) source-receiver rotation, Naville's (1986) cross correlation technique and Nicoletis et al. (1988) transmission operator and presents an alternative way to overcome the first issue based on a local vector wavefield decomposition technique.
2. Second issue relates to the horizontal slowness that is usually measured at the surface. In the case of severe overburden heterogeneity, horizontal component of the slowness vector, measured on the earth surface cannot be used at the receiver depth unless the effect of heterogeneity in the overburden has been corrected. Bakulin et al., 2000 a presents an example of how this correction can be implemented in practice.

To avoid the limitations related to the overburden heterogeneity and to avoid the requirement to separate two shear waves, Grechka and Mateeva (2007), following the

work of Williamson and Maocec (2001), Zheng and Pšenčík (2002) and Gomez et al. (2004) utilize two P-wave local measurements, the vertical slowness and the polarization dip with the vertical axis to estimate local anisotropy parameters beneath a complex structure. Dewangan and Grechka (2003) present three different scenarios for the level of complexity in the overburden but conclude that all 21 stiffness coefficients can still be found given a sufficient polar and azimuthal coverage of the data (both P- and S-waves). They showed that the errors in the estimations depend on the complexity of the overburden which determines our ability to use the horizontal components of the slowness vector (measured at the surface).

1.5 Research motivation and objectives

One of the most recent applications of anisotropic model building has been in the fields of reservoir geomechanics where time-lapse anisotropic changes in P- and S-waves velocity have been proposed to use as a tool to validate and monitor geomechanical signals of a hydrocarbon reservoir that is undergoing oil production or fluid injection (Hatchell and Bourne, 2005; Staples et al., 2007). Herwanger and Horne (2009) see a potential for application of 4D seismic measurements to infer 3D changes in triaxial stress state of a reservoir and the overburden (Sarkar et al., 2003; Sayers, 2004; Herwanger and Horne, 2005). Knowledge of the triaxial stress state has important applications in drilling and reservoir management. They describe a synthetic example of an oil reservoir under production where the reservoir compaction and the resulting overburden stretch changes the state of triaxial (nonhydrostatic) stress in the reservoir rock, in the overburden and in the underburden strata. They describe a workflow that starts with building a reservoir geomechanical model to predict subsurface deformations and the resulting stress and strain changes as the reservoir produces. Next, they propose to use a stress-sensitive rock-physics model (Mavko et al., 1995; Schoenberg and Sayers, 1995; Zatsepin and Crampin, 1997; Sayers, 2002; Prioul et al. 2004; Shapiro and Kaselow, 2005; Sarout et al., 2007; Verdon et al., 2008) to convert nonhydrostatic stress changes to anisotropic velocity changes. Finally, using predicted subsurface deformations and velocity changes, stress-induced time-lapse seismic attributes such as travel-time change in the overburden or shear wave splitting can be computed.

Herwanger and Horne (2009) use stress sensitive rock-physics model based on third-order elasticity equations of Prioul et al. (2004) that are calibrated by laboratory measurements (Prioul and Lebrat, 2004) to compute elastic stiffness tensor C_{ij} (with symmetry planes aligned with the local Cartesian coordinate system) and anisotropic P- and S-wave velocities in a new stress state as a function of stiffness tensor C_{ij}^0 in a reference stress state and changes in triaxial strains ε_{11}, ε_{22}, ε_{33}, and sensitivity coefficients c_{ijk}:

$$
\begin{aligned}
C_{11} &\cong C_{11}^0 + c_{111}\varepsilon_{11} + c_{112}(\varepsilon_{22} + \varepsilon_{33}) \\
C_{22} &\cong C_{11}^0 + c_{111}\varepsilon_{22} + c_{112}(\varepsilon_{11} + \varepsilon_{33}) \\
C_{33} &\cong C_{33}^0 + c_{111}\varepsilon_{33} + c_{112}(\varepsilon_{11} + \varepsilon_{22}) \\
C_{12} &\cong C_{12}^0 + c_{112}(\varepsilon_{11} + \varepsilon_{22}) + c_{123}\varepsilon_{33} \\
C_{13} &\cong C_{13}^0 + c_{112}(\varepsilon_{11} + \varepsilon_{33}) + c_{123}\varepsilon_{22} \\
C_{23} &\cong C_{13}^0 + c_{112}(\varepsilon_{22} + \varepsilon_{33}) + c_{123}\varepsilon_{11} \\
C_{66} &\cong C_{66}^0 + c_{144}\varepsilon_{33} + c_{155}(\varepsilon_{11} + \varepsilon_{22}) \\
C_{55} &\cong C_{44}^0 + c_{144}\varepsilon_{22} + c_{155}(\varepsilon_{11} + \varepsilon_{33}) \\
C_{44} &\cong C_{44}^0 + c_{144}\varepsilon_{11} + c_{155}(\varepsilon_{22} + \varepsilon_{33}) \qquad \textbf{(1)}
\end{aligned}
$$

Where two of the five stress sensitivity coefficients c_{144} and c_{155} can be expressed in terms of the other there coefficients as: $c_{144} = (c_{112} - c_{123})/4$ and $c_{155} = (c_{111} - c_{112})/4$.

If the axes of the local (Cartesian) coordinate system are in alignment with the principal directions of the strain change tensor (with components ε_{ij}), shear stresses disappear and related normal stress changes σ_{ij} ($i = j$) can then be computed by using inverse

Hooke's law and knowledge of static Young's modulus E and Poisson's ratio υ of the medium. In an orthorhombic media with symmetry planes aligned with the principal directions of the stress change tensor, inverse Hooke's law is given by (Jaeger et al., 2007):

$$\varepsilon_{11} = \frac{1}{E_1}\sigma_{11} - \frac{\upsilon_{21}}{E_2}\sigma_{22} - \frac{\upsilon_{31}}{E_3}\sigma_{33},$$

$$\varepsilon_{22} = -\frac{\upsilon_{21}}{E_2}\sigma_{11} + \frac{1}{E_2}\sigma_{22} - \frac{\upsilon_{32}}{E_3}\sigma_{33},$$

$$\varepsilon_{33} = -\frac{\upsilon_{31}}{E_3}\sigma_{11} - \frac{\upsilon_{32}}{E_3}\sigma_{22} + \frac{1}{E_3}\sigma_{33} \qquad \textbf{(2)}$$

Static elastic moduli of the orthorhombic medium can be determined by laboratory tests. For example E_1 is the ratio between applied stress σ_{11} and resulting strain ε_{11} in the x direction in a uniaxial stress test.

Similar to a hydrocarbon producing reservoir, injection of CO_2 into a depleted oil/gas reservoir can cause changes in the state of triaxial stress of the reservoir and the overburden rocks. Changes in the stress state of the subsurface rocks can result in the generation of new fracture systems or reactivation of the existing faults and fracture networks which in any case can lead to CO_2 leakage to overlying water reservoirs or sometimes the earth surface. A similar methodology as with Herwanger and Horne (2009) can be utilized in a CO_2 geosequestration project to record time-lapse anisotropy signals in the reservoir and the overburden rock and use these data to monitor the stress state of the subsurface in relation to fault/fracture generation or reactivation. On the other hand, estimation of the earth elastic parameters based on downhole or surface seismic measurements is still a young subject in exploration seismology where its time-lapse applications in earth stress monitoring (see Equations 1 and 2 for an orthorhombic earth) is yet to be recognized by the industry in the future. As a result, the first and necessary step in the application of time-lapse seismic anisotropy in underground stress monitoring is to realize the limitations of each elastic parameter estimation method through expressing the uncertainties in a quantitative manner.

Several available methods for estimating local P-wave anisotropy (and elastic) parameters of a medium surrounding the geophone interval in a VSP survey by utilizing slowness and polarizations measurements were described in previous parts of this chapter. Clearly, in order to use 4D elastic parameter estimates derived from borehole measurements (C_{ij} and C_{ij}^{0} in Equation 1) to infer changes in the stress state of a reservoir rock and the overburden, reliability of these estimates, applicability and limitations of each estimation method have to be quantified with respect to parameters such as the input data type and the medium conditions.

The idea of using 4D elastic parameter estimates, derived from VSP measurement to infer changes in the subsurface stress state, describing reliability of each parameter estimation method in a quantitative manner and classifying them based on the accuracy comparison of the estimation methods could be the only hope for detecting weak time lapse seismic signals as is the case with Otway site. Hence developing new methodology that can utilise changes in anisotropic elastic properties to monitor and better characterise the reservoir is the main objective of this thesis. This is in alignment with seismic monitoring and verification objectives for the CO2CRC Otway project as will be described in Chapter 2. One of the main objectives of the CO2CRC Otway project (or any) CO_2 storage project is to assure community that underground alteration as a result of CO_2 injection will not have any adverse consequences on the environment. This objective can be achieved through monitoring of the stress state of the reservoir and the overburden rocks to make sure that the stress change as a result of CO_2 injection has not reactivated the existing faults and fracture network which may subsequently lead to CO_2 leakage into shallower aquifers or the earth surface.

To conduct this research, I will first put forward a number of research questions in the next part that will help me to orient my research activity in a direction that will facilitate finding the answers to these questions.

1.6 Thesis questions and research direction

In the previous parts of this chapter, I explained the concept and importance of seismic anisotropy and pointed out numerous ways that modern seismic industry will benefit from building anisotropic earth models. I then explained the principles and challenges of

the VSP methods that are mostly used to estimate earth anisotropy parameters as a first step in building an anisotropy model. While being so popular for anisotropy parameter estimation, no accuracy comparison (the main subject of my research) has ever been attempted between these methods in a quantitative manner. However, in order to conduct a comparison, the following questions have to be first answered for every individual VSP method in the analysis. First, what is the reliability of each estimation method in the presence of measurement noise. Second, what is the accuracy of the estimated parameters with respect to VSP geometry (source-receiver offset). Third, would and how the anisotropy of the medium influences accuracy of the estimations? As soon as we establish a quantification technique that addresses the three listed issues, we will be able to make a comparison between the various methods and evaluate the limitations and applicability ranges of every method.

Now, I will summarize my main research question from which this thesis work will be based upon. The main question is: for a specific type of VSP geometry (walkaway/ 3D VSP), assuming a certain type of data measurements (slownesses only or slownesses and polarizations), using certain types of seismic wave (P- and/or S-wave) and within the certain noise level which anisotropy (or elastic) parameters can be estimated and what would be the accuracy of the estimated parameters? Would (and how) the anisotropy in the medium influence the accuracy of the parameter estimation using VSP methods?

In order to find the answer to all of the questions raised earlier, I will mostly focus on the accuracy analysis of the methods that are utilized for local VTI and Orthorhombic anisotropy parameter estimation and are based on P-wave slowness and polarization measurements. I will mostly follow and continue the work explained by Asgharzadeh et al., 2012 and Asgharzadeh et al., 2013, and use numerically generated slowness and polarization data to analyse performance of the methodology and estimate uncertainty.

In the VTI (polar) case, anisotropy is independent of measurement azimuth and has similar parameters within any vertical plane of this medium; hence, measurements along a single 2D profile should suffice the purpose of the anisotropy parameter estimation. This is the reason why walkaway VSP measurements have been traditionally used to constrain VTI elastic parameters. To analyse uncertainties related to VTI parameter

estimation methods, I will generate numerical data that are measureable in a conventional walkaway VSP experiment whereas in the orthorhombic case, data will be generated over a wide range of azimuths and phase angles to replicate the data that are measureable in a 3D VSP survey. I will also make use of synthetic VSP seismograms to evaluate the methodology and subsequently apply it to real VSP measurements acquired during stage 1 of the monitoring and verification program of the CO2CRC Otway project. The detailed explanation of methodology described above, numerical data generation and VSP dataset available to use in this analysis will be presented in the later parts.

1.7 CO2CRC Otway project for CO_2 geosequestration and previous anisotropy studies

CO2CRC Otway project is the first Australian project for CO_2 geosequestration and includes two stages of CO_2 rich gas injection into a depleted gas reservoir (stage 1) and a saline aquifer (stage 2) in the Naylor field, Victoria. Two sets of 3D 3C VSP surveys were acquired in well CRC-1 (the injection well) before the injection in 2008 and after the injection of 65000 tonnes of CO_2 in 2010 as a part of stage 1 of monitoring program in the CO2CRC Otway project. The oldest report (to the author's knowledge) about observing signatures of seismic anisotropy in the Otway basin is a publication by Turner and Hearn (1995). They carried out a shear wave splitting analysis on 3C (zero-offset) VSP data recorded in Namgib-1 well in the Otway basin. Their analysis suggests that maximum horizontal compressive stress is oriented in the SE-NW direction which is consistent with the present day regional stress regime in the area and borehole breakout study by Hillis et al. (1995) which reports a nominal maximum horizontal stress azimuth of around 125^o.

As a part of a research program designed for CO_2 monitoring and verification at the CO2CRC Otway project, Pevzner et al. (2010) compare the results of several methods of seismic anisotropy estimation from borehole seismic data. The aim was to detect changes in the reservoir properties due to CO_2 injection. A part of verification objectives was to perform a set of measurements suitable for early leak detection. Pevzner et al. (2010) tested a dataset recorded in a zero offset VSP survey at Otway basin for shear wave anisotropy using the technique introduced by Pevzner et al. (2009). They observed

shear wave splitting in both CRC-1 and Naylor-1 boreholes with fast azimuth direction at 140^o and slow azimuth direction at 50^o.

Pevzner et al. (2010) also analysed P-wave azimuthal anisotropy from 3D VSP travel times. In this work, 3D VSP transit times were utilized to compute stacking velocities as a function of azimuth for the receiver positioned at 1500 m depth. The results are consistent with the shear wave splitting analysis where a strong azimuthal anisotropy is observed with the same orientations of the fast and slow directions as obtained from shear waves. Finally the same authors showed that polarization of direct P-wave arrivals recorded by the receivers in well CRC-1 is strongly affected by the anisotropy. They use method proposed by Dewangan and Grechka (2003) to derive the full stiffness tensor from 3D 3C VSP measurements at well CRC-1 in the Otway basin. They make use of the important fact about the homogeneity in the overburden at the Otway site where the horizontal component of the slowness vector can be measured on the surface and be used in the receiver level. They found that calculated values of the stiffness tensor yield P and S velocity anisotropy that is consistent with the results of the other two methods.

Bóna et al., (2011) use 3C 3D VSP recordings of well CRC-1 in 2008 (pre-injection) and 2010 (post-injection) to study azimuthal changes in P-wave anisotropy that maybe linked to the injection of 65000 tonnes of CO_2 into Waarre C sandstone reservoir. They report azimuthal anisotropy that is observed in the form of asymmetric distribution of the dip of P-wave polarization vectors recorded by the receiver positioned at depth 1545 m. They also report observing small time-lapse change in the distribution of horizontal component of the S-wave polarization vector.

Bóna et al., (2011) use Christoffel equation to invert 3D VSP slowness and polarization measurements at well CRC-1 in 2008 and 2010 to invert for the full stiffness tensor of the medium surrounding the receiver positioned at depth 1545 m. They report fast shear wave azimuth change from 150^o in 2008 (pre-injection) to 159^o in 2010 (post-injection) for 3D VSP measurements at receiver depth 1545 m. They emphasis the accuracy (small time-lapse change in stiffness tensor) and the consistency of their inversion results with zero offset VSP analysis results and cross-dipole sonic measurements at well CRC-1 and see a potential for relating the observed azimuthal anisotropy changes to the stress filed change in the rocks overlying the injection zone. However, they suggest more

investigations including geodynamic (geomechanical) modeling to be done to reveal the nature of the anisotropy change in the overburden at the Otway injection site.

Azimuthal changes of seismic velocities are generally believed to be caused by fractures oriented in a preferred direction or an existing dominant stress direction. Pore pressure changes at the reservoir interval, caused by production of oil/gas or injection of water/gas may result in changes of the state of the stress field not only at the reservoir level, but also in the overburden (Crampin, 1990; Herwanger and Horne, 2009). Determining the nature of seismic anisotropy in the Otway geosequestration site and estimation of anisotropy parameters can assist in the production of a clearer image of the subsurface. If accurately estimated, time-lapse changes of seismic anisotropy at Otway site could be related to the changes in the state of subsurface stress as a result of CO_2 injection. However, as described before (Herwanger and Horne, 2009; Bóna et al., 2011) this has to be confirmed through geomechanical modeling of the reservoir rock and the surrounding overburden.

Changes in seismic anisotropy at Otway may also be linked to the opening of new as well as existing fracture systems and fault reactivations in the overburden as a result of CO_2 injection. Therefore, time-lapse anisotropy measurements in the overburden could be utilized as a monitoring tool to evaluate the possibility of CO_2 leakage into the shallow water reserves or even the surface.

1.8 Research methodology

This study comprises generation of large quantities of numerical slownesses and polarizations (vectors along phase and azimuthal directions) which will be contaminated by random noise vectors (taken from a random distribution) before used in an inversion algorithm for anisotropy parameter estimation. To quantify the uncertainties of anisotropy parameter estimation related to each method, inversion for a given model has to be repeated several times in order to extract a reliable value for mean and standard deviation of the estimations. However, repeating the inversions increases the analysis run time and has to be selected by bearing in mind this restriction. In this analysis, to acquire both the practical run time and reasonable parameter accuracy, I have repeated every inversion 1000 and 100 times for a given VTI and orthorhombic model,

respectively. Errors can now be computed as the difference between the mean value of the estimation and the model value. I will represent the errors in terms of maximum phase angle (polar) coverage of the data (determined by offset/depth), magnitude of the medium anisotropy and the level of noise in the measurements. For each method, efficiency of the selected method is evaluated through plots of the errors and standard deviations corresponding to each estimated parameters.

I will use finite difference generated synthetic seismograms and real VSP data measured at well CRC-1 in 2010 to estimate anisotropic parameters assuming VTI and orthorhombic anisotropy in the medium. I will investigate which parameters of the earth model fit the measurements best. Establishing the medium symmetry and later on measuring the variations in repeated anisotropy estimates would be of high importance to monitoring state of the stress in the reservoir and in the overburden rocks caused by CO_2 migration within the studied area.

Throughout of the subsequent chapters, I first start with the uncertainty analysis (as described above) for each method (VTI in Chapters 4 and 5 and orthorhombic in Chapter 6) at the beginning of the chapter. Here, the effectiveness of the selected method is evaluated by analysing the errors and standard deviations.

In the second part of each chapter, I will generate synthetic finite-difference example data for a model (walkaway VSP in Chapters 4 and 5 and Psudo-3D VSP in Chapter 6) that is constructed based on the measured borehole velocities and layer geometry of the subsurface at the location of injection well (CRC-1) in Otway. I will then use synthetic slowness and slowness-polarization data to invert for the anisotropy parameters used in the model. The inversion is iterated for different ranges of source-receiver offsets (phase angles) to evaluate the influence of offset on parameter estimation.

In Chapter 4, I will look at real VSP data measured at well CRC-1 in order to evaluate the possibility of fitting a VTI anisotropy model to the measurements. In Chapter 5, I will analyse the problem of large noise on P-wave polarization measurements that is observed in VSP experiments at large source-receiver offsets. I will show that this noise is caused by various types of interfering waves generated by geological boundaries

adjacent to the receiver interval. In Chapter 6, I will use 3D 3C VSP data that was recorded in 2010 at the location of well CRC-1 to fit an orthorhombic model that best describes the slowness measurements in this borehole. The result of every analysis and parameter estimation will be summarized in the remark section placed at the end of the each chapter.

Methods that can be used for exact inversion (method 1 in Chapter 4 and method 2 in Chapter 5) are tested for the stability of the results due to presence of noise in the data. Approximate methods (method 2 in Chapter 4 and method 1 in Chapter 5) are also tested to evaluate anisotropy range where the approximations still hold.

1.9 Thesis layout and organization of the research

Anisotropy estimations require very fine set of measurements of enviable precision as well as through knowledge about the uncertainties associated with the estimations and the limitations of the estimation methods. Hence in my study, I will address the uncertainties associated with using P-wave slowness and polarization data that can be recorded in a VSP survey to estimate P-wave local anisotropy parameters δ and ε (for VTI media in Chapters 4 and 5) and $\delta^{(1)}$, $\delta^{(2)}$, $\delta^{(3)}$, $\varepsilon^{(1)}$ and $\varepsilon^{(2)}$ (for orthorhombic media in Chapter 6) defined by Thomsen (1986) and Tsvankin (1997), respectively. I aim to show that in addition to source-receiver offset and measurement noise, magnitude of anisotropy in the medium has a significant influence on the accuracy of VSP anisotropy estimations. I will conduct my uncertainty analysis for slowness only methods and slowness-polarization methods that are commonly used for VTI and orthorhombic parameter estimation in the following order:

Chapter 2: In Chapter 2, I will start by introducing CO2CRC organization and current carbon capture and storage (CCS) activity throughout Australia. Then I will review CO2CRC's Otway demonstration project for CO_2 geosequestration. I will explain important subjects such as the objectives of the project, site selections, operations (stage 1 and 2), seismic monitoring program designed and conducted by the department of exploration geophysics, Curtin University. At the end of Chapter 2, I will describe an acoustic impedance inversion job that was carried out on 3D surface seismic data

acquired pre- and post-injection of CO_2 into Waarre C formation at Otway which was aimed to detect changes in seismic response of this reservoir as a result of CO_2 injection.

Chapter 3: This chapter provides more detail background description about two types of mediums that are the focus of majority of the existing studies of seismic anisotropy, transverse isotropy and orthorhombic. In Chapter 3, I have gathered most of the theoretical background and equations that will be required to carry out the analysis in the upcoming chapters. To better understand the equations, several examples of P-wave signatures (velocity, polarization) in such models are presented in this chapter. These examples are given in the form of graphs of P-wave velocities and polarization dip plotted against the azimuth of the plane within which the wave is propagating and phase (and group) angles. At the end of this chapter, I have explained how slowness and polarization noise is generated and added to the numerical data used in the uncertainty analysis and also I will describe the minimization algorithm which I used for parameter estimation.

Chapter 4: In this chapter, I will first explain the methodology and limitations of deriving P-wave slownesses from walkaway VSP measurements. Then I will analyse reliability of two slowness methods that are traditionally used to infer VTI anisotropy parameters from borehole measurements:

1. P-wave phase dispersion relation in VTI media.
2. Thomsen's weak anisotropy approximation

I will next present two examples of VTI parameter estimation based on the application of first method. First example is using synthetic walkaway VSP data that was generated by a finite-difference algorithm using an anisotropic (VTI) velocity model derived from velocity log at well CRC-1 in Otway. In this example I will analyse the effect of source-receiver offset on VTI parameter estimation from walkaway VSP measurements. Second example, uses P-wave travel time measurements of a three component, 3D VSP survey which was acquired at CRC-1 in 2010. Here, I will examine the validity of assuming transverse (polar) anisotropy for the geology at the recording interval at well CRC-1 borehole location.

Chapter 5: In the first part, I will look at the history of the slowness-polarization method for VTI parameter estimation and review the underlying assumptions and method limitations. Next, I will analyse the validity of two slowness-polarization methods:

1. Grechka and Mateeva (2007) approximate relationship between vertical slowness and polarization dip.
2. Exact relationship between vertical slowness and polarization dip.

I will then analyse P-wave polarization noise (nonlinear particle displacement) with respect to source offsets in VSP recordings using a synthetic seismogram recorded by receivers in a vertical borehole within a 2 layer earth model. Having understood the causes of polarization noise in P-wave recordings, I will use the exact slowness-polarization equation to invert synthetic walkaway VSP measurements for VTI anisotropy parameters ε and δ.

Chapter 6: In this chapter, my focus would be on orthorhombic anisotropy that seems to be more representative model than VTI at study location. I will first review the maths behind and the theory of modeling an effective orthorhombic medium by embedding a vertical fracture set into a VTI background rock, and then I will look at the reliability of orthorhombic anisotropy parameter estimation from P-wave slowness data. Next, I will invert synthetic slowness data generated in a pseudo 3D VSP experiment for anisotropy parameters of an orthorhombic medium. Synthetic 3D VSP is comprised of finite-difference wave recordings along 36 earth models (at every 5^o azimuthal step) with velocities taken from borehole log measurements at well CRC-1 location. Anisotropy in the orthorhombic layer is approximated by VTI anisotropy at every azimuthal direction where Thomsen parameters for each azimuth are approximated by Equations 62 and 63 of Chapter 3. At the end of Chapter 6, I will fit an orthorhombic model to P-wave velocity data that are computed from 3D VSP first arrival measurements at CRC-1 in 2010.

Chapter 2, CO2CRC Australia and CO2CRC Otway demonstration project

2.1 CO2CRC Australia

The cooperative research centre for greenhouse gas technologies (CO2CRC) is Australia's research organization in CO_2 capture and geo-sequestration. CO2CRC comprises Australian and global industry, universities and research institutes from Australia and New Zealand, and Australian commonwealth, state and international government agencies where it is supported financially by the federal government cooperative research centres program, CO2CRC participants and significant contribution from oil and gas industry. COCCRC is involved in the following highlighted activities (CO2CRC, 2013a):

1. Conducting research and development of technology for carbon dioxide capture and geological storage.
2. Risk reduction by practically demonstrating carbon capture and storage.
3. Developing sustainable opportunities for decreasing carbon emission in Australia and New Zealand.
4. Contributing the global technology development for carbon capture and storage by participating international programs and research activity.
5. Technology transfer and training industry and government staff by providing education in greenhouse technology.

At this moment, more than 100 researchers in Australia and New Zealand are collaborating to develop industry ready CCS technologies. CO2CRC research program aims to (CO2CRC, 2013b):

1. Develop new technologies that reduce the cost of capturing CO_2 (CO_2 capture stream).
2. Develop new monitoring methodologies applicable to a variety of geologically different CO_2 storage possibilities.
3. Facilitating deployment of CCS by addressing issues such as economics, risk assessments and communicating CCS.

There are several number of CCS demonstration projects underway or proposed for the future in Australia including (CO2CRC, 2013c):

1. Callide Oxyfuel project, Queensland.
2. CarbonNet Project, Victoria.
3. South West Hub Project, Western Australia
4. CO2CRC Otway Project, Victoria.
5. Gorgon Project, Western Australia.
6. International Power Carbon Capture Plant, Victoria.
7. H3 Capture Project, Hazelwood, Victoria.
8. Loy Yang Project, Victoria.
9. CO2CRC/HRL Mulgrave Capture Project, Victoria.
10. CO2CRC Uno Mk 3 Project.
11. Munmorah PCC Project, New South Wales.
12. Tarong PCC Project, Queensland.
13. Surat Basin CCS Project, Queensland

CO2CRC Otway project in Victoria is currently Australia's only operational storage demonstration project. Monitoring and verification component of this program is matured and recognized by CCS groups throughout the world. Monitoring and verification program for CO2CRC Otway project is divided in three categories that include: atmospheric monitoring, geochemical monitoring and geophysical (and seismic) monitoring. My research is within the seismic monitoring program of this project. More specifically, I aim to describe a subtle 4D seismic response at this site by using variety of geophysical techniques, some of them applied for the first time for the CCS objectives.

2.2 CO2CRC Otway demonstration project in Victoria, Australia

CO2CRC's Otway project in South-Western Victoria is the Australia's first CCS project to demonstrate that carbon capture and storage is technically and environmentally safe way to reduce Australia's greenhouse gas emissions (CO2CRC, 2013d). This project is aimed to provide technical information on geosequestration processes mainly in regards with the monitoring and verification regimes that will help to inform policy makers and

provide assurance to the community. CO2CRC's Otway project is one of the oldest and the world's largest geosequestration demonstration projects that include a comprehensive monitoring program. Some methodologies developed were adopted by other CCS projects around the world (CO2CRC, 2013d).

Figure 1 shows the location of CO2CRC's Otway project off the great ocean road, 40 km from the town of Warrnambool in South-Western Victoria, Australia.

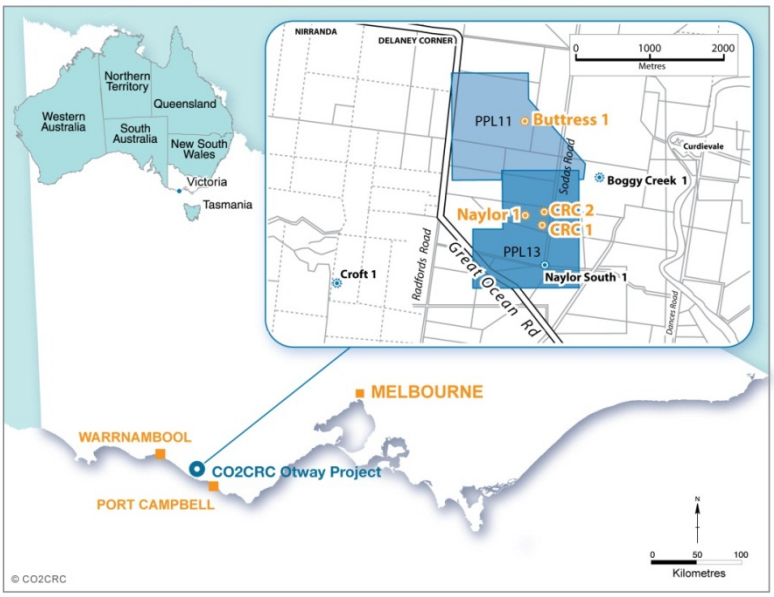

Figure 1, location of the CO2CRC's Otway project in South-Western Victoria, Australia (CO2CRC, 2013d).

CO2CRC's Otway project site location was selected by geologists at CO2CRC considering the following facts (CO2CRC, 2013d):

1. Existence of a natural carbon dioxide source in the area.
2. Available oil and gas tenements
3. Large amount of exploration data
4. Existing infrastructure
5. Well known geology and storage capacity

2.2.1 Operations

2.2.1.1 Stage 1

In this stage 65000 tonnes of CO_2 rich gas (80% CO_2, 20% Methane) was extracted from a gas well (Buttress) in the area, compressed, transported via a 2.25 km pipeline and injected into a depleted gas formation (Waarre C) 2km below the surface in the Naylor field. Naylor field is located approximately 300 km West of Melbourne, Victoria. This field was first discovered by Santos in 2001 based on bright spot reflection originating from Waarre C formation in 3D seismic survey (Curdie Vale). Field was producing methane between 2002 and 2003 when Naylor-1 was shut and abandoned. To inject CO_2 within the CCS project a new well (CRC-1) was drilled in 2007, 300 m down dip from the discovery Naylor-1 well. Naylor -1, now used as a monitoring well, detected the arrival of CO_2, some 5 months later (CO2CRC, 2013e).

2.2.1.2 Stage 2

In this stage permanent storage of CO_2 in the saline formations of the earth is investigated. In the first experiment residual gas trapping is tested where CO_2 is stored in the porous rock in tiny bubbles disconnected from each other so they cannot flow out. In this stage up to 10000 tonnes of CO_2 rich gas will be injected into a saline aquifer (Paaratte formation) located in 1400 m depth in the Naylor field. Another injector well (CRC-2) has been drilled for this purpose. This stage will become fully developed in 2015 (CO2CRC, 2013e).

2.2.2 Monitoring program

The monitoring program for the CO2CRC‘s Otway project is aimed to confirm the effectiveness and safety of the site for CO_2 storage and to understand the interaction between the injected CO_2 and the reservoir formation. Monitoring and verification (M&V) program develop technologies for future CCS projects in Australia and help Australian regulators to develop regulatory framework for CO_2 storage. The M&V program will inform and re-assure the local community that CO_2 storage is a safe way to reduce CO_2 emissions. The monitoring domain in the CO2CRC Otway project is subdivided into three main categories, atmospheric, geochemical and

geophysical (seismic) monitoring. The latter is the main subject of discussion in this chapter (CO2CRC, 2013f).

2.2.3 Seismic monitoring

An extensive seismic monitoring program is associated with the CO2CRC Otway project for CO_2 geo-sequestration. The objectives at the stage 1 include: to ensure CO_2 is contained in the reservoir (direct and indirect efforts), investigate the scenario of gas leakage and how to best detect it at an early stage by seismic methods and to develop seismic monitoring techniques applicable to CO_2 storage in depleted oil and gas fields which is of a prime importance to the industry and community in general. Having in mind these objectives the following seismic measurements were designed at the stage 1 of the CO2CRC's Otway project:

1. Time-lapse 3D seismic surveys before CO_2 injection in 2008, during and after CO_2 injection in 2009 and 2010, respectively.
2. Time-lapse (3D) VSP surveys at well CRC-1 location in 2008 (baseline) and 2010 (monitor) simultaneous with the acquisition of surface seismic surveys.
3. Zero-offset, offset and walk-away VSP surveys at Naylor-1 and CRC-1 boreholes.

The monitoring program was preceded by repeated 2D seismic tests to determine acquisition parameters and likely repeatability for the subsequent 3D seismic monitoring program. More details about seismic monitoring program designed for CO2CRC's Otway project can be found at Dodds et al. (2009).

Table 1 outlines the acquisition parameters related to seismic monitoring program (3D surface seismic and 3D VSP) at the stage 1 of the CO2CRC's Otway project (Pevzner et al., 2012).

	Survey 1		Survey 2	Survey 3	
	VSP	**Surface seismic**	**Surface seismic**	**VSP**	**Surface seismic**
Date	Dec 2007-Jan 2008	Dec 2007-Jan 2008	Jan 2009	Jan 2010	Jan 2010
Source	Weight drop, Hurricane 10	Weight drop, Hurricane 10	IVI Minnibuggy, 12 s Sweep 10-150 Hz	IVI Minnibuggy, 12 s Sweep 10-150 Hz	IVI Minnibuggy, 12 s Sweep 10-150 Hz
Source lines	15	29	29	29	29
Source spacing	20 m	20 m	20 m	20 m	20 m
Number of source points	1139	2181	2223	2223	2223
Recording tool	3C Schlumberger VSI	Seistronix EX-6	Seistronix EX-6	3C Schlumberger VSI	Seistronix EX-6
Receiver interval	1485-1620 m			1500-1605 m	
Receiver spacing	15	10	10	15	10
Receiver type		10 Hz, Single geophone	10 Hz, Single geophone		10 Hz, Single geophone
Active channels		440	837		837
Receiver lines		10	10		10
Receiver line spacing		100 m	100 m		100 m

Table 1, acquisition parameters for seismic monitoring program at the stage 1 of CO2CRC's Otway project.

2.3 Seismic response of Waarre C formation to CO_2 injection

Injection of relatively small amount of CO_2/CH_4 mixture in the supercritical state into the depleted gas reservoir Waarre C is not expected to generate large changes in the elastic properties of the reservoir formation (Li, et al., 2006; Caspari et al., 2010). This is mainly because of the relatively small porosity in Waarre C reservoir and stiff rock matrix (at 2 km depth) that counteracts the effect of fluid replacement in the rock. In the next part of this chapter, I will demonstrate the subtlety of the effect of CO_2 injection on

seismic response of Waarre C formation through a 4D acoustic impedance (AI) inversion exercise carried out on 3D seismic volumes acquired at Naylor field in 2008, 2009 and 2010.

As previously mentioned the surface seismic program consisted of three surveys. Base-line survey was recorded in 2008 that is before the injection, first monitor survey in 2009 that is after 33000 tonnes of CO_2 was injected into the formation and a second monitor survey in 2010 after CO_2 volume reaches to 65000 tonnes. A summary of surface seismic monitoring program is illustrated schematically in Figure 2.

To investigate potential changes in elastic properties of the reservoir due to CO_2 injection over time, I have inverted all three seismic surveys into acoustic impedance (AI) cubes using a model based inversion algorithm that uses acoustic impedance measurements at wells CRC-1 and Naylor-1 to build the initial impedance model. In the subsequent parts, I will describe the inversion process and discuss time-lapse changes in AI attribute (at Waarre C interval) that may have been caused by CO_2 injection process.

2.3.1 Seismic-well tie

White and Simm (2003) give a tutorial on the best practice approach to conduct a seismic-well tie process. Bearing in mind the approach taken by White and Simm (2003), pre-production logs recorded at Naylor-1 and pre-injection logs recorded at CRC-1 together with base-line zero-offset Vertical Seismic Profiles (ZVSPs) were used for calibration of seismic volumes in preparation for the inversion. Since reservoir saturation was changing over time it was also of interest to “re-construct” new log values. Caspari et al. 2010, predict very small (2 %) decrease in AI after 65000 tonnes of CO_2 were injected in Waarre C reservoir. Such change is unlikely to be detected by time-lapse seismic methods.

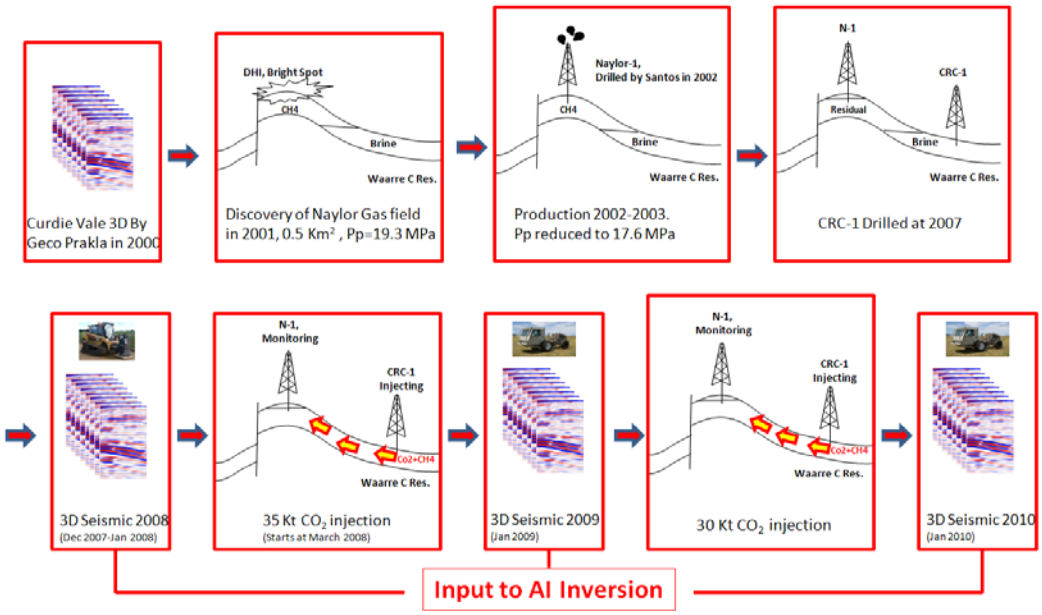

Figure 2, history of the Naylor gas field: From discovery in 2000 to production in 2002-2003 and its "revival" in 2008 via CO2CRC demonstration project.

Hence in this study, we use only pre injection logs (2008) to tie wells to seismic. A good correlation was achieved for all the wells (Figures 3-5). Figure 3 shows 81% correlation between synthetic (blue) and seismic (red) at the location of well CRC-1. This correlation was achieved along a large window of 1200 ms for this well. Sonic velocity (track 4) and density (track 3) logs at well CRC-1were used to compute acoustic impedance (track 5) and reflectivity sequence at this well location. Synthetic seismogram was generated for this well by convolving the reflectivity sequence with a zero phase wavelet with frequency band derived from seismic traces near the well location. There are however, mismatches between the synthetic and seismic at two time intervals. First mismatch is seen at the interval 590-640 ms and the second at 770 ms in Figure 3.

In general, there are several reasons to have less than a perfect match between synthetic trace generated from velocity and density log measurements in the borehole and seismic trace extracted from a seismic volume at the borehole location. Let's first assume that we are dealing with an ideal case where the log measurements in the borehole are unaffected by noise and we are able to reconstruct the earth reflectivity sequence from velocity and density logs. On the other side of the story lays seismic where appropriate

illumination of a 3D subsurface and practical considerations in acquisition (mostly cost and signal/noise ratio) will push the designers towards multi- fold/azimuth geometry recordings that is in contrast with the concept of 1D convolutional model. Seismic reflection traces coming from across various azimuthal planes and incident angles are processed to remove the noise (including the wavelet effect) and to correct for the effect of wave propagation on seismic amplitudes (spherical divergence, attenuation, source-receiver directivity, etc.) to represent the subsurface reflectivity in the zero-offset direction. To achieve this objective, traces are first oriented in a 2D plane to represent the reflections that belong to a common reflection point in the subsurface and then NMO corrected and summed up (stacked) to enhance the signal against the noise and to simulate 1D zero-offset trace that would be recorded from a collocated source-receiver acquisition geometry. The zero-offset geometry results in the normal (to the layer) wave propagation for which the recorded signal can be regarded as the earth reflectivity response in the 1D direction. However, reflection amplitudes of a specific reflector are not only influenced by propagation related factors and noise, they may also vary with azimuth (over fractured zones/ azimuthal anisotropy) and wave propagation angle as well which will be ignored in most of the traditional processing algorithms. A clear example that will reduce the quality of seismic-well tie would be the case where reflection polarity of an interface changes with the angle of incident or offset. In this case, the overall effect of trace stacking on seismic amplitudes would be destructive and will lead to a mismatch between synthetic and seismic at the given interface.

In a less than ideal world for log measurements, borehole velocity and density logs may also be erroneous as a result of borehole conditions or instrument failure. Density measurements may represent the values of the drilling mud that is infiltrated into the fractured zones to prevent further fluid loss. Sonic measurements are usually subjected to several corrections (de-spiking, shallow interval missing part) before being used to compute the reflectivity.

At well CRC-1, in the case of shallower interval (590-640 ms), two peaks observed in seismic trace are weaker in the synthetic (Figure 3). These events at almost similar times can be observed in synthetic trace at well CRC-2 (Figure 4). This observation suggests

the possibility of having erroneous well measurements at well CRC-1 for this interval. Calliper log at well CRC-1 shows a washed-out zone for this time interval that may have influenced the quality of velocity and density measurements at this well (compare calliper logs shown in Figures 3 and 4).

In the case of mismatch at 770 ms in Figure 3, the peak observed in synthetic trace is very weak in seismic trace extracted at well CRC-1 position. Looking at well CRC-2, a peak event can be seen on both the synthetic and the seismic at the same interface as in well CRC-1. This indicates that in this case, AVO effects (such as the one given in the example above) may have influenced the amplitudes at well CRC-1. To examine this possibility an AVO modeling exercise was conducted (not shown) for both the wells to understand the amplitude behaviour with offset for this interface. AVO modeling clearly shows amplitude decrease with offset for this interface at well CRC-1 whereas almost constant amplitude with offset is seen at well CRC-2. Amplitude decrease with offset for this interface at well CRC-1 can reduce the quality of stack and result in a mismatch with synthetic.

Figure 4 displays similar data as before for well CRC-2 with 81% correlation within a time window of 400-1200 ms. This well was not used in the inversion (nor in building initial model) to check against the reliability of the inversion results. Density and sonic logs were corrected for borehole conditions (wash out zones) and cycle skipping, respectively and a representative wavelet (constant in three seismic volumes) was extracted beforehand the correlation and the same wavelet was used in the inversion.

Figure 5 shows the same data generated for well Naylor-1 where 90% correlation is obtained in the time interval where log measurements exist, 1450-1550 ms.

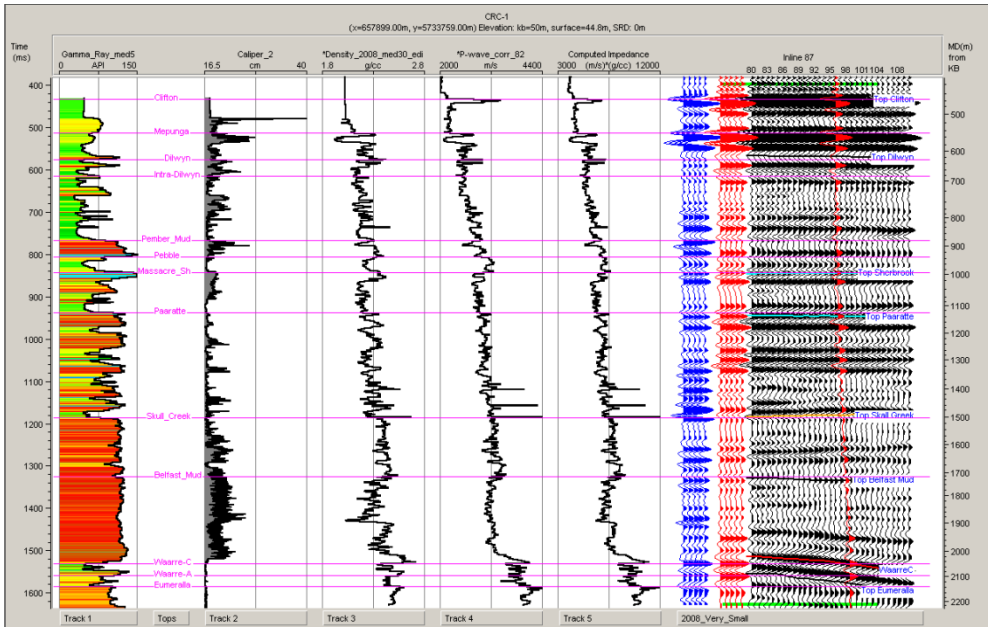

Figure 3, synthetic-seismic correlation at well CRC-1 in Otway geosequestration site. A large correlation, 82% is achieved along a large window represented by green horizontal lines on seismic display.

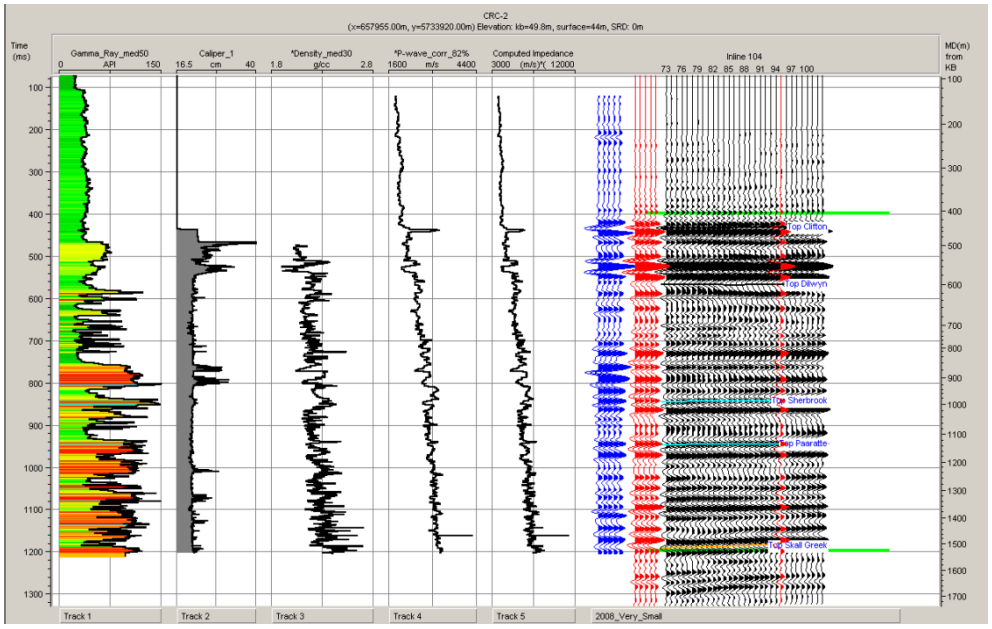

Figure 4, well CRC-2 is not included in building AI initial model as it will be used as a "blind" well to analyse inversion errors. 82% correlation is achieved for this well along a time window interval of 400-1200 ms.

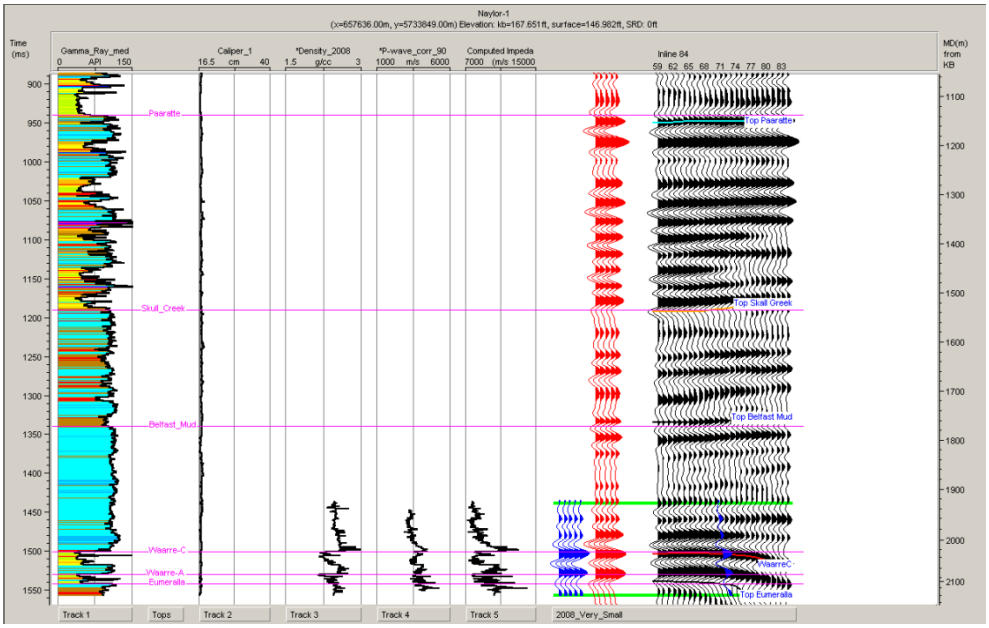

Figure 5, well Naylor-1 ties to seismic (2008) with 90% correlation across zone of interest (1440-1558 ms).

2.3.2 Initial impedance model for the inversion

AI logs reproduced from sonic and density logs in Naylor-1 (pre-production but fluid replaced to pre-injection state) and CRC-1 (pre-injection) were used to build the initial impedance model required in the inversion. Borehole impedances are extrapolated along 3D seismic horizons to create a 3D impedance model. This initial model is smoothed (filtered) to produce a low frequency trend that is absent in seismic data. This is required for model-based seismic inversion algorithms. Such initial AI model would not contain information on the small scale (high frequency) saturation changes caused by CO_2 injection into the reservoir interval. Therefore, a single initial impedance model has been utilized to invert all the three seismic volumes in the CO2CRC Otway project. The idea of producing a single impedance model for the inversion is illustrated schematically in Figure 6. A “chair” view combined of impedance model and amplitude map at top Waarre C formation in 2008 is presented in Figure 7.

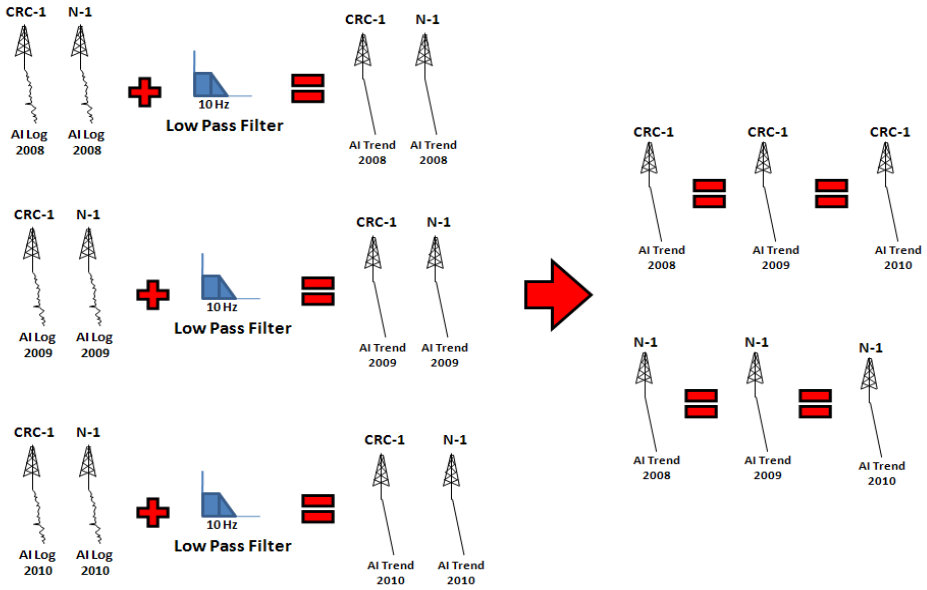

Figure 6, log-derived initial impedance model is not affected by CO_2 injection. From these two logs and 3D horizons I created a single impedance model that was subsequently used for the inversion of pre and post injection seismic cubes.

2.3.3 Acoustic impedance inversion

Model based algorithm was deployed for the inversion of 4D seismic data at Naylor field. Seismic volumes have already been processed to approximate zero-phase data and cross-equalized for the purpose of 4D inversion. Figure 8, middle column, is a comparison between the results of inversion for 2008 survey (bold black curve) and computed acoustic impedance (blue curve) at the location of well Naylor-1. Acoustic impedance extracted from the initial impedance model is also plotted (black curve) in the middle column of top Figure 8. We constrained the inversion algorithm to stay within ± 20 % of the initial model values as displayed in Figure 8, top, middle column. Inversion algorithm has been able to accurately approximate the log values in this well. Inversion parameters from this analysis will be used to invert three seismic surveys in the Otway geosequestration site.

To do seismic-well tie and the inversion, three wavelets were extracted from three surveys in the vicinity of well CRC-1 (Figure 8, bottom). Frequency content of each wavelet was taken from corresponding seismic volume at the well location (within a

radius of 50 m) and phases assumed to be zero. Figure 8, top, right column, shows the wavelet (blue) extracted from 2008 survey that is convolved with the reflectivity derived from the inverted acoustic impedance log to generate the synthetic seismogram (red) at the well location. There is a large similarity between the synthetic seismogram derived from the inversion and seismic trace (black, 2008 survey) at the well location within the specified window (yellow lines). Geological markers at Naylor-1 are plotted in purple.

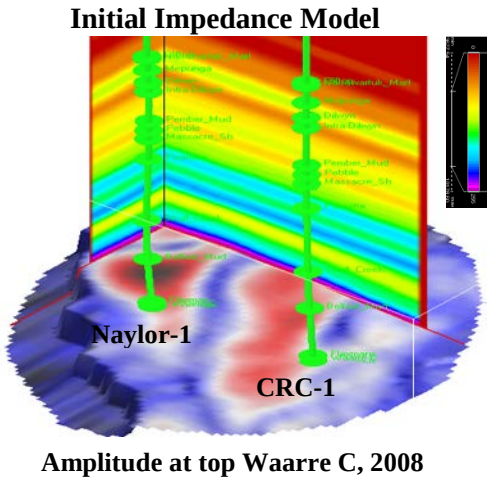

Figure 7, CRC-1 and Naylor-1 wells inserted into a "chair" display comprised of impedance model (vertical section) and pre injection, 2008 amplitude map (horizontal section cutting through Waarre C reservoir).

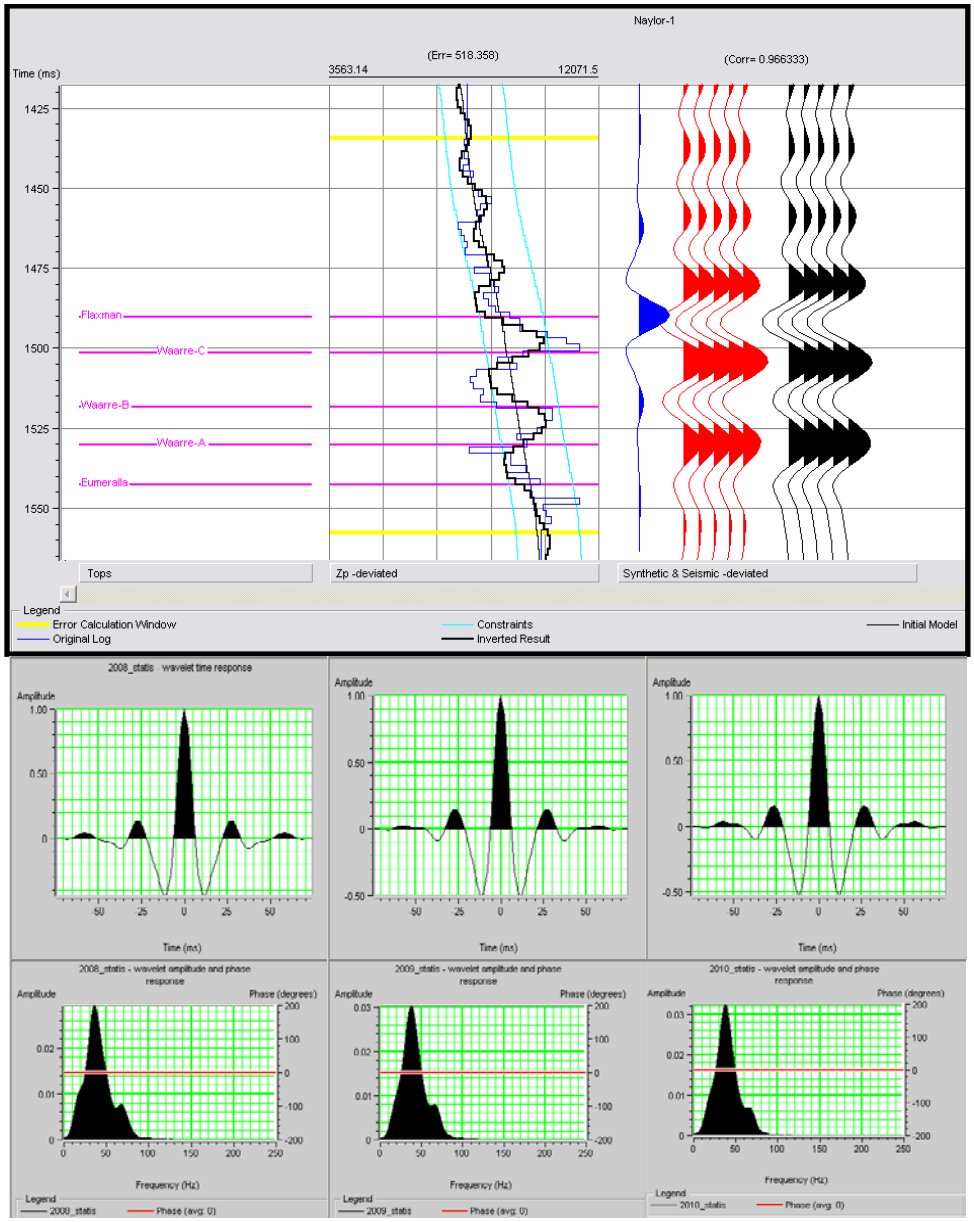

Figure 8, top, inversion analysis at well Naylor-1, 2008 survey. Bottom, three statistical wavelets extracted from seismic data for 2008 to 2010 surveys.

Figure 9 shows an arbitrary line at Waarre C interval and through wells CRC-1 and Naylor-1 that was extracted from the acoustic impedance volume of 2008 survey. Acoustic impedance logs computed from sonic and density measurements in the wells are also plotted to check the quality of the inversion. The difference between the log resolution and seismic estimations are noticeable in this plot. However, there is a

reasonable match between the log values and the inversion estimates at the well locations. A presence of small faults at the reservoir level could also be suggested from this Figure. A blind well test has been implemented for this inversion that emphasis the accuracy of the inversion in shallow intervals where CRC-2 wellbore has penetrated. AI measurements at well CRC-2 was not included in building the initial model and nor for the inversion parameter analysis. Therefore, match between the inversion results and AI log computed at CRC-1 well can be used as a measure of accuracy in the inversion. The inversion result at inline 104 of 2008 cube that intersects well CRC-2 is displayed in Figure 10. As demonstrated by Figure 10, a reasonable match is obtained between seismic derived AI and the one computed from well CRC-2 sonic and density logs.

The results of modeling seismic response for Waarre C formation (Caspari et al., 2010), predict 4-9 % amplitude change and 2 % AI change for this formation as a result of 65000 tonnes of CO_2 injection. This is in agreement with the amplitude maps shown in Figure 11, left column (notice amplitude brightening around well Naylor-1) and AI relative difference maps shown in the middle and right columns (almost no change is observed). Figure 11 shows that while amplitude of top Waarre C formation is responding to the injection of CO_2 rich gas into the reservoir and shows the expansion of CO_2 plume around well Naylor-1 location, the acoustic impedance change as a result of CO_2 injection remains undetected by seismic. This could be related to low vertical seismic resolution at Waarre C interval which will negatively impact our ability to detect subtle 4D acoustic impedance signals generated by CO_2 injection.

To calculate seismic vertical resolution at Waarre C reservoir level, an interval velocity of 3600 m/s can be estimated from velocity measurements at CRC-1 and Naylor-1 boreholes (Figures 3 and 4) and a seismic dominant frequency equal to 40 Hz can be taken from wavelet estimation shown in Figure 8. This results in a seismic wavelength equal to about 90 m and a vertical resolution of around 22 m for this depth interval. This value is almost equal to Waarre C reservoir thickness at Otway geosequestration site which enables us to separate top and base of the reservoir on seismic sections. However, vertical expansion of gas substitution zone in the reservoir caused by the injection of the

entire CO_2 volume in 2010 is estimated (from reservoir modeling) to be much thinner than this thickness and therefore well below the vertical resolution of seismic waves.

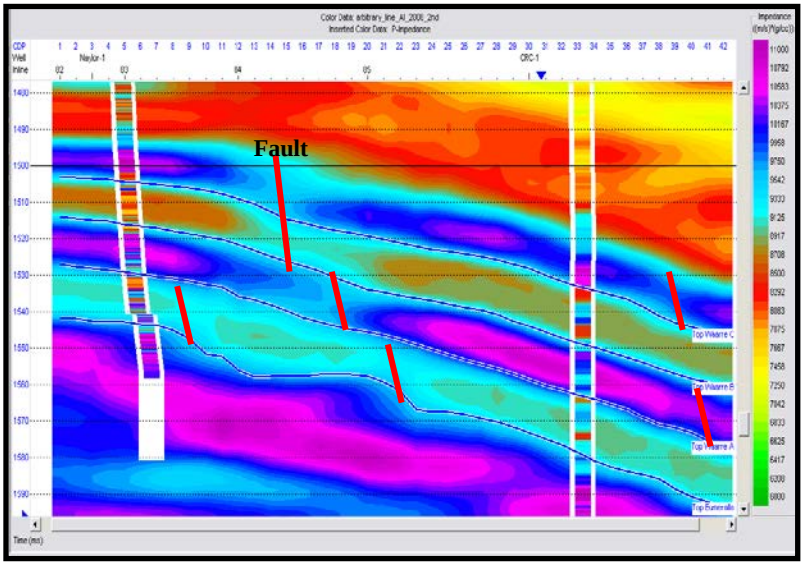

Figure 9, an arbitrary line through wells CRC-1 and Nalylor-1 extracted from AI inversion on pre injection seismic survey 2008.

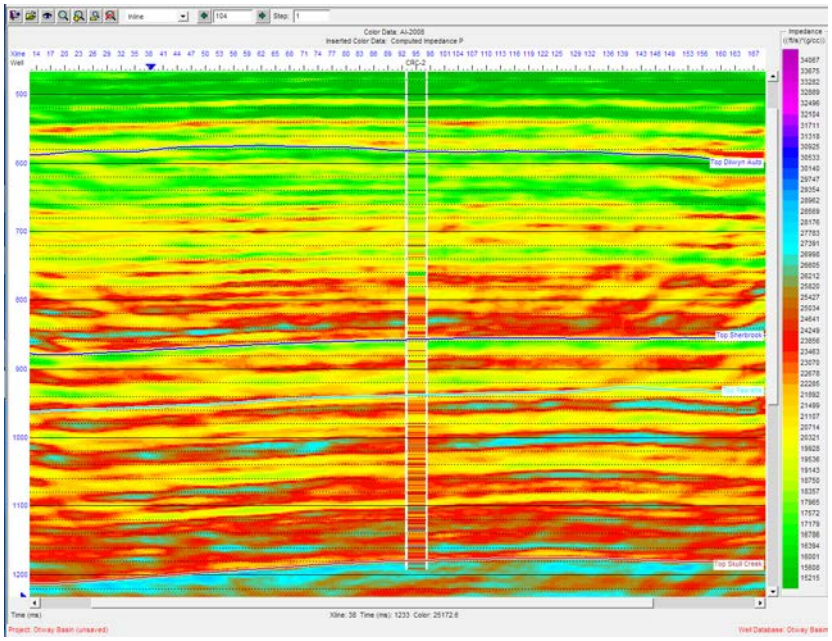

Figure 10, result of 2008 inversion versus acoustic impedance computed for the well CRC-2 in Otway geosequestration site.

2.4 Remarks and conclusion

CO2CRC's Otway project presents a unique opportunity to investigate performance and the sensitivity of both surface and borehole monitoring methodologies. It uniqueness comes from the fact that we are dealing with a gas mix, small quantities, hetergoneous and deep reservoir, and most of all depleted gas field with some residual fluid saturation left. Such situation presents a challenge for any monitoring methodology. Initial data-based verification of the time lapse signal and its intensity was achieved through inversion of time lapse seismic data.

4D seismic inversion on CO2CRC's Otway data was conducted to investigate if the CO_2 injection related changes in the reservoir produced a detectable seismic response. I observed that seismic amplitudes at top Waarre C reservoir are more responsive to the current amount of injected CO_2 than the acoustic impedance attribute derived from inversion of 3D seismic cubes. This is expected as impedance changes are amplified for corresponding reflectivity function. The subtlety of the change inspired further analysis but it was realized that it will have to be a non-conventional approach to detect such small changes in the reservoir properties.

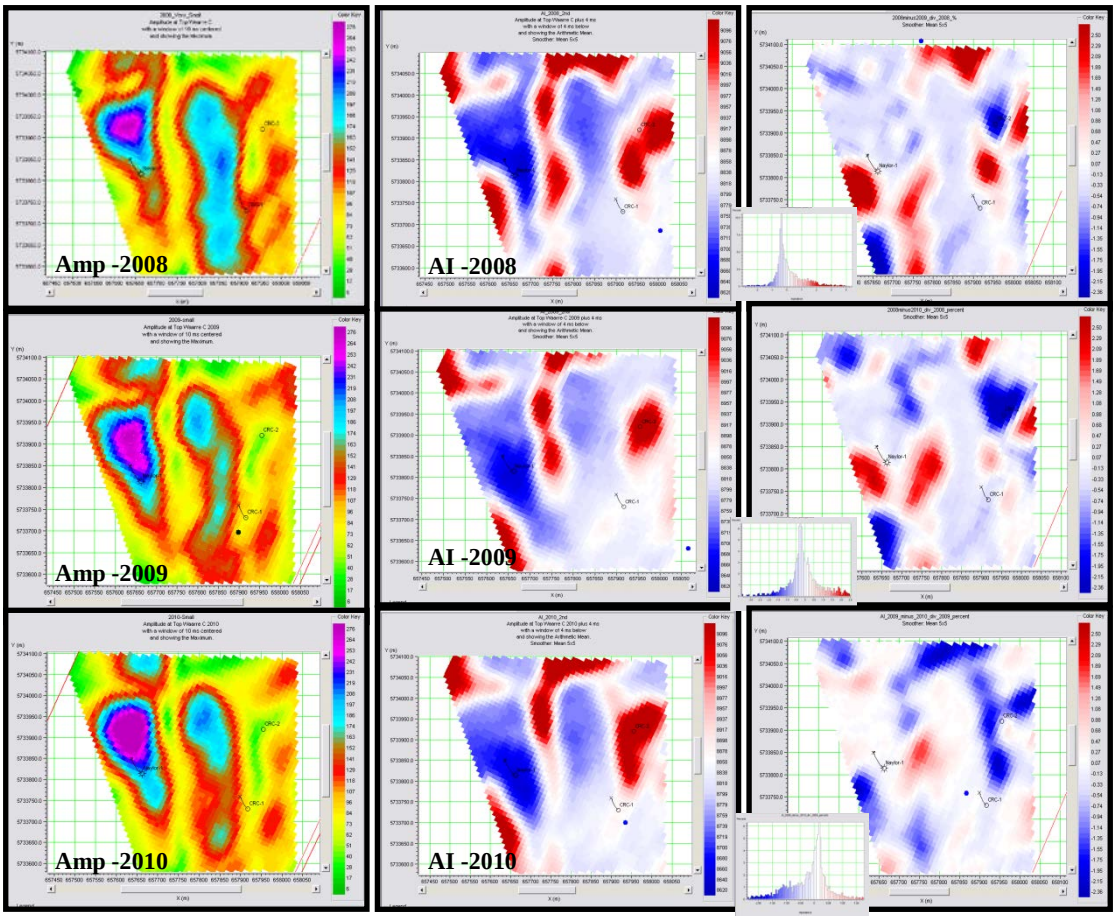

Figure 11, inversion results and amplitude maps at top Waarre C formation for 3 seismic surveys. Left, top Waarre C amplitude maps, top, 2008, middle, 2009 and bottom, 2010. In the middle, results of inversion at Waarre C interval, top, 2008, middle, 2009 and bottom, 2010. In the right, relative AI change and AI distribution of Waarre C formation, top, $AI_{2008} - AI_{2009} / AI_{2008}$ **, middle,** $AI_{2008} - AI_{2010} / AI_{2008}$ **, bottom,** $AI_{2009} - AI_{2010} / AI_{2009}$ **.**

Chapter 3, Forward modeling of P-wave propagation in anisotropic media

3.1 Introduction

This chapter is aimed to understand forward modeling of seismic wave propagation in anisotropic media. I will try to explain the important characteristics of P-wave propagation in anisotropic media by visualizing important equations in the form of plots and Figures. I will only look at the two important cases of medium anisotropy in exploration seismology i.e. transverse isotropy (TI) and orthorhombic anisotropy. This is to avoid dealing with complexity of mathematical equations normally encountered in anisotropic media with lower symmetry. I will first review the theory and fundamental equations of seismic wave propagation in anisotropic media and then present several examples of P-wave propagation characteristics (velocity, polarization) in both VTI and orthorhombic media. I first start with the Christoffel equation which is the basis for modeling wave propagation in a general anisotropic media with arbitrary symmetry. Next, I will review the equations for transverse isotropy as the simplest form of anisotropy in the earth subsurface. In this part, I will introduce Thomsen (1986) anisotropy parameterization for TI media, review phase velocity and polarization equations for in plane waves (P- and SV-wave) and explain the concept of group velocity versus phase velocity in anisotropic medium. I have also embedded simpler weak anisotropy approximations for P-wave phase and group velocity as well as P-wave polarizations in order to help understanding of more complex (exact) equations. To visualize the equations, four examples of different TI media with vertical axis of symmetry (VTI) are presented in this part where the relationship between phase, group and polarization vectors and phase and group velocities are illustrated for the given anisotropic media. In the next section of this chapter, I will introduce the orthorhombic symmetry by explaining the elasticity parameters of the stiffness matrix. Next, I will introduce Tsvankin (1997) parameterization for orthorhombic media. I will make a considerable use of this notation in the last chapter to carry out the uncertainty analysis of parameter estimation methods for orthorhombic media. In the next part, I will introduce the exact P-wave phase velocity equation in orthorhombic media, which is used for the forward modeling in the inversion of stiffness coefficients and anisotropy

parameters in the last chapter. The corresponding weak anisotropy approximation for P-wave phase velocity in orthorhombic media, derived by Tsvankin (1997) is also presented here and it will be used to compute azimuthal anisotropies $\delta(\phi)$ and $\varepsilon(\phi)$ for the generation of Pseudo 3D VSP data in the last chapter. At the end of this part, three examples of different orthorhombic media are presented where P-wave phase and group velocity, and the deviation of polarization vector and group velocity vector from phase (slowness) vector are plotted as functions of wave propagation angle and azimuth.

The last part of this chapter is allocated to our methodology to generate random noise vectors which are used to contaminate slowness and polarization vectors in the analysis of uncertainties associated with anisotropy parameter estimation.

3.2 Christoffel equation

The Christoffel equation is the basis for all predictions of the anisotropic wave behaviour. This equation is derived by substituting a harmonic plane wave into the general wave equation for anisotropic media. Wave equation for linear elastic, arbitrary anisotropic, homogeneous media is defined as (E.g., Tsvankin, 2001):

$$\rho \frac{\partial^2 u_i}{\partial t^2} - c_{ijkl} \frac{\partial^2 u_k}{\partial x_j \partial x_l} = 0, \qquad (1)$$

where ρ is the density, $\mathbf{u}=(u_1, u_2, u_3)$ is the displacement vector, t is the time and x_i are the Cartesian coordinates. c_{ijkl} denote the components of the fourth-order stiffness tensor that describes the medium elastic properties. All indices, i, j, k and l vary from 1 to 3.

A harmonic plane wave is defined as $u_k = U_k e^{i\omega(n_j x_j / V - t)}$ where $\mathbf{U}= (U_1, U_2, U_3)$ is the wave polarization vector, ω is the angular frequency, V is the phase velocity of the wave propagation and $\mathbf{n}$ is the unit vector orthogonal to the plane wave front. This substitution results in the plane wave solution of the general wave Equation 1 and results in so-called Christoffel equation for phase velocity V and polarization vector $\mathbf{U}$ (Tsvankin, 2001):

$$\begin{bmatrix} G_{11}-\rho V^2 & G_{12} & G_{13} \\ G_{21} & G_{22}-\rho V^2 & G_{23} \\ G_{31} & G_{32} & G_{33}-\rho V^2 \end{bmatrix} \begin{bmatrix} U_1 \\ U_2 \\ U_3 \end{bmatrix} = 0 \qquad (2)$$

G_{ik} are the components of the Christoffel matrix, which depend on stiffnesses and the direction of wave propagation:

$$G_{ik} = c_{ijkl} n_j n_l \qquad (3)$$

The Christoffel Equation 2 is a standard eigenvalue (ρV^2) – eigenvector (**U**) problem for the matrix G where the eigenvalues are found from (E.g., Tsvankin, 2001):

$$\det \begin{bmatrix} G_{11}-\rho V^2 & G_{12} & G_{13} \\ G_{21} & G_{22}-\rho V^2 & G_{23} \\ G_{31} & G_{32} & G_{33}-\rho V^2 \end{bmatrix} = 0 \qquad (4)$$

Equation 4 is the nontrivial solubility condition for Equation 2. Throughout this thesis, I will use Equation 2 to generate numerical slowness and polarization data for P-wave propagation in anisotropic media. Anisotropic media can be defined by P- and S-wave velocities (in the symmetry direction) and the anisotropy parameters. However, they will be transformed to stiffness coefficients and used in Equation 2. P- and S-wave velocities are derived by solving eigenvalues of Equation 4 for any given phase direction **n**. The orientation of the corresponding eigenvectors determines the polarization of each wave propagating in the direction **n**. Numerical data will play the role of measurements in our inversion analysis. Noise will be introduced to numerical data in order to examine the efficiency of our techniques.

3.3 Anisotropic symmetry systems

The influence of the medium to the wave propagation is controlled by the stiffness tensor c_{ijkl} whose structure determines velocity and polarization of different wave types at any given propagation angle (Tsvankin, 2001). A general 4th order tensor, c_{ijkl} has 81 components but they can be reduced to 21 independent coefficients because of the

symmetry in the stress and strain tensors where results in $c_{ijkl} = c_{jikl} = c_{ijlk}$ and conservation of energy (Aki and Richards, 1980; Helbig, 1994) which leads to $c_{ijkl} = c_{klij}$.

c_{ijkl} can be represented by a symmetric 6×6 matrix for any symmetry in the medium. This usually follows the so-called Voigt recipe where each pair of indices (ij and kl) is replaced by a single index as the following:

$$11 \to 1,\ 22 \to 2,\ 33 \to 3,\ 23 \to 4,\ 13 \to 5 \text{ and } 12 \to 6.$$

In the upcoming parts, I will restrict myself to only three most commonly considered symmetries in exploration seismology that have been utilized to explain wave propagation in earth sedimentary basins. I will start with the isotropic case that is too simple approximation (described by only two independent stiffness coefficients) for the earth subsurface but has been traditionally used by geophysicists in the past. Next, I will look at the most widely used anisotropic medium, transverse isotropy (TI symmetry) which has one single axis of rotational symmetry and one isotropy plane perpendicular to this axis. The reason TI symmetry is widespread in exploration seismology is that it gives a good approximation to majority of the earth physical occurrences in sedimentary basins comprising shale formations, stack of thin (compared to seismic wavelength) isotropic layers and an isotropic reservoir rock intersected with a single set of parallel fractures. Finally, I will look at the orthorhombic symmetry that can be used to generalize our subsurface approximation to a medium comprising isotropic flat layers embedded by an orthogonal system of parallel fractures.

3.3.1 Isotropic medium

In isotropic medium, the wavefront is spherical; all directions of wave propagation are equivalent and the stiffness tensor has the form (in the Voigt notation):

$$C_{ISO} = \begin{bmatrix} \lambda+2\mu & \lambda & \lambda & 0 & 0 & 0 \\ \lambda & \lambda+2\mu & \lambda & 0 & 0 & 0 \\ \lambda & \lambda & \lambda+2\mu & 0 & 0 & 0 \\ 0 & 0 & 0 & \mu & 0 & 0 \\ 0 & 0 & 0 & 0 & \mu & 0 \\ 0 & 0 & 0 & 0 & 0 & \mu \end{bmatrix} \quad (5)$$

Where λ and μ are the Lamé's constants. This medium has been traditionally used to describe seismic wave propagation in the subsurface.

3.3.2 Transversely isotropic medium

This medium has a single axis of rotational symmetry. Any plane that contains the symmetry axis is a plane of mirror symmetry. The isotropy plane, which is perpendicular to the symmetry axis, is a plane of symmetry as well. Transverse isotropy with vertical axis of symmetry (VTI) is commonly observed over horizontally layered shale formations as a result of horizontal alignment of plate-shape clay particles (Tsvankin, 2001). Periodic thin layering of isotropic layers with individual thicknesses smaller than seismic wavelength can cause TI symmetry (Tsvankin, 2001). Fractures can also lead to TI symmetry in the medium. For example, occurrence of vertically oriented fractures in an isotropic host medium can be well described by transverse isotropy with horizontal axis of symmetry (HTI) that is perpendicular to the fracture planes.

As shale formations comprise 75% of sedimentary basins, transverse isotropy is the most commonly used medium approximation in exploration seismology (Tsvankin, 2001). VTI symmetry causes the number of independent stiffnesses (stiffness coefficient) to reduce to 5 and the resulting tensor in Voigt notation is (Tsvankin, 2001):

$$C_{VTI} = \begin{bmatrix} c_{11} & c_{11}-2c_{66} & c_{13} & 0 & 0 & 0 \\ c_{11}-2c_{66} & c_{11} & c_{13} & 0 & 0 & 0 \\ c_{13} & c_{13} & c_{33} & 0 & 0 & 0 \\ 0 & 0 & 0 & c_{55} & 0 & 0 \\ 0 & 0 & 0 & 0 & c_{55} & 0 \\ 0 & 0 & 0 & 0 & 0 & c_{66} \end{bmatrix} \quad \textbf{(6)}$$

The symmetry axis of a TI medium may be tilted with respect to the earth surface, (tilted TI, TTI), as is the case for up-tilted shale formations near salt domes or dipping fracture set in an isotropic background. The stiffness matrix of a TTI medium is obtained through matrix rotation of Equation 6. If the tilt is 90 degrees, for example caused by embedding a system of parallel vertical fractures in an isotropic rock (illustrated in Figure 1), the model is called horizontal transverse isotropy or HTI. The HTI model has two mutually orthogonal vertical planes of symmetry-the symmetry axis plane and the isotropy plane. If the symmetry axis coincides with the x_1 axis (Figure 2), the stiffness matrix of HTI medium is acquired from Equation 6 by 90 degrees rotation about the x_2 axis (Tsvankin, 2001):

$$C_{HTI} = \begin{bmatrix} c_{11} & c_{13} & c_{13} & 0 & 0 & 0 \\ c_{13} & c_{33} & c_{33}-2c_{44} & 0 & 0 & 0 \\ c_{13} & c_{33}-2c_{44} & c_{33} & 0 & 0 & 0 \\ 0 & 0 & 0 & c_{44} & 0 & 0 \\ 0 & 0 & 0 & 0 & c_{55} & 0 \\ 0 & 0 & 0 & 0 & 0 & c_{55} \end{bmatrix} \quad \textbf{(7)}$$

The rotation is achieved through the application of so-called Bond transformation. An example of matrix rotation using Bond transformation will be presented in Chapter 6 where I will rotate a 6×6 fracture compliance matrix from initial direction (with fracture normal along x_1 direction) to a new direction for fracture normal that is determined by two rotation angles α and β around coordinate axis x_3 and x_2, respectively .

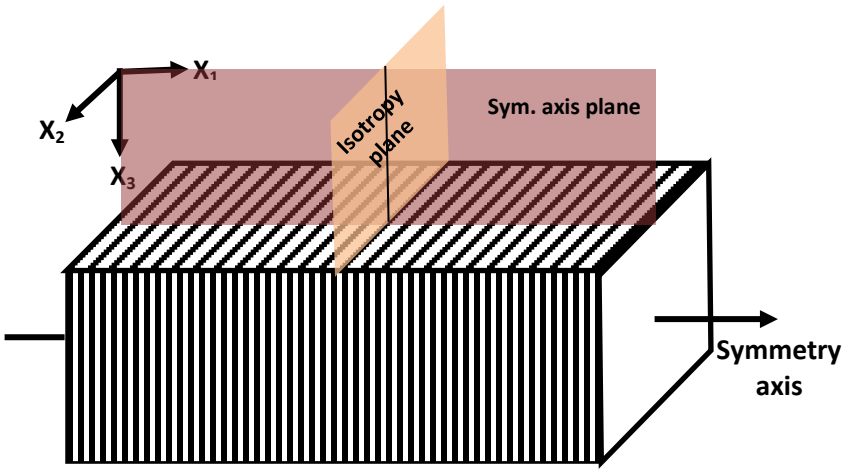

Figure 1, a single system of vertical and parallel fractures embedded in an isotropic background rock will form an HTI medium.

3.3.3 Orthorhombic media

Acquisition of wide-azimuth seismic data with the objective of better illuminating subsurface targets has opened new venues for the implementation of lower symmetry anisotropic models in the processing of seismic data. Orthorhombic symmetry seems to be the most plausible approximation of the earth sedimentary basins as it incorporates the effect of fracture/stress on seismic wave propagation as well as the geological layering within a reasonable degree of model complexity. However, orthorhombic models have not yet become as popular as TI models in seismic processing as they increase the cost by requesting estimation of extra elastic parameters thorough the application of more complex inversion methods.

Orthorhombic anisotropy is characterized by three mutually orthogonal planes of mirror symmetry as illustrated in Figure 2. Figure 2 also displays schematically, the most common occurrence of orthorhombic anisotropy in sedimentary basins where a vertical system of parallel fractures is combined with a background horizontally layered media. In the coordinate system oriented alongside of planes of symmetry, orthorhombic medium has 9 independent stiffness coefficients (Tsvankin, 2001):

$$C_{ortho} = \begin{bmatrix} c_{11} & c_{12} & c_{13} & 0 & 0 & 0 \\ c_{12} & c_{22} & c_{23} & 0 & 0 & 0 \\ c_{13} & c_{23} & c_{33} & 0 & 0 & 0 \\ 0 & 0 & 0 & c_{44} & 0 & 0 \\ 0 & 0 & 0 & 0 & c_{55} & 0 \\ 0 & 0 & 0 & 0 & 0 & c_{66} \end{bmatrix} \quad (8)$$

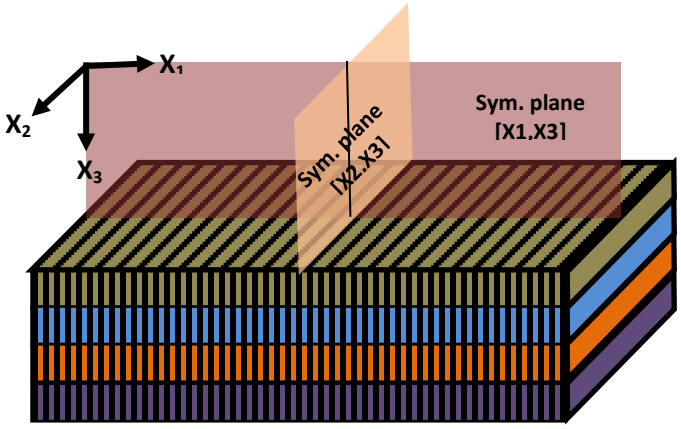

Figure 2, a single system of vertical and parallel fractures embedded in a VTI background rock will form an orthorhombic medium.

In this research, I will dedicate an entire chapter (Chapter 6) to the estimation of orthorhombic elastic coefficients (rearranged in terms of anisotropy parameters) based on using only P-wave slownesses (measureable in a 3D VSP survey) and the uncertainties associated with these estimations.

3.4 Thomsen anisotropy parameters

Thomsen (1986) suggested an alternative way of parameterizing anisotropic media, which separates the influence of the anisotropy from the isotropic P and S velocities along the symmetry axis (Tsvankin, 2001). Five elastic coefficients of a VTI media are replaced by two vertical P and S velocities and three dimensionless anisotropic parameters:

$$V_{P0} = \sqrt{\frac{c_{33}}{\rho}} \quad (9) \qquad V_{S0} = \sqrt{\frac{c_{55}}{\rho}} \quad (10) \qquad \varepsilon = \frac{c_{11} - c_{33}}{2c_{33}} \quad (11)$$

$$\delta = \frac{(c_{13} + c_{55})^2 - (c_{33} - c_{55})^2}{2c_{33}(c_{33} - c_{55})} \quad (12) \qquad \gamma = \frac{c_{66} - c_{55}}{2c_{55}} \quad (13)$$

Parameter ε, is close to fractional difference between the horizontal and vertical P velocity and γ plays the same role for SH waves. Parameter δ determines the second derivative of the P-wave phase velocity function at vertical incidence (E.g., Tsvankin, 2001):

$$\left(\frac{\partial^2 V_P}{\partial \theta^2}\right)_{\theta=0} = 2V_{P0}\delta \quad (14)$$

Important property of the dimensionless parameters ε, δ and γ is that they become zero for isotropic media.

3.5 Values of Thomsen anisotropic coefficients

Based on the studies carried out on field and laboratory measurements by several researchers (Auld, 1973, Berryman, 1979, Thomsen, 1986, Alkhalifah et al., 1996 and Berryman et al., 1999), values of the Thomsen anisotropy parameters depend mostly on the geology of the formation rock that includes layering (VTI, TTI) and fracture orientation (HTI) as well as non-hydrostatic stress orientation. Tsvankin (2001) draws the following general conclusions:

1. Values of ε in sedimentary basins range from 0.1-0.3 for moderately anisotropic rocks (stack of thin isotropic layers) and 0.3-0.5 for compacted shale formations.
2. ε is always greater than δ and $\gamma > 0$ if the TI anisotropy is caused by thin interbedding of isotropic layers.
3. $\varepsilon > \delta$ even if the TI anisotropy is caused by intrinsic anisotropy of shales.
4. Shale formations usually yield moderate and positive values for δ (in the order of 0.1-0.2).
5. Interbedding of thin isotropic layers produce small negative δ.

6. For the common value of $V_{P0}/V_{S0}=2$, (most observed value in sedimentary basins) δ never goes below -0.38 and above 0.67.

Based on these values for Thomsen anisotropy parameters in sedimentary rocks one can obtain a range of variation for both ε and δ. However, in the uncertainty analysis part of this study, I have decided to extend the range of parameters ($\delta \in [-0.4,0.7]$, $\varepsilon \in [-0.2,0.6]$) to include synthetic materials to demonstrate the generality of the uncertainty analysis and the robustness of the parameter estimation approach.

3.6 Solution of the Christoffel equation for plane waves in TI media

Phase velocity and polarizations of P- (and SV-) waves propagating in TI media can be obtained analytically from the Christoffel Equation 2 where the stiffness tensor is specified by Equations 6 and 7. Tsvankin (2001) derives the equation in terms of P (and SV) -wave propagation (phase) angle θ and Thomsen VTI parameters ε and δ as following:

$$\frac{V^2_{P,SV}(\theta)}{V^2_{P0}} = 1+\varepsilon\sin^2\theta-\frac{1-g}{2}\pm\frac{1-g}{2}\sqrt{1+\frac{4}{1-g}\sin^2\theta(2\delta\cos^2\theta-\varepsilon\cos 2\theta)+\frac{4}{(1-g)^2}\varepsilon^2\sin^4\theta} \quad (15)$$

Where $g=\frac{V_{S0}^2}{V_{P0}^2}$. Plus sign before radical corresponds to P-wave and minus sign corresponds to SV-wave. Thomsen (1986) has simplified the analytical solution by considering the weak anisotropy assumption and derives a simpler equation for P-wave phase velocity in VTI media:

$$V_P(\theta)=V_{P0}(1+\delta\sin^2\theta\cos^2\theta+\varepsilon\sin^4\theta) \quad (16)$$

3.7 Group (Ray) velocity

The group velocity vector defines a seismic ray and has the direction and speed of energy propagation (Tsvankin, 2001). Anisotropy causes the group velocity vector to be different than the phase velocity vector. In homogeneous media, the group velocity vector is in the source-receiver direction while the phase velocity vector is orthogonal to the wavefront. In the presence of anisotropy, the wavefront is not spherical and therefore

the two velocities are different. In general, V_G deviates from the phase velocity vector in both the vertical plane and azimuthal direction (Tsvankin, 2001).

If we consider the phase velocity V to be a function of polar angle θ, and azimuthal angle ϕ, then for the general anisotropy the components of the group velocity vector $\mathbf{V_G}$ can be conveniently represented in a new coordinate system as (E.g., Tsvankin, 2001):

$$V_{Gx} = V\sin\theta + \left(\frac{\partial V}{\partial \theta}\right)_{\phi=const}\cos\theta \qquad \textbf{(17)}$$

$$V_{Gz} = V\cos\theta - \left(\frac{\partial V}{\partial \theta}\right)_{\phi=const}\sin\theta \qquad \textbf{(18)}$$

$$V_{Gy} = \frac{1}{\sin\theta}\left(\frac{\partial V}{\partial \phi}\right)_{\theta=const} \qquad \textbf{(19)}$$

The new Cartesian coordinate system, $x,\ y,\ z$ is obtained from the original, $x_1,\ x_2,\ x_3$ by rotating the horizontal axes, χ around the vertical axis of the original coordinate system, x_3 by the angle ϕ. The group velocity vector for any wave type can be found by substituting corresponding phase velocity function into the Equations 17-19. However, as the Equations 17-19 express the group velocity vector in the $x,\ y,\ z$ coordinate system, they would require for each components to be projected back onto the original coordinate system. Coordinate rotation made the derivation of Equations 17-19 much easier by laying the phase velocity vector in the $[x, z]$ plane of the new coordinate system. (Tsvankin, 2001)

Equation 19 goes to zero for a VTI medium as the phase velocity of all wave types is independent of the azimuthal angle ϕ. This implies that both the phase and group velocity vectors lay in one single plane (i.e. wave propagation plane) and have no components laying outside this plane in TI media (Figure 3).

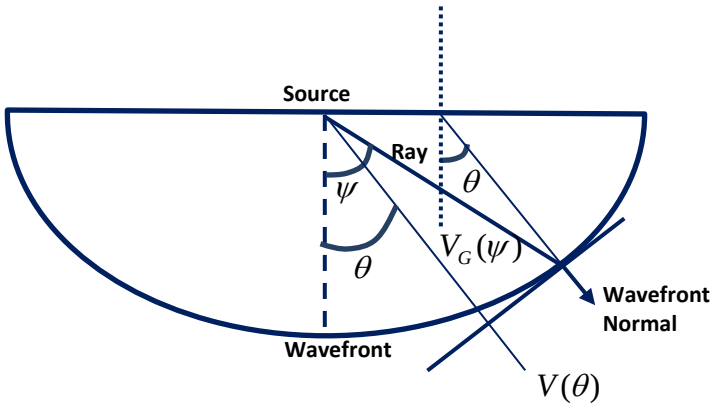

Figure 3, phase velocity $V(\theta)$ (measured in the direction normal to the wavefront) is different than the group velocity $V_G(\psi)$ (measured in the ray direction) for anisotropic media. Both of the velocities will have no component outside the wave propagation plane in a TI media.

3.8 Group velocity, phase velocity and polarization vectors in VTI medium

In VTI medium, group velocity component orthogonal to the vertical propagation plane (Equation 19) becomes zero as phase velocity of all three wave types is independent of azimuth angle ϕ. Magnitude V_G, and direction of group velocity vector, ψ of any wave type can be found by substituting corresponding phase velocity V, into the Equations 17-19. For P and SV waves, Equations 17-19 become (E.g., Tsvankin,1996):

$$V_G = V\sqrt{1+(\frac{1}{V}\frac{dV}{d\theta})^2} \qquad \textbf{020)}$$

$$\tan\psi = \frac{\tan\theta + \frac{1}{V}\frac{dV}{d\theta}}{1-\frac{\tan\theta}{V}\frac{dV}{d\theta}} \qquad \textbf{(21)}$$

Where V is defined in Equation 15 and θ is the phase angle.

In the weak anisotropy limit, we obtain for P-waves (Tsvankin, 1996):

$$\tan\psi = \tan\theta\ [1 + 2\delta + 4(\varepsilon - \delta)\sin^2\theta)] \qquad (22)$$

Or equivalently:

$$\psi = \theta + [\delta + 2(\varepsilon - \delta)\sin^2\theta]\sin 2\theta \qquad (23)$$

Vector of particle motion or polarization vector plays important role in processing and interpretation of multi-component data (Tsvankin, 2001). For a given phase (slowness) direction θ, the polarization directions of the three body waves are mutually orthogonal as they are eigenvectors of the Christoffel equation. The angle ν between the polarization vector of the P or SV waves in VTI medium and the vertical direction is (Tsvankin, 1996):

$$\tan\nu = \frac{(c_{13} + c_{55})\sin\theta\cos\theta}{\rho V^2 - c_{11}\sin^2\theta - c_{55}\cos^2\theta} \qquad (24)$$

Where ρ is the density, V is the phase velocity and c_{13} , c_{55} and c_{11} are stiffness coefficients of the anisotropic medium. In the weak anisotropy limit, P-wave approximation (Equation 16) can be substituted in Equation 24, which gives an expression for P-wave polarization angle in VTI medium (Rommel, 1994 and Tsvankin, 1996):

$$\tan\nu = \tan\theta\ [1 + 2B(\delta + 2(\varepsilon - \delta)\sin^2\theta)] \qquad (25)$$

Here $B = 1/2\, f$ where $f = 1 - \frac{V_{S0}^2}{V_{P0}^2}$.

For P-waves, the direction of polarization vector is closer to the direction of the group velocity vector than to the direction of the phase velocity vector (Tsvankin, 1996).

3.9 Group velocity, phase velocity and polarization vectors- various VTI examples

In this part, to understand the equations responsible for the P-wave propagation in VTI media, I will look at several numerical examples of P-wave phase and group velocities and group angle as well as the direction of P-wave polarization vector. In each example,

P-wave group angle and polarization dip are plotted against phase angles to understand wave's behaviour in response to various VTI anisotropy in the medium. Overlaid on the curves in the top of the Figures are the weak anisotropy approximations for P-wave group angle ψ and polarization dip ν defined in Equations 22 and 25, respectively. In each example, P-wave group velocity plotted as a function of group angle is compared with P-wave phase velocity which is plotted as a function of phase angle.

Figures 4-7, top, demonstrate how the dip of P-wave group velocity vector, ψ (Equation 21) and the dip of the polarization vector, ν (Equation 24) deviate from the phase angle (plotted as horizontal axis) in various VTI mediums. In all the cases, $V_{P0} = 3000$ m/s, $V_{S0} = 1500$ m/s and $\rho = 2300$ kg/m^3. Weak anisotropy approximations for both the P-wave group angle, ψ (Equations 22 and 23) and polarization dip, ν (Equation 25) are also plotted in these Figures. Figures 4-7, bottom, are the plots of P-wave phase velocity (Equation 15) and group velocity (Equation 20) for the same VTI media as in the top Figures. Phase velocity is plotted versus phase angle and group velocity is plotted versus group angle derived from Equation 21.

In general, the difference between P-wave phase angle and group angle varies as a function of wave propagation angle and the VTI anisotropy parameters. The difference can be as large as 20 degrees for some directions of P-wave propagation. Figures 5 and 6, top, show two examples of a large difference between P-wave phase and group angles for the wave propagation at angles between 40 and 70 degrees. However, the difference between the P-wave polarization dip and phase angle is always smaller than the difference between P-wave group angle and phase angle. The largest deviations of polarization dip and group angle from P-wave phase angle appear when δ and ε acquire opposite signs (Figures 6 and 7 top).

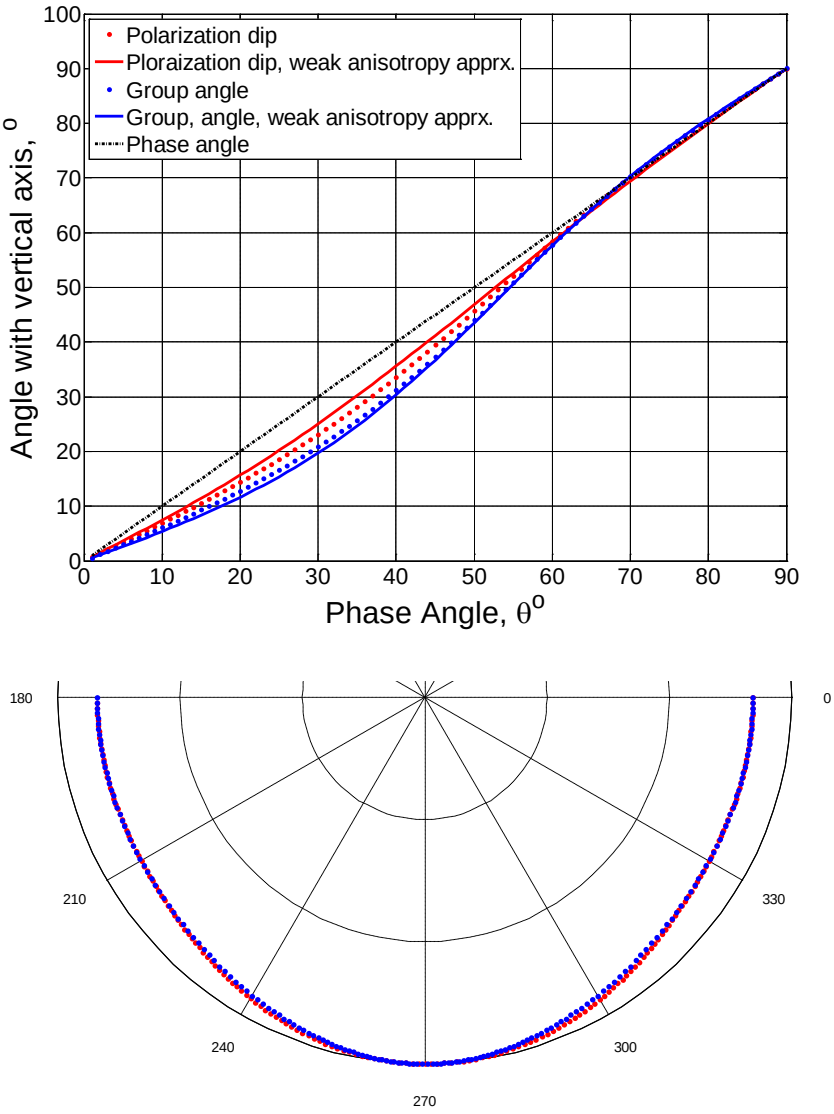

Figure 4, top, polarization angle, red dots (weak anisotropy approximation, red curve) and group angle, blue dots (weak anisotropy approximation, blue curve) are plotted versus the phase angle (black dash dots) for a P-wave traveling in a VTI medium with anisotropy parameters defined as: $V_{P0} = 3000$ **m/s,** $V_{S0} = 1500$ **m/s,** $\delta = -0.2$ **and** $\varepsilon = -0.1$**. Bottom, P-wave's phase velocity (red dots) is plotted versus group velocity (blue dots) in the same VTI medium as in top. The angle is phase angle for phase velocity curve and group angle for the group velocity curve.**

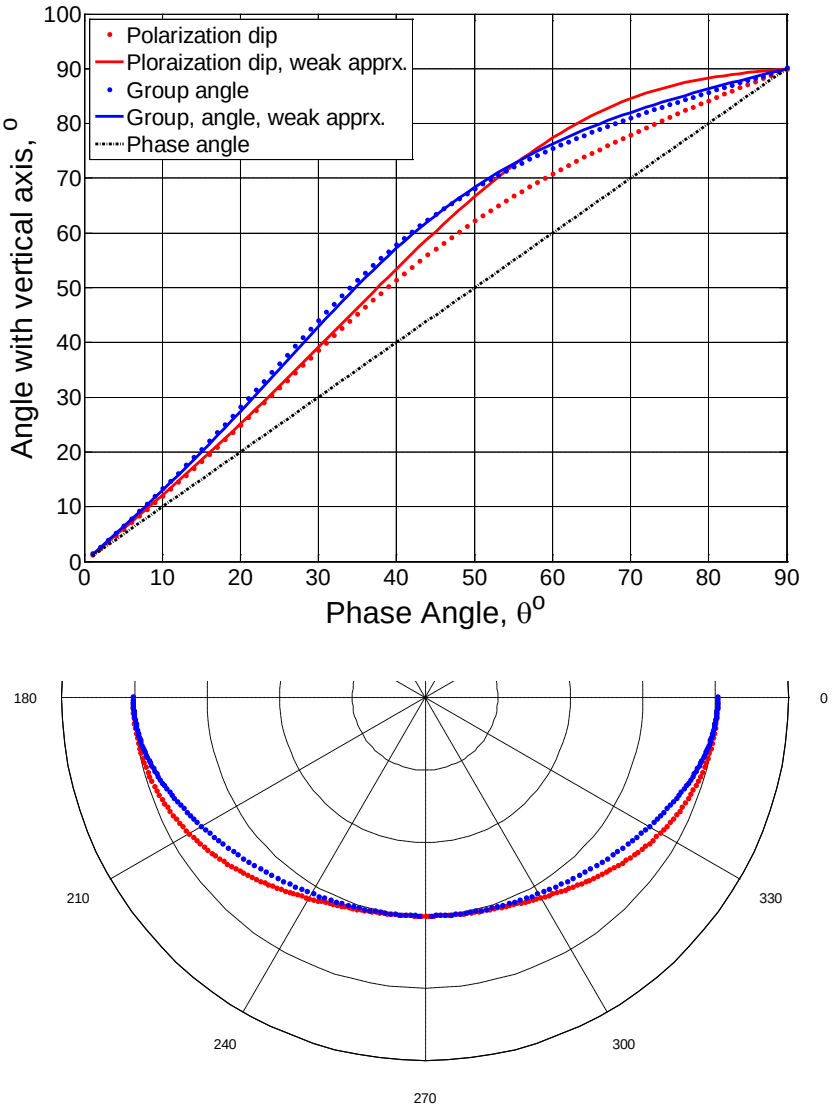

Figure 5, top, polarization angle, red dots (weak anisotropy approximation, red curve) and group angle, blue dots (weak anisotropy approximation, blue curve) are plotted versus the phase angle(black dash dots) for a P-wave traveling in a VTI medium with anisotropy parameters defined as: $V_{P0} = 3000$ **m/s,** $V_{S0} = 1500$ **m/s,** $\delta = 0.15$ **and** $\varepsilon = 0.4$**. Bottom, P-wave's phase velocity (red dots) is plotted versus group velocity (blue dots) in the same VTI medium as in top. The angle is phase angle for phase velocity curve and group angle for the group velocity curve. This medium can represent a shale formation in sedimentary basins.**

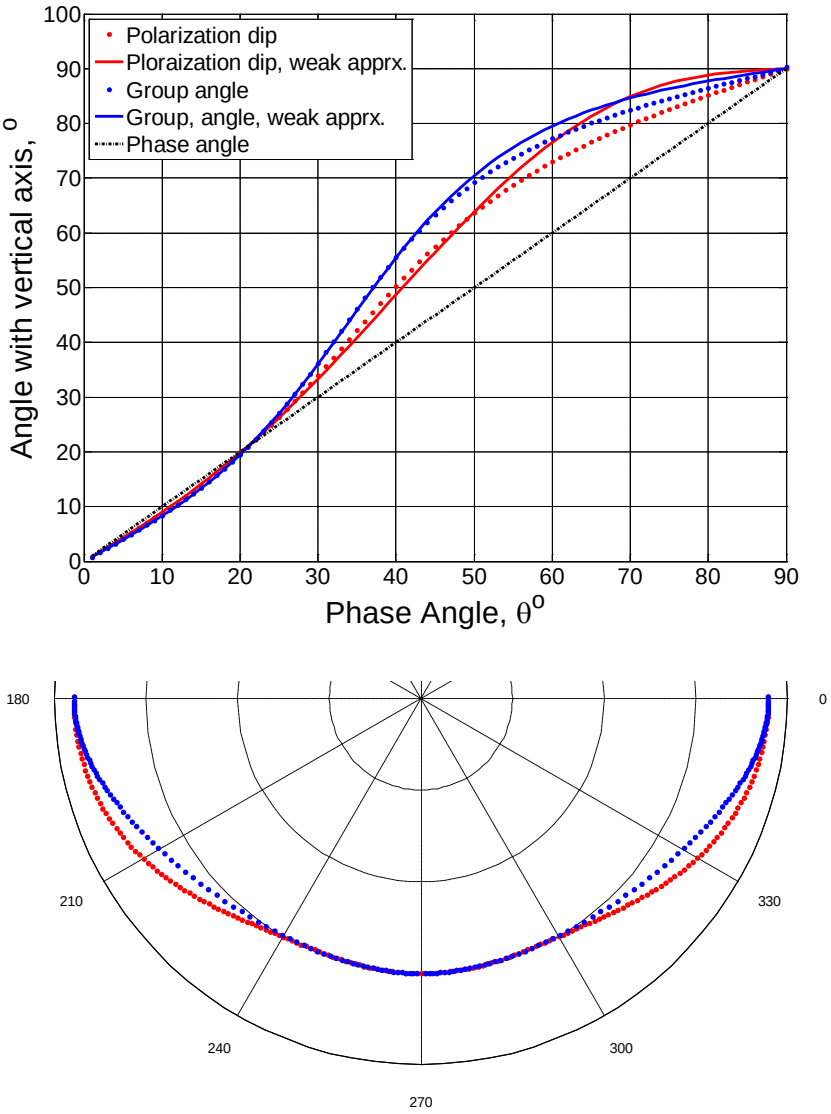

Figure 6, top, polarization angle, red dots (weak anisotropy approximation, red curve) and group angle, blue dots (weak anisotropy approximation, blue curve) are plotted versus the phase angle(black dash dots) for a P-wave traveling in a VTI medium with anisotropy parameters defined as: $V_{P0} = 3000$ **m/s,** $V_{S0} = 1500$ **m/s,** $\delta = -0.1$ **and** $\varepsilon = 0.3$**. Bottom, P-wave's phase velocity (red dots) is plotted versus group velocity (blue dots) in the same VTI medium as in top. The angle is phase angle for phase velocity curve and group angle for the group velocity curve. This medium can represent anisotropy caused by interbedding of thin isotropic layers in sedimentary basins.**

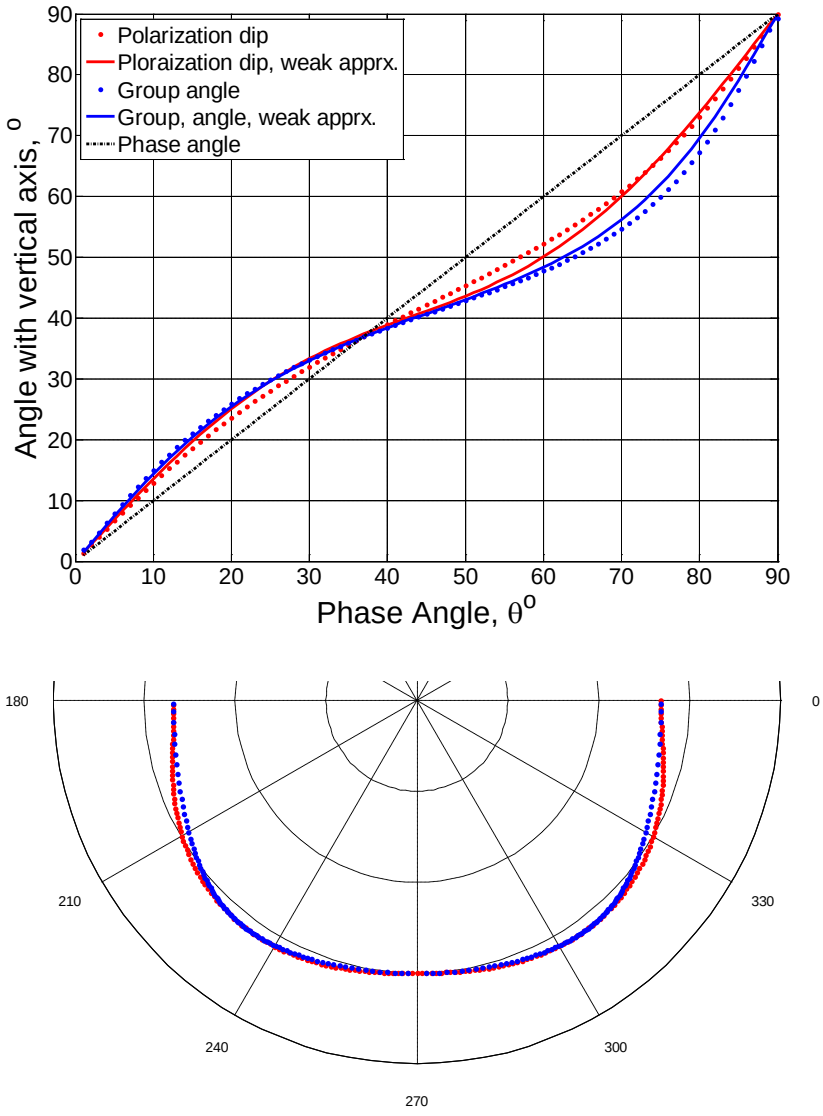

Figure 7, top, polarization angle, red dots (weak anisotropy approximation, red curve) and group angle, blue dots (weak anisotropy approximation, blue curve) are plotted versus the phase angle(black dash dots) for a P-wave traveling in a VTI medium with anisotropy parameters defined as: $V_{P0} = 3000$ **m/s,** $V_{S0} = 1500$ **m/s,** $\delta = 0.3$ **and** $\varepsilon = -0.1$**. Bottom, P-wave's phase velocity (red dots) is plotted versus group velocity (blue dots) in the same VTI medium as in top. The angle is phase angle for phase velocity curve and group angle for the group velocity curve.**

Thomsen parameters in Figures 4-7 were chosen to include examples of any possible VTI encounter in a sedimentary basin and graphs can be used to visually describe P-

wave characteristic signals in TI media as well as the validity of the approximations in each case. Conclusions can be drawn for two cases that represent most of the geological occurrence of TI anisotropy in sedimentary basins:

1. Where the anisotropy is caused by shale formations with large positive ε and small positive δ (see 3.5), one example presented in Figure 5, P-wave polarization dips lay between the group angle and the phase angle (closer to group angle) for rays with dips up to $\psi = 74^o$ ($\theta = 55^o$) from vertical. Weak approximation works well for polarization dips for rays with propagation dips of up to $\psi = 57^o$ ($\theta = 40^o$). Group angles are almost perfectly reproduced by weak anisotropy approximation for the entire range of ray propagation angles.
2. If the cause of anisotropy is the interbedding of thin (compared to seismic wavelength) isotropic layers, one will expect moderate positive ε and small negative δ (see 3.5). An example of such a medium is presented in Figure 6 where $\delta = -0.1$ and $\varepsilon = 0.3$. Amazingly the medium seems isotropic with respect to P-wave polarization dip, group and phase angles and group and phase velocities for propagation dips of up to around $\theta = \psi = 27^o$. This dip range is the acquisition plan that is considered for most of the traditional seismic surveys and requires source-receiver offset to be the same size as the target depth.

3.10 Anisotropic parameterization of orthorhombic media

Tsvankin (1997) follows Thomsen's recipe and uses the analogy of the symmetry planes of an orthorhombic media to a VTI media to parameterize the orthorhombic media. The stiffness coefficients are replaced with a number of anisotropic parameters that can characterize seismic signatures of an orthorhombic medium both in and outside the symmetry planes. The parameterization in $[x_1, x_3]$ symmetry plane is as the following:

$$V_{P0} = \sqrt{\frac{c_{33}}{\rho}} \tag{26}$$

$$V_{S0} = \sqrt{\frac{c_{55}}{\rho}} \tag{27}$$

$$\varepsilon^{(2)} = \frac{c_{11} - c_{33}}{2c_{33}} \tag{28}$$

$$\delta^{(2)} = \frac{(c_{13} + c_{55})^2 - (c_{33} - c_{55})^2}{2c_{33}(c_{33} - c_{55})} \tag{29}$$

$$\gamma^{(2)} = \frac{c_{66} - c_{44}}{2c_{44}} \tag{30}$$

Here, V_{P0} is the vertical velocity of the P-wave and V_{S0} is the velocity of the split shear wave which is polarized in the x_1 direction. $\varepsilon^{(2)}$, $\delta^{(2)}$ and $\gamma^{(2)}$ are analogues to the VTI parameters ε, δ and γ defined in the symmetry plane $[x_1,\ x_3]$ of the orthorhombic medium. For $[x_2,\ x_3]$ symmetry plane, the parameterization is:

$$\varepsilon^{(1)} = \frac{c_{22} - c_{33}}{2c_{33}} \tag{31}$$

$$\delta^{(1)} = \frac{(c_{23} + c_{44})^2 - (c_{33} - c_{44})^2}{2c_{33}(c_{33} - c_{44})} \tag{32}$$

$$\gamma^{(1)} = \frac{c_{66} - c_{55}}{2c_{55}} \tag{33}$$

The only remaining stiffness c_{12} is replaced with $\delta^{(3)}$ which is a dimensionless anisotropy parameter defined for the symmetry plane $[x_1,\ x_2]$:

$$\delta^{(3)} = \frac{(c_{12} + c_{66})^2 - (c_{11} - c_{66})^2}{2c_{11}(c_{11} - c_{66})} \tag{34}$$

This notation preserves all the important features of Thomsen parameters in wave propagation in the symmetry planes of orthorhombic media. I will make use of this notation to define orthorhombic media in our analysis in Chapter 6.

3.11 P-wave phase velocity in orthorhombic media

Equation 4 leads to a solution of a cubic equation for phase velocity that is valid for any homogeneous anisotropic medium (Schoenberg and Helbig, 1997):

$$x^3 + ax^2 + bx + c = 0 \qquad (35)$$

Where

$$x = \rho V^2 \qquad (36)$$

$$a = -(G_{11} + G_{22} + G_{33}) \qquad (37)$$

$$b = G_{11}G_{22} + G_{11}G_{33} + G_{22}G_{33} - G_{12}^2 - G_{13}^2 - G_{23}^2 \qquad (38)$$

$$c = G_{11}G_{23}^2 + G_{22}G_{13}^2 + G_{33}G_{12}^2 - G_{11}G_{22}G_{33} - 2G_{12}G_{13}G_{23} \qquad (39)$$ 0

Through a change of variable ($x = y - \frac{a}{3}$) Equation 35 reduces to:

$$y^3 + dy + q = 0 \qquad (40)$$

where

$$d = -\frac{a^2}{3} + b \qquad (41)$$ and $$q = 2(\frac{a}{3})^3 - \frac{ab}{3} + c \qquad (42)$$

Matrix G is symmetric and it can be shown that the coefficient d is negative (Schoenberg and Helbig, 1997). For real roots in Equation 40 we need:

$$Q = (\frac{d}{3})^3 + (\frac{q}{2})^2 \le 0 \qquad (43)$$

The three solutions of Equation 40 can be represented as (Korn and Korn, 1968):

$$y_{1,2,3} = 2\sqrt{\frac{-d}{3}}\cos\left(\frac{\alpha}{3} + k\frac{2\pi}{3}\right) \quad (44)$$

Where $k = 1,\ 2,\ 3$ and $$\cos\alpha = -\frac{q}{2\sqrt{(-d/3)^3}} \qquad 0 \le \alpha \le \pi \quad (45)$$

The phase velocity is found from:

$$\rho V^2 = y - \frac{a}{3} \quad (46)$$

The largest root (k=0) yields the phase velocity of the P-wave.

To evaluate phase velocity for orthorhombic media, we use Christoffel matrix for orthorhombic media:

$$G_{11} = c_{11}n_1^2 + c_{66}n_2^2 + c_{55}n_3^2 \quad (47)$$

$$G_{22} = c_{66}n_1^2 + c_{22}n_2^2 + c_{44}n_3^2 \quad (48)$$

$$G_{33} = c_{55}n_1^2 + c_{44}n_2^2 + c_{33}n_3^2 \quad (49)$$

$$G_{12} = (c_{12} + c_{66})n_1n_2 \quad (50)$$

$$G_{13} = (c_{13} + c_{55})n_1n_3 \quad (51)$$

$$G_{23} = (c_{23} + c_{44})n_2n_3 \quad (52)$$

Where, c_{ijkl} is the stiffness tensor of the orthorhombic media as defined in Equation 8 and n_1, n_2 and n_3 are the components of the unit vector **n** that is normal to the wavefront and defines the direction of the wave propagation (directional cosines).

Tsvankin (1997) derives Christoffel matrix for orthorhombic media as a function of anisotropic parameters:

$$\frac{G_{11}}{\rho} = n_1^2V_{P0}^2(1+2\varepsilon^{(2)}) + n_2^2V_{S0}^2(1+2\gamma^{(1)}) + n_3^2V_{S0}^2 \quad (53)$$

$$\frac{G_{22}}{\rho} = n_1^2 V_{S0}^2 (1+2\gamma^{(1)}) + n_2^2 V_{P0}^2 (1+2\varepsilon^{(1)}) + n_3^2 V_{S0}^2 \frac{1+2\gamma^{(1)}}{1+2\gamma^{(2)}} \quad \textbf{(54)}$$

$$\frac{G_{33}}{\rho} = n_1^2 V_{S0}^2 + n_2^2 V_{S0}^2 \frac{1+2\gamma^{(1)}}{1+2\gamma^{(2)}} + n_3^2 V_{P0}^2 \quad \textbf{(55)}$$

$$\frac{G_{12}}{\rho} = n_1 n_2 V_{P0}^2 (1+2\varepsilon^{(2)}) D \sqrt{1+2\delta^{(3)}/D} \quad \textbf{(56)}$$

$$D = 1 - \frac{V_{S0}^2}{V_{P0}^2} \frac{1+2\gamma^{(1)}}{1+2\varepsilon^{(2)}} \quad \textbf{(57)}$$

$$\frac{G_{13}}{\rho} = n_1 n_3 V_{P0}^2 f \sqrt{1+2\delta^{(2)}/f} \quad \textbf{(58)}$$

$$\frac{G_{23}}{\rho} = n_2 n_3 V_{P0}^2 E \sqrt{1+2\delta^{(1)}/E} \quad \textbf{(59)}$$

$$E = 1 - \frac{V_{S0}^2}{V_{P0}^2} \frac{1+2\gamma^{(1)}}{1+2\gamma^{(2)}} \quad \textbf{(60)}$$

Where $f = 1 - \frac{V_{S0}^2}{V_{P0}^2}$.

In Equations 53-60, n_i are the directional cosines of the slowness (or phase velocity) vector and it is assumed that the anisotropy is mild ($c_{12} + c_{66} \geq 0$, $c_{13} + c_{55} \geq 0$ and $c_{23} + c_{44} \geq 0$) as defined by Schoenberg and Helbig (1997).

Equations 53-60 establish a relationship between the Christoffel matrix and the anisotropy parameters of the orthorhombic media (defined by Tsvankin, 1997) and can be used together with phase velocity Equations 35-46 to invert for anisotropy parameters of the orthorhombic medium. However, I was not able to generate a unique and reliable estimate of the anisotropy parameters by minimizing the least-square objective function (see 3.15) using the inversion algorithm *fminsearch* of MATLAB program. On the other hand, I was able to use Equations 35-52 to reliably invert P-wave numerical and

measured slownesses for the elasticity coefficients of the orthorhombic media in the uncertainty analysis and in the CRC-1 well example, respectively. Anisotropy parameter estimations were then calculated from inverted elastic coefficients of the orthorhombic media.

3.12 Weak anisotropy approximation for P-wave phase velocity in orthorhombic media

Tsvankin (1997) derives a weak anisotropy approximation for P-wave phase velocity outside the symmetry planes of orthorhombic media by linearizing the exact equations in the anisotropic coefficients:

$$V_P = V_{P0}[1 + \delta(\phi)\sin^2\theta\cos^2\theta + \varepsilon(\phi)\sin^4\theta] \quad (61)$$

Where

$$\delta(\phi) = \delta^{(1)}\sin^2\phi + \delta^{(2)}\cos^2\phi \quad (62)$$

$$\varepsilon(\phi) = \varepsilon^{(1)}\sin^4\phi + \varepsilon^{(2)}\cos^4\phi + (2\varepsilon^{(2)} + \delta^{(3)})\sin^2\phi\cos^2\phi \quad (63)$$

In Equation 61, V_{P0} is the P-wave velocity along the vertical symmetry axis of the orthorhombic media (Equation 26), θ is the phase angle (measured from vertical) and $\delta(\phi)$ and $\varepsilon(\phi)$ are the Thomsen anisotropy parameters in the azimuthal plane defined by ϕ. Based on this approximation, an orthorhombic media (with two vertical and one horizontal symmetry planes) can be reconstructed by a combination of VTI symmetry planes that are oriented in the azimuthal direction ϕ with the anisotropy parameters defined by $\delta(\phi)$ and $\varepsilon(\phi)$. Anisotropy parameters $\varepsilon^{(2)}$, $\delta^{(2)}$, $\varepsilon^{(1)}$, $\delta^{(1)}$ and $\delta^{(3)}$ are as defined in Equations 28, 29, 31, 32 and 34, respectively. I will make use of this analogy between orthorhombic and VTI media in Chapter 6 to approximate a 3D orthorhombic media by 2D VTI models. I will generate synthetic seismograms over 2D VTI models along 36 azimuthal directions where the anisotropy parameters are estimated by Equations 62 and 63. Slownesses measured along various azimuths and phase angles will then be inverted for medium stiffnesses and anisotropy parameters of the orthorhombic medium will be computed (Equations 28-34).

3.13 P-wave Group velocity, phase velocity and polarization vector in orthorhombic medium

To gain a better understanding of the P-wave propagation in orthorhombic media, herein I will present three examples of different orthorhombic media. Becoming more complex than VTI case, P-wave group velocity and polarization vector deviate from the direction of P-wave propagation vector (slowness vector) in both the dip and azimuth directions. In each example, orthorhombic anisotropy is generated by introducing a system of vertical fractures in a VTI background (in all the cases, $V_{P0} = 3000$ m/s, $V_{S0} = 1500$ m/s and $\rho = 2300$ kg/m^3) where the fracture normals are in the x_1 direction (see Chapter 6 for more description). Model fractures are dry and rotationally invariant with fracture weakness $\delta_N = 0.4$ (Schoenberg and Helbig, 1997). In each case, P-wave phase velocity, group velocity and deviation of polarization and group velocity vectors from the slowness vector are computed and plotted for the entire azimuth and dip range.

1. First example is illustrated in Figure 8, P-wave phase velocity, the magnitude of group velocity vector and the deviation of polarization/group velocity vectors from the slowness vector have been plotted for the orthorhombic medium that is generated by combining a VTI background ($\delta = -0.2$ and $\varepsilon = -0.1$) and a dry vertical fracture set ($\delta_N = 0.4$) with fracture normals in the x_1 (East-West) direction. As is evident in the Figure 8 (top), the phase velocity (left) and group velocity (right) are different in this medium and vary as a function of dip angle and azimuth. The smallest velocity is in the horizontal direction and perpendicular to the fracture plane (along x_1 direction, East-West) and the largest is in the fracture plane and along vertical axis (x_3). In the vertical plane, the deviation of the group velocity vector from the phase velocity vector is very similar to the deviation of the polarization vector from the phase velocity vector (Figure 8, middle right and bottom right) whereas in the horizontal plane this deviation is less comparable (Figure 8, middle left and bottom left).
2. In the second example illustrated in Figure 9, P-wave phase velocity, the magnitude of group velocity vector and the deviation of polarization/ group velocity vectors from the slowness vector have been plotted for the orthorhombic medium that is

generated by combining a VTI background ($\delta = 0.2$ and $\varepsilon = 0.1$) and a dry vertical fracture set ($\delta_N = 0.4$) with fracture normals in the x_1 (East-West) direction. The smallest velocity (phase/group) is measured in the horizontal direction (x_1) and perpendicular to the fracture plane where as the largest velocity is measured along the x_2 (North-South) direction and within the fracture plane. In the vertical plane, deviation of group velocity vector from phase velocity vector is very similar to the deviation of polarization vector from phase velocity vector (Figure 9, middle right and bottom right) whereas in the horizontal plane this deviation is less comparable (Figure 9, middle left and bottom left).

3. In the third example illustrated in Figure 10, P-wave phase velocity, the magnitude of group velocity vector and the deviation of polarization/ group velocity vectors from the slowness vector have been plotted for the orthorhombic medium that is generated by combining a VTI background ($\delta = -0.1$ and $\varepsilon = 0.3$) and a dry vertical fracture set ($\delta_N = 0.4$) with fracture normals in the x_1 (East-West) direction. The largest velocity is measured along the x_2 (North-South) direction whereas the smallest velocity is measured along the x_3 (vertical axis) and two more directions rotated by $\pm 45^{o}$ within the $[x_1, x_3]$ plane. In the vertical plane, deviation of group velocity vector from phase velocity vector is very similar to the deviation of polarization vector from phase velocity vector (Figure 10, middle right and bottom right) whereas in the horizontal plane this deviation is less comparable (Figure 10, middle left and bottom left).

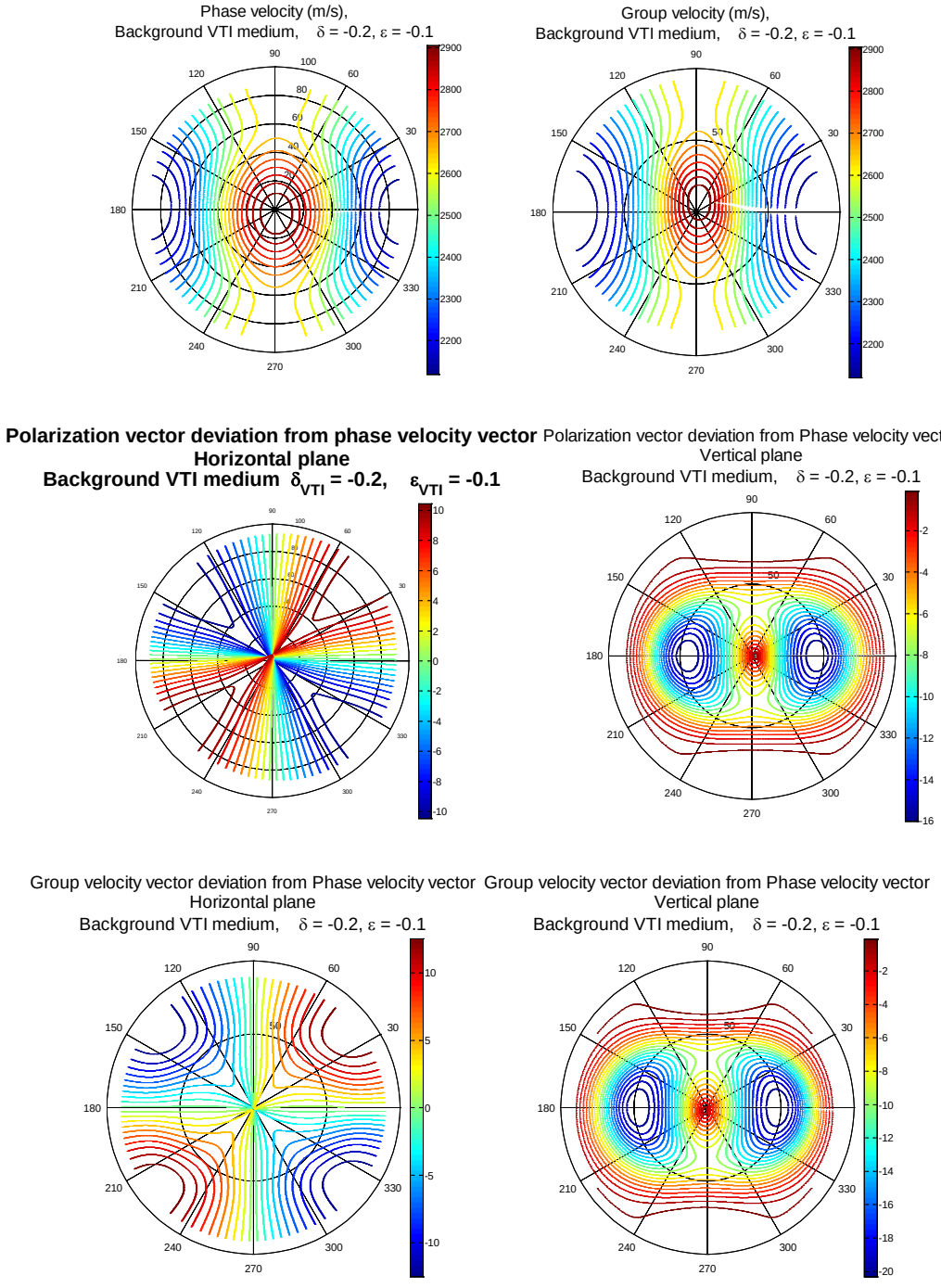

Figure 8, P-wave phase velocity (top left), group velocity (top right), deviation of polarization and group velocity vectors from the slowness vector (middle and bottom, respectively) for the orthorhombic medium that is generated by combining a VTI background ($\delta = -0.2$ and $\varepsilon = -0.1$) and a dry vertical fracture set ($\delta_N = 0.4$) with fracture normals in the x_1 direction.

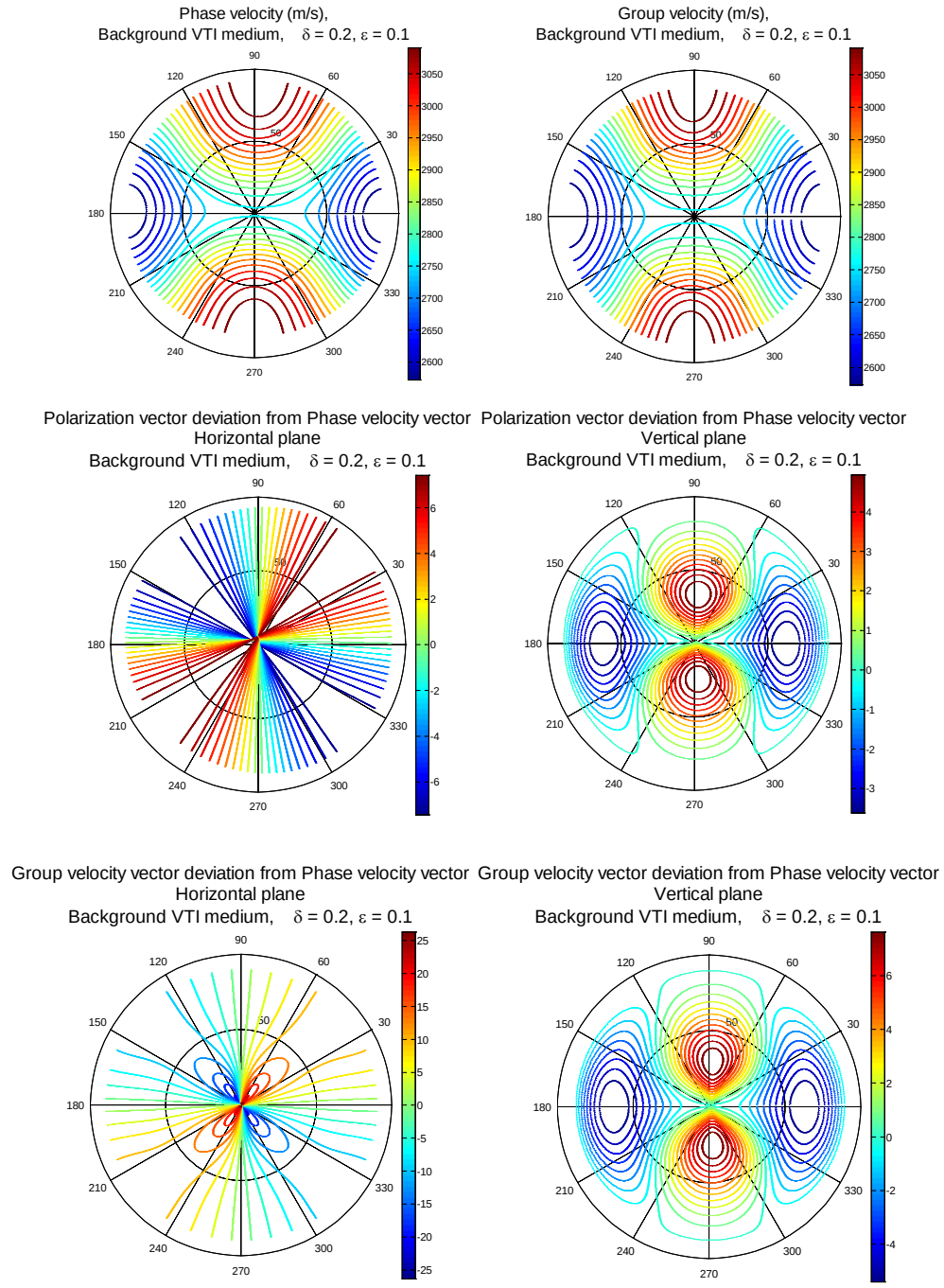

Figure 9, P-wave phase velocity (top left), group velocity (top right), deviation of polarization and group velocity vectors from the slowness vector (middle and bottom, respectively) for the orthorhombic medium that is generated by combining a VTI background ($\delta = 0.2$ and $\varepsilon = 0.1$) and a dry vertical fracture set ($\delta_N = 0.4$) with fracture normals in the x_1 direction.

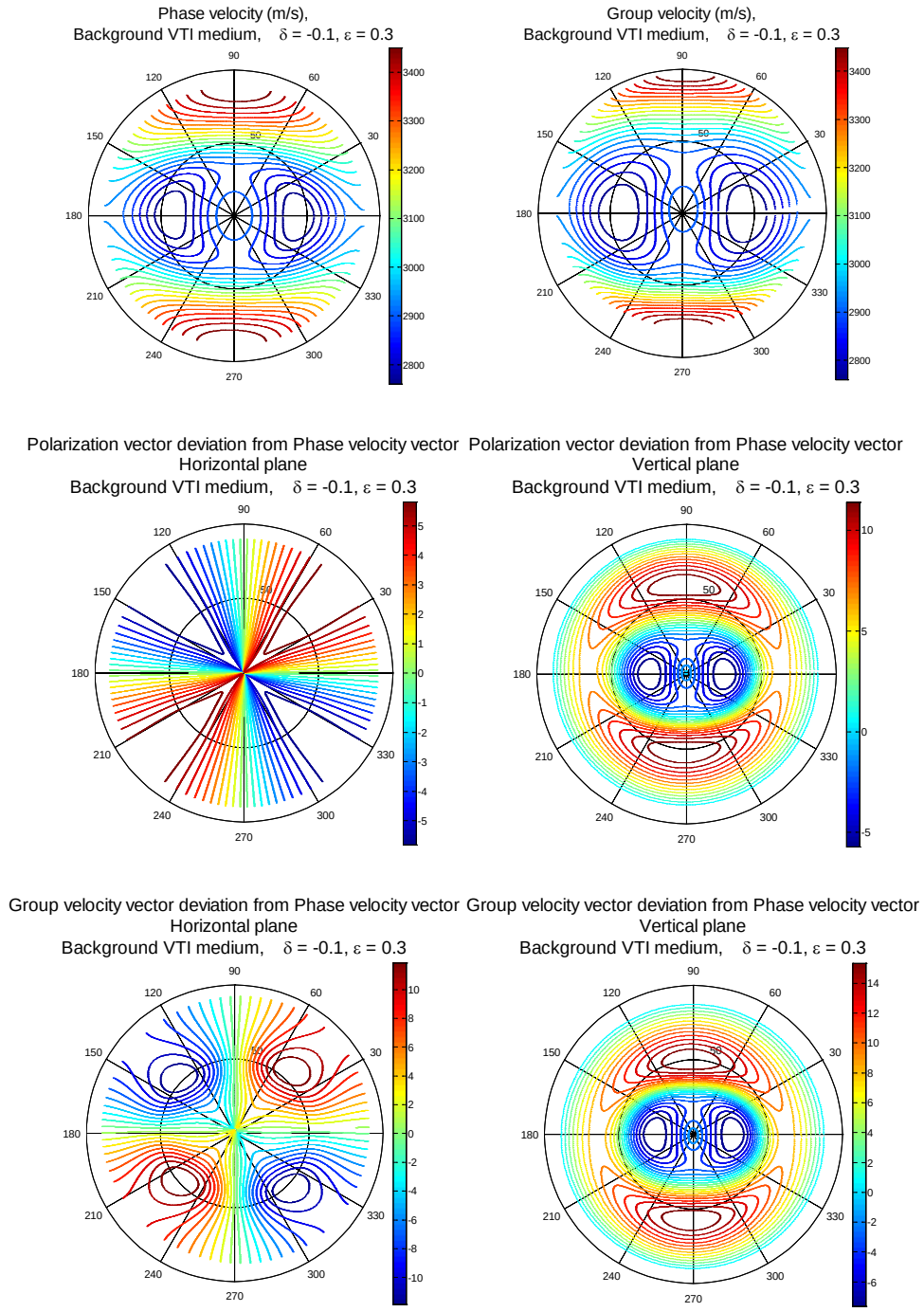

Figure 10, P-wave phase velocity (top left), group velocity (top right), deviation of polarization and group velocity vectors from the slowness vector (middle and bottom, respectively) for the orthorhombic medium that is generated by combining a VTI background ($\delta = -0.1$ and $\varepsilon = 0.3$) and a dry vertical fracture set ($\delta_N = 0.4$) with fracture normals in the x_1 direction.

3.14 Adding noise to slowness and polarization data

Three component VSP recordings can be utilized to measure subsurface particle displacement as a result of wave propagation in the medium surrounding the geophones in the borehole. Particle displacement measurements are usually presented in the form of polarization vectors as they have both the magnitude and a direction. Another important wave measurement that can be obtained from VSP data is the local slowness vector at the location of borehole receivers. Vertical component of this vector, q for a specified receiver depth can be easily computed from the time recordings of an array of receivers where the centre of the array is positioned at the given receiver depth. q can be calculated as the rate of wave's first arrival time change with the geophone depth. If the overburden predominately consists of horizontal layers geometry with laterally homogeneous rock formations, horizontal components of the slowness vector, p can be measured on the earth surface and transferred to the receiver depth. This transformation is based on the Snell's law for plane wave propagation in horizontally stratified media which states that the horizontal component of the wave's slowness vector, p will not change with depth as the wave propagates downward. In this case, horizontal components of the slowness vectors are regarded as the rate of wave's first arrival change with the distance between VSP sources on the surface. These vector measurements will then be used to derive anisotropy parameters of the medium that is local to the receiver location in the borehole. In order to be able to quantify the uncertainties of using VSP data for anisotropy parameter estimation, I will use Christoffel equation to generate numerical slowness and polarization vectors for a range of anisotropic media and within a range of wave propagation (phase) angles. This data will be used as (synthetic) measurements to invert for the parameters of the corresponding anisotropic media. If the inversion model is an exact equation, then errors will be introduced to vector measurements to evaluate the efficiency of the method in the presence of the noise in the measurements. In our analysis, errors are represented in the form of randomly normally distributed vectors in the space that are added to the numerical slowness and polarization vectors. This method can be mathematically expressed for vectors in 2D space with the following equations:

$$S=\begin{bmatrix} p_1 & p_2 & \cdots & p_n \\ q_1 & q_2 & \cdots & q_n \end{bmatrix}, \qquad (64) \qquad L=\begin{bmatrix} l_1 & l_2 & .. & l_n \end{bmatrix}, \qquad 065)$$

$$l_i=\sqrt{p_i^2+q_i^2}\,, \qquad 066) \qquad A=\begin{bmatrix} a_{11} & a_{12} & \cdots & a_{1n} \\ a_{21} & a_{22} & \cdots & a_{2n} \end{bmatrix}, \qquad (67)$$

$$E=e*A*\begin{bmatrix} l_1 & 0 & .. & 0 \\ 0 & l_2 & .. & 0 \\ : & : & .. & : \\ 0 & 0 & .. & l_n \end{bmatrix}, \qquad (68) \qquad S_{err}=S+E\,. \qquad 069)$$

In the above, matrix S represents the original numerical data in which horizontal and vertical components of n data (slowness/polarization) vectors are represented by the values in the first and second rows of the matrix, respectively. Vector L represents the norm of the data vectors taken from matrix S. Matrix E is the error matrix comprising two rows and n columns. The error matrix is computed by multiplying matrix A with a diagonal matrix of the data vectors and the error value e. Elements in the columns of matrix A are randomly drawn from a standard distribution of numbers (with $\mu=0$ and $\sigma=1$). Matrix S_{err} represents the data vectors that are contaminated with noise taken from E. In 3D space, both the data (slowness/polarization) and error vectors will have one additional vector component in the horizontal direction and hence the corresponding matrixes, S and E as well as matrix of randomly distributed numbers, A will include one more row of elements. Figure 11 shows an example of our methodology to add random noise vectors, E (red arrows) to slowness vectors, S (black arrows) in 2D space. In Figure 11, original slowness data consist of P-wave slowness vectors computed along 9 phase directions in a vertical plane within the VTI medium defined by $V_{P0}=3000$ m/s, $V_{S0}=1500$ m/s, $\varepsilon=0.2$, $\delta=0.1$, and density $\rho=2000$ kg/m^3. Slowness vectors are contaminated with $e=0.05$ (5%) noise and are displayed with dot-dash arrows to represent S_{err}.

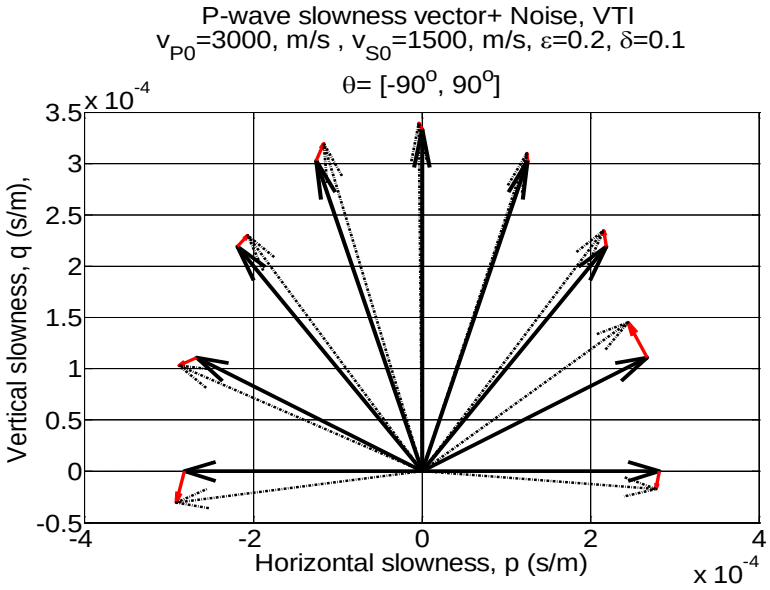

Figure 11, P-wave slowness vectors (black solid arrow in 9 phase directions) are contaminated by normally distributed random noise vectors (red arrow) to generate new slowness vectors (black dot-dash arrows) for the error analysis.

3.15 Minimization algorithm, *fminsearch*

I will use MATLAB's minimization tool, *fminsearch* throughout of my numerical analysis of determining the uncertainties related to the estimation of VTI / orthorhombic anisotropy parameters using P-wave slowness and polarization data. This function finds a local minimum of unconstrained multivariable function using derivative-free (simplex search) method usually referred to as *unconstrained nonlinear optimization*. Numerical analysis shows that, the objective function, L_2 norm of the mismatch between measured and modeled values returns a local minima with respect to anisotropy (elastic) parameters for all the methods used in this study for the inversion of VTI / orthorhombic anisotropy parameters using P-wave slowness and polarization data. As a result, I expect MATLAB's *fminsearch* minimization tool to be an appropriate algorithm that can be utilized to constrain the anisotropy (elastic) parameters for both the slowness only and slowness-polarization methods analysed in this study.

Function *fminsearch* does not use numerical or analytic gradients. It starts at the initial point x_0 and returns a value x that is a local minimizer of the objective function defined

as f . Function *fminsearch* uses the Nelder-Mead simplex algorithm as described by Lagarias et al., (1998). The nelder-Mead technique was proposed by Nelder and Mead (1965) and is a technique to minimize an objective function in multi-dimensional space. A *simplex* is geometrical figure formed by a set of n+1 points in an n-dimensional space. If n is the length of x (variable vector), a simplex in n-dimensional space is characterized by the n+1 distinct vectors that are its vertices. In two dimensional space, a simplex is a triangle; in three dimensional space, it is a pyramid.

The basic idea in this method is to compare the values of the objective function at the n+1 vertices of the simplex and move it toward the optimum point in an iterative manner. At each step of the search, a new point in or near the current simplex is generated. The function value at the new point is compared with the function's values at the vertices of the simplex and, usually, one of the vertices is replaced by the new point, giving a new simplex. This step is repeated until the diameter of the simplex is less than the specified tolerance. Figure 12 demonstrates a simplex in a three dimensional variable space (black) which has moved one step toward the minimum point of the objective function by making a new simplex (red). In this algorithm, values of the objective function corresponding to the vertices of the simplex are first sorted from the smallest to the highest value X_{high}. Then, X_{high} is replaced by a reflection point X_r in the opposite direction of the simplex to acquire the smallest value in a newly formed simplex. This process continues iteratively until the minimum point is reached.

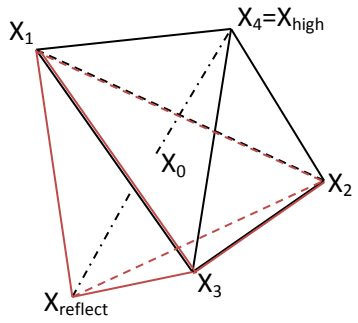

Figure 12, construction of the reflection point in the simplex method.

3.16 Summary and remarks

This chapter is aimed to briefly review the important equations and background theory of P-wave propagation in transverse isotropy (TI) and orthorhombic media. TI media with vertical axis of symmetry can be the representative of shale formations which comprise a large portion of formation rocks in the earth sedimentary basins. TI media with horizontal axis of symmetry can represent a hydrocarbon reservoir comprising an isotropic sandstone rock and a single set of vertical fractures embedded in the background rock. An orthorhombic medium with lower symmetry than HTI, would represent a rock formation composed of a TI background embedded with a vertical system of fractures.

Christoffel equation is the basis for all the equations that are used to model seismic wave propagation in anisotropic media with arbitrary symmetry. For any given direction in the medium, solution of Equation 4 yields three phase velocities that correspond to one P-wave and two S-waves. Eigenvectors will determine the polarization of each type of the wave. In the subsequent chapters of this thesis, I will use Christoffel equation to generate numerical slowness and polarization data for P-wave propagation in various TI and orthorhombic media and within the specified ranges of dips and azimuthal angles. I will use Thomsen (1985) and Tsvankin (1997) notations to define TI and orthorhombic media, respectively. As required, slowness or polarization information generated by Christoffel equation will be used to quantify the uncertainties associated with the available methods (mostly based on VSP data) in anisotropy parameter estimation. Equations 35-52 will be used to invert P-wave slowness data for elastic coefficients of the orthorhombic medium in Chapter 6. Function *fminsearch* fails to constrain the anisotropy parameters of the orthorhombic medium by inversion of P-wave slownesses (1/velocities) using Equations 53-60 most likely because of large degree of non-linearity in the equations that leads to generation of several local minimas in the objective function. However, *fminsearch* successfully constrains most of the elastic coefficients of the orthorhombic medium when Equations 47-52 are used to calculate Christofell's matrix.

I will use Equations 62 and 63 in Chapter 6 to approximate a 3D orthorhombic media by equivalent 2D VTI models. I will generate synthetic (finite-difference) seismograms over 2D VTI models along 36 azimuthal directions where the anisotropy parameters are defined by Equations 62 and 63. Slownesses measured along various azimuths and phase angles will be inverted for anisotropy parameters of the orthorhombic medium (Equations 28-34).

Chapter 4, VTI anisotropy parameter estimation using P-wave slownesses only

4.1 Introduction

In this chapter I will evaluate and discuss P-wave slownesses method for estimation of elastic anisotropic parameters from walkaway VSP measurements. A particular attention is given to the limitations and the assumptions of the method. The errors are computed and quantified in an attempt to establish the general validity of P-wave slowness method. For that purpose I utilize both 2D walk-away and 3D VSP data. Through parts 4.3 to 4.5, I will explain the theory of two commonly practiced slowness methods for VTI parameter estimation and quantify the uncertainties associated with each method. First method, analysed in Sections 4.3 and 4.4, uses P-wave phase dispersion relation in VTI media derived by Miller and Spencer (1994). The second method, described in Section 4.5, is based on Thomsen's weak anisotropy approximation for P-wave phase velocity in VTI media. I will quantify the estimation errors with respect to P-wave's maximum phase angle, medium anisotropy and noise in the measurements. In Sections 4.6 and 4.7, I will present two examples for VTI parameter estimation based on the application of first method. First example, described in Section 4.6, is using synthetic walkaway VSP data that were generated by a finite-difference wave propagation algorithm over a velocity model that represents the subsurface at the location of well CRC-1 in CO2CRC's Otway geosequestration site. Interval velocity values have been extracted from log measurements at CRC-1 well location. Second example, in Section 4.7, uses P-wave travel time measurements of a three component, 3D VSP survey which was acquired at well CRC-1 location in 2010. The last part of this chapter is dedicated to discuss the observations and remarks.

4.2 Estimation of P-wave slowness vector from multi-offset VSP data

Within the conventional configuration of borehole surveys, strings of receivers are positioned along a vertical borehole and there is no possibility for travel time measurements in the perpendicular directions. As such, travel time changes in the horizontal direction (horizontal components of the slowness vector) have to be estimated on the earth surface where horizontal movement of sources can be used to estimate horizontal slownesses on the surface. For a laterally homogeneous and horizontal

stratification in the overburden, horizontal slownesses measured on the surface can be transferred to the receiver location in the borehole by the application of Snell's law. As a result, estimation of local P-wave slowness vector from travel times that are recorded by downhole geophones in a VSP measurement would largely be dependent on the overburden conditions. If the overburden is complex and laterally heterogeneous, horizontal components of the slowness vector have to be corrected before transferring to the receiver location (Bakulin et al., 2000). Based on the Snell's law for horizontal layers, horizontal component of the slowness vector is conserved as the wave propagates in depth. To measure the horizontal component of P-wave slowness vector generated by a given source on the surface, VSP data are sorted to common-receiver domain where traces recorded by a given geophone at a given depth level are grouped together. In this domain, the gradient of P-wave first arrivals with the distance between the sources (in a window) is regarded as the horizontal component of the slowness vector for the given receiver. For the given receiver in the borehole, horizontal components of the slowness vector will be measured for every source location on the surface by sliding the source window along the survey line (Figure 1).

On the other hand, vertical component of the P-wave's slowness vector is measured locally in the borehole. First arrivals of the wave excited at the surface are recorded by a string of geophones in the (vertical) borehole. To measure vertical component of the slowness vector, VSP data are sorted in common-shot gathers (Figure 1, left). In this domain, traces (of a single shot) that are recorded by all the geophones in the borehole are gathered together. For the given receiver position in shot domain (above example), the gradient of P-wave's first arrivals with depth is regarded as the vertical component of the slowness vector. Vertical component of the slowness vectors (for the given receiver), are computed for all the sources on the surface. The technique that only uses P-wave slowness vectors to estimate local VTI anisotropy parameters is known as slowness method (Gaiser, 1990; Miller and Spencer, 1994; Jilek et al., 2003, Slawinski et al., 2003).

In the case of strong lateral heterogeneity in the overburden, local P- and S-wave slowness and polarization measurements have been used by researchers to estimate local

VTI parameters (Horne and Leaney, 2000). Polarization information is extracted from three component geophone measurements in the borehole. However, identification and separation of SV- and SH-waves beneath complex velocity structures will sometimes restrict the applicability of this method. Grechka and Mateeva (2007) present an example of using only P-wave slownesses and polarizations to estimate VTI parameters beneath a complex overburden. Slowness-polarization methods that use only P-wave data seem to be less dependent on the overburden conditions as they don't require the horizontal component of the slowness vector and shear wave separation. However, they produce unstable results in the presence of noisy P-wave polarization measurements. Generation of noise in a VSP survey and contamination of P-wave polarization measurements with noise will be explained in detail in a separate chapter.

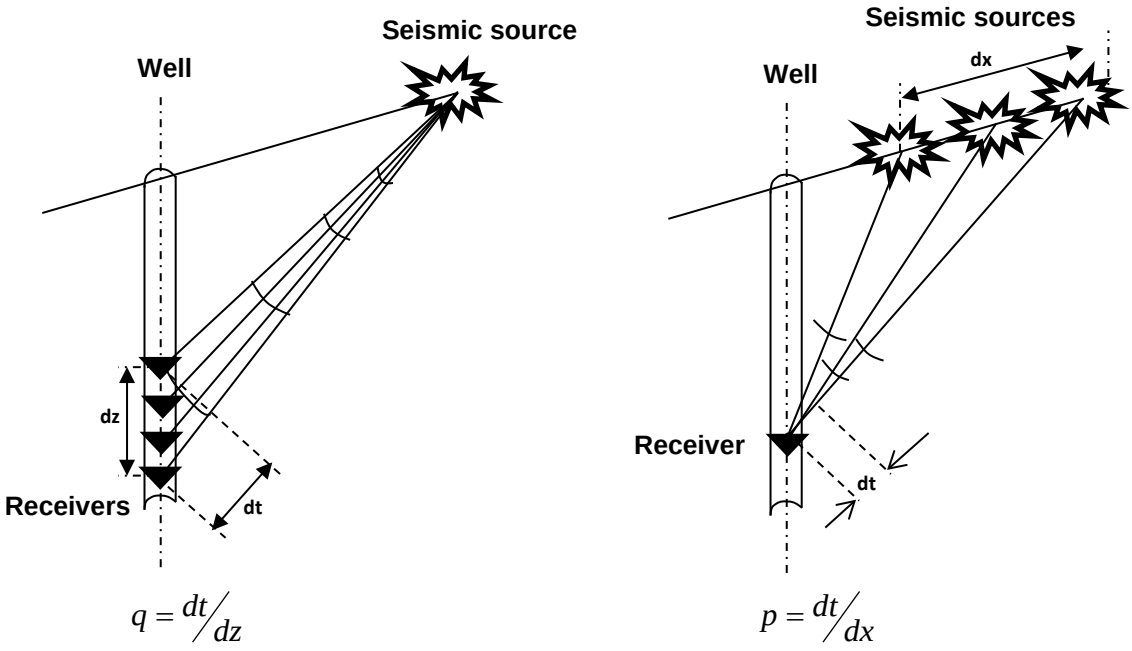

Figure 1, P-wave's vertical component of the slowness vector is measured in the borehole (left) and is local to the receiver location. Horizontal component of the P-wave's slowness vector is measured on the surface (right) and can be transferred to the receiver location if the overburden is laterally homogeneous.

4.3 VTI parameter estimation using P-wave's phase dispersion relationship

Miller and Spencer (1994) derived a phase dispersion relation for P (or SV) -waves in VTI medium from Christoffel equation. This relationship can be rearranged into a quadratic equation for horizontal slowness squared, p^2, in terms of the vertical slowness squared, q^2 and the five density normalized stiffness coefficients of the VTI medium a_{11}, a_{13}, a_{33} and a_{55}:

$$a_{11}a_{55}p^4 + (-a_{11} - a_{55} + Aq^2)p^2 + a_{33}(a_{55}q^4 - q^2) + 1 - a_{55}q^2 = 0 \qquad \textbf{01)}$$

Where $A = a_{11}a_{33} + a_{55}^2 - (a_{13} + a_{55})^2$. Vertical component of the P-wave slowness vector $\boldsymbol{q}$ is the rate of P-wave first arrival time change with respect to the distance in the vertical direction. Figure 2, top, shows an example of how vertical component of the P-wave's slowness vector can be estimated from offset VSP data which has been sorted to shot domain. In this synthetic example, P-wave is generated by a source located at offset= 2000 m (well is located at x= 3000 m) and recorded by the receivers positioned in the borehole (Figure 2, top right). Here, the distance between the receivers is 10 m. Let us assume we are interested in estimating q, in the vicinity of a receiver located at depth of 1250 m. Figure 2, top left, shows P-wave first arrivals that are recorded by a string of receivers where the selected receiver is positioned at the center of the string. To measure vertical component of the P-wave's slowness vector for this interval, P-wave first arrivals are plotted versus the receiver depth and a regression line is fitted to the data. The slope of the fitting line can be regarded as the vertical component of the slowness vector for the P-wave generated by the source located at offset=2000 m. As a result, a vertical component of the P-wave slowness vector, q can be estimated for every source located on the surface.

To measure p, the horizontal component of the P-wave slowness vector, we ideally need an array of receivers (tens of meters long) which are positioned in the horizontal direction in the borehole. This is obviously not achievable in the conventional VSP surveys where the receivers are positioned along the wellbore in typically vertical direction. For a laterally homogeneous overburden, the solution is to measure this component on the earth surface and transfer it to the receiver level by the use of Snell's law (White et al., 1983; Gaiser, 1990; Miller and Spencer, 1994; Dewangan and Grechka , 2003; Jilek et al., 2003; Grechka et al., 2006). Figure 2, bottom shows an example of synthetic walkaway VSP data from which the horizontal component of the P-wave's slowness vector can be estimated. In this Figure, sources are positioned on the earth surface at every 20 m intervals. Let us assume we want to estimate the horizontal component of the P-wave slowness vector, p for the same example receiver and source located at depth 1250 m and offset 2000 m, respectively. Figure 2, bottom left, shows VSP data recorded by this receiver and sorted in the receiver-domain. In the receiver domain, traces corresponding to the P-waves generated by the sources on the surface and recorded by a receiver are grouped together. To estimate q, for the source at 2000 m offset (source_x =5000 m), an array of traces is considered where the example source is located in the centre (Figure 2, bottom right). P-wave first arrivals are plotted versus the distance between the sources. A regression line is then fitted to the data where the slope of this line can be regarded as the horizontal component of the slowness vector. To estimate p for the P-wave generated by any other source, the array has to be centred on that source location.

As shown in the examples above, vertical seismic profiling, VSP provides measurements of both vertical and horizontal components of P-wave slowness vector which can be used to estimate VTI anisotropy parameters. The accuracy of VSP anisotropy estimates based on only slownesses are dependent on the accuracy of the slowness measurements which is related to the lateral heterogeneity in the overburden. For a laterally heterogeneous overburden, horizontal components of the P-wave slowness vector cannot be easily transferred to the receiver location. Other important parameters are the

acquisition design which determines the maximum angle (with the vertical axis) for P-wave propagation and the magnitude of the anisotropy in the medium.

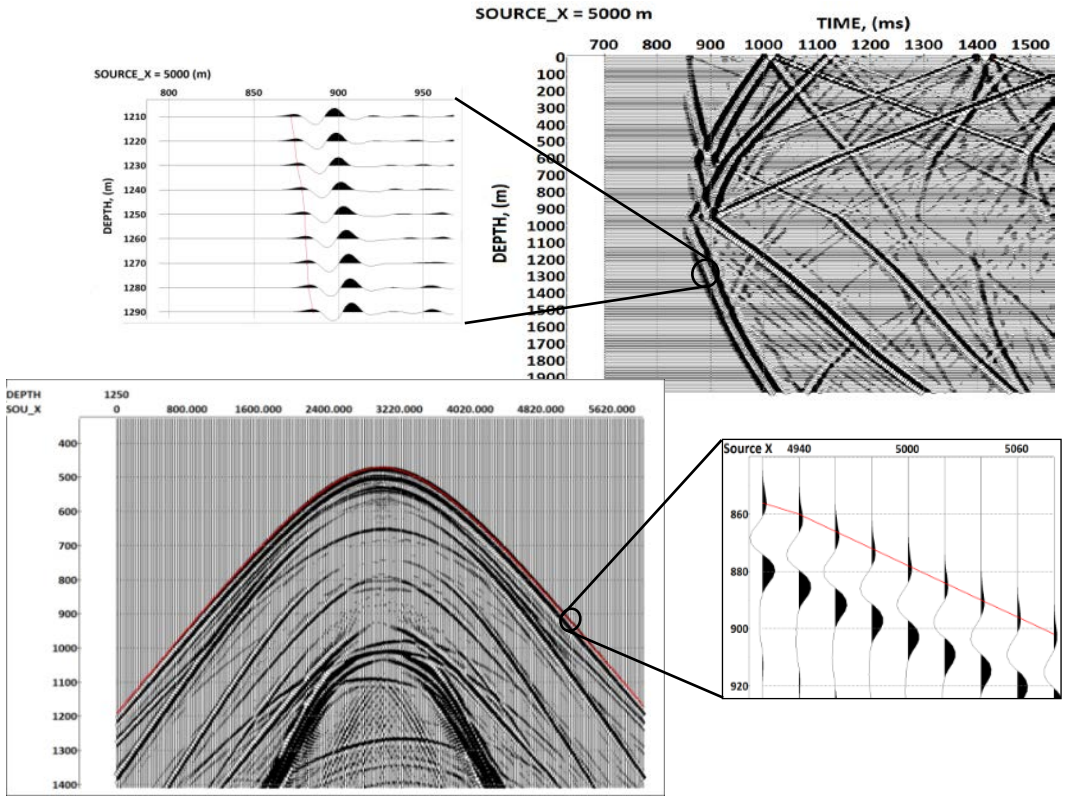

Figure 2, VSP measurements can be used to estimate both vertical and horizontal components of P-wave's slowness vector. Vertical component of the slowness vector is measured in the shot domain (top). In this example, vertical component of the slowness vector is measured for a source located at offset=2000 m and a receiver located at depth=1250 m. Horizontal component is measured in the receiver domain (bottom). In this example, horizontal component of the slowness vector is measured for a source located at offset=4980 m and a receiver at depth=1250 m.

4.4 Uncertainty of VTI parameter estimation using P-wave dispersion relationship

The estimation of VTI anisotropy parameters based on using Equation 1 is easily implemented but it is troubled by various factors. I have quantified the uncertainties in the estimation as a function of P-wave maximum propagation angle, magnitude of the anisotropy in the medium and the amount of noise in the measurements. Maximum propagation angle of the P-wave in a layered medium is mainly determined by the depth of the receiver, source offset and the gradient of the layer velocity. Amount of noise in the slowness measurements is mainly determined by our ability to accurately transfer the horizontal component of the slowness vector (measured on the surface) to the receiver level. This would be difficult where the overburden is geometrically complex.

4.4.1 Forward modeling and generation of numerical data

The analysis presented is based purely on synthetic (numerical) data that are generated by Christoffel equation (see Section 3.2) and can be measured in a walkaway VSP experiment as described in previous section. Synthetic numerical data here consist of P-wave slowness vectors computed for a range of VTI parameters (see Section 3.5), $V_{P0} = 3000$ m/s, $V_{S0} = 1500$ m/s, $\delta \in \left[-0.4,\ 0.7\right]$, $\varepsilon \in \left[-0.2,\ 0.6\right]$ and density $\rho = 2000$ kg/m^3. As mentioned earlier, for a given velocity model, the source offset (measured from the well head) and the receiver depth dictate the dip angles of the slowness vector. To quantify the effect of source offset on VTI parameter estimation, I consider four increasing dip ranges for the slowness vectors, $\theta \in \left[-\theta_{\max},\ \theta_{\max}\right]$, where $\theta_{\max} = 30^o$, $\theta_{\max} = 45^o$, $\theta_{\max} = 60^o$ and $\theta_{\max} = 80^o$ I compute slowness vectors with 1^o step within the dip range. As the equation is exact, to quantify the efficiency of this method I will add error to the slowness vectors which are normally distributed random vectors with relative standard variation of 1 % (see 3.14 for more explanation).

4.4.2 Inversion algorithm and objective function

Simulated results are subsequently inverted for anisotropy parameters. For that purpose I used MATLAB's *fminsearch* function that was described in Section 3.15. The estimated

(δ_{est}, ε_{est}) are subtracted from the initial values (δ, ε) to calculate the errors ($\delta_{est} - \delta$, $\varepsilon_{est} - \varepsilon$). As random noise is introduced to the data, each inversion is repeated over1000 iterations to generate a distribution function to estimate inversion errors. For each inversion, an average value and a standard deviation are extracted from the distribution function and are used to generate final uncertainty plots.

A more intuitive but cumbersome way of defining the objective function here is to resolve Equation 1 and derive squared value of horizontal slowness p^2 as a function of stiffness coefficients and squared value of the vertical slowness q^2 and then define the objective function as the sum of the squared differences between derived p^2 and the same parameter from the measurements. However, an elegant way is to just minimize the residuals in the Equation 1 that is to minimize the sum of the terms in the left hand side of Equation 1. Here, we assume that a_{33} and a_{55} are given by V_{P0} and V_{S0}, respectively and we minimize the objective function for the two stiffness coefficients a_{11} and a_{13}.

Figure 3, illustrates the methodology used to analyse the uncertainty of VTI parameter estimation based on P-wave slownesses only from synthetic numerical data. In this Figure, we assume that seismic waves can propagate in a wide range of phase angles in the anisotropic medium as a result of favourable acquisition geometry.

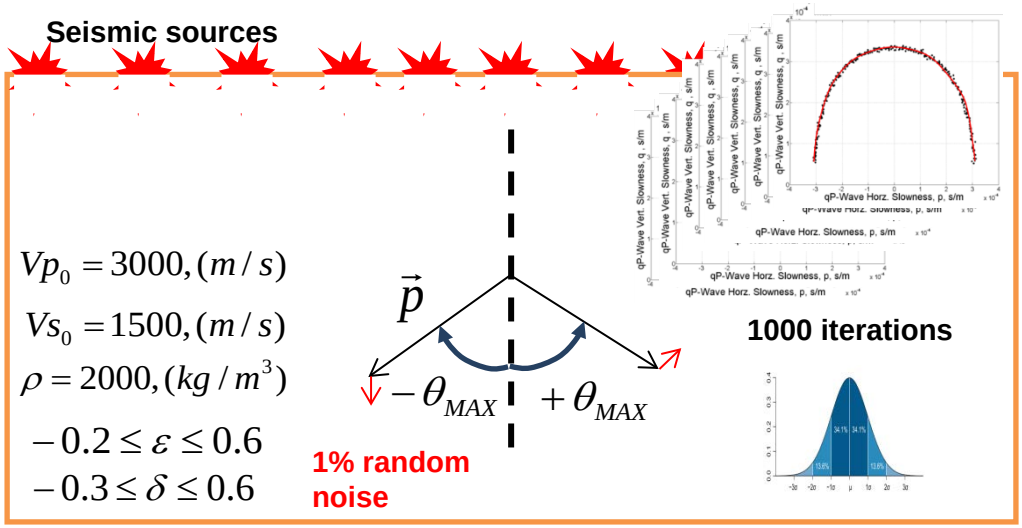

Figure 3, schematic illustration of the methodology that uses numerical data to analyse the uncertainty of VTI parameter estimation based on P-wave slowness measurements.

To quantify how the noise in the slowness measurement influences VTI parameter estimation, I reiterated the analysis with this time 3 % noise added to the slowness vector. The results of the inversions are summarized in Figures 4 and 5 for 1% and Figures 6 and 7 for 3% added noise. Figures 4 and 6 show the difference between the median of 1000 inversions and the true values of δ and ε for the considered range of anisotropy values. Figures 5 and 7 show the standard variations of the inverted values for the inversions shown in Figure 4 and 6, respectively. $\theta_{\max}$ increases from 30^o to 80^o from top to the bottom of the all Figures.

Figures 4 and 5, display the errors and the standard deviations corresponding to the 1000 inversions for VTI parameters using Equation 1. In this case, 1% random noise (as described before) has been added to P-wave slowness vectors. In general, Equation 1 performs reasonably well in estimating anisotropy parameter δ even for the small range of wave propagation angles, $\theta_{\max} = 30^o$ (top left, Figures 4 and 5). In this range, errors

and standard deviations are less than 10% and 6%, respectively for the entire anisotropy range. Estimation of δ largely improves with increased maximum phase angle. Where $\theta_{\max} = 45^o$ (second row left, Figures 4 and 5), errors and standard deviations decrease to less than 4% and 3%, respectively. Where $\theta_{\max} \geq 60^o$ (third and bottom row left, Figures 4 and 5), both errors and standard deviations decrease to less than 2% in the entire range of anisotropy. On the other hand, estimations for ε are not as reliable as for δ in the small range of propagation angles (top right, Figures 4 and 5). In this range, errors and standard deviations for ε estimation are more than 20% and 10%, respectively for the entire anisotropy range. However, ε estimations rapidly improve by wave propagation at grazing angle. For example, increasing $\theta_{\max}$ to 60^o, decrease both the error and standard deviation in ε estimations below 1% (third row right, Figures 4 and 5).

Figures 6 and 7, display the errors and the standard deviations corresponding to the 1000 inversions for VTI parameters using Equation 1. Here, 3% error has been added to P-wave slowness vectors. In contrary to the case with 1% noise, δ estimations are usually unreliable up to $\theta_{\max} = 60^o$ where the error and standard deviation decrease to less than 12% and 5%, respectively (left-first,-second and -third rows, Figures 6 and 7). Propagation angles have to increase to $\theta_{\max} = 80^o$ in order to achieve a reasonable accuracy (less than 5%) in estimating δ (left-fourth row, Figures 6 and 7). ε estimations become reasonably valid for propagation angles $\theta_{\max} = 60^o$ (right-third row, Figures 6 and 7). A reliable estimation of ε can be obtained by increasing $\theta_{\max}$ to 80^o where both the errors and the standard deviations decrease below 2% (right-fourth row, Figures 6 and 7).

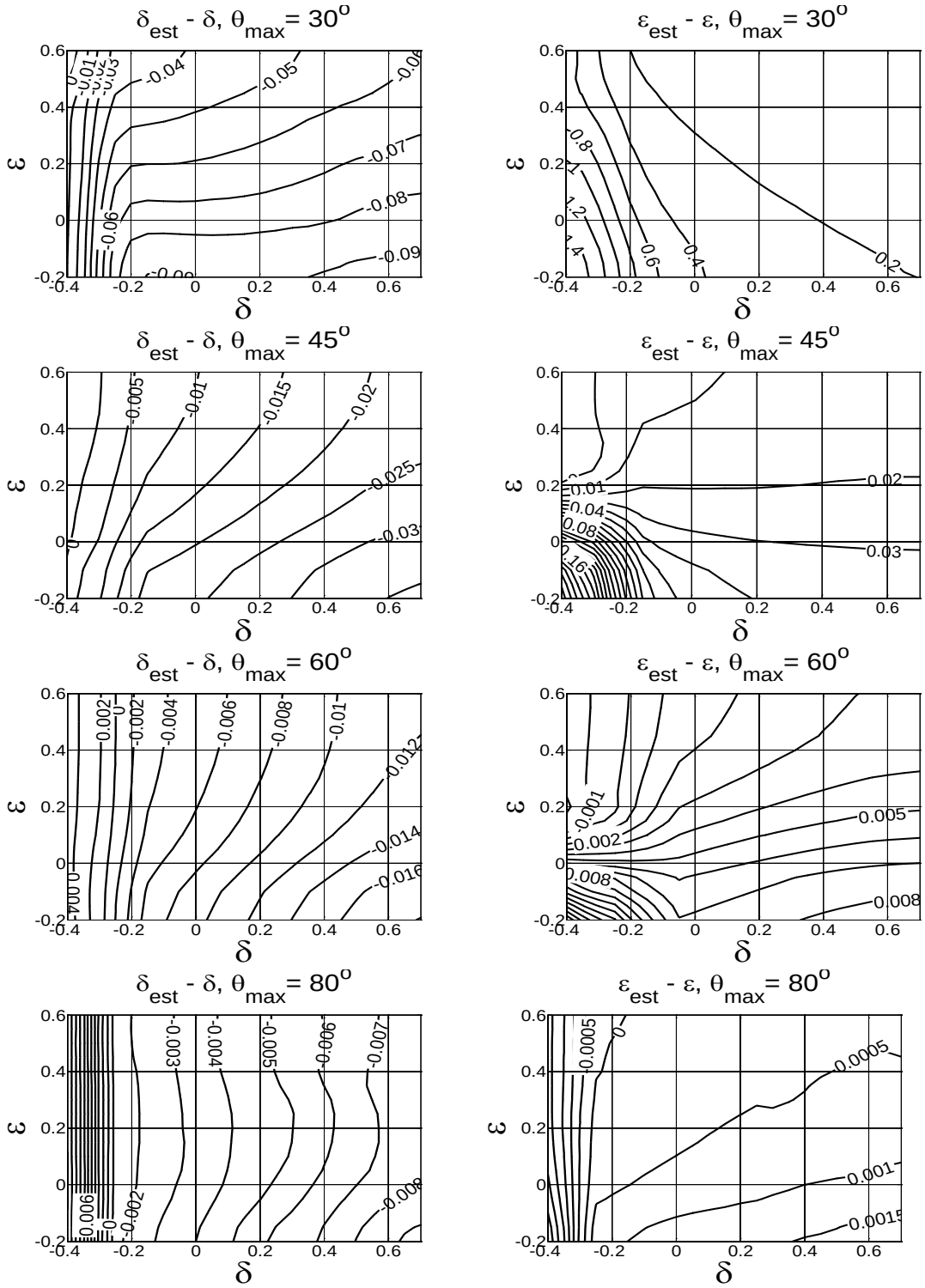

Figure 4, maps of errors associated with the inversion of synthetic P-wave slownesses using Equation 1 as functions of the true anisotropy parameters ε and δ . 1% random noise has been added to the slowness vector.

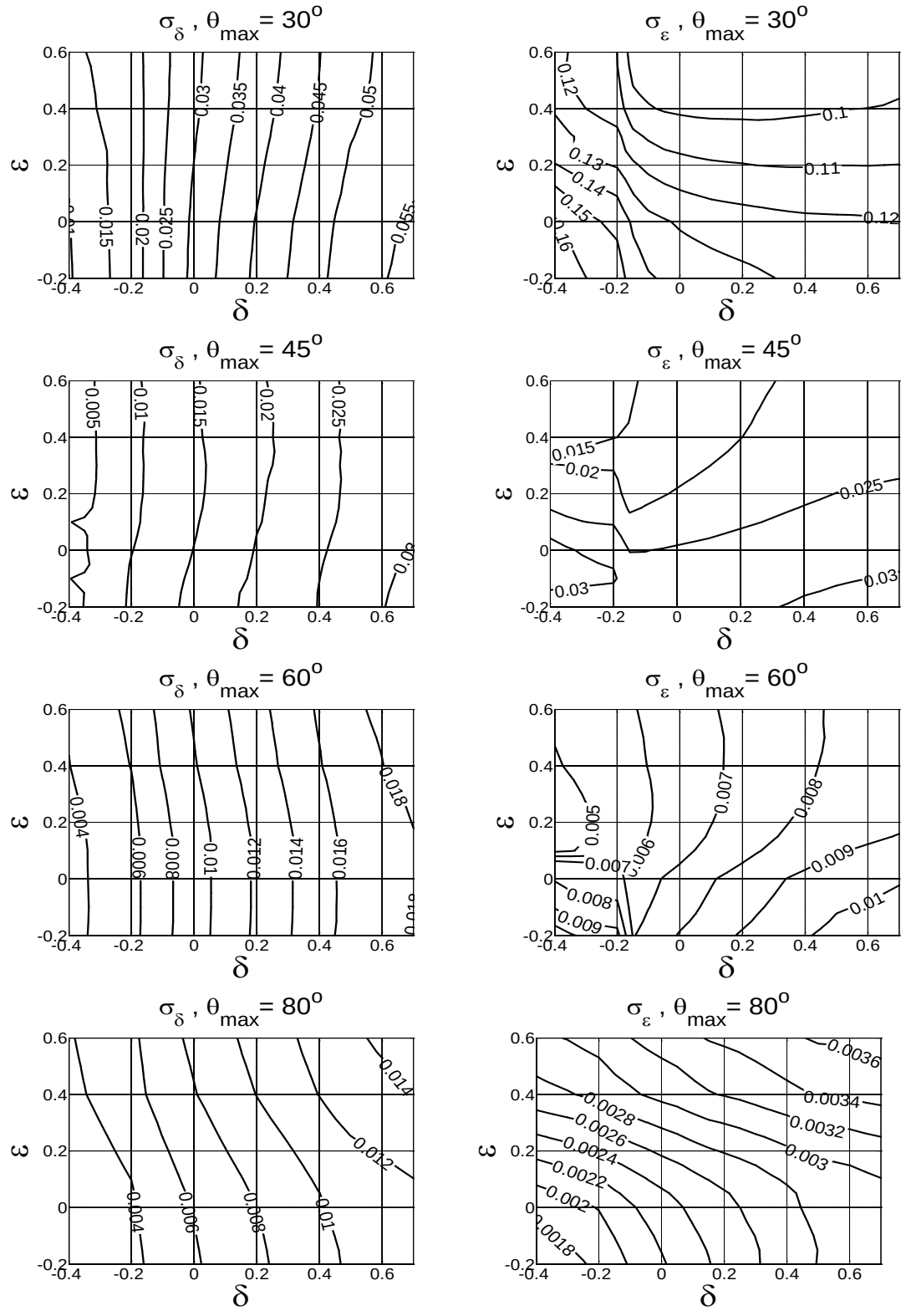

Figure 5, standard deviations for the corresponding quantities shown in Figure 4.

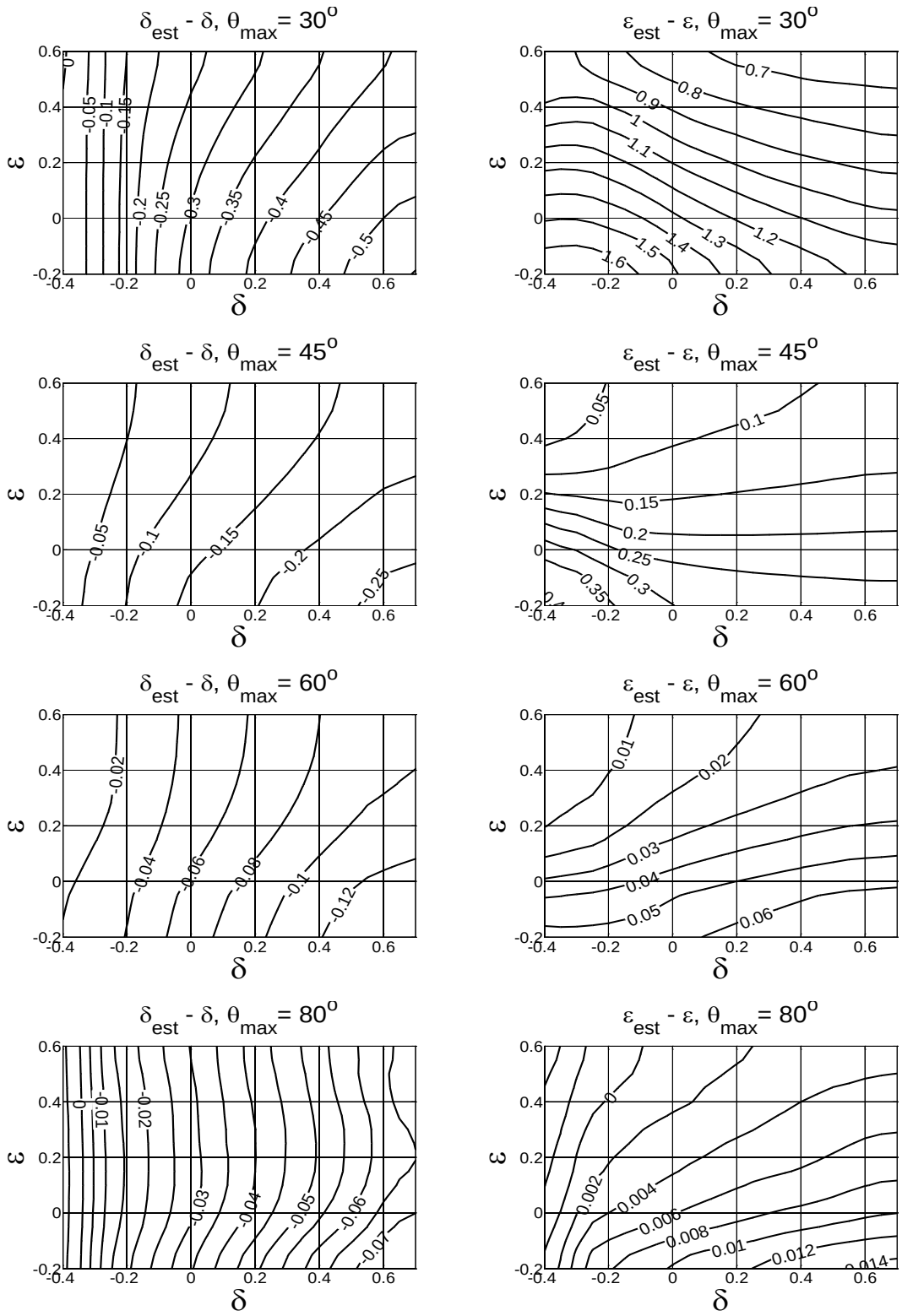

Figure 6, maps of errors associated with the inversion of synthetic P-wave slownesses using Equation 1 as functions of the true anisotropy parameters ε and δ . 3% random noise has been added to the slowness vector.

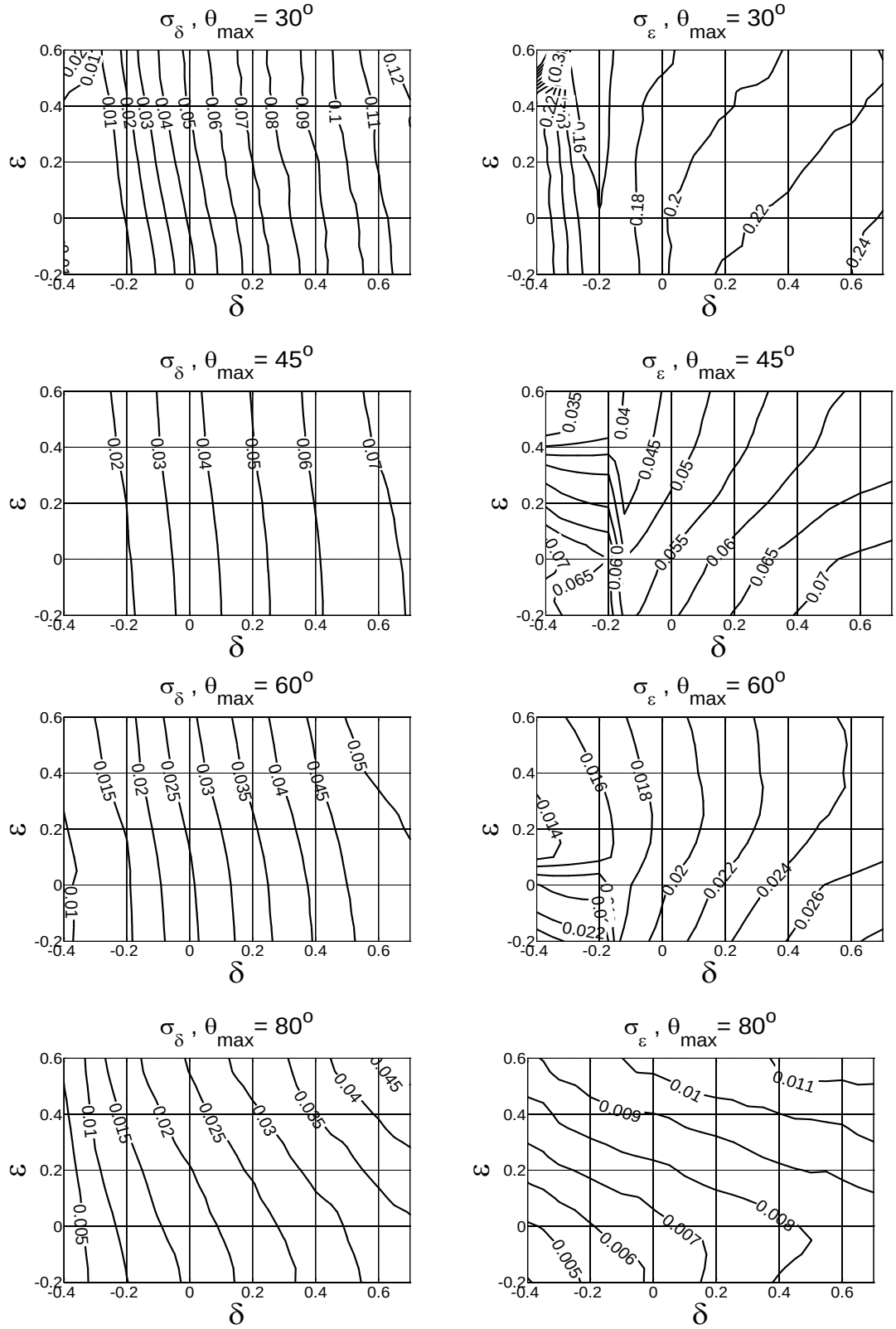

Figure 7, standard deviations for the corresponding quantities shown in Figure 6.

An important observation can be made from uncertainty Figures represented in this chapter. Errors in VTI parameter estimation show specific dependency on the magnitude of anisotropy in the medium. Figures 4 and 6, bottom left (where there is highest accuracy in the estimations) show accuracy in δ estimation is largely dependent on the values of δ and less dependent on the values of ε in the medium (contours tend to be parallel to ε axis) . The accuracy of δ estimation decreases for strong anisotropy and large values of δ . The same way as for δ , Figures 4 and 6, bottom right show that the accuracy in estimation of ε is less dependent on values of δ as error contours tend to lay parallel to the ε axis. The errors in ε estimation increase as the values of ε decrease and become negative.

By making a comparison between the graphs in Figures 4-7, it is evident that the slowness method is sensitive to random noise in the slownesses and is more vulnerable to the presence of random noise for δ estimation than it is for ε estimation. Figure 6 (and 7), left panel shows that the method will not obtain a reasonable accuracy with 3% added noise before $\theta_{\max}$ increases to about 80^o whereas this level of accuracy was easily obtainable for 1% added noise at $\theta_{\max} = 30^o$ (Figures 4 and 5, top left). However, in the case of ε , while accurate estimations can be obtained at $\theta_{\max} = 45^o$ for 1% added noise (shown in Figure 4 and 5, right), $\theta_{\max}$ has to increase to only 60^o for 3% added noise to obtain similar accuracy as with the case with 1% noise addition (Figure 6 and 7, right).

4.5 VTI parameter estimation using Thomsen's weak anisotropy approximation for P-wave phase velocity in VTI media

Thomsen (1986) derived a simple relationship (Equation 16, Chapter 3) for P-wave phase velocity in VTI medium based on the assumption of weak anisotropy ($|\varepsilon| \langle\langle 1$, $|\delta| \langle\langle 1$):

$$V_P = V_{P0}(1 + \delta \sin^2\theta \cos^2\theta + \varepsilon \sin^4\theta) \qquad (2)$$

where V_{P0} is P-wave velocity in the vertical (symmetry) direction. Numerical phase velocities at varying dips are again computed using the same medium parameters as defined in previous method. To assess the accuracy of the approximation given by Equation 2, I used *error-free* phase velocities for the VTI parameters δ and ε for inversion. The results of this inversion are summarized in Figure 8.

Figure 8 demonstrates the accuracy of using Equation 2 for VTI parameter estimation where maximum P-wave propagation angle increases from $\theta_{\max} = 30^o$ (Figure 8, top) to $\theta_{\max} = 80^o$ (Figure 8, bottom). The equation is generally accurate for estimating anisotropy parameters within the region of moderate anisotropy ($\delta \in [-0.2,\ 0.2]$ and $\varepsilon \in [-0.2,\ 0.2]$). Notice that, beyond this range, δ estimations lose accuracy for large propagation angles (Figure 8, bottom left). In contrast to δ, ε estimation has larger accuracy over the whole range of tested magnitudes of anisotropy by increasing wave propagation angles to $\theta_{\max} = 80^o$.

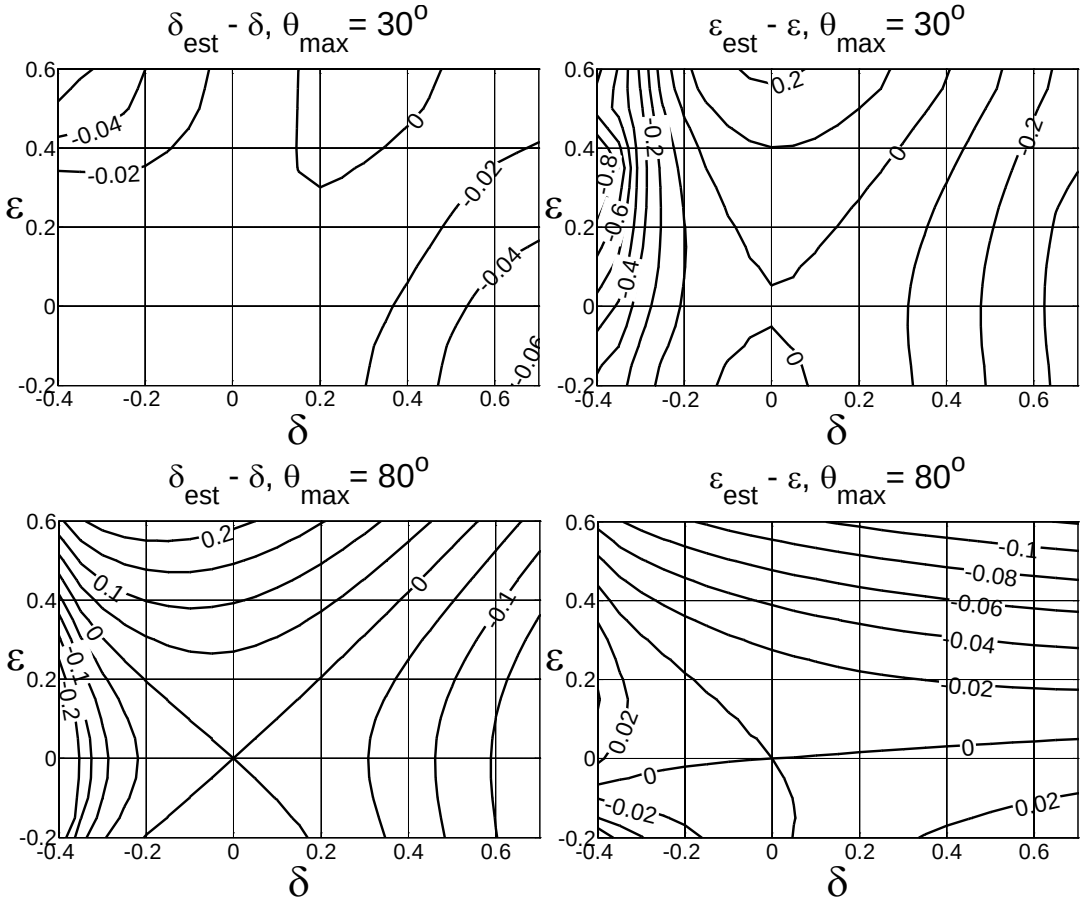

Figure 8, errors inherent in the approximate Equation 2 used in the inversion of error-free synthetic phase velocities to VTI parameters ε and δ. $\theta_{\max}$ reaches 30^o (top) and 80^o (bottom).

As Equation 2 is valid only for moderate anisotropy, I will restrict my error analysis to this range. Here, 1% random noise is added to the slowness vectors (the same way as with the previous method) and then synthetic velocities are computed only for $\theta_{\max} = 30^o$ and $\theta_{\max} = 80^o$. Equation 2 is then used to invert the data for VTI parameters ε and δ. The results are summarized in Figures 9 and 10. Figure 9 shows the difference between the mean value of 1000 inversions and the true values of δ and ε. Figure 10 shows the standard deviations of the inverted values displayed in Figure 9.

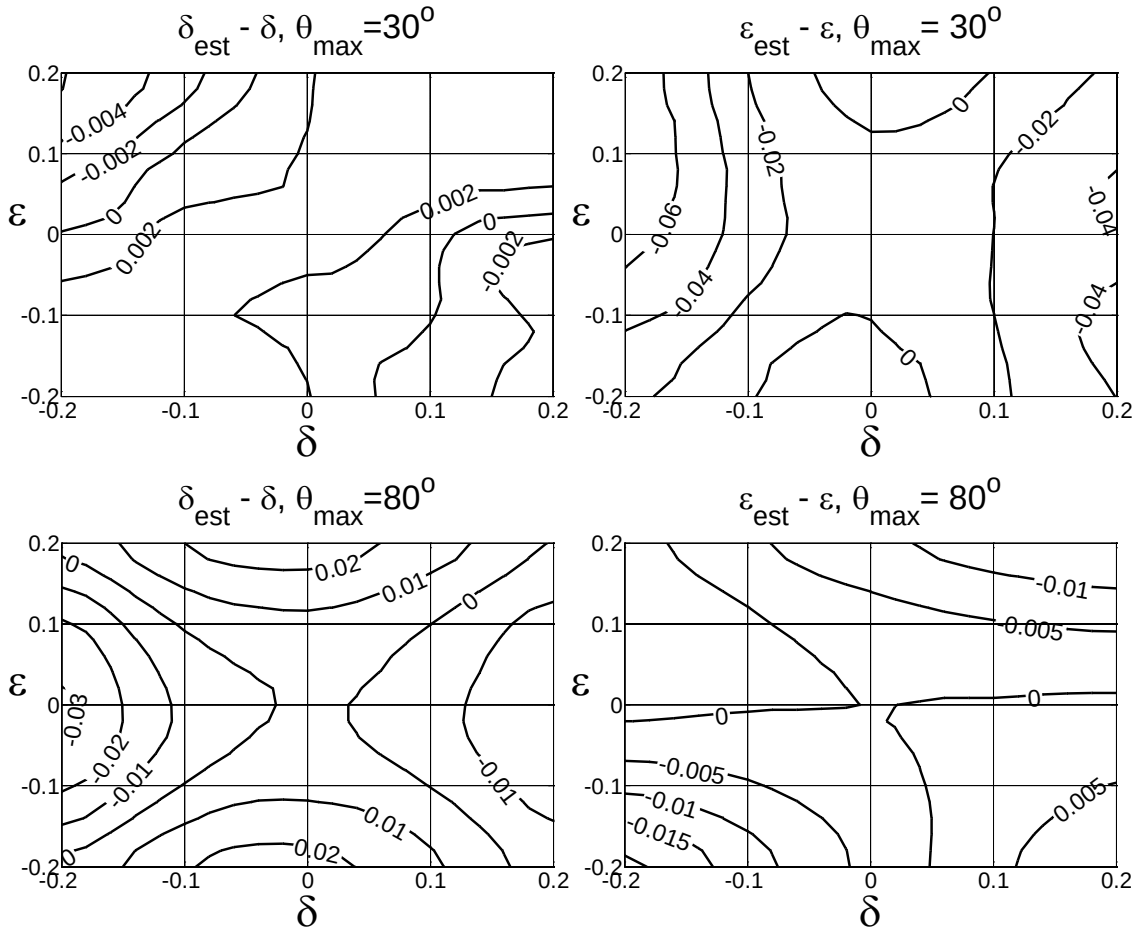

Figure 9, error maps, associated with the inversion of synthetic P-wave velocities using Equation 2 as functions of the true anisotropy parameters ε and δ. Maximum phase angle reaches 30^o (top) and 80^o (bottom). 1% random noise is added to the slowness vectors where the velocities are derived from.

In general, Thomsen's (1986) weak anisotropy approximation for P-wave phase velocity in VTI medium has been able to accurately estimate ε and δ for the moderate anisotropy range and small angles of wave propagation (Figure 9, top). This is important observation as the other method based on Equation 1 was unsuccessful in estimating ε for short range of wave propagation angles. However, large values in standard deviation map (Figure 10, top right) will restrict a straightforward application of this method. To alleviate this problem, at least from the statistical point of view, a number of independent measurements have to be averaged to obtain a reliable estimation. As the

propagation angles increase to $\theta_{max} = 80^o$, estimations become very accurate and both the errors and the standard deviation decrease significantly, (compare top and bottom in Figures 9 and 10).

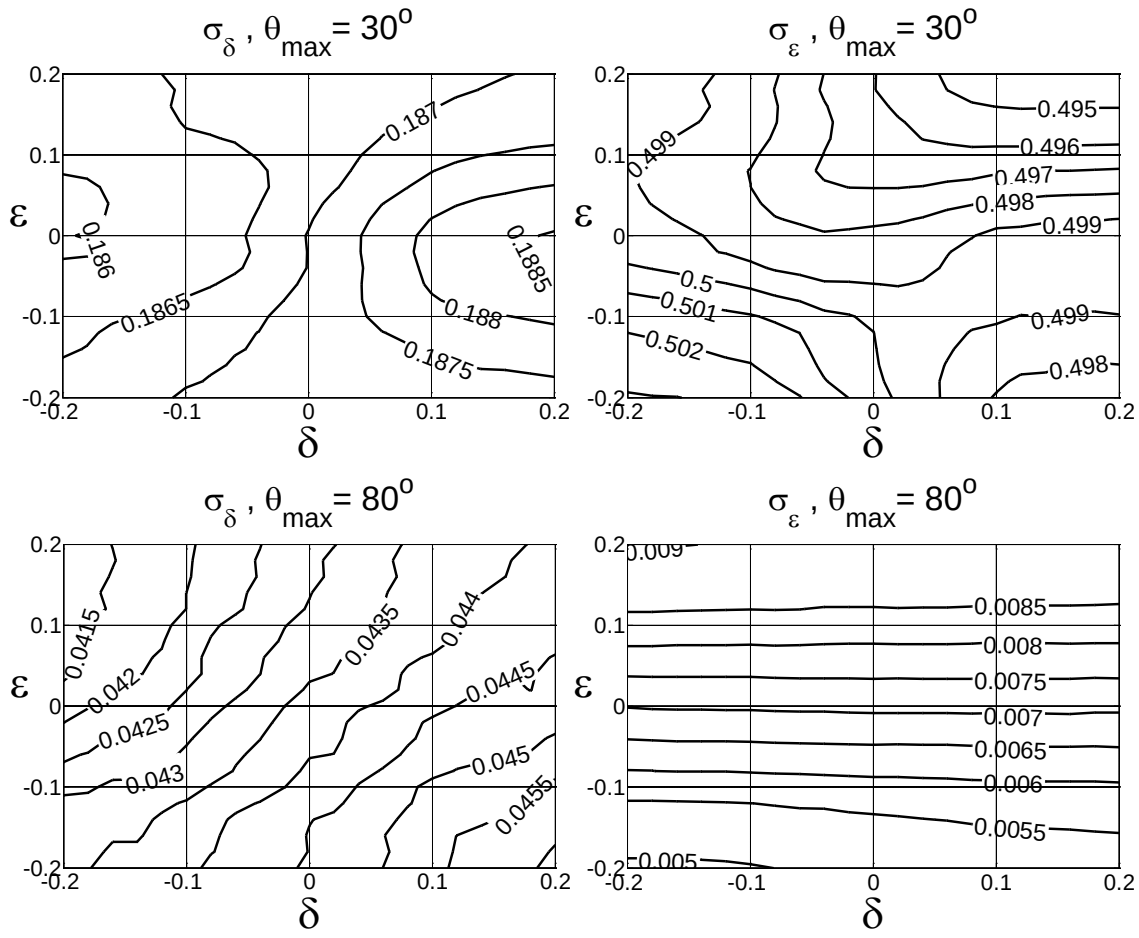

Figure 10, standard deviations for the corresponding quantities shown in Figure 9.

4.6 VTI parameter estimation, well CRC-1, synthetic walkaway VSP

To get an idea about the possibility of estimating anisotropy parameters from walkaway VSP measurements at Naylor field, I have used synthetic walkaway VSP measurements in the first step of my analysis. Synthetic VSP data has been acquired over a 2D velocity model with layer geometry similar to the geometry of geological formations at the location of well CRC-1 in the Naylor field. Figure 11 displays the geometry of the earth model where the synthetic walkaway VSP has been acquired using finite difference wave propagation algorithm. Layer properties are taken from available

velocity and density log measurements at well CRC-1. Velocity values at this well location are believed to be laterally invariant and are listed in Table 1.

Other studies in the Otway basin have indicated the existence of seismic azimuthal anisotropy which is thought to be caused by the existing differential (non-hydrostatic) stress regime in the area (see Chapter 1). However, as the first exercise to model velocity anisotropy which has also been observed in VSP recordings of well CRC-1, I start with simple VTI anisotropy that can be caused by the shale formations or geological layering. Anisotropy starts from fourth layer and is represented by Thomsen (1986) parameters $\varepsilon = 0.08$ and $\delta = -0.14$. Anisotropy values in this example have been taken from the other studies at the location of well CRC-1. Synthetic walkaway VSP survey comprises 301 sources spaced at every 20 meters on the surface and distributed symmetrically on both sides of the well head along the survey line. Maximum offset reaches to 3000 m from the well head. Downhole receivers which are spaced at every 10 meters, start from the surface of the model and continue down to 2000 m depth. Both vertical and horizontal components of the wave-field are recorded at every receiver location.

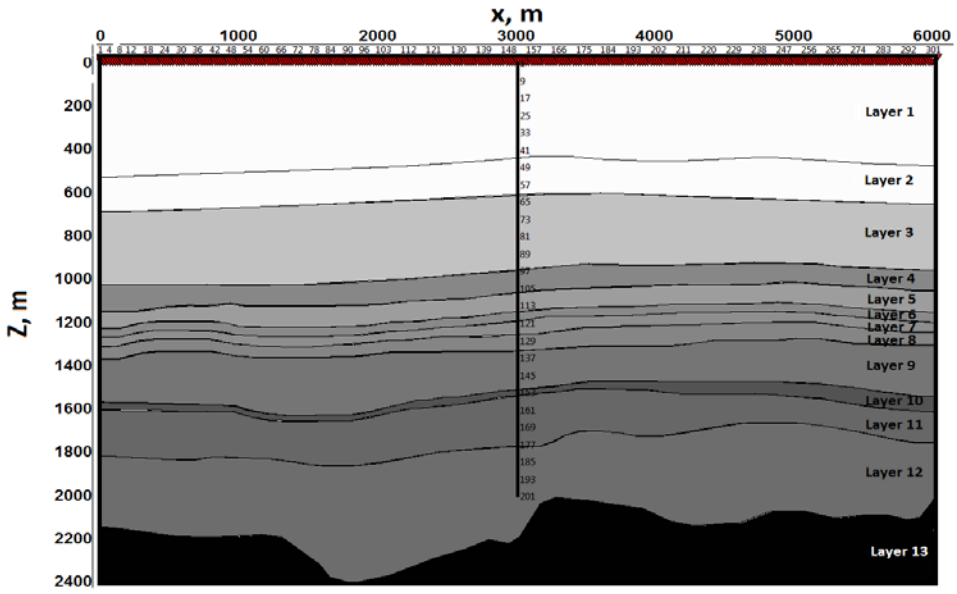

Figure 0-11, geometry of the earth model used to generate synthetic walkaway VSP data. 3C Receivers are located at every 10 m interval from the surface of the model to 2 km depth. Sources are symmetrically distributed around the wellhead at every 20 m distances.

Property / Layer	Vp_0 (m/s)	Vs_0 (m/s)	ρ (kg/m^3)	δ	ε	γ
1	**2329**	**1089**	**2141**	**0**	**0**	**0**
2	**2329**	**1089**	**2141**	**0**	**0**	**0**
3	**2689**	**1279**	**2212**	**0**	**0**	**0**
4	**3051**	**1596**	**2287**	**-0.14**	**0.08**	**0.07**
5	**2915**	**1514**	**2215**	**-0.14**	**0.08**	**0.07**
6	**3040**	**1595**	**2260**	**-0.14**	**0.08**	**0.07**
7	**3007**	**1618**	**2258**	**-0.14**	**0.08**	**0.07**
8	**3063**	**1657**	**2282**	**-0.14**	**0.08**	**0.07**
9	**3164**	**1735**	**2309**	**-0.14**	**0.08**	**0.07**
10	**3375**	**1801**	**2322**	**-0.14**	**0.08**	**0.07**
11	**3251**	**1779**	**2420**	**-0.14**	**0.08**	**0.07**
12	**3214**	**1635**	**2358**	**-0.14**	**0.08**	**0.07**
13	**3878**	**2287**	**2491**	**-0.14**	**0.08**	**0.07**

Table 1, layer properties of the geological model displayed in Figure 11.

Figure 12, left, displays an example of vertical component of the wavefield generated by all the sources and recorded by a receiver at depth of 1250 m. P-wave first arrival times, in red is picked from the data (common receiver domain) and is used to calculate P-wave horizontal slownesses for every source position on the surface. In the middle of Figure 12, there is a zoom picture of P-wave first break times that corresponds to a window of sources where an example source (at X=5000 m) is located in the centre. In the right side of Figure 12, there is a graph showing how horizontal slowness of P-wave corresponding to the example source is computed from travel times. Slope of a regression line passing through travel times is regarded as the horizontal slowness of P-wave generated by the source in the middle.

As an example of how to calculate P-wave vertical slowness, Figure 13, on top right displays vertical component of the wavefield generated by the same source location as in Figure 12 and recorded by all the receivers in the borehole. Below, are events associated with first arrivals of P-wave recorded by an array of 9 geophones where the example

geophone positioned at depth = 1250 m is in the middle. On top left, a straight line is fitted to first break times of the geophone array where the slope of this line can be regarded as vertical slowness of P-wave generated by the example source at X=5000 m.

In the next step, source window is centred over a new position (in common receiver domain at 1250 m) to calculate a new horizontal slowness. The receiver array (still at the same depth) will use data corresponding to new source to calculate a new vertical slowness. This process is then repeated for all source positions corresponding to every receiver level and for all the depths. Figure 14 shows P-waves phase angle, θ as a function of depth that is computed from the synthetic slowness measurements in the borehole (described above). In this example, data from sources with more than 2000 m offset have been dropped to avoid headwaves generated at critical angle. The destructive effect of headwaves on slowness measurements is apparent at depths 600 and 1000 meters in this example (also look at Figure 20). As expected, maximum P-wave (phase) propagation angle recorded by the recivers decreases with increasing depth. Figure 15 displayes the range of data that can be used for the inversion at the receiver depth=1250 m. Here, vertical component of P-wave slowness vector, q is plotted against the horizontal component, p for various amounts of $\theta_{\max}$. Measured data ($p-q$ pairs) together with Equation 2 are put into an inversion algorithm and estimated stiffnesses are used to calculate Thomsen (1986) anisotropy parameters ε and δ. Displayed also in Figure 15 are the result of fitting Equation 2 (solid red line) to measured p and q values (black circles).

The whole process is repeated for all the receiver locations and plots of estimated VTI parameters are generated as documented in Figures 16 to 19. Here, I will increase the range of accepted $\theta_{\max}$ for the inversion from 30^{o} (in Figure 16) to 80^{o} (in Figure 19), to see how this influences VTI parameter estimation at the well location. In these Figures, recovered Thomsen (1986) anisotropy parameters (black dots) are plotted versus those used in the model (red line). At large depths (below 1200 m), where $\theta_{\max}$ never goes beyond 60^{o} (look at Figure 14), increasing this value in the inversion algorithm will have no effect (compare Figures 18 and 19). However, at shallow depths, (less than 1200

m), the improvement is significant (compare Figures 17 and 18). On the other hand, too much increase in the accepted range of θ_{max} in the shallow parts will increase the amount of noise coming from the head waves as described in Figure 14 (depths =600 and 1000 m) and also reappeared in Figure 19. In the inversion process, density and both vertical P-and S- velocities at each depth interval are directly imported from the model. In real examples, an estimation of these values are assumed to be given for example by downhole logs or VSP measurements.

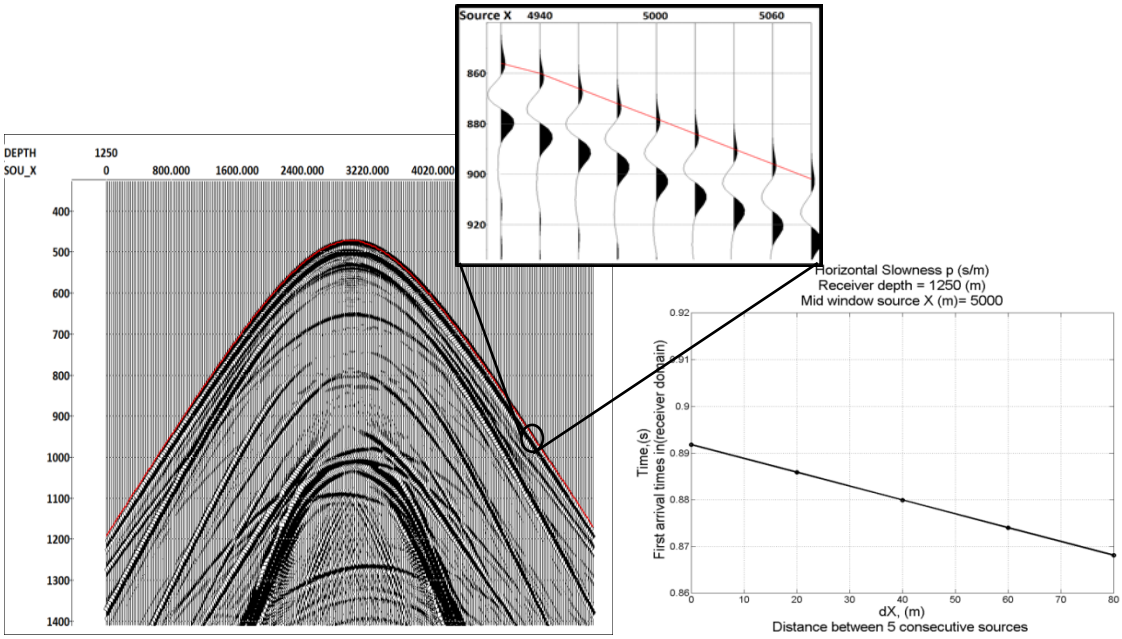

Figure 10-2, left, a sample common receiver domain data which shows vertical component of the wavefield generated by all the VSP sources and recorded by the receiver at depth 1250 m. First arrival times of the P-wave are picked in this domain and used to compute horizontal component of the slowness vector. In the middle top, travel times corresponding to a window of sources are displayed where the example source (X=5000m) is located in the middle. The graph on the right shows how a straight line is fitted to travel times of the window where the slope of this line is regarded as horizontal slowness of the P-wave generated by the example source.

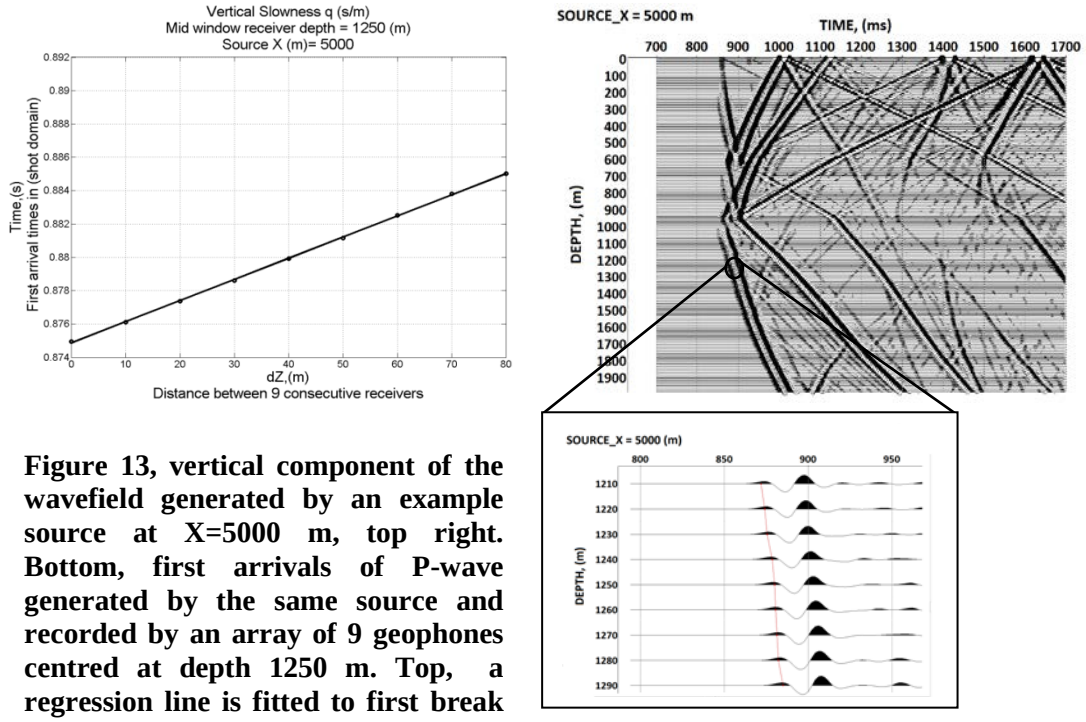

Figure 13, vertical component of the wavefield generated by an example source at X=5000 m, top right. Bottom, first arrivals of P-wave generated by the same source and recorded by an array of 9 geophones centred at depth 1250 m. Top, a regression line is fitted to first break times of P-wave generated by the example source where the slope of this line is regarded as horizontal slowness of this wave.

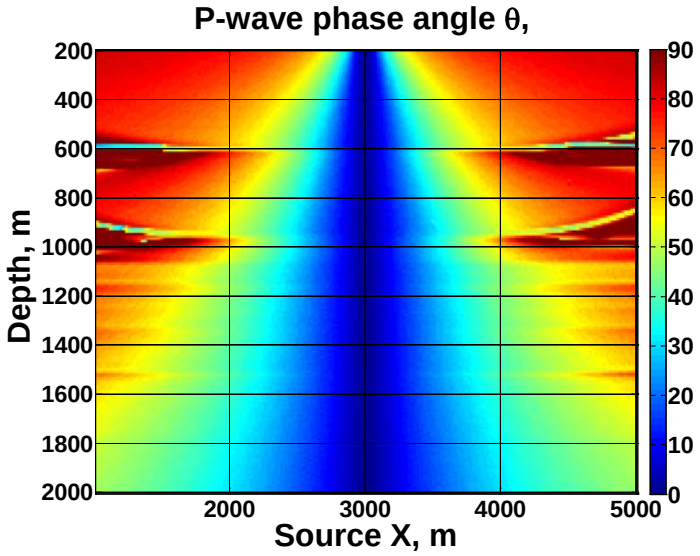

Figure 14, P-wave phase angles computed from the slowness measurements in the borehole for the model depicted in Figure 11. Notice how P-wave maximum propagation angle decreases with depth.

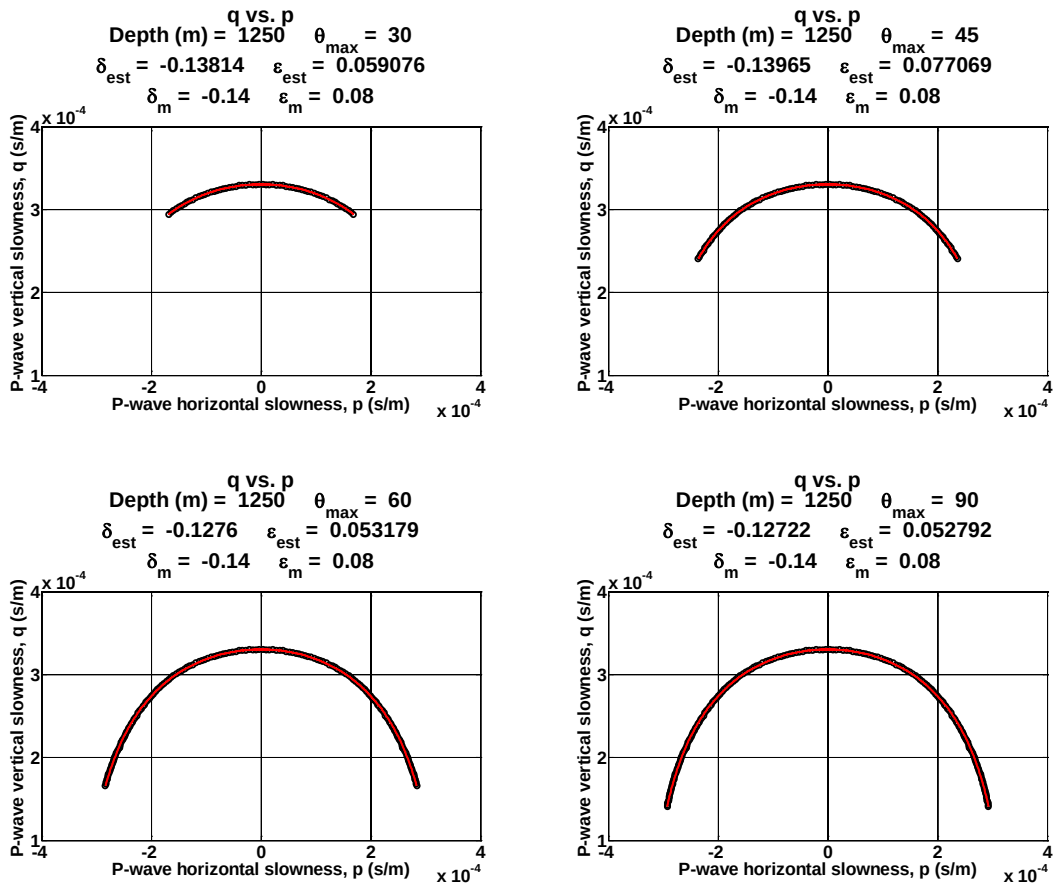

Figure 15, P-wave slownesses at various maximum phase angles plotted for the receiver located at the depth 1250 m.

Figure 20, shows the case of inaccuracy in slowness measurements as the result of head waves being recorded before the transmitted P-wave. At depth = 600 m, P-wave generated by the source located at X=1020 m (bottom) will produce headwaves which will travel in the lower layer (with higher velocity) and will arrive first at the receiver location. These first arrivals can be wrongly regarded as P-wave first arrivals and used to calculate slowness vectors.

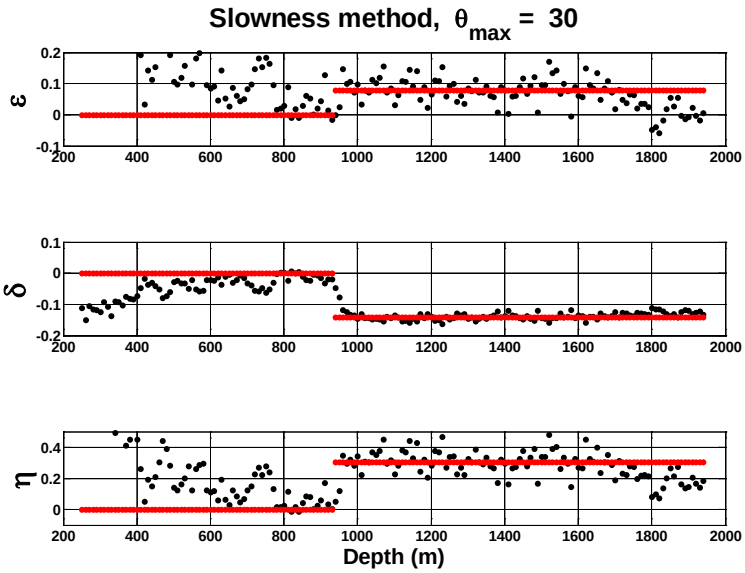

Figure 16, VTI parameter estimation from synthetic VSP data measured in the earth model displayed in Figure11. Maximum phase angle is limited to less than 30^o.

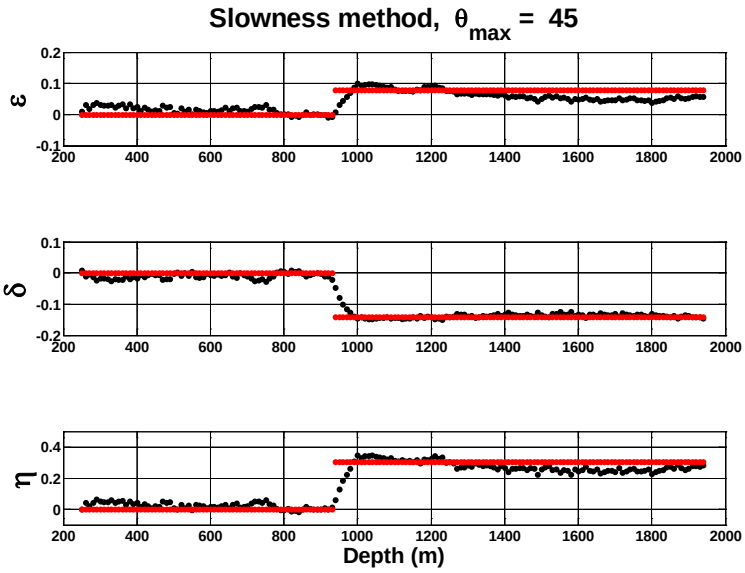

Figure 17, VTI parameter estimation from synthetic VSP data measured in the earth model displayed in Figure11. Maximum phase angle is limited to less than 45^o.

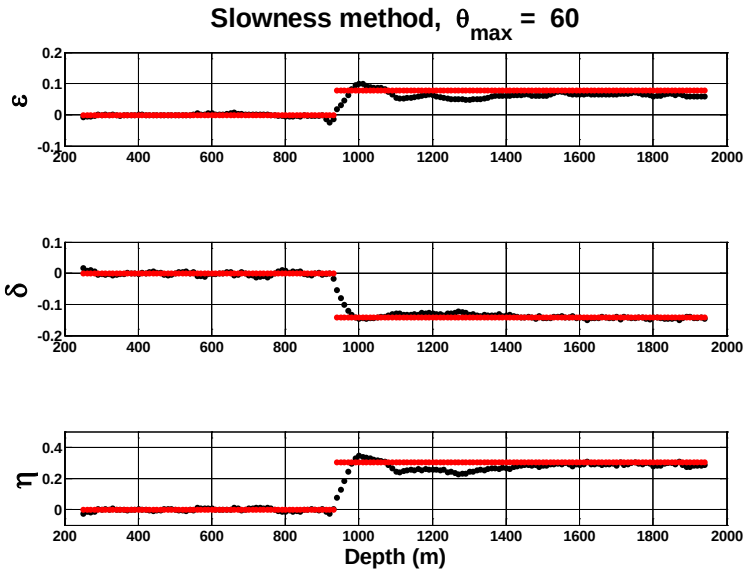

.

Figure 18, VTI parameter estimation from synthetic VSP data measured in the earth model displayed in Figure11. Maximum phase angle is limited to less than 60^o.

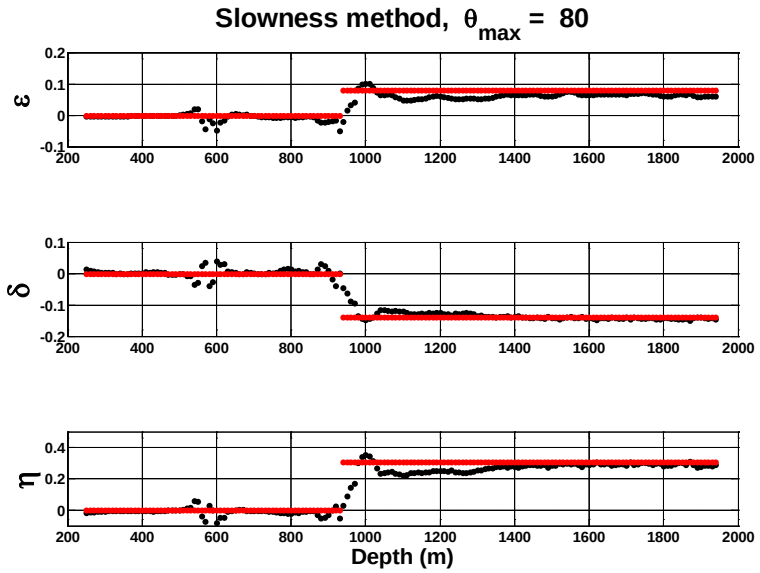

Figure 19, VTI parameter estimation from synthetic VSP data measured in the earth model displayed in Figure11. Maximum phase angle is limited to less than 80^o**. Notice the head wave effect in the estimations at depth 600 m.**

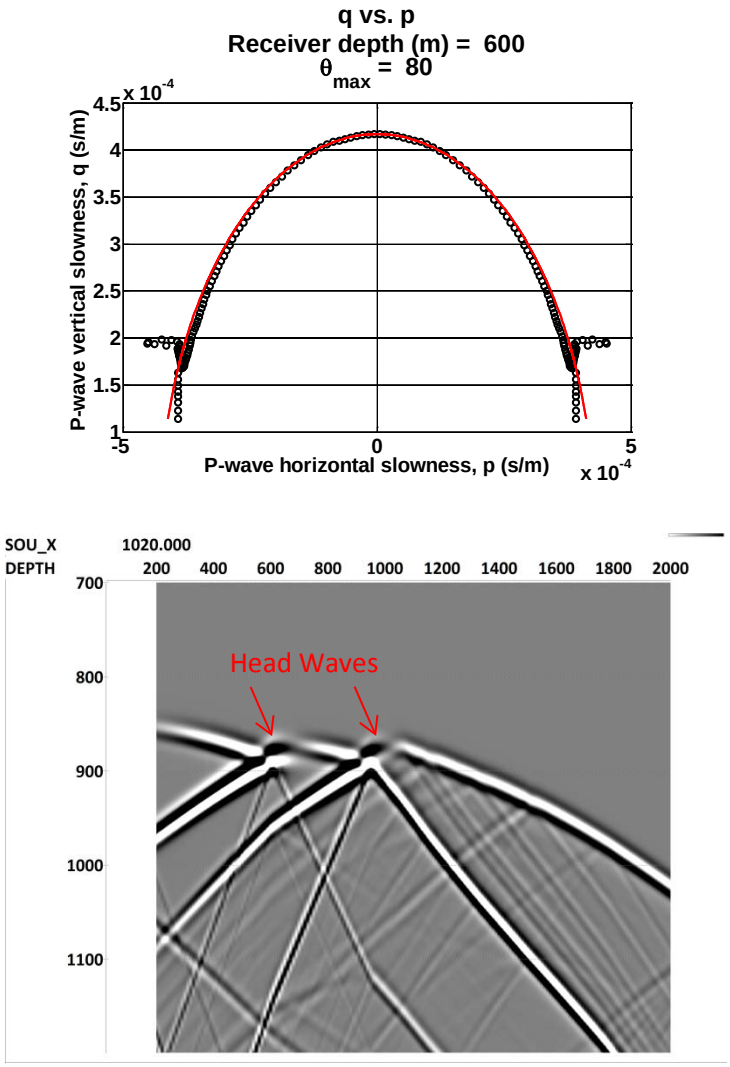

Figure 20, top, P-wave vertical slowness plotted against horizontal slowness for the receiver located at depth of 600 m. Slowness measurements for the sources at large offsets are noisy and inaccurate. At this depth, head waves precede the P-waves generated by the sources located at large offsets (bottom, SOU_X =1020 m) and can be wrongly picked as P-wave first arrivals.

4.7 VTI parameter estimation, 3D VSP example from CO2CRC's Otway geosequestration site

In this case, I assume that the shale formation in which the receivers of well CRC-1 are positioned, is a VTI formation. Based on 3D surface seismic data available in the area, the overburden at well CRC-1 location is not geometrically complex as the fault

displacements are small and geological formation are laying almost horizontally. As a result, horizontal components of P-wave slowness vector can be measured on the surface and used in the receiver interval. The only correction that has to be done is to estimate and apply elevation related statics to the measured travel times. I will first estimate P-wave slowness vectors from 3D VSP data and then I will cross plot two components of the slowness vector (as with synthetic case in Figure 14) to examine whether or not the VTI assumption is valid.

P-wave slowness vectors had to be extracted for all the sources on the surface. At any given source location, travel times recorded from neighbouring sources (within a given radius) are used to estimate three components of the P-wave slowness vector. The radial zone from which the sources are taken for slowness calculation has to be chosen with respect to the distance between the source lines. The distance between sources along a source line is usually very small (10-20 m) and supply greater data density in this direction. However, the source line spacing is usually in the order of hundreds of meters (100 meters in 2010 survey) and supply smaller data density in the cross line direction. A too large zone will overly smooth computed slownesses where as a too small zone will be short of measurements in the cross line direction. At Otway site, I selected 300 m radius to include sufficient number of source lines in the analysis.

In the next step, vertical component of the slowness vector, q and horizontal components p_1 and p_2 are estimated by solving, in a least-square sense, a system of equations $A*X=B$ where matrix A contains the coordinates $[x,\ y,\ z]$ of the measured travel times, matrix B contains the recorded travel times and matrix X is the solution. Coordinates, x and y, belong to the position of the source on the surface while z corresponds to the depth of the receiver in the borehole. Magnitude of the P-wave slowness vector **P**, phase velocity, V_P and phase angle, θ can now be computed from the slowness measurements:

$$|P| = \sqrt{p^2 + q^2} \quad \textbf{(3)} \qquad V_P = \frac{1}{|P|} \quad \textbf{(4)} \qquad \theta = \cos^{-1}\frac{q}{|P|} \quad \textbf{05)}$$

Where the horizontal slowness is:

$$p = \sqrt{p_1^2 + p_2^2} \qquad (6)$$

Figure 21 displays P-wave phase velocity, V_P computed from the slownesses (Equation 4) that are derived from 3D VSP recordings at well CRC-1. Horizontal components of the slowness vectors (p_1 and p_2) are measured on the surface. Then, p_1 and p_2 are transferred and used in the receiver level by assuming that the overburden surrounding well CRC-1 is homogeneous. Vertical component of the slowness vectors is measured at the receiver level inside the shale formation. To increase the accuracy, slownesses measured for sources near the edges of the survey lines have been removed from being input to the analysis (not shown in the maps). For a source located near the edge of the survey, there would be smaller number of sources that lay within the 300 m radius than would be for a source located in the inner area. Notice the asymmetrical variations in P-wave velocity with respect to source offset and azimuth.

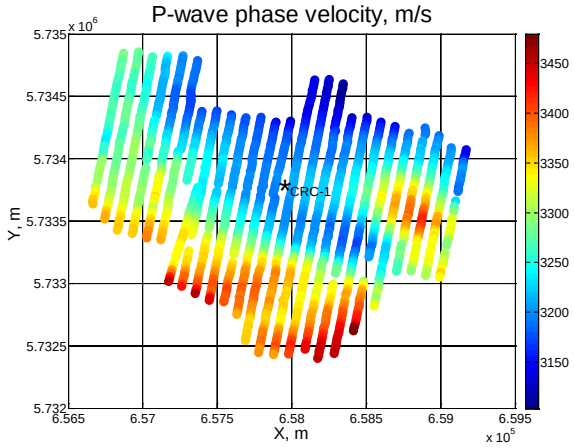

Figure 21, P-wave phase velocity estimated from 3D VSP measurements at well CRC-1.

Figure 22, top shows P-wave phase angles calculated from the slowness vectors. Notice that P-wave phase angle increases to about $\theta_{\max} = 50^o$ for the sources located in the edges of the survey. In the bottom, values of source offsets have been presented for

comparison. In this example, we can calculate P-wave group angle as the dip of a straight line between a given source and a receiver in the borehole. In Figure 22, group angle for the P-wave generated by the source located at far North-West in the survey area can be approximated as $\psi = \tan^{-1}\left[\frac{Source_{offset} = 1500\ m}{Geophone_{depth} = 1550\ m}\right] \approx 44^{o}$. There is a small difference between the group angle and the phase angle (Figure 22, left) for this source which can be the result of anisotropy or error in the measurements.

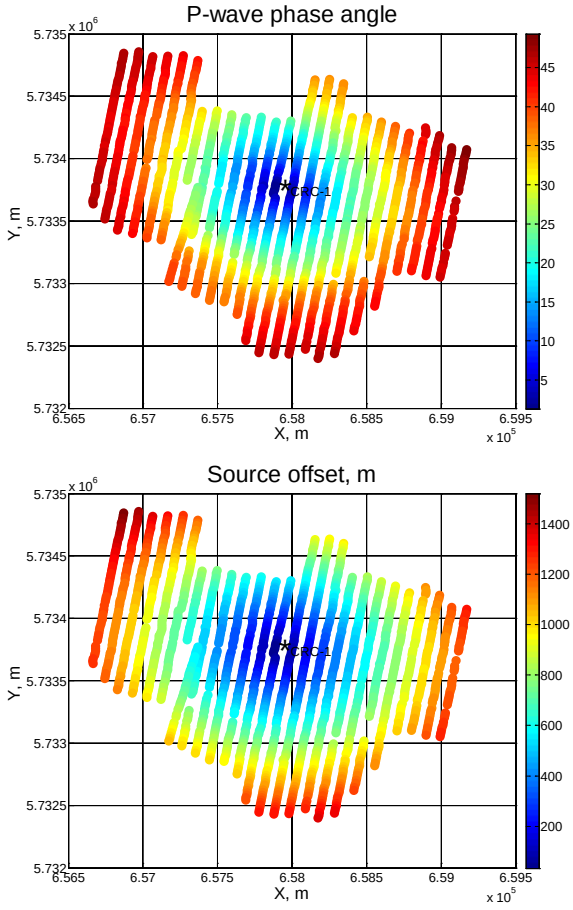

Figure 22, top, P-wave phase angles calculated from 3D VSP measurements at well CRC-1 and bottom, values corresponding to source offsets. For VTI anisotropy, this range of slowness data is wide enough to constrain elastic parameters (see also Figure 18).

A better analysis of P-wave propagation in this medium can be made by plotting phase angle as a function of source offset on the surface (Figure 23). At large offsets (more than 1200 m), recorded phase angle, θ can vary as much as 5^o for the waves generated by the sources located along the entire azimuthal range. This effect can be the result of layer geometry (dip) or the presence of azimuthal anisotropy in a medium which contains lower symmetry than transverse (polar) anisotropy. As in Otway example, geological dips are almost negligible; we suspect the case of having anisotropy with symmetry lower than VTI. In this part, I will examine whether or not polar anisotropy is a valid assumption for the shale formation at well CRC-1. Figure 24 displays vertical component of the slowness vector plotted against the horizontal component for the P-waves generated by all the sources in 3D VSP survey. Equation 1 predicts that the data would have followed a hyperbolic curve (for the entire azimuthal range) if they were measured within a VTI medium. However, large scatter in this case suggests that the medium has lower symmetries than a simple VTI. For this reason further VTI-based analysis will be terminated for this site. Subsequent analysis, as shown in Chapter 6, will utilise lower symmetries in the analysis to more accurately predict phase velocities.

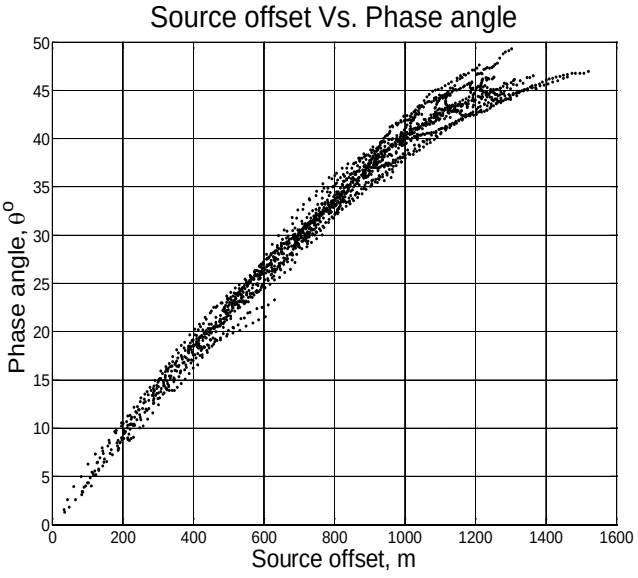

Figure 23, P-wave phase angle as a function of source offset derived from 3D VSP measurements at well CRC-1.

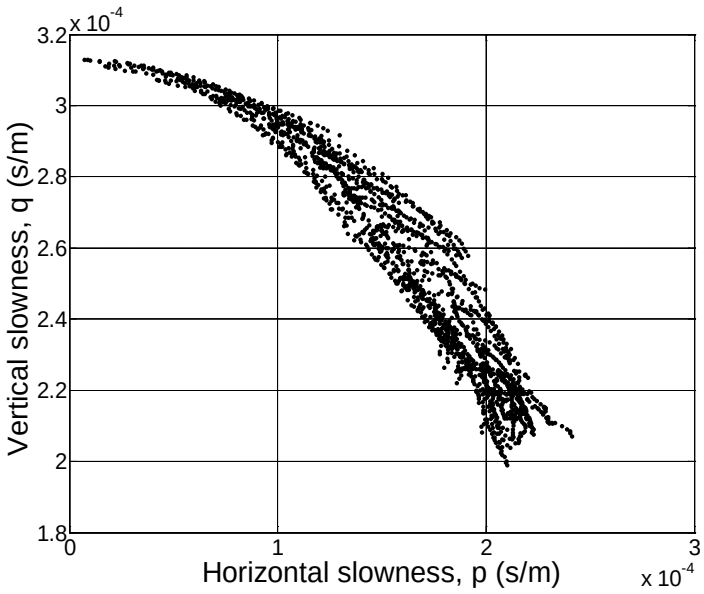

Figure 24, P-wave vertical component of the slowness vector plotted against the horizontal component derived from 3D VSP measurements at well CRC-1. Deviation from a hyperbolic curve is an indication of azimuthal anisotropy.

4.8 Discussion, remarks and conclusion

In this chapter, I have analysed the reliability of VTI parameter estimation for P-wave slowness data measured in a walkaway VSP experiment. I have reviewed the assumptions and the limitations of the (slowness) method and shown how to compute P-wave slowness vector from travel time recordings of the VSP survey. I have quantified the uncertainties (errors and standard variation) related to VTI parameter estimation as a function of noise in slowness measurements, medium anisotropy and acquisition geometry. The uncertainties are also dependent on the equation (the forward model) which we use for the inversion. As a general rule, the accuracy in VTI parameter estimation increases with increasing $\theta_{\max}$ and decreasing the anisotropy of the medium and the measurements noise. However, medium anisotropy may sometimes reverse this rule and produce better accuracy for smaller angles of wave propagation. As an example, with the same level of noise in the slowness (3% in Figure 6), the accuracy of estimating parameter ε in the range of $0.4 \le \varepsilon \le 0.6$ and $\delta \le -0.2$ is larger for $\theta_{\max} = 60^o$ than for

another range $\varepsilon \le 0$ and $\delta \ge 0.6$ with $\theta_{\max} = 80^o$. Another important point in estimations is the value of standard deviation. This value is as important as the error itself as it determines the departure of estimated values from the exact value. Statistically, a large standard deviation value for the estimation would require repeating the experiment and averaging the results. This may not be possible in practice. In general, the following conclusion can be deducted from our uncertainty analysis:

A. Where Equation 1 has been used for the inversion:
    1. If the noise level is small (1%), δ can be estimated even within the small range of P-wave propagation angles ($\theta_{\max} = 30^o$). However, $\theta_{\max}$ has to increase to around 45^o in order to reliably estimate parameter ε.
    2. If the noise level in slowness measurements is large (3%), maximum P-wave propagation angle, $\theta_{\max}$ has to be increased to more than 60^o in order to acquire a reasonable accuracy for parameter δ. Again, $\theta_{\max}$ has to increase to more than 60^o in order to reliably estimate parameter ε.
    3. Where the estimations acquire highest accuracy ($\theta_{\max} = 80^o$), both the δ and ε estimations tend to be dependent (parallel contours to one axis) on their corresponding values in the medium and show less dependency to the value of the other parameter (perpendicular error contours to the other axis).

B. Equation 2 has been used to invert medium velocities (1/slownesses) within the mild anisotropy range (less than ±20%) where 1% noise has been added to the slowness vectors:
    1. This equation has demonstrated good accuracy for estimating parameter ε within the short angles of wave propagation ($\theta_{\max} = 30^o$), where the other method based on Equation 1 has failed in the estimation. The standard deviations are larger than the method based on Equation 1. The accuracy increases with increasing $\theta_{\max}$.

2. The accuracy of using Equation 2 for estimating parameter δ is excellent within $\theta_{\max} = 30^o$ and increases with increasing $\theta_{\max}$.

I have demonstrated (in Section 4.6) the effect of maximum P-wave propagation angle, $\theta_{\max}$ (determined by maximum source offset and receiver depth) on VTI parameter estimation at the location of well CRC-1 in the synthetic walkaway VSP example. For any given receiver depth, the accuracy of the estimations increases with the source offset. However, slowness measurements can be contaminated in the presence of head waves and result in lower accuracy. Head waves are usually generated at shallow intervals where P-waves can propagate at large angles beyond the critical angle for the medium.

Through 2D synthetic walkaway VSP analysis, I have shown that slownesses computed from P-wave first arrivals are not significantly influenced by noise at the depth interval (1500 to 1600 m) where permanent 3C receivers are located at well CRC-1 (Figure 14). This analysis shows that the Snell's law is a valid assumption at the location of well CRC-1 and can be used to transfer horizontal components of P-wave slowness vector from the surface to the receiver level. The analysis also indicates that the geometry of the existing 3D VSP survey is capable of producing sufficient slowness data range (see Figure 22) to accurately estimate VTI anisotropy parameters (see Figure 18).

In the 3D VSP example of well CRC-1 data, I have shown the existence of azimuthal anisotropy in the shale formation where 3C receivers are permanently attached to the rock. The azimuthal anisotropy becomes evident by plotting vertical component of P-wave slowness vector against the horizontal component. The azimuthal anisotropy appears as scattered points that would have otherwise followed a hyperbolic curve in a VTI medium. As a result of this observation, I will focus my analysis on azimuthal anisotropy in Chapter 6 where I will fit an orthorhombic model to P-wave slownesses that are computed from 3D VSP time measurement.

Chapter 5, VTI anisotropy parameter estimation using P-wave slownesses and polarizations

5.1 Introduction

In the first part of this chapter (Section 5.2), I will briefly look at the history of the slowness-polarization method for VTI parameter estimation and review the underlying assumptions and method limitations. In the second part (Section 5.3), I will conduct a numerical analysis to evaluate the validity of using Grechka and Mateeva (2007) approximate slowness-polarization relationship for VTI parameter estimation. I will quantify the errors of VTI parameter estimation using this approximation as a function of medium anisotropy and P-wave propagation angles. In Section 5.4, in a similar analysis as in Section 5.3, I will use the exact relationship between P-wave vertical slowness and polarization dip to quantify the errors in VTI parameter estimation. In this case, the errors will be quantified in terms of maximum P-wave propagation angle, medium anisotropy and noise in the measurements. In Section 5.5, to understand the sources of P-wave polarization noises in VSP measurements and because of its importance in anisotropy parameter estimation, I will analyse several examples of synthetic seismograms recorded by the receivers in a vertical borehole within a two-layer earth model. I will show that P-wave recorded by 3C geophones in the borehole will cause nonlinear particle displacement in the medium near the interface between two layers because of the influence of numerous wave types that interfere P-wave polarization measurements. Having understood the causes of polarization noise in P-wave recordings, I will use the exact slowness-polarization equation to invert synthetic walkaway VSP measurements obtained over the two-layer earth model for VTI anisotropy parameters δ and ε. In Section 5.6, I will use P-wave polarization dips and vertical components of the slowness vectors measured at Otway's synthetic walkaway VSP experiment (Section 4.6) to invert for VTI parameters in the model by using exact slowness-polarization relationship. Section 5.7 is dedicated to discussing the results and conclusion.

5.2 Slowness-polarization method, assumptions and limitations

Replacing horizontal components of P-wave slowness vector at the geophone location (in the borehole) with those measured on the earth surface is no longer possible in the presence of lateral heterogeneity in the overburden and other parameter estimation methods have to be examined. White et al. (1983), de Parscau (1991) and Hsu et al. (1991), Bóna et al., (2008) have combined two local measurements: vertical component of the slowness vector and polarization vector to estimate local VTI anisotropy parameters from VSP measurements. Vertical component of the slowness vector is measured in a wellbore by differentiating first P-wave arrivals along the borehole. Polarization vector is measured by three-component (3C) geophones in the borehole. This method does not require measurements of the horizontal components of the slowness vector and as a result can be applied to a subsurface with any complexity. De Parscau (1991), Hsu et al. (1991) and Horne and Leaney (2000) have indicated that to estimate VTI anisotropy parameters based on slowness-polarization method both P and SV data are required (with propagation angles up to 80^o) and neither P nor SV data alone cannot uniquely constrain VTI parameters.

Williamson and Maocec (2001), Zheng and Psencik (2002) and Grechka and Mateeva (2007) have discussed the difficulties in identifying SV arrivals in the data and separating them from SH-waves as there are usually no independent azimuth measurements for geophone components. Based on their discussion, avoiding shear waves in the inversion might increase the accuracy of anisotropy parameter estimation as they are usually noisier than P-wave measurements and there is no need to identify the type of shear modes. To overcome this issue, they have proposed different techniques for VTI parameter estimation that are solely based on P-wave slowness and polarization measurements. Nevertheless, Williamson and Maocec (2001) noticed that the ratio of the vertical velocities V_{P0}/V_{S0} had to be known a priori to be able to resolve Thomsen δ and ε parameters. Zheng and Psencik (2002) propose a parameter combination that is more definitive but is restricted to weak anisotropy. Grechka and Mateeva (2007) claim that we can extend Zheng and Psencik (2002) technique to moderate and strong anisotropy by proposing two new anisotropy parameters δ_{VSP} and

η_{VSP} that are comparable to that of Thomsen coefficient δ and Alkhalifah-Tsvankin (1995) anellipticity coefficient η. These new anisotropy parameters δ_{VSP} and η_{VSP} absorb the need for knowing a priori V_{S0} in VTI parameter estimation. I will analyse their claim in the next section, where I will quantify the accuracy of the weak anisotropy approximation with respect to VTI anisotropy in the medium and P-wave propagation angles.

5.3 VTI parameter estimation using approximate relationship between P-wave's vertical slowness and polarization dip

Grechka and Mateeva (2007) have discussed that avoiding shear waves will benefit anisotropy parameter estimation from 2D VSP measurements beneath complex overburden velocity structures and proposed a relationship for weak anisotropy that relates P-wave vertical slowness, q to the polarization vector dip angle ν (measured from vertical direction):

$$q(\nu) \approx \frac{\cos\nu}{V_{P0}}(1+\delta_{vsp}\sin^2\nu+\eta_{VSP}\sin^4\nu) \qquad (1)$$

Where $\delta_{VSP}=(f_0-1)\,\delta$, $\eta_{VSP}=(2f_0-1)\,\eta$, $f_0=1\Big/\sqrt{1-\frac{V_{S0}^2}{V_{P0}^2}}$, δ is Thomsen (1986) anisotropy coefficient and η is Alkhalifah-Tsvankin (1995) anellipticity coefficient. Grechka and Mateeva (2007) have also concluded that Equation 1 is sufficiently accurate in moderate and strong anisotropy. In this analysis, I will establish the range of anisotropic parameters δ and ε in which the approximation is valid. I will use Equation 1 to invert synthetic *error-free* data for parameters δ and ε.

I will generate numerical data for P-wave propagation in VTI media by using the Christoffel Equation 2 of Chapter 3. Synthetic numerical data here consist of P-wave slowness and polarization vectors that are computed for reasonably weak VTI media

defined as: $\varepsilon \in [-0.2,\ 0.2]$, $\delta \in [-0.2,\ 0.2]$ and $V_{P0} = 3000$ m/s, $V_{S0} = 1500$ m/s, $\gamma = 0.07$ and density $\rho = 2000$ kg/m^3. To quantify the effect of wave propagation angles (related to source offset) on VTI parameter estimation using Equation 1, P-wave propagation (phase) angle, we consider two ranges of the phase angle: θ is first increased (in 1^o steps) from 0^o to 30^o and then from 0^o to 80^o. In order to establish the range of validity in the approximation, no error is added to this data.

I will invert numerical slowness and polarization data for anisotropy parameters δ_{VSP} and η_{VSP} using MATLAB's *fminsearch* minimization algorithm as with the slowness only method described in Chapter 4. Here, V_{P0} and V_{S0} are regarded as known values in the inversion and they are not estimated. Final estimations (δ_{est}, ε_{est}) are calculated from δ_{VSP} and η_{VSP}, and are subtracted from the initial values (δ, ε) in the models to calculate the errors ($\delta_{est} - \delta$, $\varepsilon_{est} - \varepsilon$). Since no random noise is introduced to the data as was in Chapter 4, only one single inversion is carried out and there are no estimations of standard deviation and no average values computed. A least square objective function is minimized in this inversion which comprises the sum of squared residuals between the numerical vertical slownesses and the predictions from model (Equation 1). This objective function is expected to have only a global minimum to be discovered by *fminsearch* algorithm.

Results of the inversions are displayed in Figure 1. In Figure 1, I plot the absolute difference between the actual and the inverted values of the parameters. To improve the inversion, I allow the dip range to increase to 80 degrees.

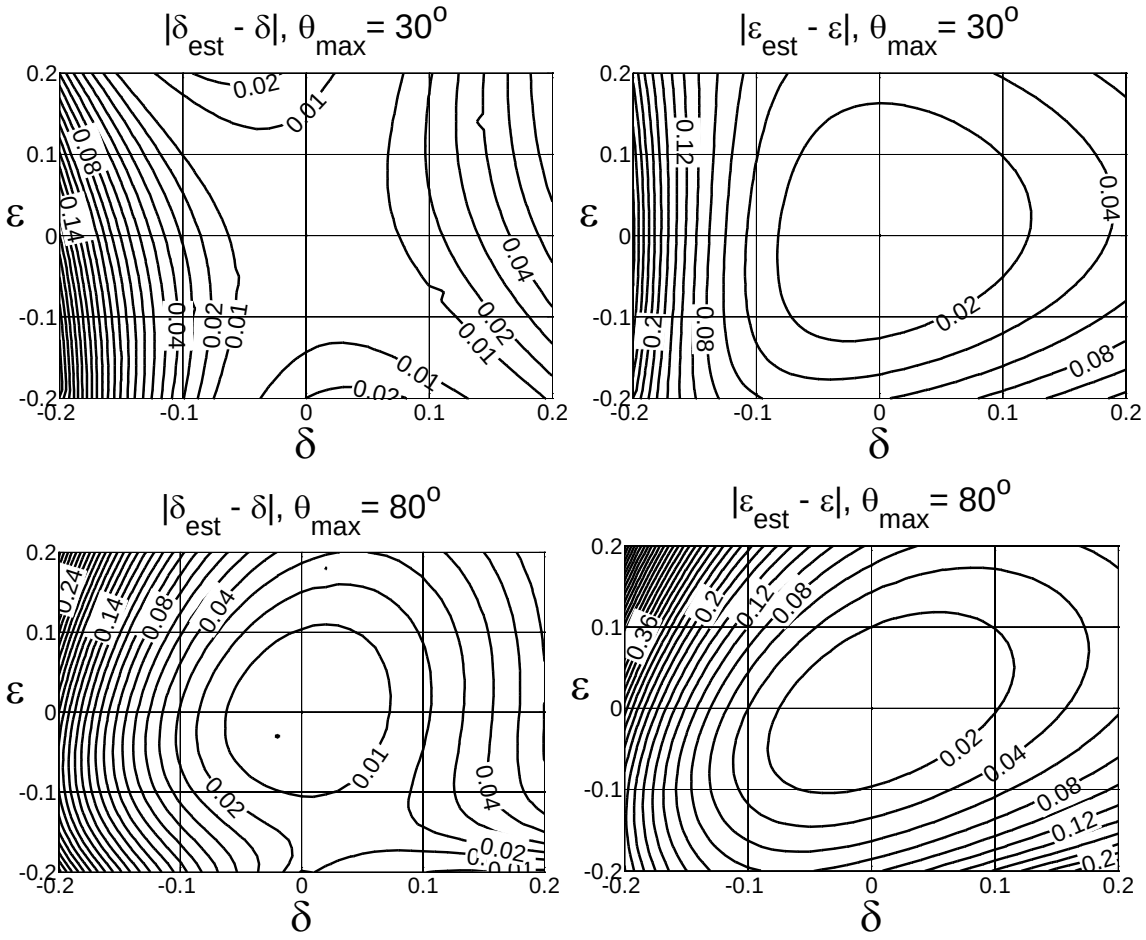

Figure 1, absolute errors associated with the inversion of synthetic P-wave slowness and polarization using approximate slowness-polarization relationship, Equation 1, with $\theta_{\max} = 30^o$ (top) and $\theta_{\max} = 80^o$ (bottom). Since the data was not contaminated with errors, this Figure illustrates the errors inherent in the approximation used by the method.

Figure 1 shows that Equation 1 is valid reasonably well only for a small range of δ and ε, approximately from -5% to 5% even for the large dip range of $\theta_{\max} = 80^o$. Increasing wave propagation angles has not improved the estimations. Due to the limited range of validity of this approximation, I will not present any further error analysis for this method.

5.4 VTI parameter estimation using exact relationship between P-wave vertical slowness and polarization dip

The exact equation for calculating P-wave phase angle θ from polarization angle ν in VTI media (de Parscau, 1991; Williamson and Maocec, 2000 and Grechka and Mateeva 2007) is represented by:

$$(a_{11}-a_{55})\tan^2\theta+2(a_{13}+a_{55})\cot 2\nu\tan\theta-(a_{33}-a_{55})=0 \qquad (2)$$

where a_{11}, a_{13}, a_{33} and a_{55} are density normalized stiffness coefficients of the VTI medium. Vertical component of the slowness vector q is related to ν through the P-wave velocity in VTI medium V_P:

$$q=\frac{\cos\theta}{V_P} \qquad 03)$$

where the velocity of P-wave in VTI media is defined as:

$$2V_P^2=(a_{11}+a_{55})\sin^2\theta+(a_{33}+a_{55})\cos^2\theta +\sqrt{((a_{11}-a_{55})\sin^2\theta-(a_{33}-a_{55})\cos^2\theta)^2+4(a_{13}+a_{55})^2\sin^2\theta\cos^2\theta} \qquad (4)$$

Equation 4 represents another form of Equation 15 in Chapter 3, which represents P-wave velocity in VTI media in terms of density normalized stiffnesses a_{11}, a_{13}, a_{33} and a_{55}.

In this method, we have used the exact slowness-polarization relationship given by Equations 2 to 4 to invert P-wave numerical slowness and polarizations for Thomsen (1986) anisotropy parameters δ and ε.

Numerical data are generated the same way as in Section 5.3 but for a wider range of VTI anisotropy parameters in the medium: $\varepsilon\in[-0.2,\ 0.6]$, $\delta\in[-0.4,\ 0.7]$. To evaluate the effect of noise on parameter estimation, 1 and 5 % random noises are added to slowness vector and polarization vector, respectively, and following the methodology described in Section 3.14. With the introduction of noise to data, every inversion is

repeated 1000 times to generate a distribution function for the estimated values. Uncertainty analysis here would be in the form of discussing both the mean error and the standard deviation for the computed distributions. Similar to the approximate method in Section 5.3, I will reiterate the inversions for $\theta_{\max} = 30^o$ (31 slowness directions) and $\theta_{\max} = 80^o$ (81 slowness directions) to evaluate the effect of increasing source offset on estimations.

Inversion algorithm will use an objective function that is defined as the sum of absolute differences between squared values of numerically computed vertical slownesses and those predicted by Equations 2 to 4. To estimate the errors in every model case, I will first minimize the objective function for two density normalized stiffnesses a_{11} and a_{13} (the other two, a_{33} and a_{55} in Equations 2 to 4 are taken from model V_{P0} and V_{S0}, respectively) and next use Equations 11 and 12 in Chapter 3 to calculate VTI parameters. This is then repeated 1000 times to derive a distribution function for the estimations from which an average value (δ_{est}, ε_{est}) and a standard deviation (σ_δ, σ_ε) are extracted and used to compute errors as: $\delta_{est} - \delta$ and $\varepsilon_{est} - \varepsilon$.

The results of the VTI parameters inversion based on using P-wave exact slowness-polarization relationship (Equations 2 to 4) and adding 1% slowness noise and 5% polarization noise are summarized in Figures 2 and 3. Figure 2 shows the difference between the median of 1000 inversions and the model values of δ and ε for the input anisotropy range. Figure 3 shows the standard variation of the inverted values for the inversions displayed in Figure 2.

To demonstrate the sensitivity of this method to the errors in polarization measurements, I will reiterate the analysis with a smaller error added to the polarization vector. This time, only 2% noise is randomly added to the polarization vector and noise for the slowness vector remains as before (1%). The results are shown in Figures 4 and 5.

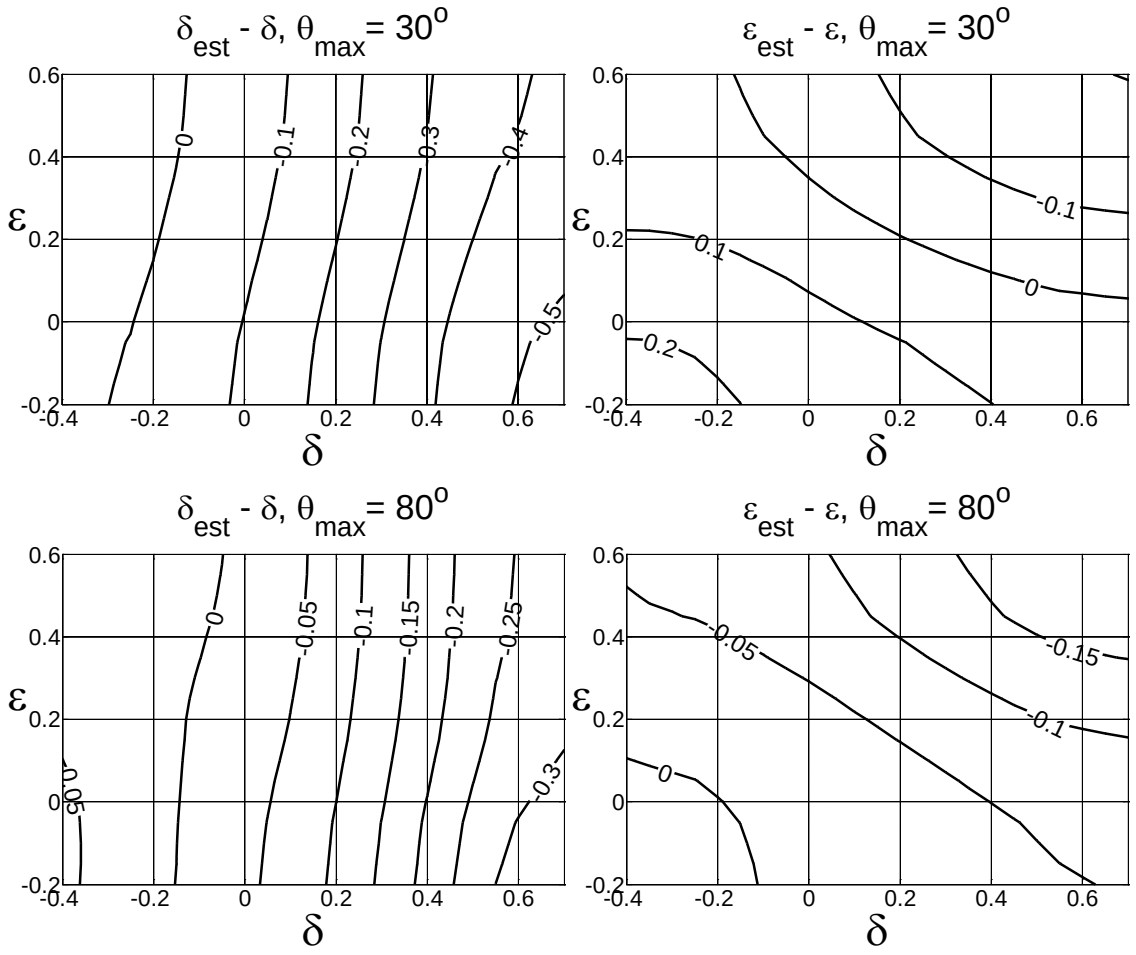

Figure 2, errors of 1000 inversions of synthetic P-wave slowness and polarization using the exact slowness-polarization relationship, Equations 2 to 4, as functions of true anisotropy parameters ε and δ. In the top, $\theta_{\max} = 30^o$ and $\theta_{\max} = 80^o$ in the bottom. Slowness and polarization vectors are contaminated with 1 and 5 % random noises, respectively.

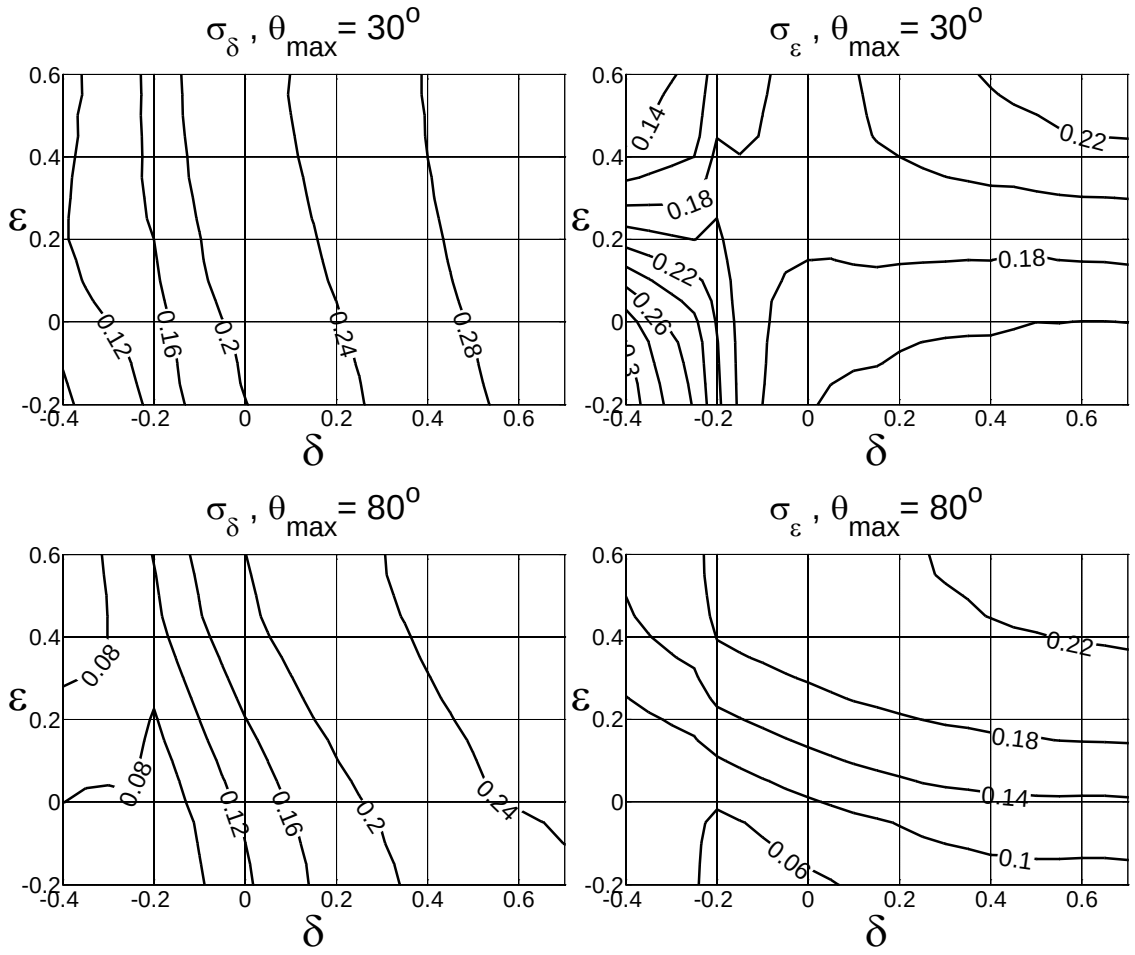

Figure 3, Standard deviations for the corresponding quantities shown in Figure 2.

Figures 2 and 3, display the estimation errors ($\delta_{est} - \delta$, $\varepsilon_{est} - \varepsilon$) and their standard deviations (σ_δ , σ_ε) where 5% and 1% random noise has been introduced on polarization and slowness vectors, respectively. Although error estimations display some improvement as $\theta_{\max}$ increases to 80^o , the presence of large standard deviations, depicted in Figure 3, questions the reliability of using exact slowness-polarization method for the estimation of VTI parameters in the presence of large polarization noise.

To analyse the response of this method to the accuracy of the polarization measurements, we decrease the error on polarization vector from 5% to 2% and reiterate the analysis (Figures 4 and 5). With only 2% noise added to polarization vectors, ε

estimation errors have become very small (even in the case of $\theta_{\max} = 30^o$) and δ estimations are improved as well (in the case of $\theta_{\max} = 80^o$). However, large values on standard deviation plots (Figure 5) mean that the reliability of an inversion from one data set is relatively weak for this method.

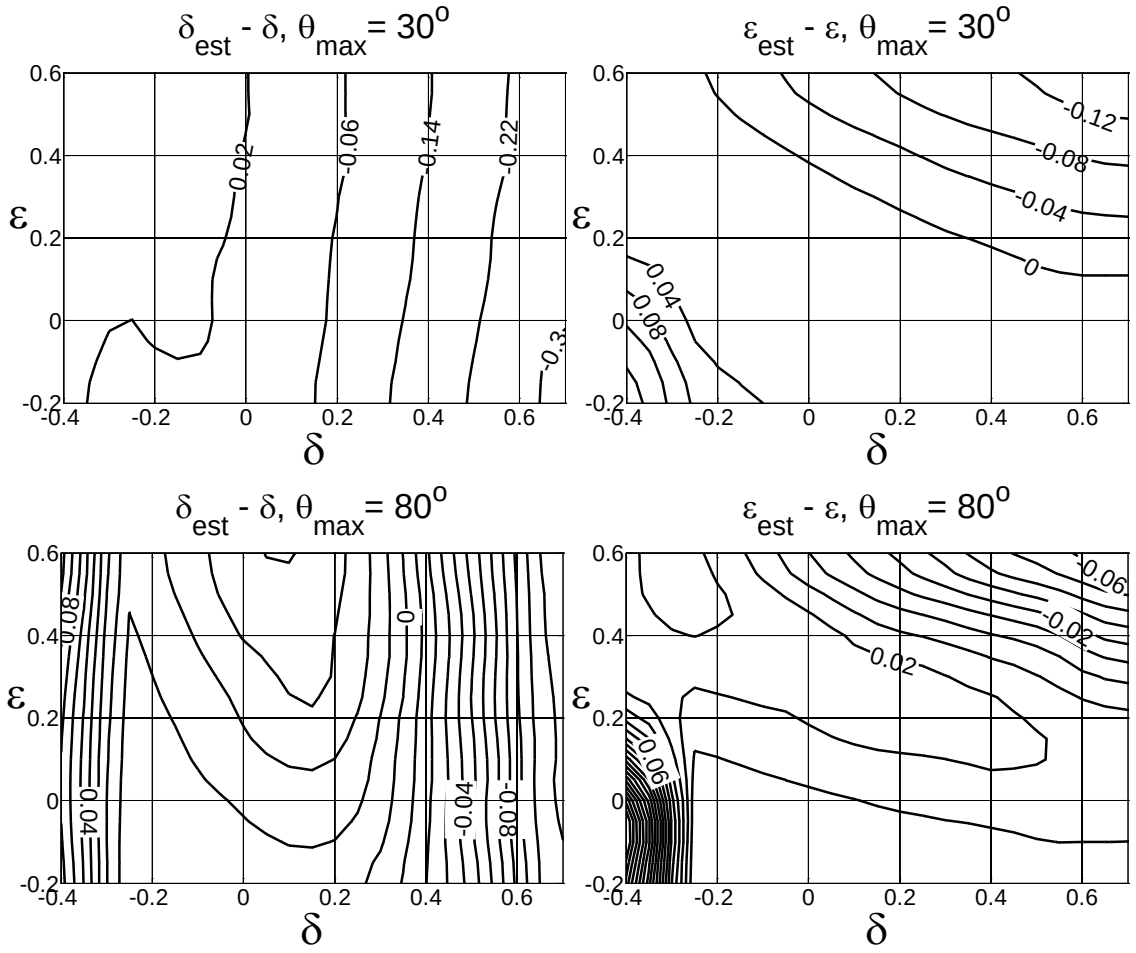

Figure 4, errors of the inversion of synthetic P-wave slowness and polarization using the exact slowness-polarization relationship, Equations 2 to 4, as functions of true anisotropy parameters ε and δ. In the top, $\theta_{\max} = 30^o$ and $\theta_{\max} = 80^o$ in the bottom. Here, the error on polarization vector has been reduced to 2% while the error on slowness vectors remains 1%.

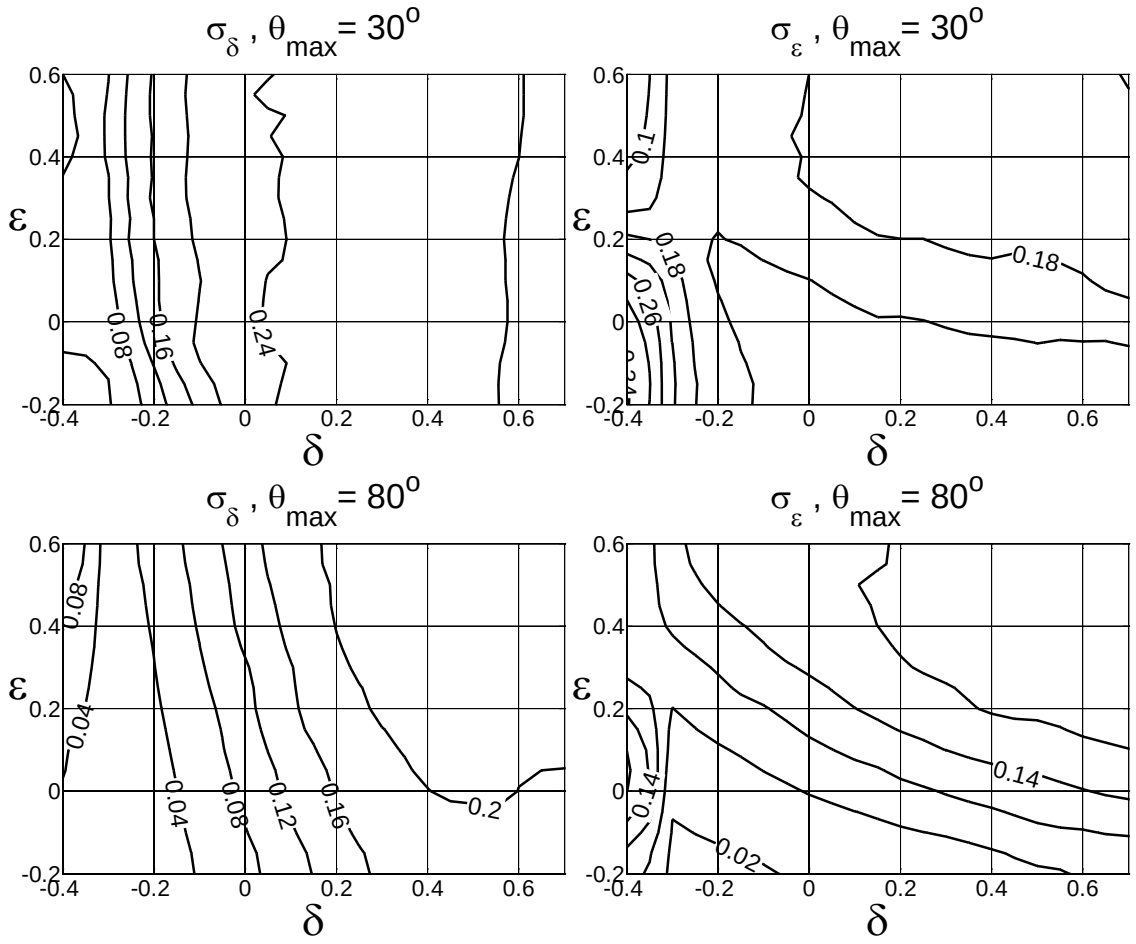

Figure 5, Standard deviations for the corresponding quantities shown in Figure 4.

This method too, relaxes the assumption of lateral homogeneity in the overburden as horizontal slownesses are not required for the inversion. However, an accurate estimation of VTI anisotropy parameters based on this method is largely dependent on the accuracy of polarization measurements, and slightly on the coverage of wave propagation angles. Large standard deviation values shown in Figure 5 (bottom) indicate that even with accurate measurements of polarization vectors and availability of large offsets, one is not guaranteed to obtain a reliable parameter estimates of either δ or ε.

5.5 Noise in P-wave polarization measurements, non-linear particle displacement near the elastic boundaries

Plane waves in anisotropic media can be represented by:

$$u_k = U_k e^{i\omega(\frac{n_j x_j}{V} - t)} \qquad 05)$$

where u_k are the components of the displacement vector **u**. U_k are the components of the polarization vector **U**. ω is the angular frequency, V is the phase velocity, and **n** is the unit vector orthogonal to the plane wavefront. From Equation 5, particle displacement at any given point is defined as a simple harmonic motion over a straight path for any type of plane wave propagating in elastic anisotropic media. However, P-wave particle displacement can become largely non-linear (ellipsoidal) as a result of interference from various modes of waves propagating in the medium.

To illustrate the effect of wave interferences on particle displacement (and polarization measurements) of a plane wave, a synthetic offset VSP was acquired over a two-layer medium as depicted in Figure 6 . In Figure 6, only vertical component of the recorded wavefield is demonstrated where receivers are positioned at every 10 m space in the borehole and source offset is 1520 m. The interface between the two elastic media is located at depth = 800 m and the elastic parameters of the media are shown in the figure. P-wave generated by the offset source impinges the interface near the borehole with a large angle and generates converted down going and up going shear waves as well as reflected and transmitted P-waves.

Particle displacements for down going P-wave are derived from both the vertical and the horizontal trace components and are illustrated in example geophones positioned at every 100 m intervals in the borehole. The example receivers positioned nearby the interface between the two boundaries (depths 700, 800 and 900 m) are affected by the interference phenomenon that appears as nonlinearity in P-wave particle motion. Receiver located at the interface (depth=800 m) records a wavefield which causes nearly a circular particle motion.

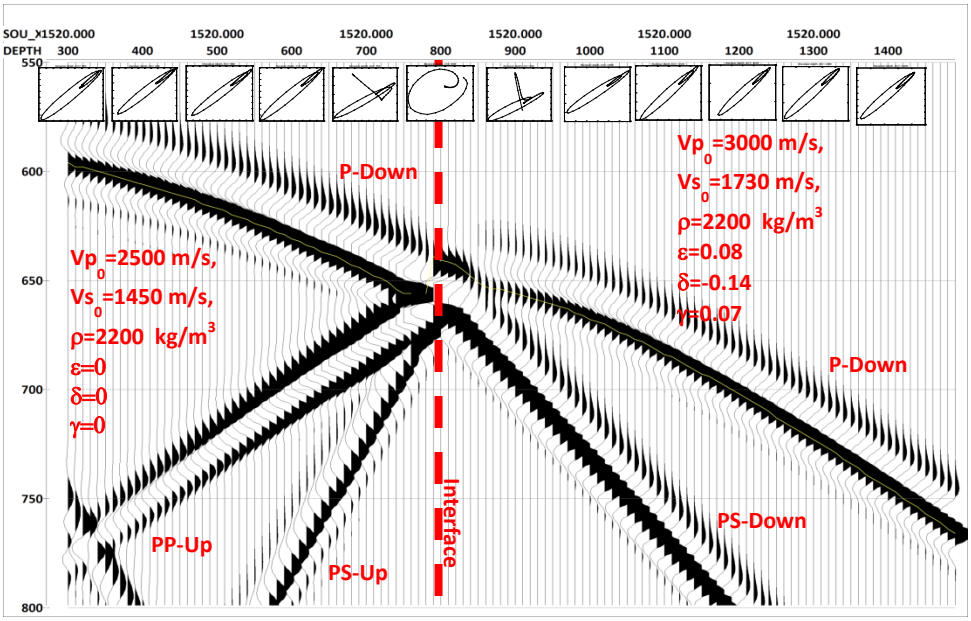

Figure 6, P-wave vertical component of particle displacement recorded in a synthetic offset VSP experiment with source positioned at offset=1520 m. P-wave polarizations become distorted near to the elastic boundary at depth=800 m.

Wave interference between down going P-wave and reflected up going P-wave and converted shear waves (down going and up going) in the vicinity of the elastic boundaries (Figure 6) can influence the accuracy of polarization measurements and consequently the reliability of using slowness-polarization methods for VTI parameter estimation. The interference between down going P-wave and other existing wave types in the medium (down going and up going P- and S-waves and etc.) appear to be offset dependent. The phenomenon starts at zero offset where reflected P-wave interferes down going P-wave at the elastic boundary. As the source offset increases, two down going and up going converted shear waves start to influence (down going) P-wave polarizations as well. To this point, interference between various wave types seems to take place only in the vicinity of the interface. However, at large offsets, beyond medium's critical angle for P-wave propagation, the distortion effect in P-wave polarization seems to spread over a wider depth range above the elastic boundary. To illustrate these concepts, I use a simple two-layer velocity model with a horizontal interface between the two layers where the wave interference phenomenon is expected to take place. Figure 7 displays the model and acquisition geometry (a walkaway VSP)

where elastic properties are depicted in each layer. In this model, receivers are positioned at every 10 meters spacing, starting from depth=200 m to depth=2000 m along a vertical borehole. Sources are positioned on the surface at every 20 m spacing. The length of the model is 6000 m and the horizontal interface is at depth = 965 m. Well position will be varying to study the effect of source offset on P-wave polarization measurements.

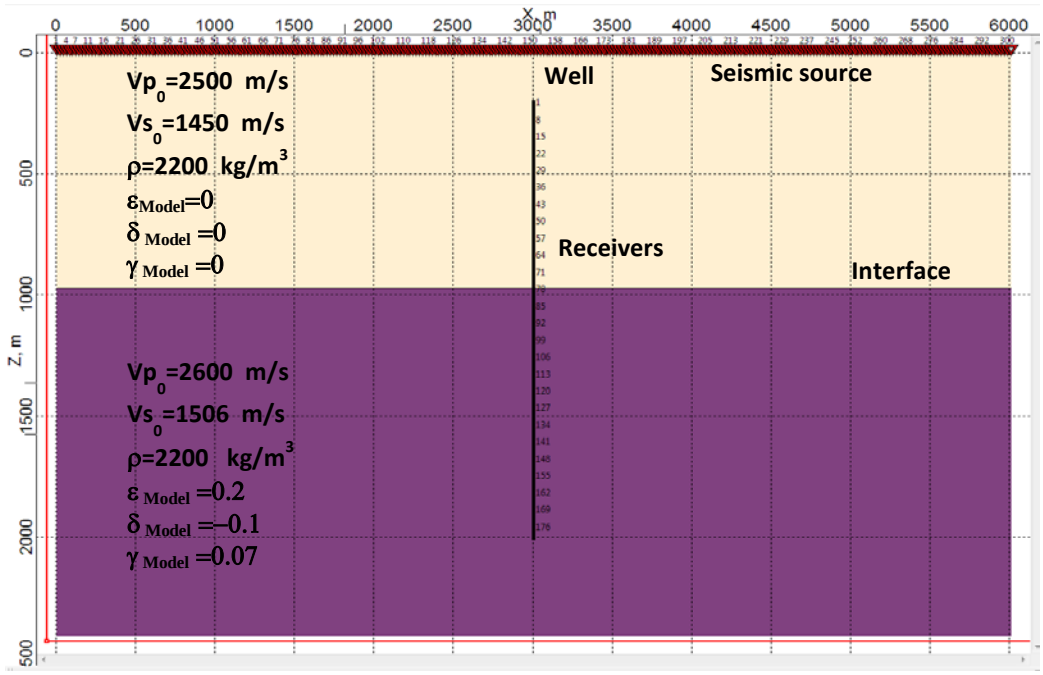

Figure 7, Synthetic VSP recordings acquired over a two-layer model used to investigate wave interference effect on P-wave polarization measurements. Receivers are positioned in the borehole at every 10 m intervals from 200 m to 2000 m. Sources are located on the surface at every 20 m intervals.

I will first start with a zero offset source. Figure 8 (top) illustrates a snapshot at time= 0.47 s of the wavefield generated by zero-offset source on the surface. Both the vertical and the horizontal components of the particle velocity vector are recorded by the receivers in the borehole. Vertical component of the recorded wavefield is displayed in Figure 8 (middle). Recorded wavefield is mainly composed of down going P-wave and the resulting up going reflection from the boundary. Also displayed in Figure 8 (bottom) is the linearity factor L, plotted with depth and hodograms of particle motion at some

selected receiver positions. Grechka and Mateewa (2007) introduce the concept of linearity factor in their slowness-polarization analysis to quality control the linearity of P-wave polarizations entering the inversion. L varies from zero for a spherical particle motion to one for purely linear. To compute L for the P-wave first breaks recorded within a time interval of 3C seismic trace ($X_i(k)$, $i = 1,\ 2,\ 3$ and $k = 1,\ 2,\ 3\ ,...,n$), a symmetric 3×3 covariance matrix is formed as:

$$M_{ij} = \sum_{k=1}^{n} [X_i(k) - \overline{X}_i][X_j(k) - \overline{X}_j],\ i,\ \ j = 1,\ 2,\ 3 \qquad \textbf{(6)}$$

where $\overline{X}_i = mean[X_i(k)]$. Matrix M is positive semidefinite and has three nonnegative eigenvalues μ_l that are used to compute the linearity factor as:

$$L = \frac{1}{2}\left(\frac{3\max \mu_l}{\sum_{l=1}^{3} \mu_l} - 1 \right). \qquad \textbf{(7)}$$

In general, particle motion caused by first arrivals of down going P-wave and recorded by the receivers in the borehole seems to stay mostly linear (L=0.99) along the vertical direction for the entire depth interval. However, there is a kink in linearity value at the interface depth; where the interference effect of reflected (up going) P-wave begins to influence the recording.

Now, let's look at the data recorded this time at source offset =1000 m. To do this, borehole is transferred to X=1000 m while source position stays at X=0 m. Figure 9 illustrates the same data as in Figure 8 for source offset = 1000 m. Going to longer offset, enables us to record converted shear waves that are generated at the interface by down going P-wave. Particle motion stays fairly linear with depth, except at the interface where the interference effect of up going P-wave and converted shear waves deteriorate the linear motion to an ellipse with L= 0.85. Nevertheless, P-wave, polarization direction can still be recognized along the longer axis of the ellipse. Another important observation is that, linearity factor acquires lower values below the interface. This can be related to the generation of down going PS-wave in the lower media. Figure 10 top,

displays a snapshot at time =0.86 s of the wavefield generated by the source located at offset=2000 m in the model. Figure 10 also shows the vertical component of the particle velocity vector recorded by the receivers in the borehole (middle) and L factor plotted as a function of depth with hodograms overlain (bottom). Despite the measurements seem to be influenced by the same interference as with the previous case (offset=1000 m), the linearity function has been significantly decreased to about 0.43 at the interface level. Although not apparent in this figure, large source offset has enabled the receivers to record head waves that are generated by a down going P-wave that is travelling at an incident angle equal to the critical angle. Head waves interference is now adding up to the destructive interference effect caused by up going P-wave and converted shear waves and the result is a significant decrease in L factor. Head waves are generated when the incident angle increases to beyond the critical angle. In this case, the horizontal P-wave velocity in the lower medium is: $V_{P2}\ (90) = V_{P2}(0)\ (1+\varepsilon) = 2600\ (1+0.2) = 3120$ m/s, where ε is the Thomsen VTI parameter in the lower medium. From the Snell's law, P-wave's critical angle for the interface is: $\theta_{Critical} = \sin^{-1}\dfrac{V_{P1}(0)}{V_{P2}(90)} = \dfrac{2500}{3120} = 53.25^{o}$. This angle corresponds to the source offset: $Offset_{Critical} = Depth_{Interface}.\tan\ (\theta_{Critical}) = 965 \times 1.33 = 1292$ m, which is smaller than the source offset in Figure 10. Head wave interference is not restricted to the interface level and spreads to depth= 850 m.

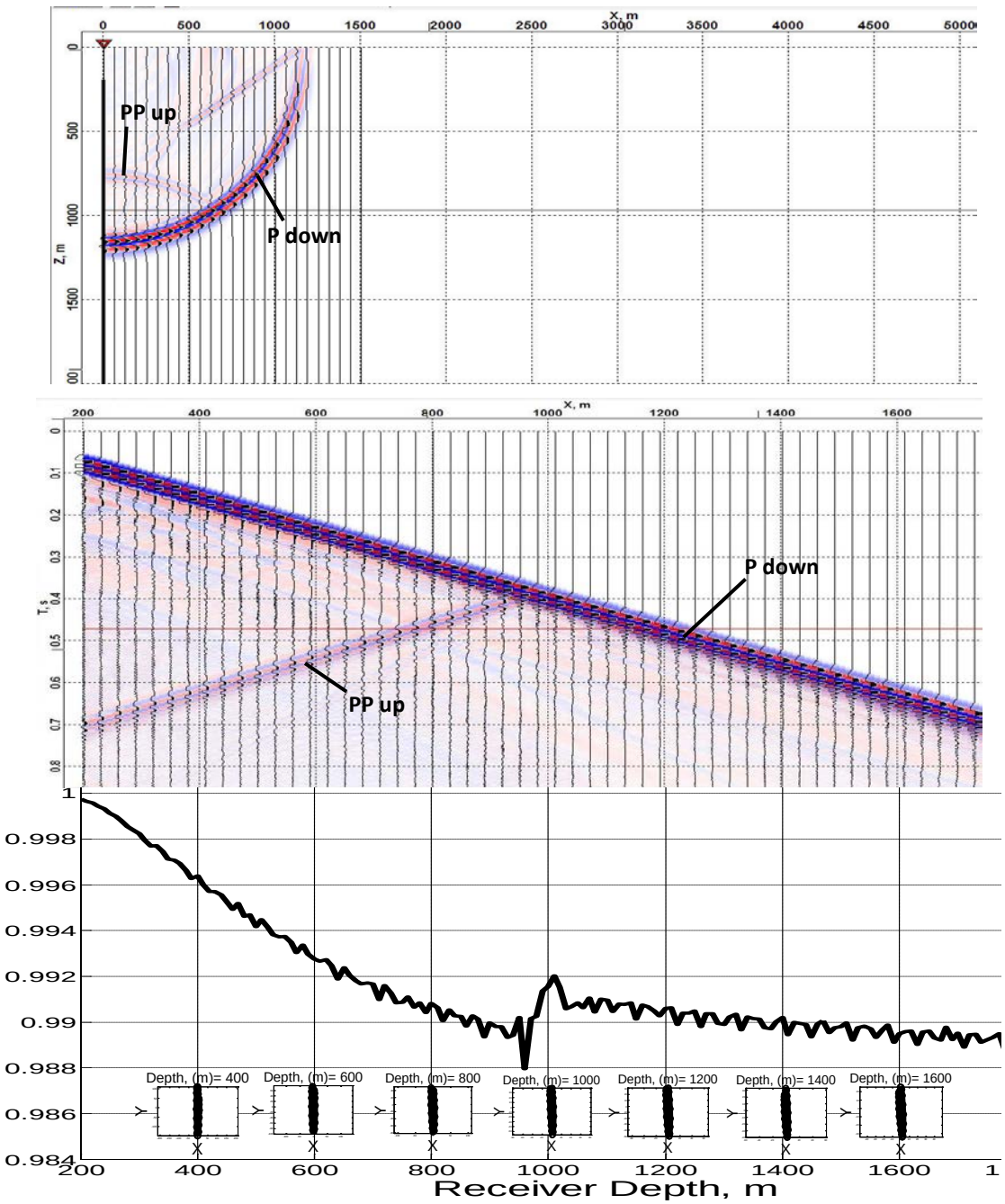

Figure 8, (top) illustrates a snapshot at time= 0.47 s of the wavefield generated by zero offset source. Vertical component of the recorded wavefield is displayed in the middle. The linearity factor L and plots of particle motion hodograms at some selected receivers are shown in the bottom.

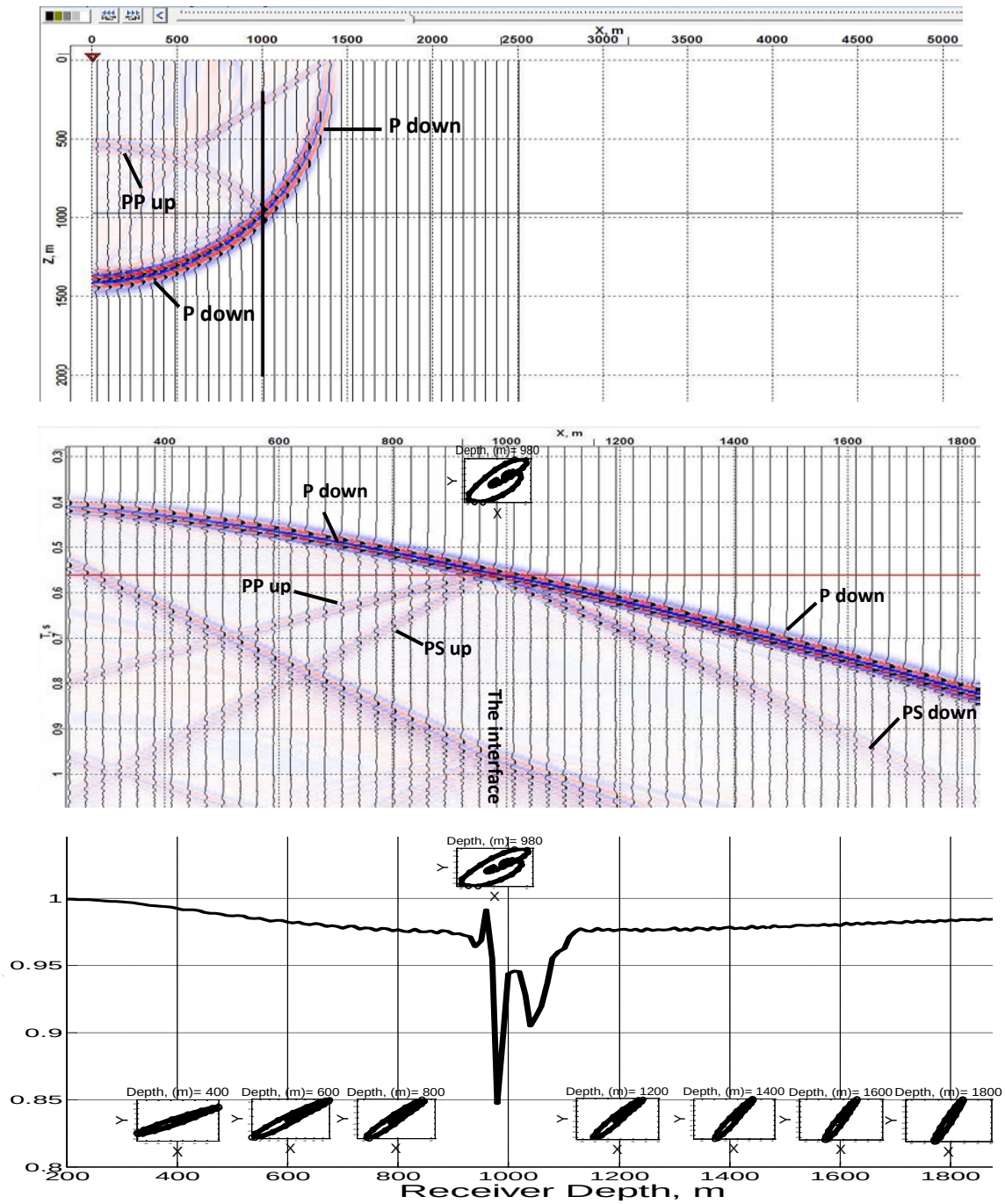

Figure 9, (top) illustrates a snapshot at time= 0.56 s of the vertical component of the particle velocity vector from the wavefield generated by source at offset =1000 m. Vertical component of the recorded wavefield is displayed in the middle. The linearity factor L and plots of particle motion hodograms at some selected receivers are shown in the bottom of the figure.

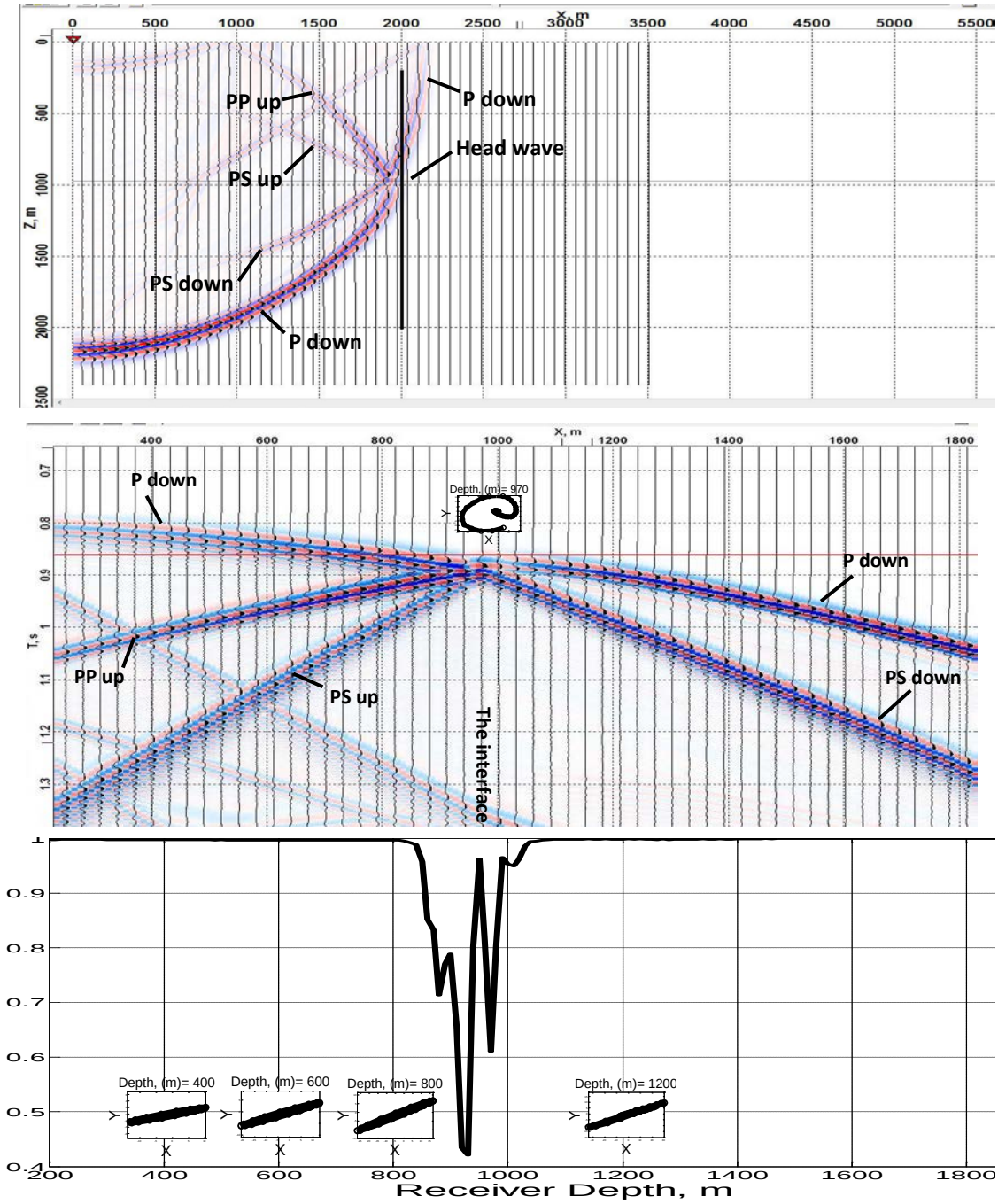

Figure 10 (top) illustrates a snapshot at time= 0.86 s of the vertical component of the particle velocity vector from the wavefield generated by source at offset =2000 m. Vertical component of the recorded wavefield is displayed in the middle. The linearity factor L and plots of particle motion hodograms at some selected receivers are shown in the bottom of the figure.

Now let's increase the source offset to 3000 meters. Figure 11 illustrates the same data as in previous cases but recorded with source offset = 3000 m. Large offset together with large recording time allow the receivers to record the head wave which has been separated from down going P-wave in the upper medium as a result of larger velocity in the lower medium. The overall effect on P-wave polarization can be explained by looking at the values of linearity function. Interference between the head wave and down going P-wave seems to have small influence on linearity and polarization (depth = 700-800 m). From depth=800 m to the interface at 965 m, first arrivals recorded by the receivers are the head wave and P-wave arrives at a later time. Particle motion is still fairly linear (L= 0.8) but polarization vector has acquired the direction of the head wave.

To further emphasis the observation made at the experiment with source offset = 3000 m, I now increase the source offset to 4000 m. The recordings are shown in Figure 12. Again, head wave is interfering P-wave in the interval depth from 470 to 600 m. Despite the interference between the two waves, linearity is reasonably preserved and P-wave polarization direction doesn't change. Where the first arrivals are the head waves, depth interval from 600 m to the interface (965 m), particle motion is highly linear and polarization vector will be in the direction of the head wave.

In summary, the effect of up going reflected P-wave on polarization measurements is very subtle (Figure 8). Converted down- and up-going shear waves have larger influence on polarization measurements than up-going reflected P-wave (compare Figures 8 and 9). Largest error in polarization measurements appear when the interference effect of head waves is added to the effect of converted shear waves (Figure 10). At larger offsets, polarization measurement based on first arrivals would be related to head waves as P-waves arrive in later times.

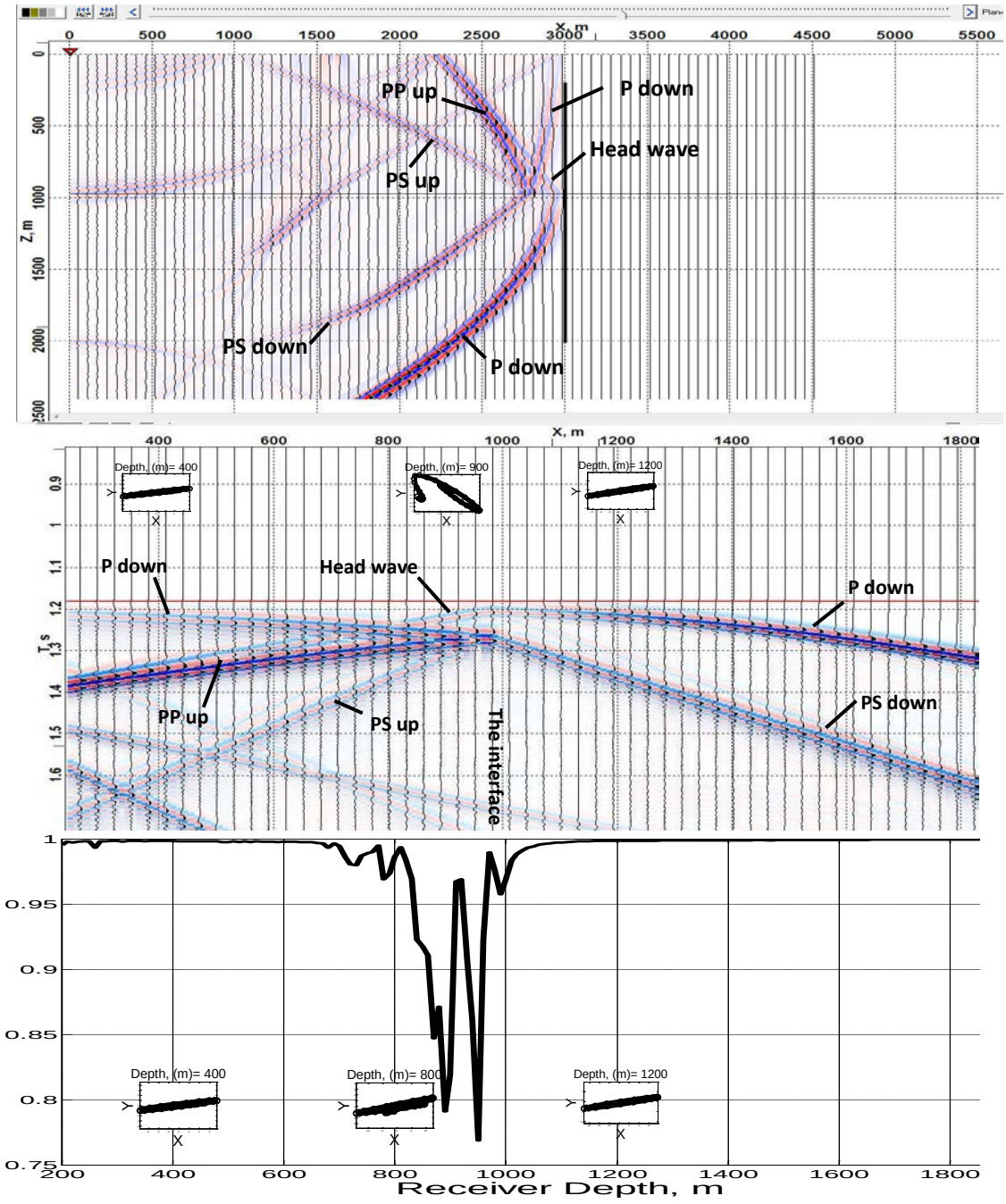

Figure 11 (top) illustrates a snapshot at time= 1.18 s of the vertical component of the particle velocity vector from the wavefield generated by source at offset =3000 m. Vertical component of the recorded wavefield is displayed in the middle. The linearity factor L and plots of particle motion hodograms at some selected receivers are shown in the bottom of the figure.

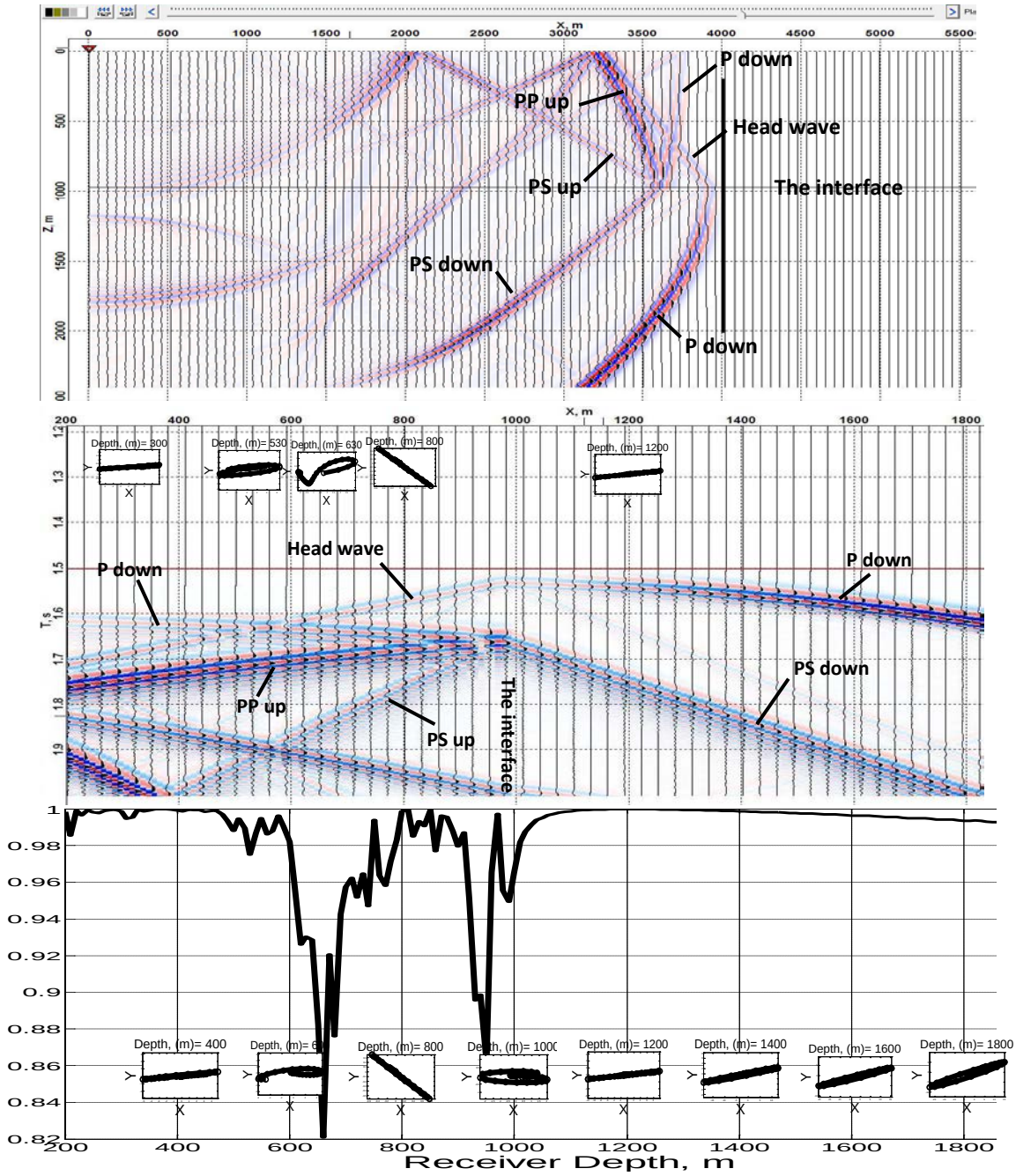

Figure 12 (top) illustrates a snapshot at time= 1.5 s of the vertical component of the particle velocity vector from the wavefield generated by source at offset =4000 m. Vertical component of the recorded wavefield is displayed in the middle. The linearity factor L and plots of particle motion hodograms at some selected receivers are shown in the bottom of the figure.

Now, let's use all the sources in the model (positioned on the surface at every 20 m interval) and estimate VTI anisotropy parameters by using slowness and polarization measurements. I will pick P-wave first arrival times in the receiver domain; however, this simple task becomes tedious in large offsets where head waves arrive first and interfere with P-wave. Figure 13 shows an example data recorded by the vertical component of the receiver positioned at depth 900 m. This depth was selected deliberately based on the data displayed in Figure 11 (offset=3000 m). At this depth, head waves arrive earlier than the P-waves generated by sources positioned at large offsets. In Figure 13, head waves are apparent beyond source offset = 5420 m in the form of a polarity change in the recorded wavefield.

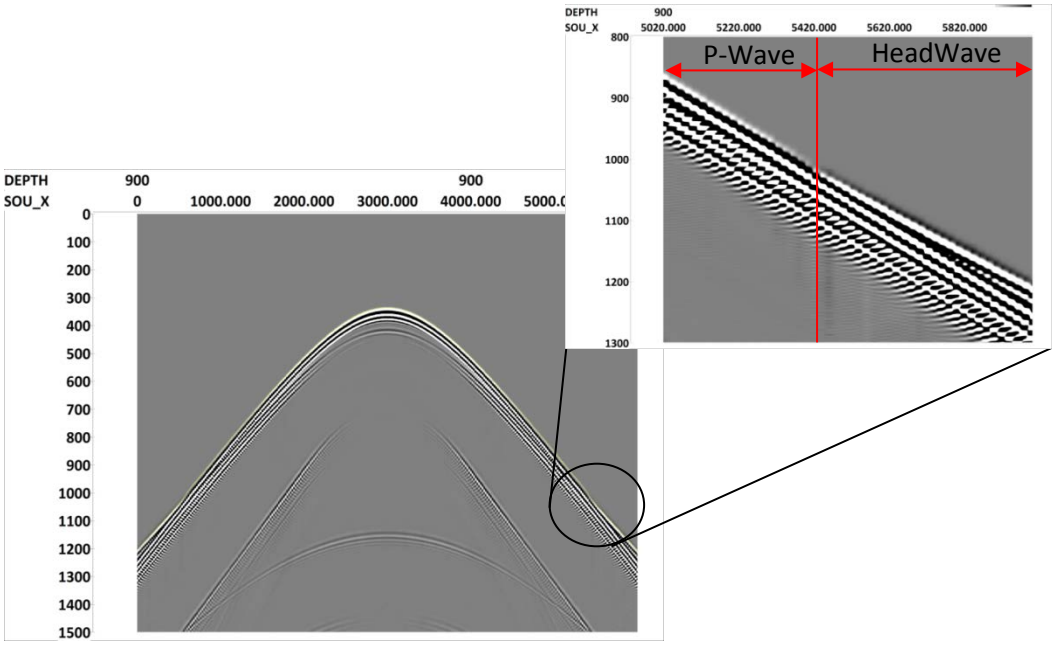

Figure 13, bottom, vertical component of the wavefield generated by all the sources in Figure 7 and recorded by the receiver located at depth=900 m. P-wave first arrivals are picked and displayed with yellow curve in this figure. Top right, is a display of data recorded from sources at large offsets (>5000 m) where head waves have preceded P-waves.

Figure 14 is an illustration of P-wave travel time field that is produced by picking first arrivals of the wave generated by all the sources and recorded by the receivers in the

borehole. P-wave phase angles are illustrated in Figure 15. To estimate propagation directions (phase angles) for plane P-waves in this model both the vertical and the horizontal components of the slowness vector are required. Summation of the plane waves propagating at phase angles shown in Figure 15 will represent the P-wave front in this model. Vertical component of the slowness vector is the derivative of the time field with respect to the distance in the vertical direction. Horizontal component of the slowness vector is the derivative of the time field with respect to the distance in the horizontal direction. Phase angle is then computed as the angle between P-wave slowness vector and the vertical direction. At the interface, P-wave phase angle shows abnormal values at offsets longer than 1300 m. As already discussed in Figure 11 and Figure 13, this is caused by the introduction of head waves that precede P-waves at this offset. Figure 16 shows the estimated dip angle which P-wave polarization vector makes with the vertical axis. P-wave polarizations too are influenced by the arrival of head waves at large offsets. Figure17 demonstrates the difference between the direction (dip) of P-wave polarization vector $\mathcal{V}$ and the slowness vector $\mathcal{O}$. The difference is zero at the shallow isotropic layer; but it increases up to 13 degrees in the deeper anisotropic layer.

Medium parameters of the deeper anisotropic layer ($\varepsilon = 0.2$, $\delta = -0.1$, $V_{P0} = 2600$ m/s and $V_{S0} = 1506$ m/s are very close to parameters defined in the example shown in Figure 6 of the Chapter 3. Figure 6 in Chapter 3 represents characteristics of P-wave propagation in a VTI medium with $\varepsilon = 0.3$, $\delta = -0.1$, $V_{P0} = 3000$ m/s and $V_{S0} = 1500$ m/s. These two examples can be representative of the anisotropy in sedimentary basins that is caused by the interbedding of thin isotropic layers: $0.1 \le \varepsilon \le 0.3$ and $-0.1 \le \delta \le 0$ (see the discussion in Section 3.5). Figure 6 of the Chapter 3 (top) demonstrates that the difference between polarization vector (red dots showing polarization dip) and the slowness vector (black dot-dash) is very small up to around 27^o propagation (from vertical) in this medium. This character can also be observed by making a comparison between data displayed in both Figures 15 and 16. Figure 17 demonstrates that the difference between the slowness vector and the polarization vector remains small up to around 30^o (area restricted by the trapezoid copied from Figure 15).

Equation 25 of the Chapter 3 can be used (in weak anisotropy limits) to find the direction of what I call *polarization isotropy*, $\theta_{Pol-Iso}$ in a VTI media in which P-wave polarization direction is oriented along the propagation direction:

$$\theta_{Pol-Iso} = sin^{-1} \pm \sqrt{\left(\frac{\delta}{2(\delta - \varepsilon)} \right)} \qquad (8)$$

On the other hand, this is not characteristic of P-wave anisotropy caused by shale formations (see example in Figure 5 of the Chapter 3).

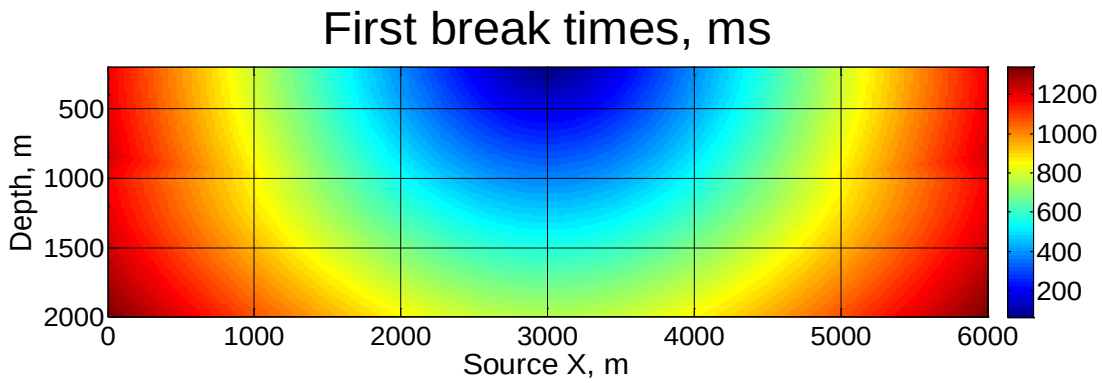

Figure 14, first arrival times of the P-wave generated by all the sources in Figure 7 and recorded by all the receivers in the borehole.

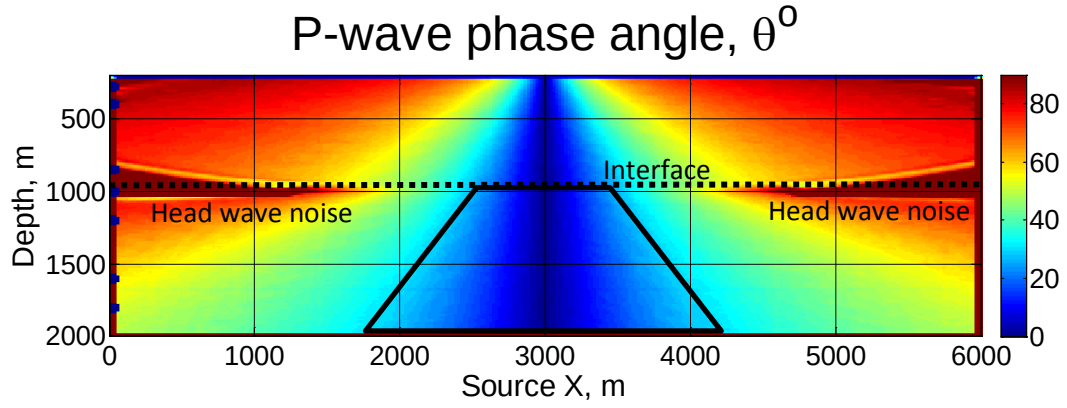

Figure 15, P-wave phase angles as a function of source offset and receiver depth for the model displayed in Figure 7. Notice the noise caused by head wave interference near the interface. Phase angles lower than 30^o is restricted within the trapezoid.

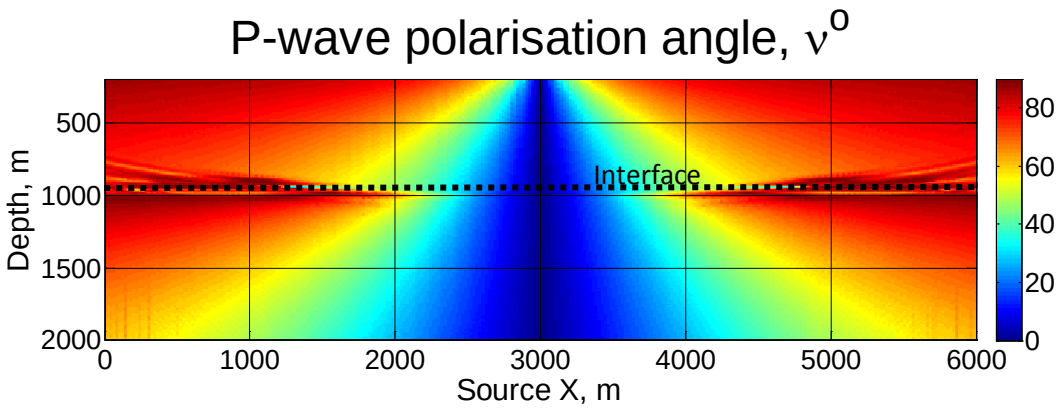

Figure 16, P-wave polarization dip angles as a function of source offset and receiver depth for the model displayed in Figure 7. Head wave interference effect introduce noise in polarization measurements near the interface.

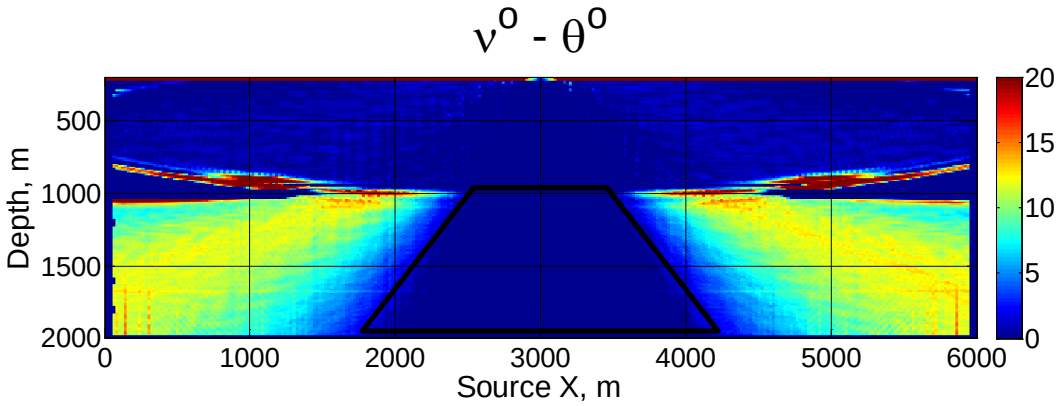

Figure 17, difference between P-wave polarization dip and phase angle as a function of source offset and receiver depth for the model displayed in Figure 7. The deviation is small for propagation angles up to 30^o but increases up to 13^o for larger phase angles.

To invert slowness and polarization measurements to VTI anisotropy parameters used in the model, I will use the exact VTI relationship (Equations 2 to 4) introduced in Section 5.4 of this chapter. In the inversion algorithm, I will minimize the objective function for the stiffnesses c_{11} and c_{13}. The other two stiffnesses; c_{33} and c_{55} are usually regarded as known parameters that can be obtained from velocity log measurements in the borehole.

Figure 11 and Figure 12, show two examples where the linearity function can still acquire large values in the zone where head waves are the first arrivals. If the linearity function is used as data selection criterion in the inversion algorithm, head wave polarization information will be misinterpreted as down going P-wave in the inversion algorithm. However, this shouldn't be a problem if corresponding head wave slownesses is incorporated into the inversion.

The observations made in Section 5.4 clearly indicate that the accuracy of the slowness-polarization method is largely dependent on the accuracy of the polarization measurements and is not much improved by increasing the range of P-wave propagation angles. Therefore, I will sacrifice a small improvement in the accuracy of parameter estimation (caused by the inclusion of large offsets) to gain a large improvement in polarization measurements and in the inversion results by restricting the phase angles to less than the critical angle. Below the critical angle, main source of polarization noise no longer exists as head waves are excluded from the measurements.

Figures 18 and 19 show two examples of synthetic slowness-polarization data (black dots) which are selected for the inversion at the vicinity of the interface. Figure 18 shows the data recorded by the receiver located at depth = 900 m and inside the isotropic layer. Figure 19 shows the data recorded by the receiver at depth=1100 m inside the anisotropic layer. Black curve is the best fit function to the data which derives δ_{est} and ε_{est} by minimizing the objective function described in Section 5.4. Data displayed by green dots are the slownesses and corresponding polarization dips which are computed numerically by solving Christoffel equation using elastic properties taken from the two layer model. This is to control the accuracy of the slowness and polarization measurements derived from synthetic data. The green curve (overlapped by red curve here) shows the exact VTI slowness-polarization relationship (Equations 2 to 4) introduced in Section 5.4. Obviously, green curve fits perfectly the green dots and both can be used as a measure of the reliability of the measurements. Red curve is Grechka and Mateeva (2007) approximation presented as Equation 1 in Section 5.3.

At the interface level (depth=965 m), the head waves will precede the P-waves for the sources beyond the critical offset ($Offset_{Critical} = 1292\ m$) and will be recorded first by the receivers in the borehole (apparent on Figure 15, 16 and 17). To avoid the head wave interferences at this depth, only P-waves propagating below the critical angle ($\theta_{Critical} = 53.25^{o}$) should be allowed into the inversion algorithm. At other depths, however, P-wave phase angles can be increased a little further based on the information displayed in Figure 15 and 16. In both Figures 18 and 19, polarization dip angle has been increased to around 60^{o} as the noise caused by head wave appears at larger offsets than the critical offset of the interface. This is also evident from the quality of the fit at large polarization angles in both Figures 18 and 19.

Figure 20 shows the inversion results using exact Equations 2 to 4 and slowness and polarization data which correspond to P-wave propagation angles below the critical angle at the interface level. In this example, P-wave vertical component of the slowness vector has been computed by differentiating first arrival times with respect to geophone depth in the borehole. At each level, the gradient was calculated within a window of 7 consecutive receivers (window length=60 m). Vertical and horizontal trace recordings within a 60 ms window (starting at FBPICK) have been used to compute P-wave polarization vector and the corresponding dip (Figure 16). I first convert particle velocities measured by the receivers to particle displacements by cumulative sum of the sample values. Then, I fit a line in $[x,\ y,\ z]$ space (a least square solution) to displacement points measured in the window. Finally, I calculate the angle between this line and the vertical axis Z. Elastic stiffnesses c_{33} and c_{55} have been calculated from V_{P0} and V_{S0} at each depth, respectively. The objective function (described in Section 5.4) has been minimized by MATLAB's *fminsearch* for c_{11} and c_{13}.

A careful look at the results of the inversion in Figure 20 shows that both the ε and δ values have been underestimated in this example. However, inversion has managed to estimate VTI anisotropy parameters ε_{est} and δ_{est} that are within the same order of magnitude as the parameter itself. In this example, I restricted the phase angles to less

than the medium's critical angle to avoid incorporating head waves and their destructive effect on polarization measurements.

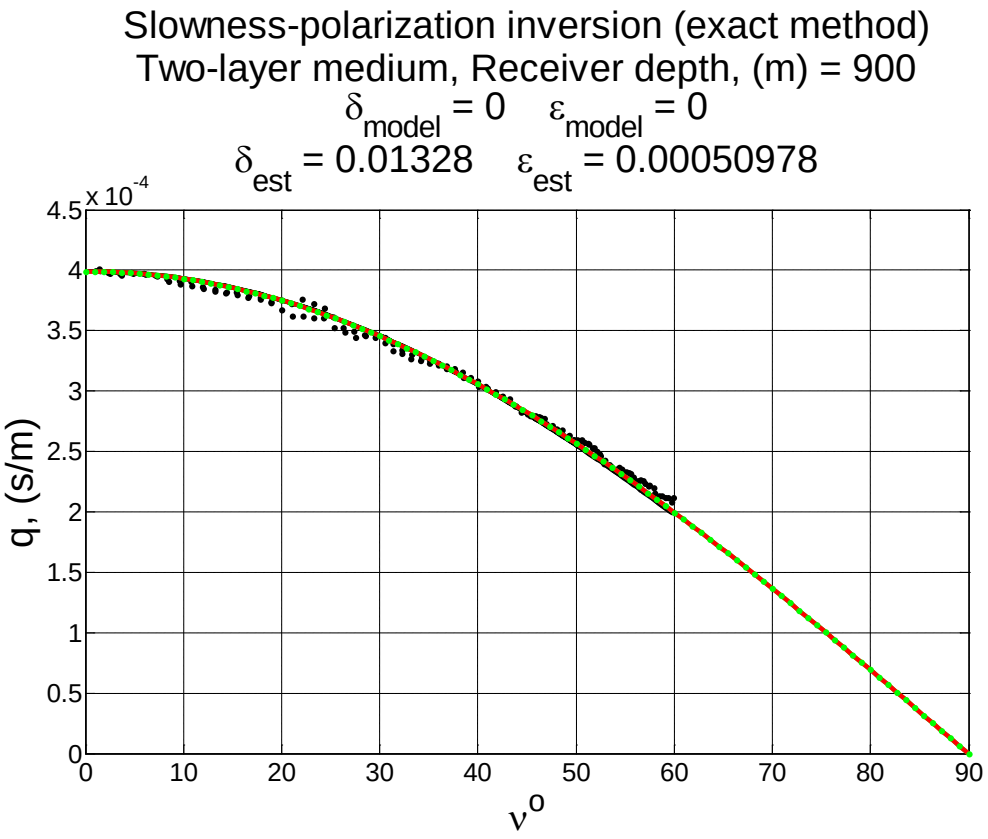

Figures 18, synthetic slowness-polarization data (black dots) selected for the inversion at depths=900 m. Black curve, is the best fit function to the data. Green dots are the slowness and polarization data which are generated by the application of Christoffell equation with elastic properties taken from the first layer in the model. The green curve (overlapped by red curve here) is the same data derived by using exact VTI slowness-polarization relationship (Equations 2 to 4). Red curve is Grechka and Mateeva (2007) approximation.

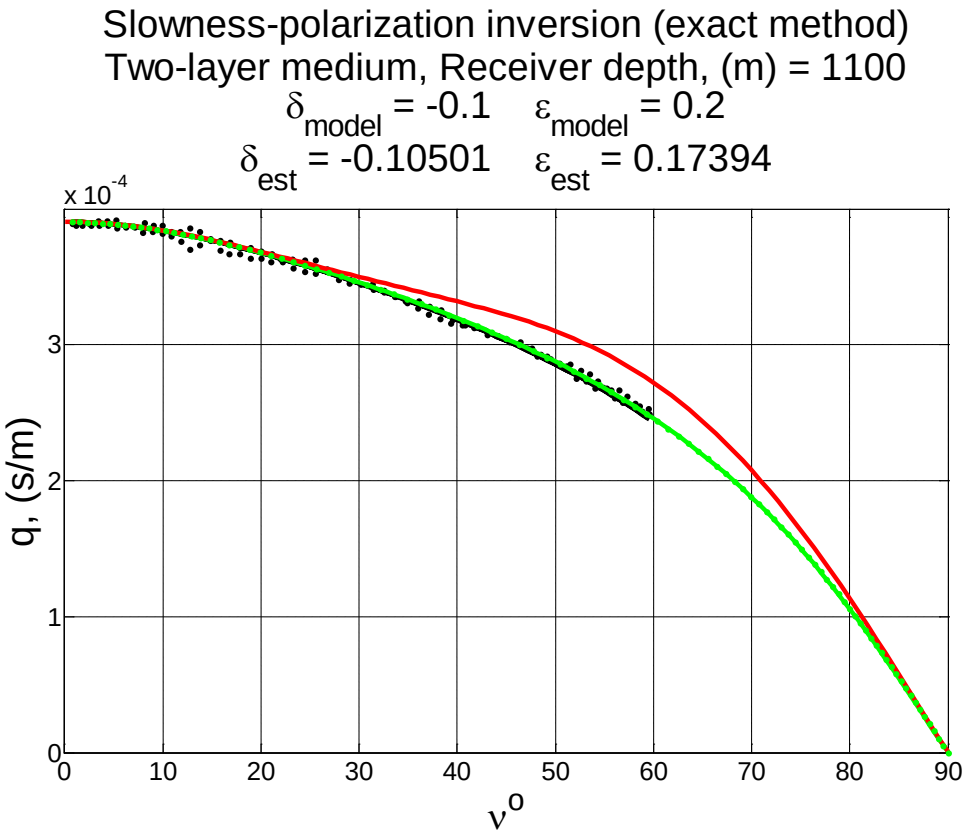

Figures 19, synthetic slowness-polarization data (black dots) selected for the inversion at depths=1100 m. Black curve, is the best fit function to the data. Green dots are the slowness and polarization data which are generated by the application of Christoffell equation with elastic properties taken from the second layer in the model. The green curve is the same data derived by using exact VTI slowness-polarization relationship (Equations 2 to 4). Red curve is Grechka and Mateeva (2007) approximation.

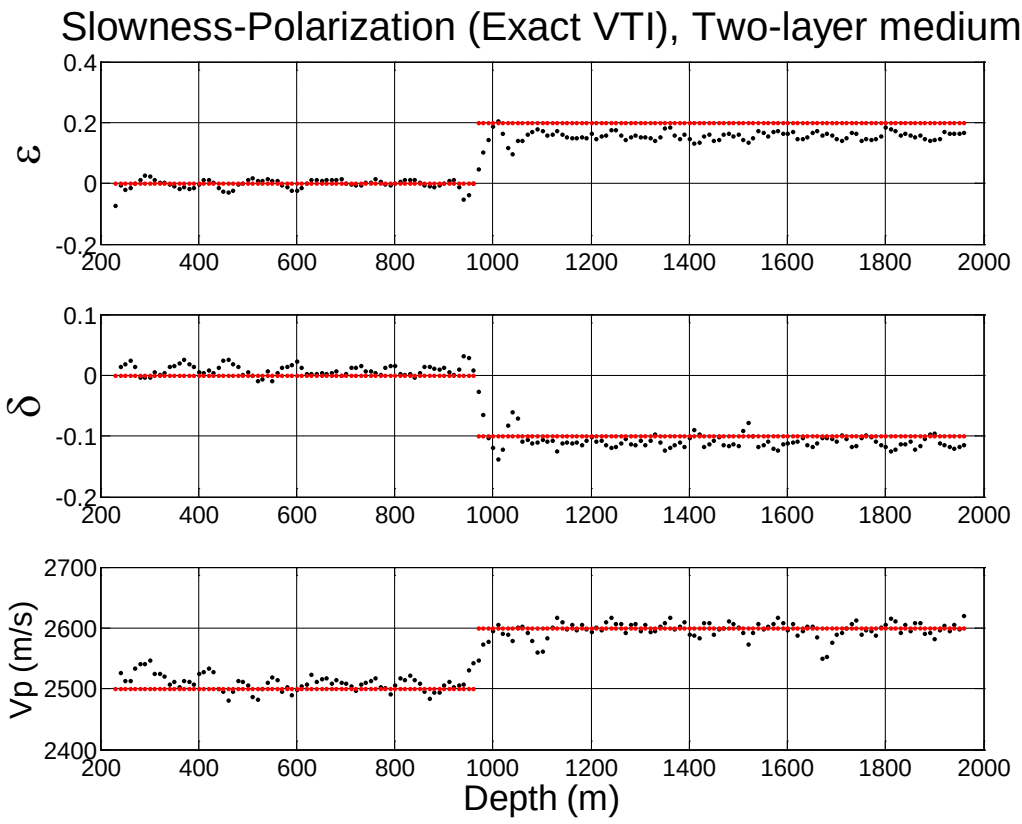

Figures 20, the results of VTI inversion using exact slowness-polarization relationship for the data acquired in two-layer model shown in Figure 7.

5.6 VTI parameter estimation, well CRC-1 synthetic walkaway VSP

In Section 4.6, a 2D anisotropic velocity model that represents the earth subsurface at the location of well CRC-1, Naylor field was presented. Model parameters are given in Table 1 of Chapter 4. In this model, VTI anisotropy starts from the forth layer and is represented by constant Thomsen (1986) parameters $\varepsilon = 0.08$ and $\delta = -0.14$ (taken from other studies in the area). Synthetic walkaway VSP consists of 150 sources on either sides of the borehole and spreads symmetrically over 3 km offset with 20 m source spacing. Three component receivers start from the surface with 10 m spacing and continue to 2000 m.

Figure 21 shows P-wave polarization dips (with vertical axis), ν derived from the synthetic walkaway VSP data of the CRC-1 2D model with source offsets less than 2000

m and for the receivers positions from 200 to 2000 m in the borehole. In this case, a 40 ms window delayed by 10 ms relative to P-wave first arrivals was used to extract P-wave particle velocity as a function of time. Then I converted particle velocities to particle displacements by cumulative sum of the sample values. Finally, I generated polarization vectors by fitting a straight line in $[x,\ y,\ z]$ space (a least square solution) to displacement points measured in the window.

Similar to the slowness only method in Section 4.6, data from sources with more than 2000 m offset have been disregarded in order to alleviate headwave's destructive effect on polarization measurements that appear for large source distances to well head. Figure 14 of Chapter 4 showed how P-wave slowness measurements (and hence phase angles) can be influenced by the destructive effect of headwaves that are generated in the shallow intervals from sources at large offset. The effect of headwaves on P-wave polarization measurements in the form of larger dip values leaking lateraly into the smaller polarization zone is evident for the receiver depths 600 and 1000 m in Figure 21. In the deeper intervals below 1000 m, subtle polarization leakage noise is still observed as denoted in Figure 21. Plorarization leakage will decrease the accuracy of VTI parameter estimation based on slowness-polarization methods by reducing the range of polarization dips that can be used in the inversion.

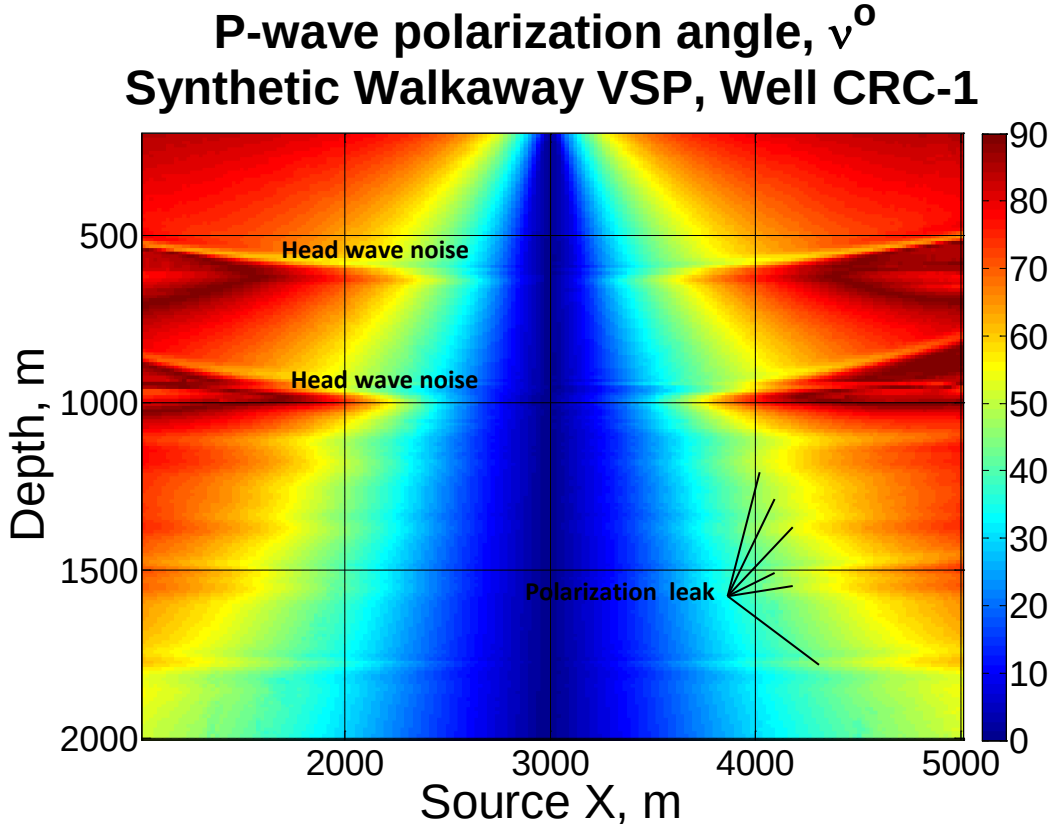

Figures 21, P-wave polarization dip, ν computed from 3C receiver measurements of the synthetic VSP acquired on CRC-1 model.

Figure 22 shows the result of the inversion using slowness-polarization data derived from the synthetic walkaway VSP at well CRC-1 (Figure 21) and using the exact relationship given by Equations 2-4. Figure 22, top is a comparison between the inverted ε (black dots) and ε values in model (red dots) plotted with respect to depth. Figure 22, bottom shows the δ estimations (black dots) versus δ values in the model (red dots). In this inversion, I have minimized a least square objective function for the stiffnesses c_{11} and c_{13} and the other two stiffnesses c_{33} and c_{55} are taken directly from layer velocities in the model. The results shown in Figure 22 have been estimated by incorporating P-wave polarization dip angles ν of up to 70^o in the inversion. This will have no effect on the inversion for deeper intervals in the model (1800-2000 m) where there are no ν values larger than 50^o in the data. Including large range of input data in the analysis will assist in stabilizing the inversion for the shallower intervals. However,

this will have destructive effect on the accuracy of parameter estimation for the intervals where headwaves are introduced. As an example, both the δ and ε estimations have been negatively influenced by the introduction of headwave noise on polarization measurements for the interval between 500 and 1000 m (see also Figure 21). Based on the inversion results shown in Figure 22, Slowness-polarization inversion using exact Equations 2-4 has been able to fairly accurately recover VTI parameters of the well CRC-1 2D model in the deep intervals (1000 to 1700 m).

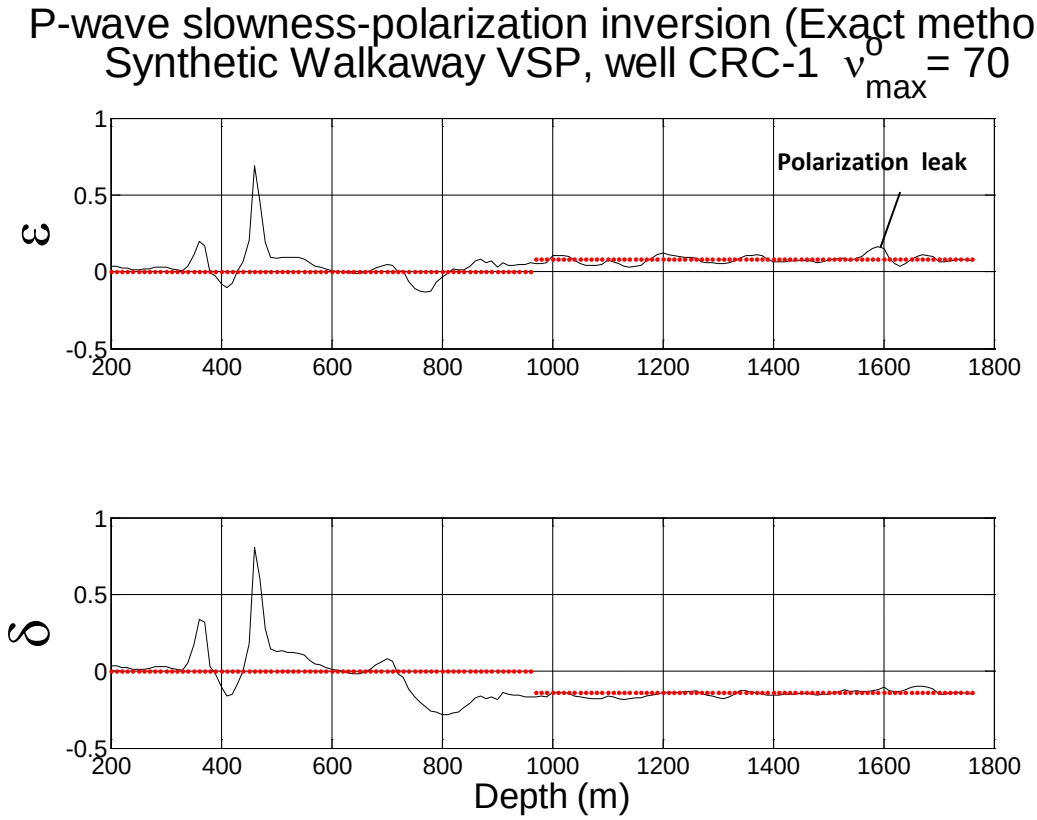

Figure 22, results of the inversion using slowness-polarization data derived from the synthetic walkaway VSP at well CRC-1 and using exact relationship given by Equations 2-4.

5.7 Remarks and conclusion

Slowness-polarization method can be theoretically used to estimate VTI anisotropy parameters in places with complex subsurface structure where horizontal component of the slowness vector cannot be transferred to the receiver location because of lateral heterogeneity. However, both the measurements of P and SV-wave (separated from SH-waves) are required for a unique VTI parameter estimation which is hardly obtained without independent measurements of geophone azimuth in the borehole.

Slowness-polarization method can be restricted to only P-wave measurements to increase the accuracy of the method by removing the shear wave measurements. However, the ratio of the vertical velocities V_{P0}/V_{S0} has to be known to resolve δ and ε parameters. This ratio can be derived from the borehole velocity measurements.

Grechka and Mateeva (2007) relationship is valid only in a small range of medium anisotropy and cannot be used to estimate large VTI parameters. Increasing the range of P-wave propagation angles has little effect on the inversion results.

The exact slowness-polarization relationship (Equations 2 to 4) can be used to estimate any VTI anisotropy in the medium if accurate polarization measurements exist. This method is highly dependent on the accuracy of the polarization measurements and slightly on the range of wave propagation angles.

Accuracy of P-wave polarization measurements in the borehole rapidly deteriorates by the generation of head waves for large source offsets and slightly by wave interferences phenomenon due to the reflection and conversion to other wave types that exist in the vicinity of the elastic boundaries. As a result, restricting the wave propagation angles (related to source offset) to less than the critical angle of the medium will improve polarization measurements in a VSP survey.

VTI parameter estimation example presented at the end of this chapter shows that by restricting the phase angles to less than the critical angle in the medium ($\theta_{Critical} = 53.25^{o}$) we can increase the accuracy of the polarization measurements by avoiding head waves

and hence acquire reasonable accuracy in VTI parameter estimation using slowness-polarization method.

Slowness-polarization method based on the exact Equations 2-4 has been able to (within a reasonable accuracy) recover VTI anisotropy parameters ε and δ for the depth interval below 1000 m of the well CRC-1 2D model. To derive VTI parameters ε and δ, elastic parameters c_{11} and c_{13} have been minimized for in the inversion whereas c_{33} and c_{55} were taken directly from the model. This is based on the fact that P- and S-wave velocities in the vertical direction and density are usually measured separately in the borehole and can be used to obtain c_{33} and c_{55}. The accuracy in the inversion of VTI anisotropy parameters for the deeper interval is mainly because of the accuracy in P-wave polarization measurements that are not destroyed by the interference with other wave types for up to $\nu_{\max} = 70^o$. On the other hand, P-wave polarizations recorded at the shallower intervals contain significant interference noise caused by head wave interference with P-wave waves that are generated by sources at large offsets in the model. This has significantly decreased the accuracy of parameter inversion for shallow intervals by reducing $\nu_{\max}$ in the inversion to less than 50^o.

Chapter 6, Orthorhombic anisotropy parameter estimation, P-wave slownesses only

In the previous chapters, I have discussed the subject of VTI anisotropy parameter estimation using P-wave slowness and slowness-polarization methods. Uncertainties in VTI parameter estimation have been quantified and synthetic examples were presented. However, real earth in sedimentary basins is usually composed of dipping layers with embedded fractures which cause lower symmetries than simple TI anisotropy. Differential horizontal stress caused by the earth tectonic forces can also produce lower symmetries even in a layer-cake earth environment. Seismic velocity in such medium is a function of azimuth as well as wave propagation dip. Creation of a single set of vertical fractures in a VTI shale formation as a result of non-hydrostatic state of stress in the earth subsurface can decrease medium symmetry to orthorhombic and exhibit azimuthal variation of seismic velocities for the shale formation. Azimuthal variation of P-wave velocities in the overburden shale formation in Otway suggests the existence of lower symmetries in the medium and will be the focus of my analysis in this chapter. Orthorhombic anisotropy in Otway can be produced by a combination of shale intrinsic anisotropy (of VTI type) and a single set of vertical fractures oriented in the direction of maximum horizontal stress in the region. Shear wave splitting observed in well CRC-1 VSP recordings (see 1.4.2) has confirmed the presence of anisotropic stress field in the Otway basin. To analyse this case, I will first review the theory of effective anisotropic media caused by a system of vertical fractures imbedded in a VTI background followed by the analysis of uncertainty of orthorhombic anisotropy parameter estimation from P-wave slowness data. Next, I will use slowness measurements of a synthetic pseudo 3D VSP survey to estimate anisotropy parameters of an orthorhombic medium. Pseudo 3D VSP seismograms are generated by finite difference algorithms using 2D earth models that are oriented along several azimuthal directions and have layer geometry and velocities structure similar to the subsurface at well CRC-1. In the final stage, field data will be analysed where I will fit an orthorhombic model to the velocity data that are computed from slownesses measurements of well CRC-1 3D VSP survey in 2010.

6.1.Fracture induced anisotropy, HTI and Orthorhombic symmetries caused by fractures

As a result of the large scale of the forces that are acting in the earth subsurface, rock fractures usually occur in the form of sets (systems) with similar orientations (Macbeth, 2002). The intensity of fracturing is usually quantified by the fracture density that is counting the number of fractures for a unit distance and in the direction perpendicular to the fracture plane. Seismic wavelength is usually much larger than the fracture spacing and therefore, fractured rocks are modelled by effective anisotropic mediums. For example, a formation rock which contains only a single set of vertical fractures can be modelled by the simple HTI, if the background rock is isotropic (such as sandstones) and orthorhombic, if the background rock is VTI (such as shales). Medium symmetry will decrease if more sets of fractures are added to the background rock or dip of the existing fracture set varies.

Parameters of the effective anisotropic medium caused by fractures depend on the intensity and orientation of the fracture set(s) and the properties of the material filling the fractures, as well as on the elastic coefficient of the host rock. To obtain the parameters, Schoenberg (1980 and 1983) considers the fractures as either infinitely thin and highly complaint layers or planes of weakness with linear-slip boundary conditions where the two representations are equivalent in long wavelength limit. Bakulin et al. (2000 b and c), use this equivalence to derive the parameters of the effective anisotropic model caused by the fractures. They first use Backus (1962) averaging procedure for parallel thin layers embedded in an isotropic matrix to derive effective compliance matrix S:

$$S = S_b + S_f \qquad 01)$$

Where, S_b is the compliance matrix of the host rock and S_f is the excess compliance associated with the layers. Then, they prove that for vertical layers orthogonal to the x_1 axis, S_f is given by:

$$s_f = \varsigma \begin{bmatrix} s_{11f} & 0 & 0 & 0 & s_{15f} & s_{16f} \\ 0 & 0 & 0 & 0 & 0 & 0 \\ 0 & 0 & 0 & 0 & 0 & 0 \\ 0 & 0 & 0 & 0 & 0 & 0 \\ s_{15f} & 0 & 0 & 0 & s_{55f} & s_{56f} \\ s_{16f} & 0 & 0 & 0 & s_{56f} & s_{66f} \end{bmatrix} \qquad \textbf{02)}$$

where, ς is the fraction of the total volume occupied by the thin layers and s_{ijf} are the compliances of the layer's material. Bakulin et al. (2000 b and c) believe that the Equations 1-2 can also be used to describe a set of parallel fractures with the fracture normal **n** parallel to the x_1 axis.

Next, they treat the fractures as planes of weakness with non-welded boundary conditions and assume that (for the purpose of deriving the effective parameters) the medium containing these fractures is equivalent to the thin layer model. From there, the matrix of the excess fracture compliances is represented as the following:

$$s_f^{GN,x_1} = \begin{bmatrix} K_N & 0 & 0 & 0 & K_{NV} & K_{NH} \\ 0 & 0 & 0 & 0 & 0 & 0 \\ 0 & 0 & 0 & 0 & 0 & 0 \\ 0 & 0 & 0 & 0 & 0 & 0 \\ K_{NV} & 0 & 0 & 0 & K_V & K_{VH} \\ K_{NH} & 0 & 0 & 0 & K_{VH} & K_H \end{bmatrix} \qquad \textbf{(3)}$$

Where K_N is the normal fracture compliance relating the jump of the normal (to the fracture) displacement u_1 to the normal stress σ_{11}. K_V and K_H are the two shear compliances along the vertical (x_3) and horizontal (x_2) directions. The compliance K_{NV} is the coupling factor between the jump of the normal displacement u_1 and the shear stress σ_{13} or, equivalently, between u_3 and σ_{11}.

Schoenberg and Sayers (1995) derive the simplest form of the excess fracture compliance matrix (rotationally invariant) by assuming zero coupling between the slips along the coordinate directions and a purely isotropic microstructure of the fracture surfaces:

$$s_f^{RI,x_1} = \begin{bmatrix} K_N & 0 & 0 & 0 & 0 & 0 \\ 0 & 0 & 0 & 0 & 0 & 0 \\ 0 & 0 & 0 & 0 & 0 & 0 \\ 0 & 0 & 0 & 0 & 0 & 0 \\ 0 & 0 & 0 & 0 & K_T & 0 \\ 0 & 0 & 0 & 0 & 0 & K_T \end{bmatrix} \quad \textbf{(4)}$$

Where, $K_{NV} = K_{NH} = K_{VH} = 0$ and $K_V = K_H = K_T$ (Hsu and Schoenberg, 1993). K_N and K_T have the physical meaning of the normal and tangential compliances added by the fractures to the host rock.

Using Equations 1 and 4, Schoenberg and Helbig (1997) derive the resulting stiffness tensor (by inverting S) for an effective orthorhombic medium caused by a single system of vertical fractures embedded in a VTI background. If the fracture faces are perpendicular to the x_1 axis, the effective stiffness matrix **c** has the following form:

$$C_{ortho} = \begin{bmatrix} c_{11}(1-\delta_N) & c_{12}(1-\delta_N) & c_{13}(1-\delta_N) & 0 & 0 & 0 \\ c_{12}(1-\delta_N) & c_{11}(1-\delta_N \frac{c_{12}^2}{c_{11}^2}) & c_{13}(1-\delta_N \frac{c_{12}}{c_{11}}) & 0 & 0 & 0 \\ c_{13}(1-\delta_N) & c_{13}(1-\delta_N \frac{c_{12}}{c_{11}}) & c_{33}(1-\delta_N \frac{c_{13}^2}{c_{11}c_{33}}) & 0 & 0 & 0 \\ 0 & 0 & 0 & c_{44} & 0 & 0 \\ 0 & 0 & 0 & 0 & c_{44}(1-\delta_V) & 0 \\ 0 & 0 & 0 & 0 & 0 & c_{66}(1-\delta_H) \end{bmatrix}$$

05)

Where c_{ij} are the stiffness coefficients of the VTI background medium and $\delta_N = \frac{K_N c_{11}}{1+K_N c_{11}}$, $\delta_V = \frac{K_V c_{44}}{1+K_V c_{44}}$ and $\delta_H = \frac{K_H c_{66}}{1+K_H c_{66}}$ are the normal and tangential weaknesses that vary from 0 (no fracture) to 1(intensive fracturing).

Grechka and Tsvankin (2003), derive an exact expression for the most general fracture rheology (described by six independent excess fracture compliances, s_f^{GN,x_1}) of a

general arbitrarily oriented fracture set. In their representation shown in Figure 1, the fracture planes are orthogonal to the unit vector **n** defined by the azimuth α and dip β in the Cartesian coordinate frame $[x_1,\ x_2,\ x_3]$:

$$n = \{\cos\alpha\cos\beta, \sin\alpha\cos\beta, -\sin\beta\} \qquad \textbf{(6)}$$

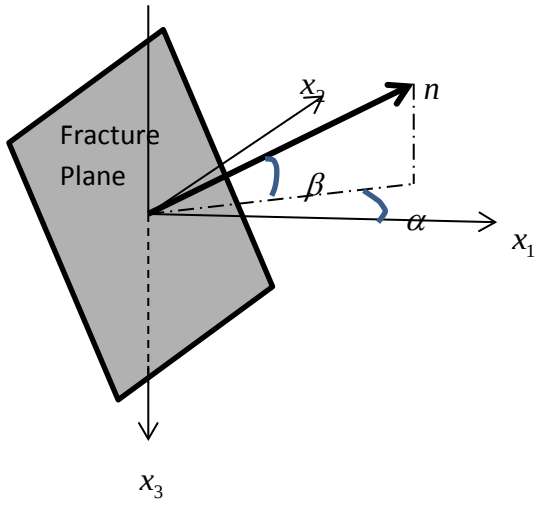

Figure 1, orientation of the most general fracture set is defined the azimuth α and dip β of the unit vector n that is orthogonal to the fracture plane.

To obtain S_f^{GN}, the compliance matrix S_f^{GN,x_1} is rotated in two steps: the rotation A^β by the angle β around the x_2 axis and another rotation A^α by the angle α around the x_3 axis:

$$A = A^\alpha A^\beta = \begin{bmatrix} \cos\alpha & -\sin\alpha & 0 \\ \sin\alpha & \cos\alpha & 0 \\ 0 & 0 & 1 \end{bmatrix} \begin{bmatrix} \cos\beta & 0 & \sin\beta \\ 0 & 1 & 0 \\ -\sin\beta & 0 & \cos\beta \end{bmatrix} \qquad \textbf{(7)}$$

The transformation of the compliance matrix S_f^{GN,x_1} is known as Bond transformation and has the form:

$$s_f = B\, s_f^{GN,x_1} B^T \qquad (8)$$

An explicit expression for the 6×6 matrix B in terms of the elements of matrix A is given in Winterstein (1990).

Based on linear-slip theory (Schoenberg, 1980, 1983; Nichols et al., 1989; Schoenberg and Muir, 1989; Schoenberg and Sayers, 1995), the effective compliance matrix **s** of a medium containing N sets of fractures is given by:

$$s = s_b + \sum_{i=1}^{N} s_f^{(i)} \qquad 09)$$

Where s_b and $s_f^{(i)}$ are the compliance matrices of the unfractured background and the ith fracture set, respectively. The effective stiffness matrix c is the inverse of the compliance matrix.

$$c = s^{-1} \qquad (10)$$

The equations presented constitute a foundation for the analysis of the uncertainties associated with orthorhombic anisotropy parameter estimation in the next part of this chapter.

6.2. Uncertainty of Orthorhombic anisotropy parameter estimation

In this part, I will quantify the uncertainties associated with the estimation of anisotropy parameters of an orthorhombic medium using numerical P-wave slownesses derived from Christoffel equation. Anisotropy parameters here are defined by Tsvankin (1997). For the purpose of this analysis, I will model the orthorhombic medium by inserting a single set of rotationally invariant fractures within a VTI medium as described in Section 6.1. Fractures are regarded as dry (filled with gas) and with fracture normal in the direction of x_1 axis. Intensity of the fracturing in the medium is defined by fracture weaknesses, δ_N as described in Section 6.1. I will increase δ_N from minor fracturing ($\delta_N = 0.1$) to moderately fractured ($\delta_N = 0.3$) and then to intensely fractured ($\delta_N = 0.5$) to study the effect of fracture intensity on orthorhombic parameter estimation. Background VTI medium is defined by parameters, $V_{P0} = 3000$ m/s, $V_{S0} = 1500$ m/s,

$\gamma = 0.1$, $\delta \in [-0.3,\ 0.6]$, $\varepsilon \in [-0.2,\ 0.6]$ and density $\rho = 2000$ kg/m^3. The resulting stiffness matrix is inserted into the Christoffel equation to compute numerical P-wave slownesses over a range of equi-sampled phase and azimuth angles. Phase aperture ($\theta \in [0,\ \theta_{\max}]$) and azimuth range ($\varphi \in [0,\ 360]$) is close to those used in a 3D VSP acquisition at the CO2CRC's Otway project. The objective here is to invert numerical data by using two inversion methods in order to arrive at the methodology of choice for this type of investigations. The first step is to analyse the case of weak anisotropy by utilizing the approximation for P-wave phase velocity in orthorhombic media as proposed by Tsvankin (1997). For this approximation we first need to define a range in which weak anisotropy formulation is valid. For this purpose, I will use the approximate relationship to invert *error-free* numerical data and plot the errors as a function of background anisotropy parameters (δ and $\mathcal{E}$) and the fracture weakness δ_N. Then, if there is a valid region for the approximation, I will introduce noise to assess the uncertainty of the inversion.

An alternative is to use the exact relationship for P-wave phase velocity in orthorhombic media (Equations 35-52 of Chapter 3) to invert numerical velocities (derived from slownesses) for orthorhombic anisotropy parameters. As this equation is exact, it is of exploration interest to simulate the case of P-wave slownesses being contaminated with various amount of noise and evaluate the performance of the inversion.

6.2.1. Anisotropy parameters of an orthorhombic medium generated by inserting fractures in a VTI medium

Figure 2 illustrates three scenarios to numerically model an orthorhombic medium by inserting a single set of vertical fractures in a VTI background. Fractures here are assumed to be rotationally invariant, dry and with fracture normals in the x_1 direction. Intensity of the fracturing in the medium is defined with fracture weaknesses as described in Section 6.1. In Figure 2, fracture intensity is minor in the left column ($\delta_N = 0.1$) and increases to moderately fractured in the middle column ($\delta_N = 0.3$) and intensely fractured medium in the right column ($\delta_N = 0.5$). Background VTI medium is represented by δ and ε values on horizontal and vertical axes, respectively.

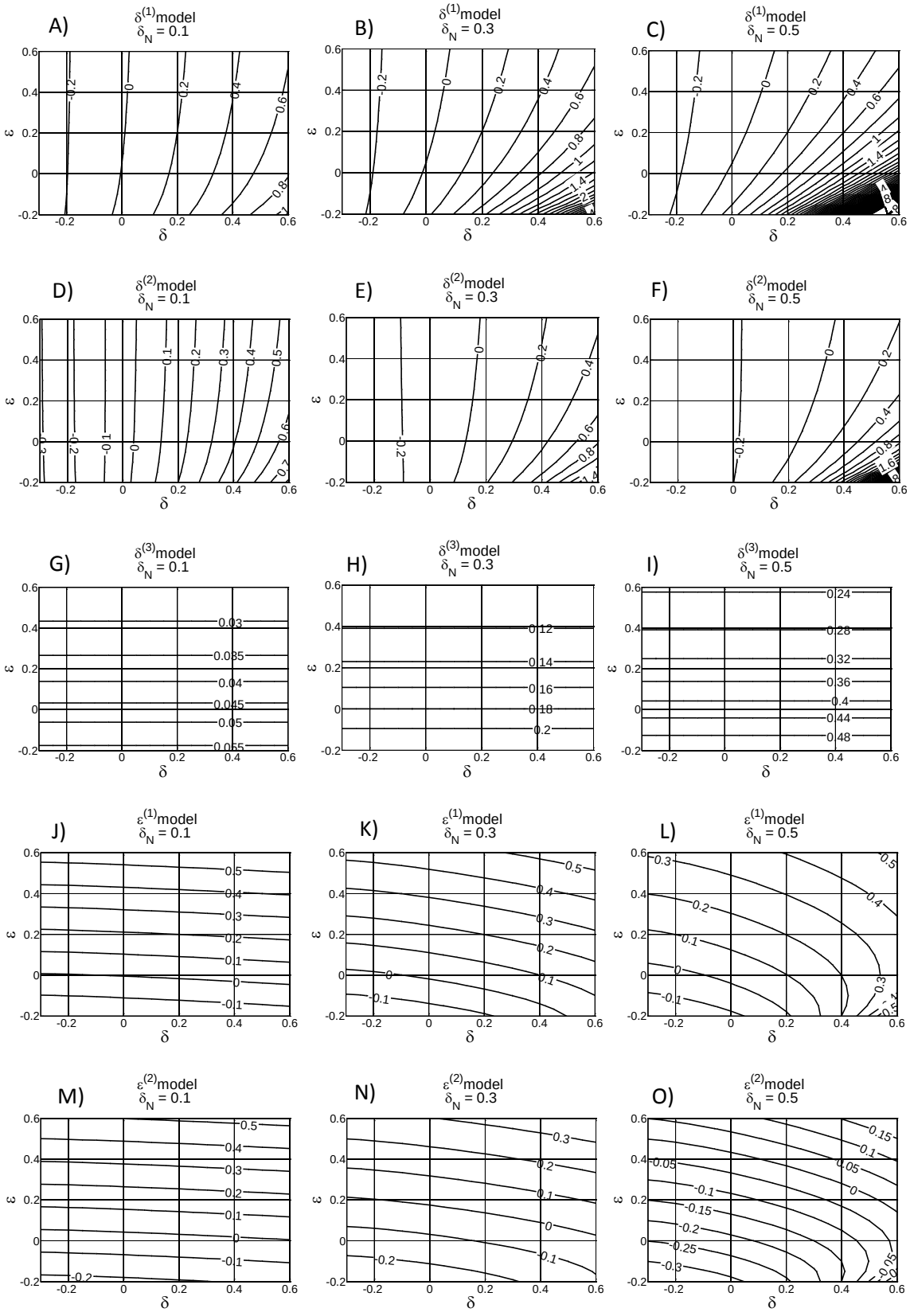
A)
$\delta^{(1)}$model
δ_N = 0.1
B)
$\delta^{(1)}$model
δ_N = 0.3
C)
$\delta^{(1)}$model
δ_N = 0.5
D)
$\delta^{(2)}$model
δ_N = 0.1
E)
$\delta^{(2)}$model
δ_N = 0.3
F)
$\delta^{(2)}$model
δ_N = 0.5
G)
$\delta^{(3)}$model
δ_N = 0.1
H)
$\delta^{(3)}$model
δ_N = 0.3
I)
$\delta^{(3)}$model
δ_N = 0.5
J)
$\varepsilon^{(1)}$model
δ_N = 0.1
K)
$\varepsilon^{(1)}$model
δ_N = 0.3
L)
$\varepsilon^{(1)}$model
δ_N = 0.5
M)
$\varepsilon^{(2)}$model
δ_N = 0.1
N)
$\varepsilon^{(2)}$model
δ_N = 0.3
O)
$\varepsilon^{(2)}$model
δ_N = 0.5
δ
ε

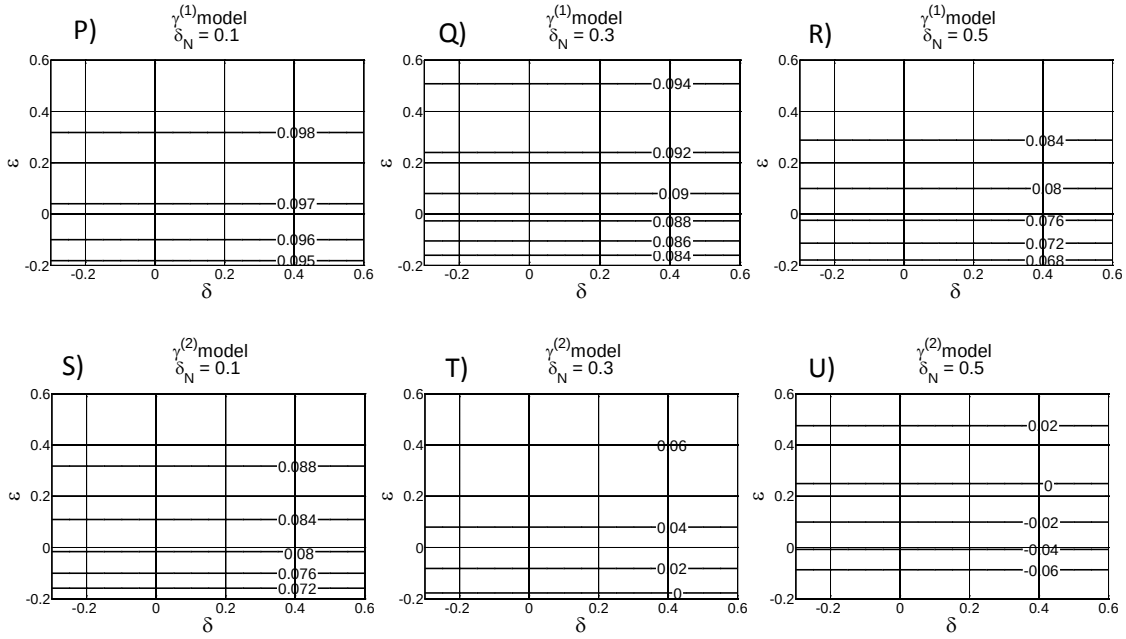

Figure 2, anisotropy parameters of the orthorhombic medium that is generated by inserting a single set of vertical fractures in a VTI background. Fractures are assumed to be rotationally invariant, filled with gas (dry) and oriented along x_2 direction. Intensity of the fracturing in the medium (defined with fracture weaknesses) is minor in the left column ($\delta_N = 0.1$) and increases to moderately fractured in the middle column ($\delta_N = 0.3$) and intensely fractured in the right column ($\delta_N = 0.5$). Background VTI medium is represented by δ and ε values on horizontal and vertical axes, respectively.

In Figure 2, for anisotropy parameters defined in the fracture plane, $[x_2,\ x_3]$ when fracturing is minor ($\delta_N = 0.1$) value of the anisotropy parameter $\delta^{(1)}$ is close to δ only for $\delta \le 0.2$ (A). As fracturing intensifies (B and C), the difference between $\delta^{(1)}$ and δ increases significantly. Anisotropy parameter $\varepsilon^{(1)}$ is always close to ε for $\delta_N = 0.1$ (J), but deviates as fracturing intensifies (K and L). Similarly, the difference between $\gamma^{(1)}$ in the fracture plane and γ is small for $\delta_N = 0.1$ (P) but increases with fracturing (Q and R). For anisotropy parameters defined in the plane perpendicular to the fracture plane $[x_1,\ x_3]$, similar to $\delta^{(1)}$, $\delta^{(2)}$ is close to δ only for minor fracturing $\delta_N = 0.1$ and

$\delta \le 0.2$ (D) and deviates significantly with fracturing (E and F). For minor fracturing $\delta_N = 0.1$, in contrast to $\varepsilon^{(1)}$, $\varepsilon^{(2)}$ is close to ε only for $\varepsilon \le 0.2$ (M). When fracturing intensifies (N and O), the difference between $\varepsilon^{(2)}$ and ε increases largely. The difference between $\gamma^{(2)}$ and γ is small for $\delta_N = 0.1$ (S), but increases as fracturing intensifies (T and U).

6.2.2. Inversion using approximate phase velocity for P-wave in orthorhombic media

To find the range of parameters for which the approximate relationship is valid, the inversion was carried out on *noise-free* data. Valid range is the region of VTI parameters for the background medium and the fracture weakness where the inversion error becomes zero. To compute the errors of the inversion, estimated parameters ($\delta^{(1)}$, $\delta^{(2)}$, $\delta^{(3)}$, $\varepsilon^{(1)}$ and $\varepsilon^{(2)}$) are subtracted from the model values used to generate the data ($\delta^{(1)}_{model}$, $\delta^{(2)}_{model}$, $\delta^{(3)}_{model}$, $\varepsilon^{(1)}_{model}$ and $\varepsilon^{(2)}_{model}$). I will use Christoffel equation to compute numerical phase velocities for the orthorhombic model at every 1^o of the dip aperture, $\theta \in [0,80^o]$ and the azimuth range $\varphi \in [0,360]$.

The inversion error for estimating each orthorhombic parameter ($\delta^{(1)}$, $\delta^{(2)}$, $\delta^{(3)}$, $\varepsilon^{(1)}$ and $\varepsilon^{(2)}$) and the model parameters are displayed in Figures 3 and 4. The errors are plotted with respect to VTI anisotropy parameters of the background medium and the fracture weakness δ_N. To evaluate the effect of fracture intensity on orthorhombic parameter estimation using approximate relationship, inversion errors are computed for two cases, $\delta_N = 0.1$ (Figures 3) and $\delta_N = 0.3$ (Figures 4).

Figure 3, A and C display the errors related to the estimation of parameters $\delta^{(1)}$ and $\delta^{(2)}$ where fracture weakness $\delta_N = 0.1$. B and D display the same corresponding values in the orthorhombic model. Approximate relationship seems to have smallest inversion error in the region where fracturing has little effect on background VTI anisotropy ($\delta^{(1)} \approx \delta$ in B and $\delta^{(2)} \approx \delta$ in D).

Figure 3, E, G and I display the errors related to the estimation of parameters $\delta^{(3)}$, $\varepsilon^{(1)}$ and $\varepsilon^{(2)}$. The corresponding model values are displayed in F, H and J. The approximate relationship shows very small error in the entire range of VTI anisotropy of the background rock.

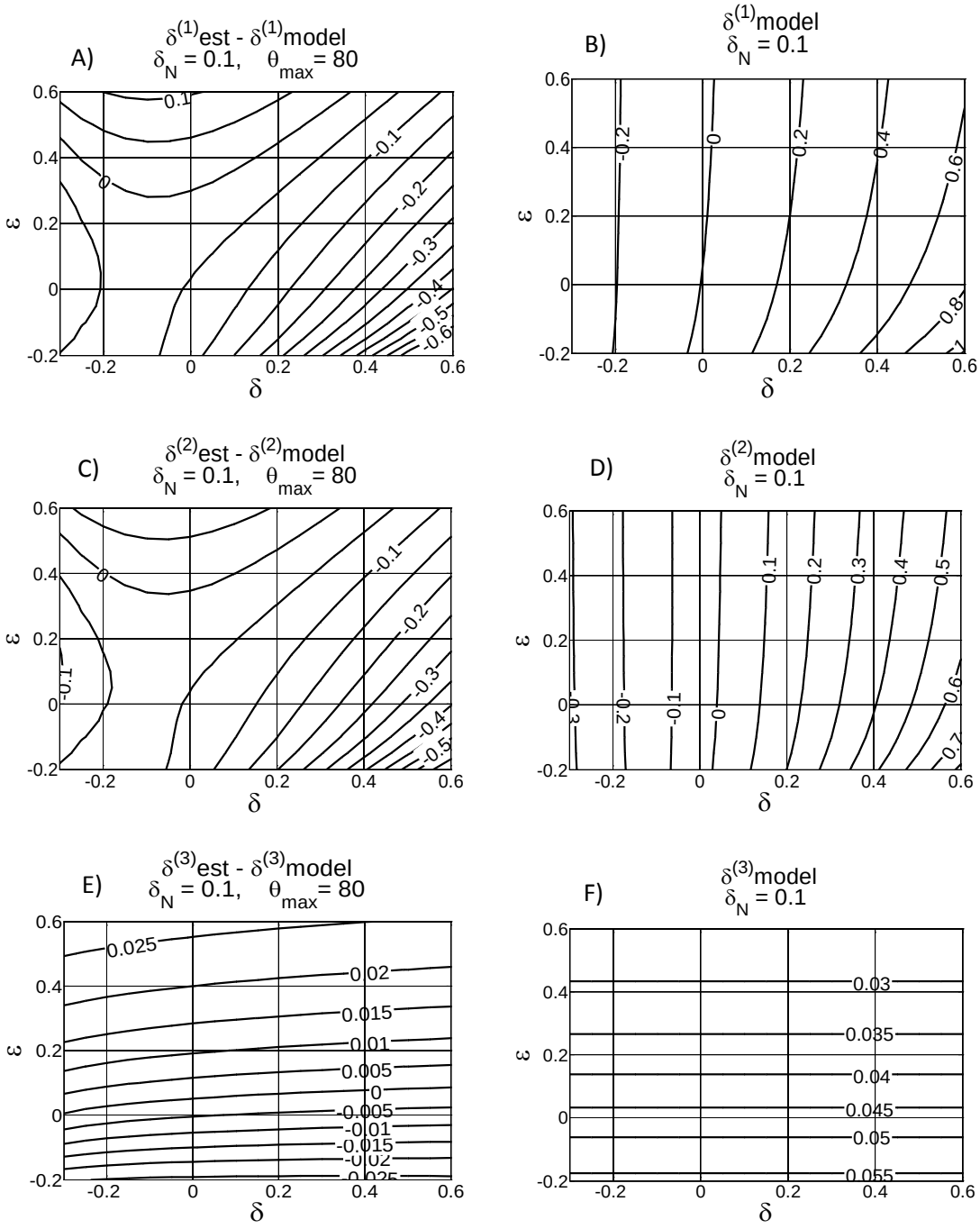

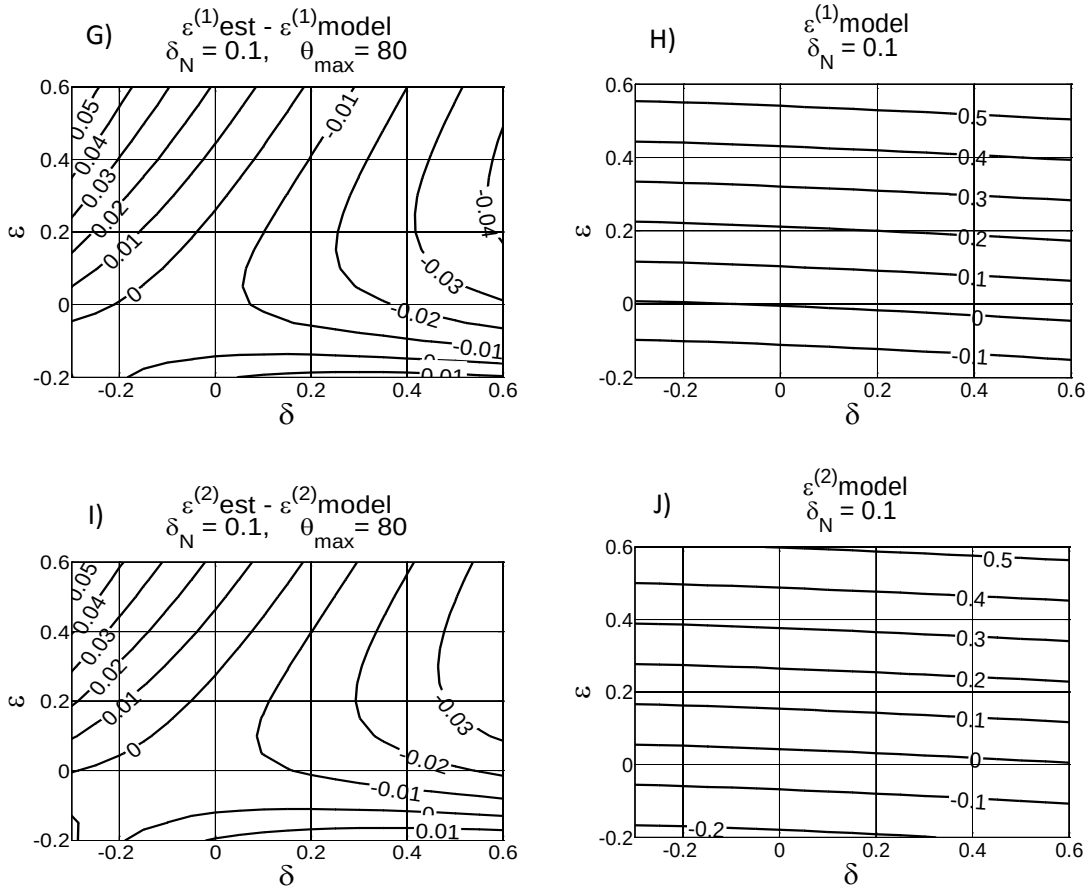

Figure 3, Estimation of the valid range for the approximate relationship of P-wave velocity in orthorhombic media. Numerical velocities are generated by using Christoffel equation. To estimate the validity of the approximation, no error is added to the velocities. Orthorhombic medium, described in the right side of the Figure, is created by inserting a single set of vertical fractures ($\delta_N = 0.1$) into a VTI background medium (ε and δ) where fractures are parallel to x_2 direction.

Figure 4, A and C display the errors related to the estimation of parameters $\delta^{(1)}$ and $\delta^{(2)}$ where fracture weakness has increased to $\delta_N = 0.3$. B and D display again the corresponding values in the orthorhombic model. In this case, the effect of fracturing on background medium is significant and values for $\delta^{(1)}$ and $\delta^{(2)}$ can no longer be approximated with δ (B and D). As a result, the exact region in the inversion plot becomes very small in comparison with the case where $\delta_N = 0.1$ (compare A and C in Figures 4 and 3). Figure 4, E, G and I display the errors related to the estimation of

parameters $\delta^{(3)}$, $\varepsilon^{(1)}$ and $\varepsilon^{(2)}$. The corresponding model values are displayed in F, H and J. This time, in contrast to the case with $\delta_N = 0.1$, orthorhombic model parameters $\varepsilon^{(1)}$ and $\varepsilon^{(2)}$ are significantly different than the VTI parameter ε. However, $\varepsilon^{(1)}$ and $\varepsilon^{(2)}$ approximations represent very small error in the entire range of VTI anisotropy (G and I).

As a conclusion to this part, orthorhombic anisotropy parameter estimation using the approximate relationship is less reliable in estimating parameters $\delta^{(1)}$ and $\delta^{(2)}$ than estimating parameters $\delta^{(3)}$, $\varepsilon^{(1)}$ and $\varepsilon^{(2)}$. Estimation of parameters $\delta^{(1)}$ and $\delta^{(2)}$ using approximate relationship seems to be strongly influenced by the presence of the fractures. On the other hand, estimation of parameters $\delta^{(3)}$, $\varepsilon^{(1)}$ and $\varepsilon^{(2)}$ is less sensitive to the fractures in the medium. Because of the limited range of accuracy in this method for estimating $\delta^{(1)}$ and $\delta^{(2)}$, I will not carry out any further error analysis.

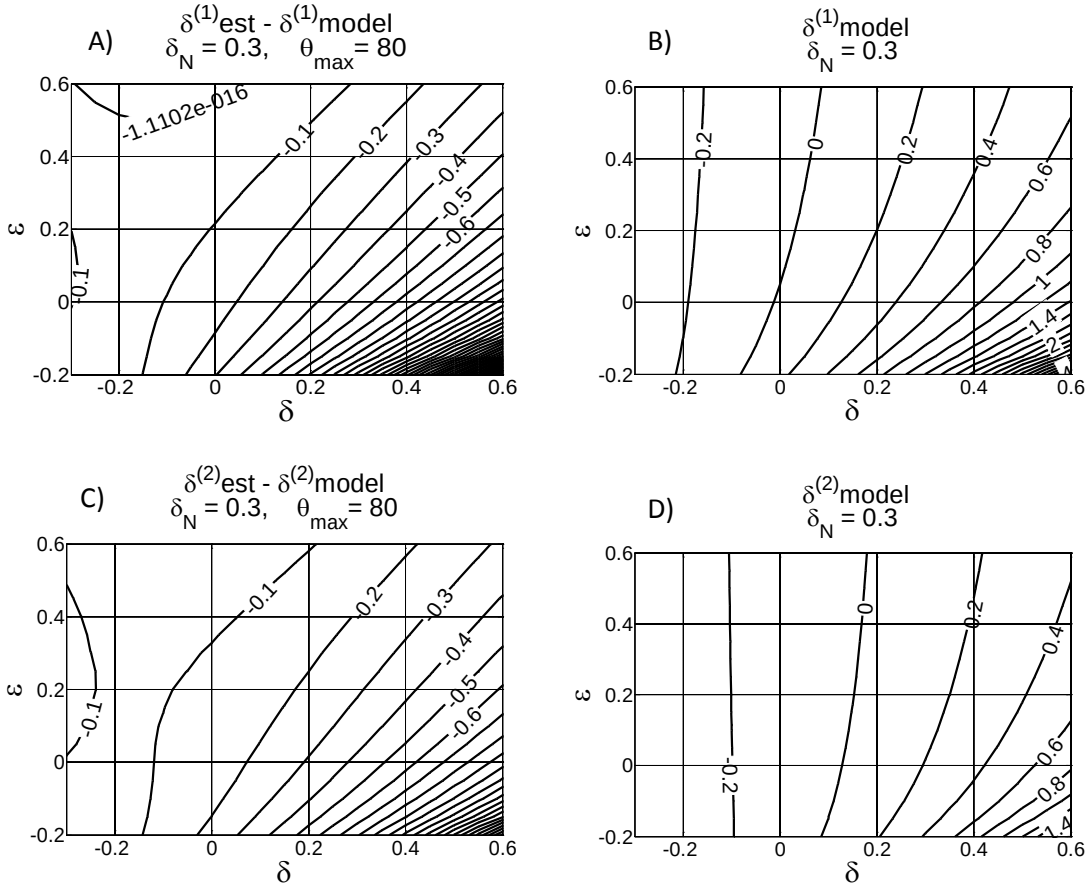

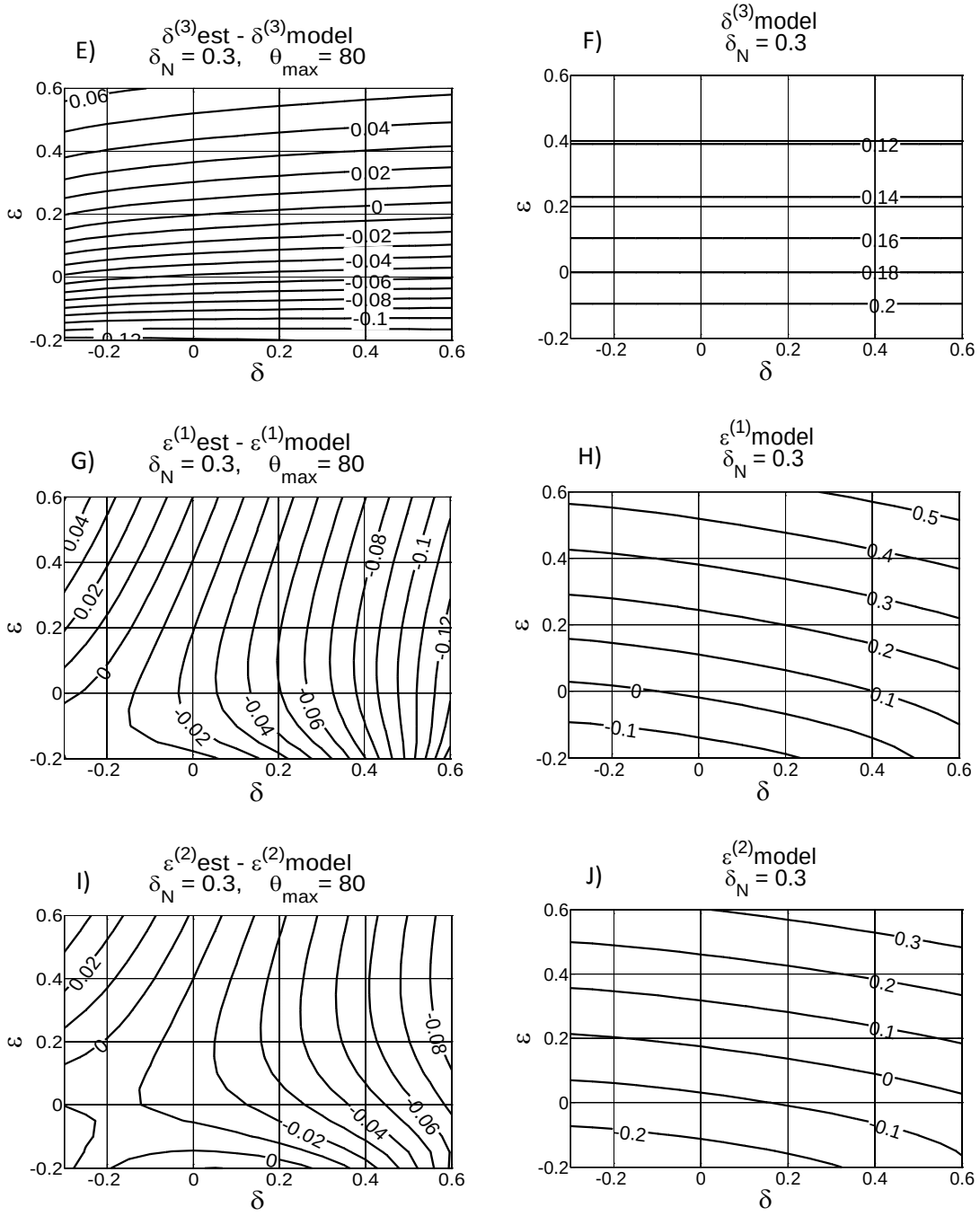

Figure 4, estimation of the valid range for the approximate relationship of P-wave velocity in orthorhombic media. Numerical velocities are generated by using Christoffel equation. To estimate the validity of the approximation, no error is added to the velocities. Orthorhombic medium, described in the right side of the Figure, is created by inserting a single set of vertical fractures ($\delta_N = 0.3$) into a VTI background medium (ε and δ) where fractures are parallel to x_2 direction.

6.2.3. Inversion using exact phase velocity in Orthorhombic media

Exact phase velocity of P-waves in orthorhombic media was described in Chapter 3. In this part, I will use the exact relationship (Equations 35-52 of Chapter 3) to invert numerically computed P-wave phase velocities for anisotropy parameters $\delta^{(1)}$, $\delta^{(2)}$, $\delta^{(3)}$, $\varepsilon^{(1)}$ and $\varepsilon^{(2)}$ of an orthorhombic media. The orthorhombic medium is numerically modeled by inserting a system of vertical fractures (with fracture normal in the x_1 direction) into the same VTI medium as previous part (6.2.2). To evaluate the effect of fracture intensity on orthorhombic parameter estimation, I will compute fractures with three different fracture weaknesses, $\delta_N = 0.1$, $\delta_N = 0.3$ and $\delta_N = 0.5$. The resulting stiffness matrix is then inserted into the Christoffel equation to compute numerical slowness vectors (and phase velocities) for the phase aperture $\theta \in [0, \theta_{\max}]$ and azimuth range $\varphi \in [0,\ 360]$. For given layer geometry and receiver depth in the borehole, P-wave maximum propagation angle, $\theta_{\max}$ is determined by the source offset at the surface. To measure the effect of source offset on orthorhombic parameter estimation, $\theta_{\max}$ starts from 80^o and decreases to 60^o, 46^o and 30^o. To decrease computational time and resemble more realistic 3D VSP field measurement, phase angles are computed at every 2^o steps and azimuth at every 10^o step. To assess the efficiency of the method in the presence of noise in the measurements, 1% error in the first example and 3% in the second example are added to the P-wave slowness vector. Errors are normally distributed random vectors with relative standard variation of 1% (see 3.14). Using numerical data contaminated with noise, I invert the data for anisotropy parameters. The estimated values ($\delta_{est}^{(i)}$, $\varepsilon_{est}^{(j)}$, $i = 1,\ 2,\ 3$ and $j = 1,\ 2$) are subtracted from the model values ($\delta_{model}^{(i)}$, $\varepsilon_{model}^{(j)}$, $i = 1,\ 2,\ 3$ and $j = 1,\ 2$) to calculate the errors ($\delta_{est}^{(i)} - \delta_{model}^{(i)}$, $i = 1,\ 2,\ 3$ and $\varepsilon_{est}^{(j)} - \varepsilon_{model}^{(j)}$, $j = 1,\ 2$). As random noises are added to the data, the inversion is repeated 100 times to generate a distribution function for the estimated value. The mean value of this distribution is regarded as the error in the estimation.

The errors are related to the estimation of each parameter as a function of VTI parameters in the background medium (horizontal and vertical axes), fracture weakness

and maximum P-wave propagation angle $\theta_{\max}$. To highlight the area with reliable inversion, errors are color coded within ±5%.

6.2.3.1 Example 1: slowness vectors contaminated with 1% random noise.

Figures 5 to 9 show the errors related to the estimation of anisotropy parameter $\delta^{(1)}$, $\delta^{(2)}$, $\delta^{(3)}$, $\varepsilon^{(1)}$ and $\varepsilon^{(2)}$ when only 1% random noise has been added to the slowness vectors. In these figures, $\theta_{\max}$ decreases from top to bottom (80^o, 60^o, 46^o and 30^o) and fracture weakness increases from left to right ($\delta_N = 0.1$, $\delta_N = 0.3$ and $\delta_N = 0.5$). Vertical and horizontal axes represent anisotropy parameters of the background VTI medium.

Figure 5 shows that the method is capable of estimating anisotropy parameter $\delta^{(1)}$ for the entire range of VTI anisotropy and embedded fracture intensity if $\theta_{\max} \geq 60^o$. However, the method fails to recover $\delta^{(1)}$ for strong VTI medium ($\delta \geq 0.4$) if dip angle coverage reduces to $\theta_{\max} \leq 45^o$.

Figure 6 shows similar performance for estimating $\delta^{(2)}$ as with $\delta^{(1)}$ discussed in Figure 5. The method is able to estimate anisotropy parameter $\delta^{(2)}$ within the entire range of VTI anisotropy and embedded fracture intensity if $\theta_{\max} \geq 60^o$. However, the method fails to recover $\delta^{(2)}$ for strong VTI medium ($\delta \geq 0.4$) if dip angle coverage reduces to $\theta_{\max} \leq 45^o$.

Figure 7, displayes the errors related to the estimation of parameter $\delta^{(3)}$. The estimations are accurate only where $\theta_{\max} = 80^o$ and $\delta_N \leq 0.3$.

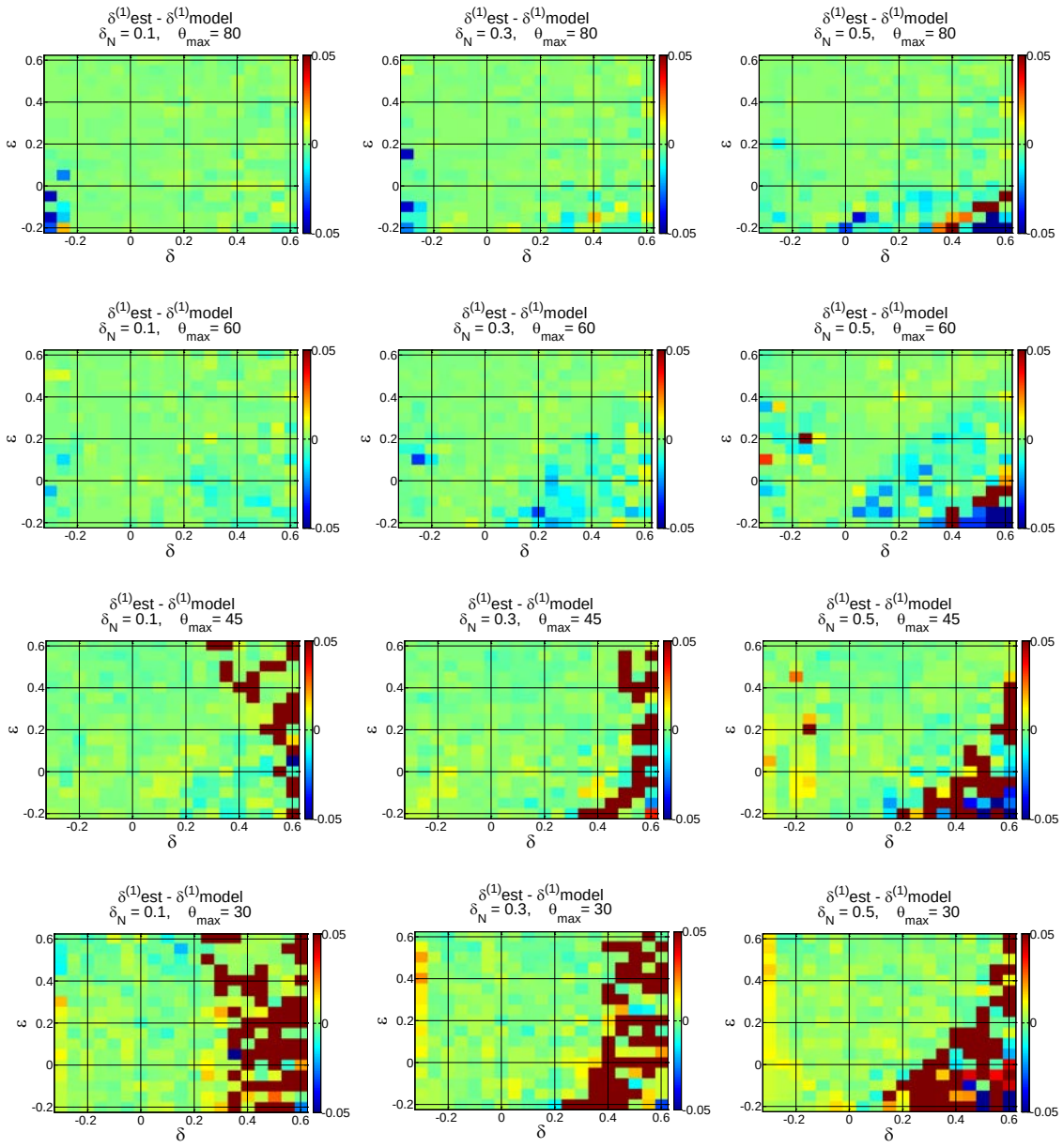

Figure 5, the errors related to the inversion of the exact velocity relationship in orthorhombic medium for the anisotropy parameter $\delta^{(1)}$ where 1% random noise has been added to the slowness vectors. $\theta_{\max}$ decreases from 80^o (top) to 30^o (bottom) and fracture weakness increases from left to right ($\delta_N = 0.1$, $\delta_N = 0.3$ and $\delta_N = 0.5$). Vertical and horizontal axes represent anisotropy parameters of the background VTI medium.

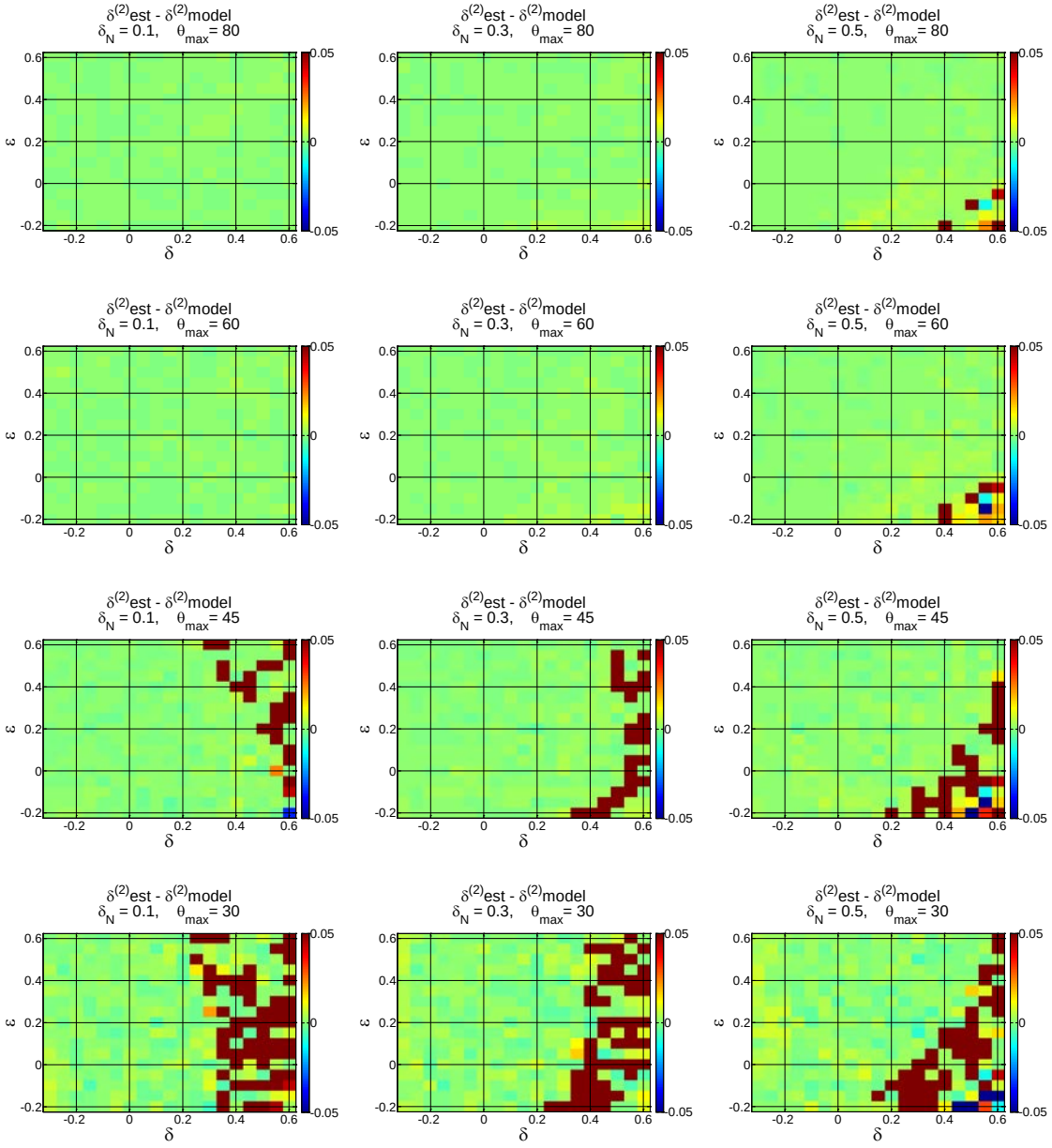

Figure 6, the errors related to the inversion of the exact velocity relationship in orthorhombic medium for the anisotropy parameter $\delta^{(2)}$ where 1% random noise has been added to the slowness vectors. $\theta_{\max}$ decreases from 80^o (top) to 30^o (bottom) and fracture weakness increases from left to right ($\delta_N = 0.1$, $\delta_N = 0.3$ and $\delta_N = 0.5$). Vertical and horizontal axes represent anisotropy parameters of the background VTI medium.

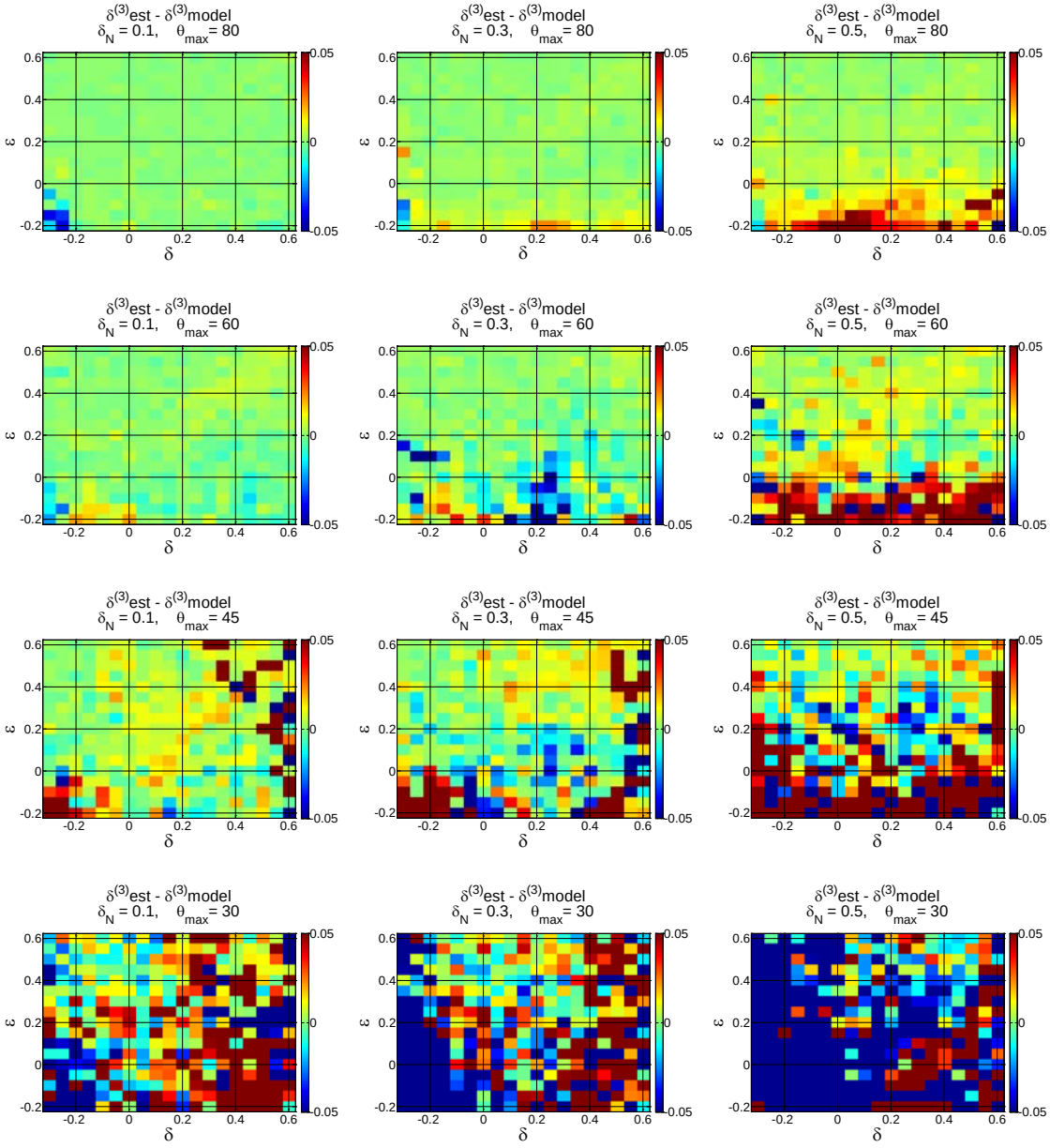

Figure 7, the errors related to the inversion of the exact velocity relationship in orthorhombic medium for the anisotropy parameter $\delta^{(3)}$ where 1% random noise has been added to the slowness vectors. $\theta_{\max}$ decreases from 80^o (top) to 30^o (bottom) and fracture weakness increases from left to right ($\delta_N = 0.1$, $\delta_N = 0.3$ and $\delta_N = 0.5$). Vertical and horizontal axes represent anisotropy parameters of the background VTI medium.

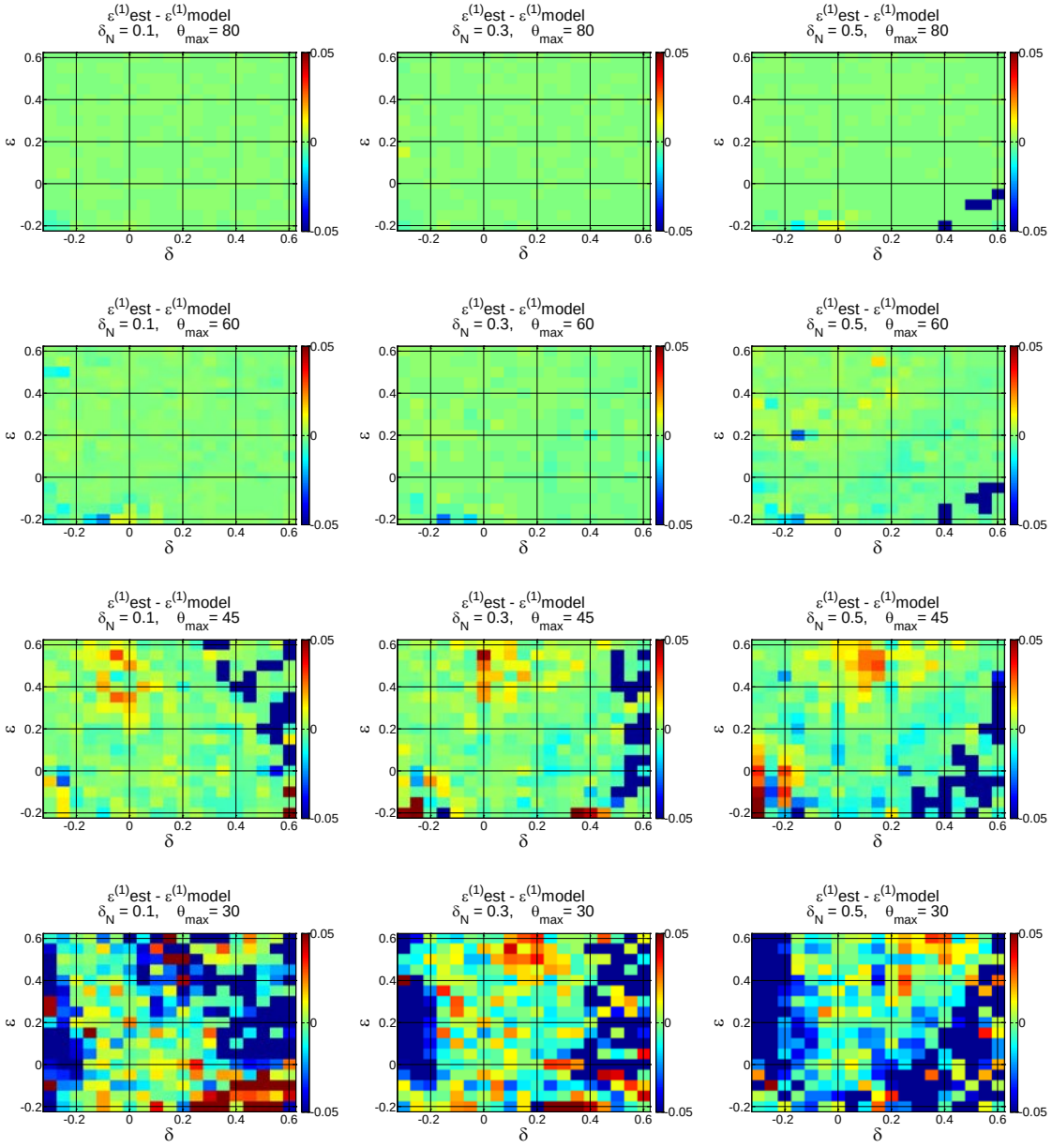

Figure 8, the errors related to the inversion of the exact velocity relationship in orthorhombic medium for the anisotropy parameter $\varepsilon^{(1)}$ where 1% random noise has been added to the slowness vectors. $\theta_{\max}$ decreases from 80^o (top) to 30^o (bottom) and fracture weakness increases from left to right ($\delta_N = 0.1$, $\delta_N = 0.3$ and $\delta_N = 0.5$). Vertical and horizontal axes represent anisotropy parameters of the background VTI medium.

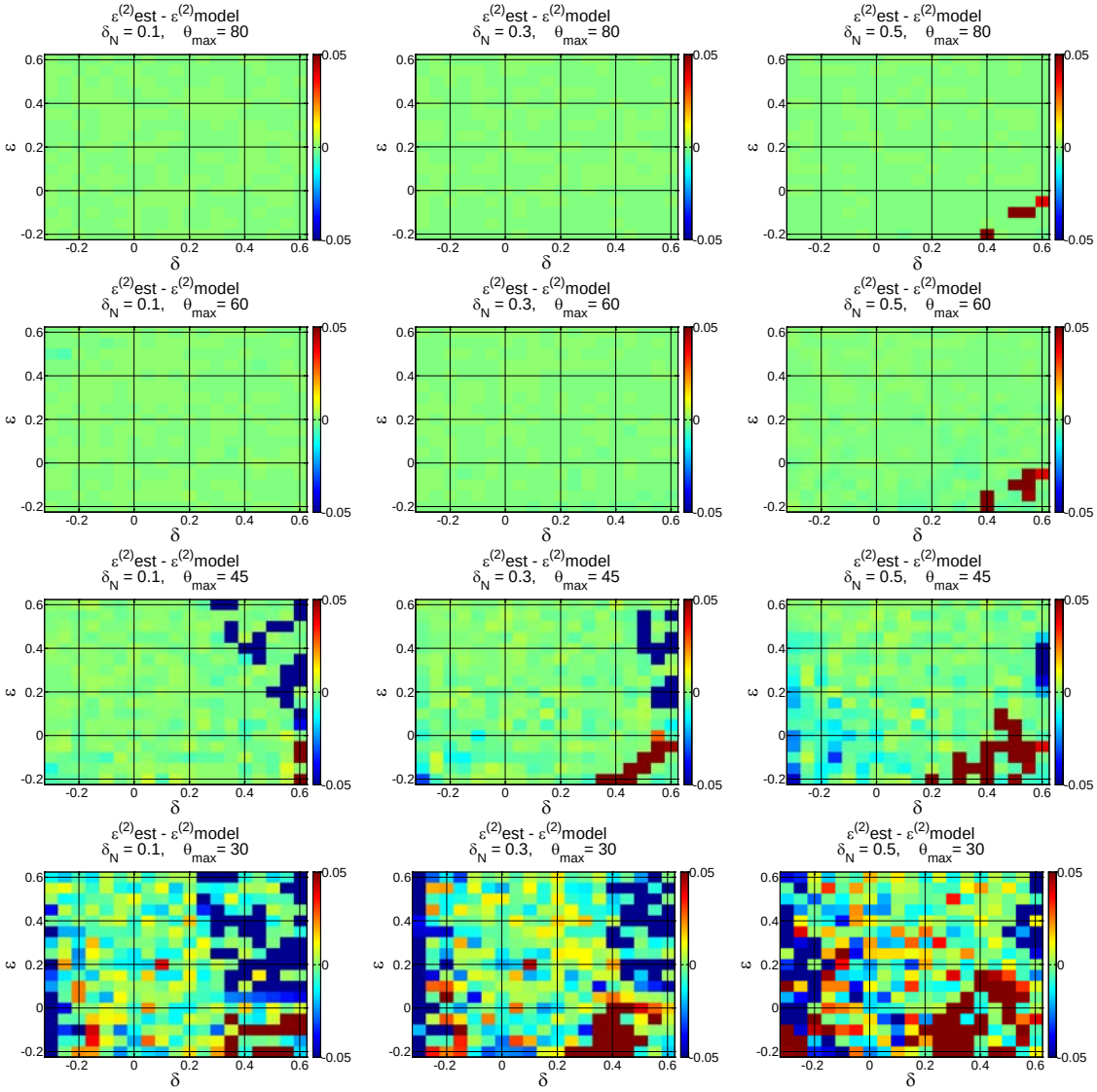

Figure 9, the errors related to the inversion of the exact velocity relationship in orthorhombic medium for the anisotropy parameter $\varepsilon^{(2)}$ where 1% random noise has been added to the slowness vectors. $\theta_{\max}$ decreases from 80^o (top) to 30^o (bottom) and fracture weakness increases from left to right ($\delta_N = 0.1$, $\delta_N = 0.3$ and $\delta_N = 0.5$). Vertical and horizontal axes represent anisotropy parameters of the background VTI medium.

Figure 8, displayes the errors related to the estimation of parameter $\varepsilon^{(1)}$. The estimations are sufficiently accurate for the entire range of tested VTI anisotropy and fracturing if $\theta_{\max} \geq 60^o$. For $\theta_{\max} = 45^o$, the method fails to recover $\varepsilon^{(1)}$ if $\delta \geq 0.4$. The

estimations for $\theta_{\max} = 30^o$ are not reliable. Figure 9, displayes the errors related to the estimation of parameter $\varepsilon^{(2)}$. Similar to the estimation of parameter $\varepsilon^{(1)}$, the estimations are very accurate for the entire range of VTI anisotropy and fracturing if $\theta_{\max} \geq 60^o$. For $\theta_{\max} = 45^o$, method fails to recover $\varepsilon^{(2)}$ if $\delta \geq 0.4$. However, The estimations are slightly better than the case for $\varepsilon^{(1)}$. The estimations for $\theta_{\max} = 30^o$ are not reliable.

6.2.3.2 Example 2: slowness vectors contaminated with 3% random noise.

Figures 10 to 14 show the errors related to the estimation of anisotropy parameter $\delta^{(1)}$, $\delta^{(2)}$, $\delta^{(3)}$, $\varepsilon^{(1)}$ and $\varepsilon^{(2)}$ where this time 3% random noise has been added to the slowness vectors. In these figures, $\theta_{\max}$ decreases from top to bottom ($80^o, 60^o$, 46^o and 30^o) and fracture weakness increases from left to right ($\delta_N = 0.1$, $\delta_N = 0.3$ and $\delta_N = 0.5$). Vertical and horizontal axes represent anisotropy parameters of the background VTI medium. Figure 10 displays the errors related to the estimation of parameter $\delta^{(1)}$. In general, the estimation errors are slightly larger than the case with 1 % added noise. Method's inaccuracy for strong VTI medium now appears in maximum propagation angle as large as $\theta_{\max} = 80^o$. Figure 11 displays the errors related to the estimation of parameter $\delta^{(2)}$. Similar to $\delta^{(1)}$ case, the estimation errors are slightly larger than the case with 1 % added noise. Method's inaccuracy for strong VTI medium only appears for maximum propagation angle $\theta_{\max} = 30^o$ or for the large fracture weakness $\delta_N = 0.5$. Figure 12 displays the errors related to the estimation of parameter $\delta^{(3)}$. Similar to the case with 1% noise level, accurate estimations are achieved only for largest maximum wave propagation angle, $\theta_{\max} = 80^o$, and where the fracture weakness in the medium is small, $\delta_N \leq 0.3$. Figure 13 displays the errors related to the estimation of parameter $\varepsilon^{(1)}$. The estimations are accurate in the entire range of VTI anisotropy and fracture weakness where the maximum propagation angles are larger than 60^o. Figure 14 displays the errors related to the estimation of parameter $\varepsilon^{(2)}$. The estimations are accurate in the entire range of VTI anisotropy and fracture weakness where the maximum propagation angles are larger than 45^o.

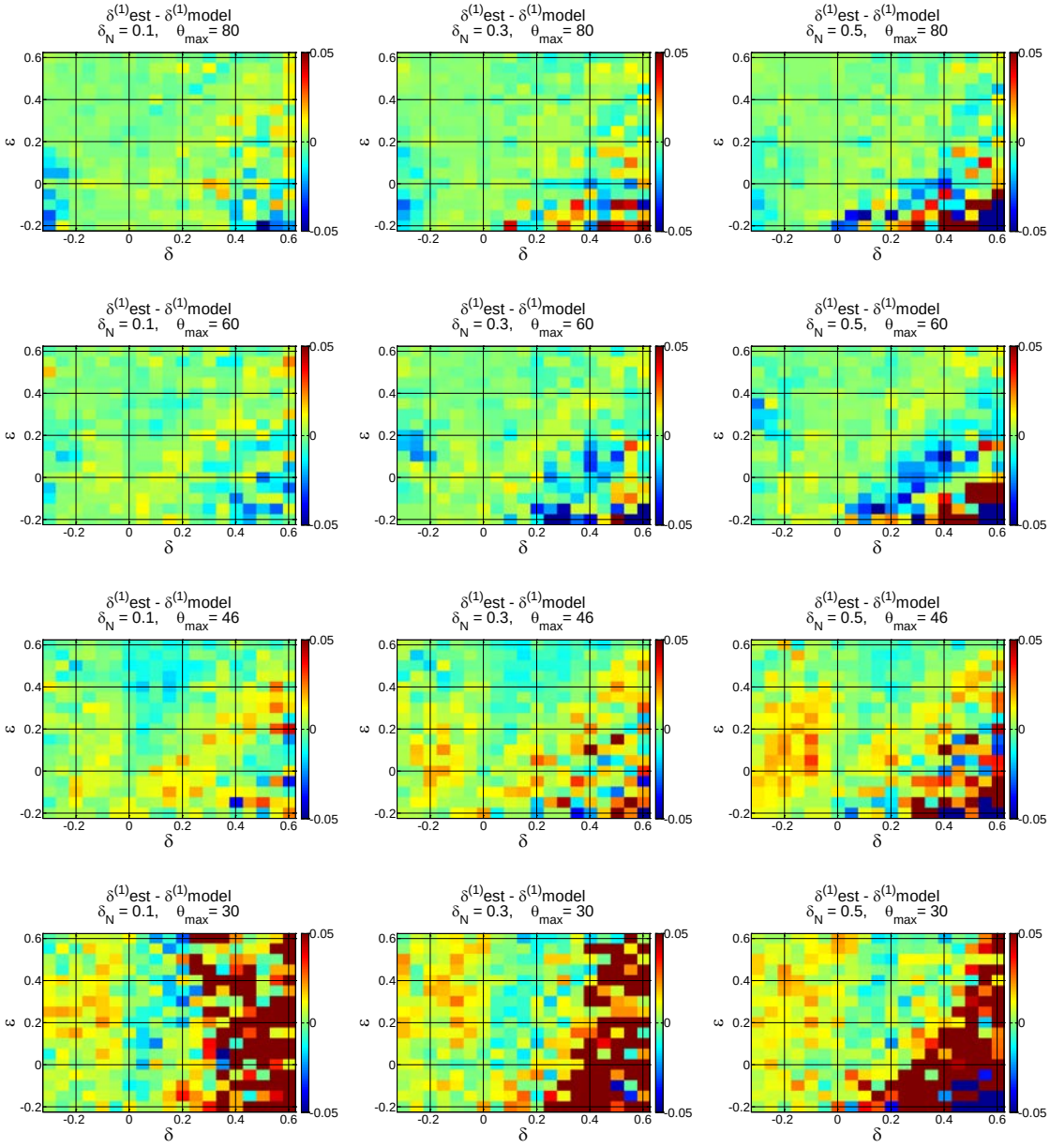

Figure 10, the errors related to the inversion of the exact velocity relationship in orthorhombic medium for the anisotropy parameter $\delta^{(1)}$ where 3% random noise has been added to the slowness vectors. $\theta_{\max}$ decreases from 80^o (top) to 30^o (bottom) and fracture weakness increases from left to right ($\delta_N = 0.1$, $\delta_N = 0.3$ and $\delta_N = 0.5$). Vertical and horizontal axes represent anisotropy parameters of the background VTI medium.

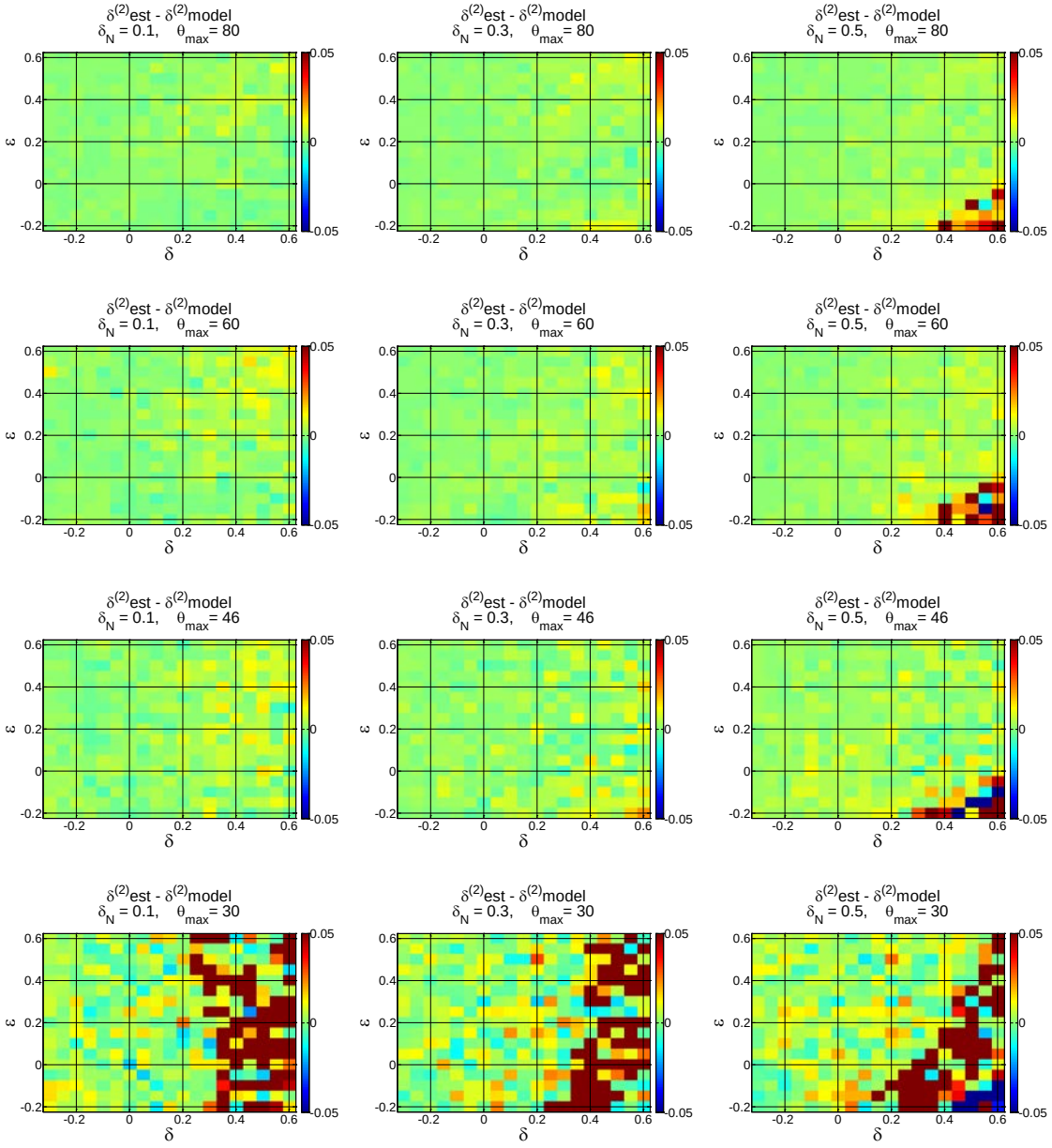

Figure 11, the errors related to the inversion of the exact velocity relationship in orthorhombic medium for the anisotropy parameter $\delta^{(2)}$ where 3% random noise has been added to the slowness vectors. $\theta_{\max}$ decreases from 80^o (top) to 30^o (bottom) and fracture weakness increases from left to right ($\delta_N = 0.1$, $\delta_N = 0.3$ and $\delta_N = 0.5$). Vertical and horizontal axes represent anisotropy parameters of the background VTI medium.

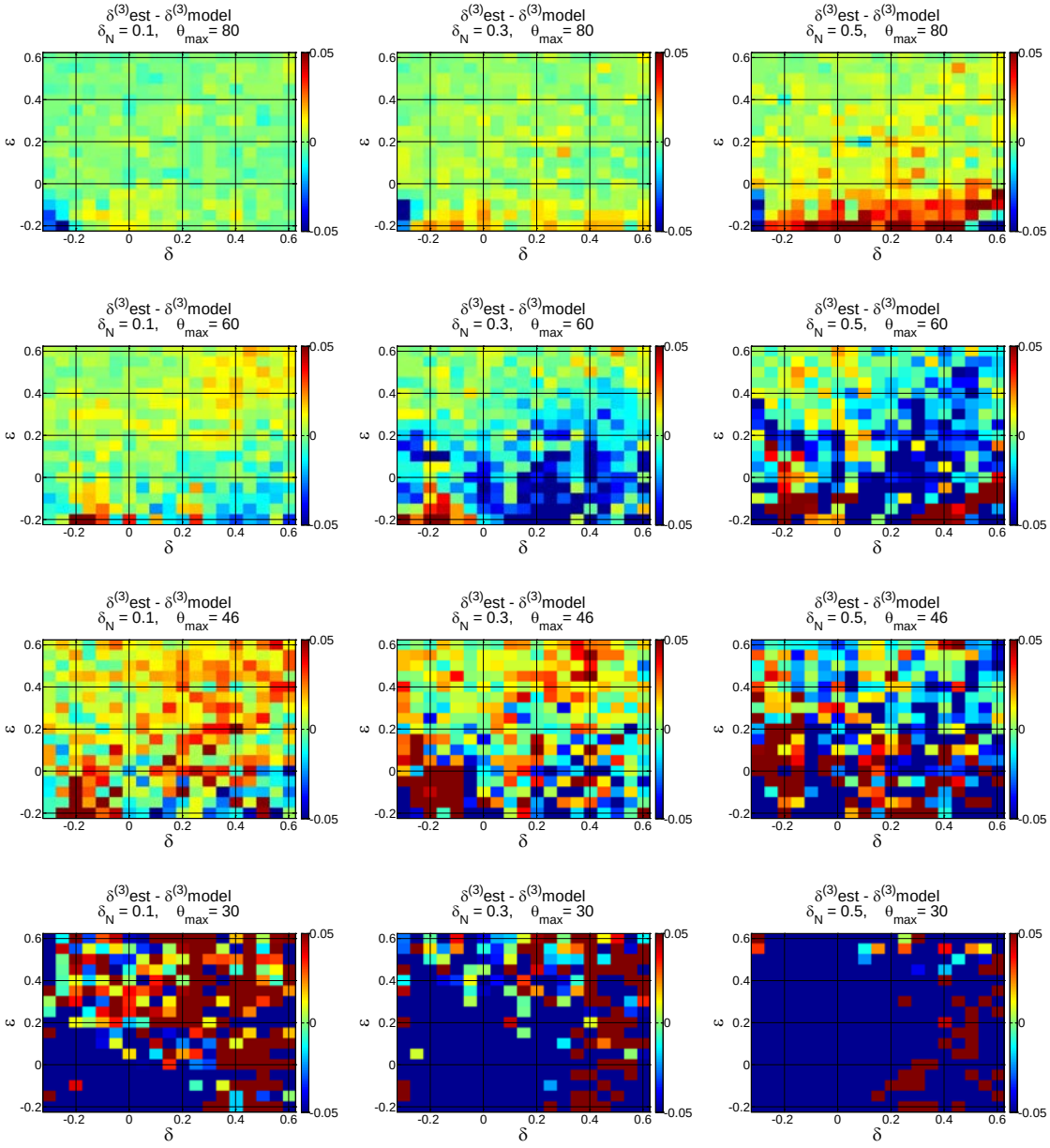

Figure 12, the errors related to the inversion of the exact velocity relationship in orthorhombic medium for the anisotropy parameter $\delta^{(3)}$ where 3% random noise has been added to the slowness vectors. $\theta_{\max}$ decreases from 80^o (top) to 30^o (bottom) and fracture weakness increases from left to right ($\delta_N = 0.1$, $\delta_N = 0.3$ and $\delta_N = 0.5$). Vertical and horizontal axes represent anisotropy parameters of the background VTI medium.

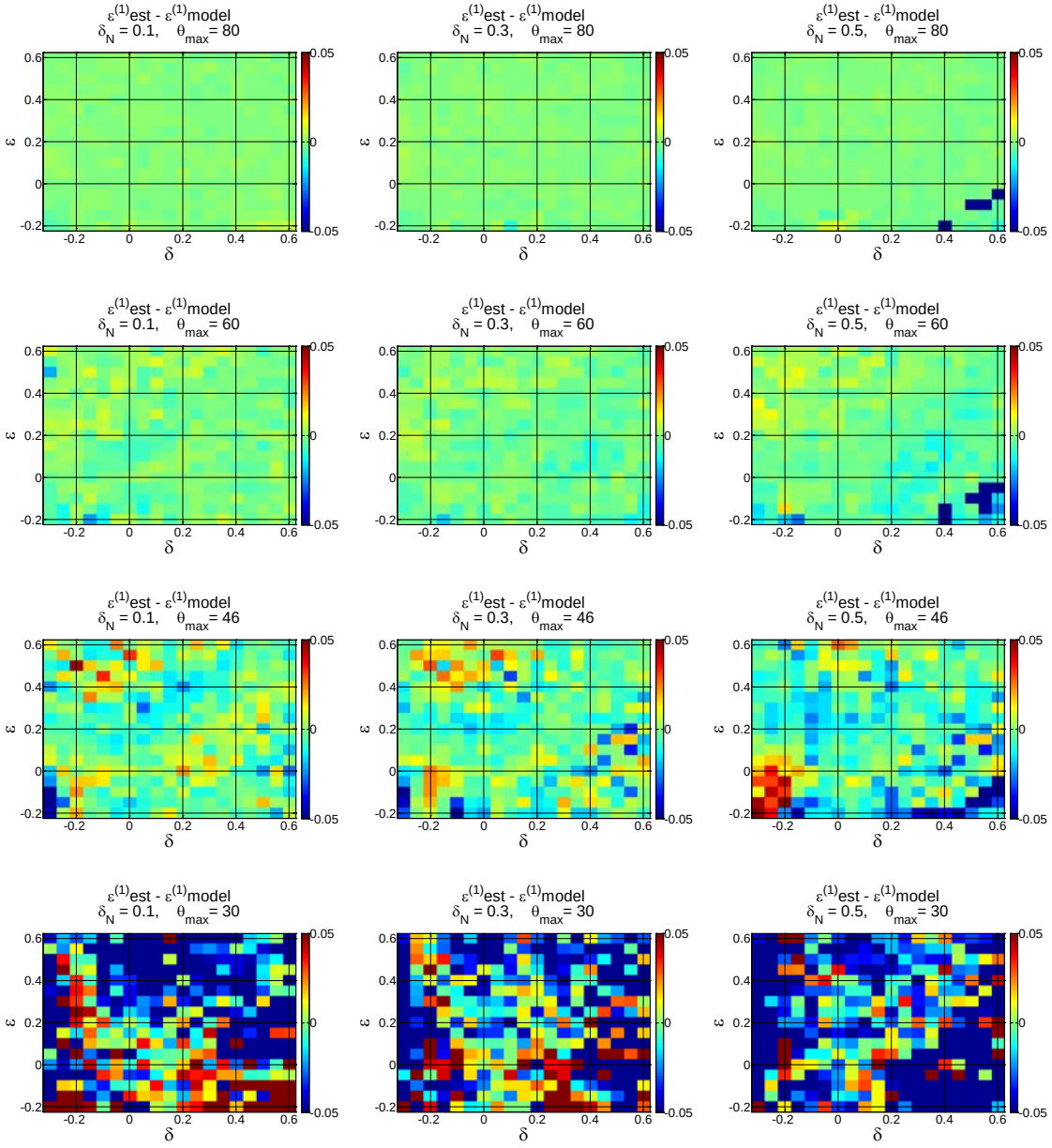

Figure 13, the errors related to the inversion of the exact velocity relationship in orthorhombic medium for the anisotropy parameter $\varepsilon^{(1)}$ where 3% random noise has been added to the slowness vectors. $\theta_{\max}$ decreases from 80^o (top) to 30^o (bottom) and fracture weakness increases from left to right ($\delta_N = 0.1$, $\delta_N = 0.3$ and $\delta_N = 0.5$). Vertical and horizontal axes represent anisotropy parameters of the background VTI medium.

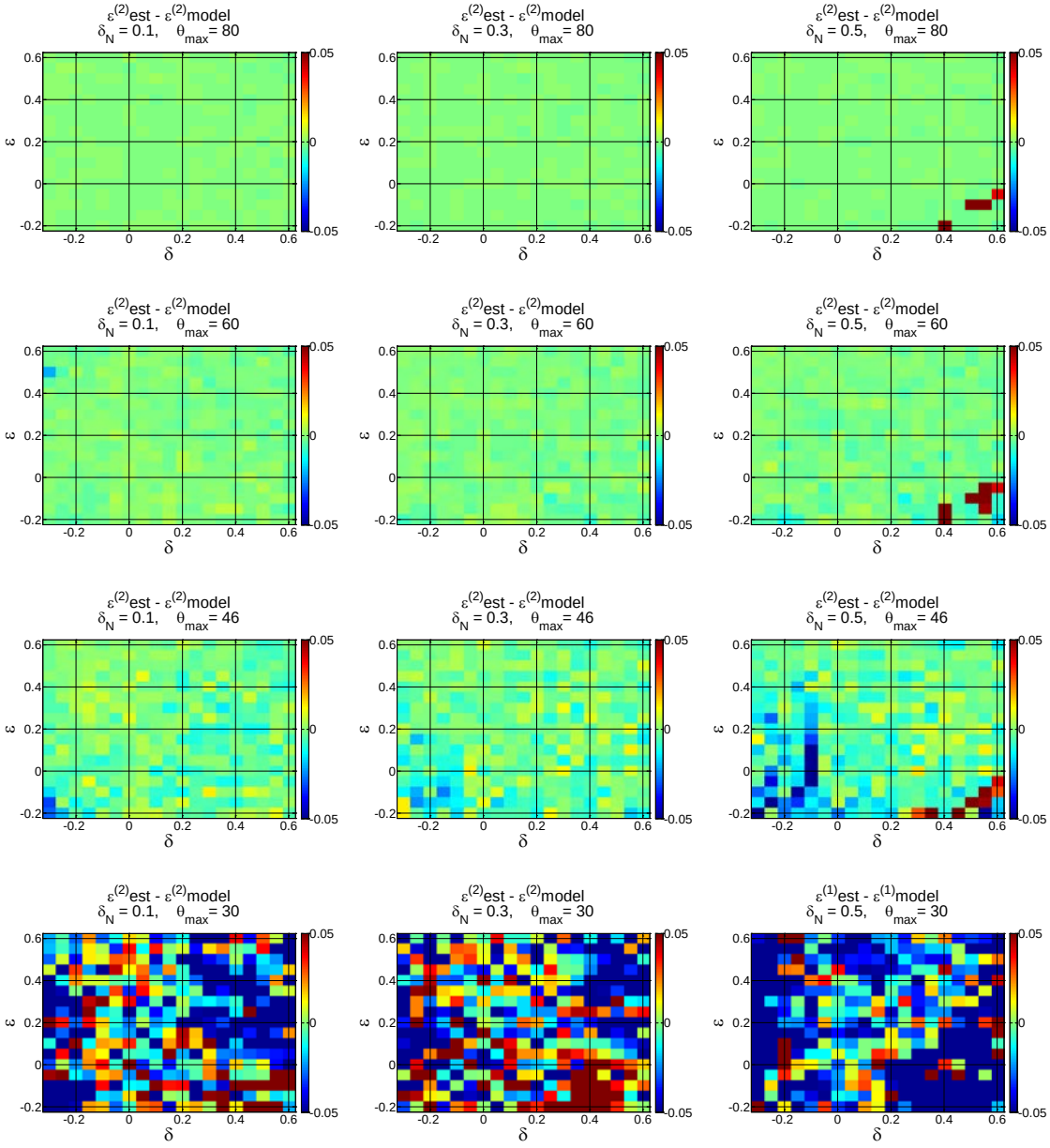

Figure 14, the errors related to the inversion of the exact velocity relationship in orthorhombic medium for the anisotropy parameter $\varepsilon^{(2)}$ where 3% random noise has been added to the slowness vectors. $\theta_{\max}$ decreases from 80^o (top) to 30^o (bottom) and fracture weakness increases from left to right ($\delta_N = 0.1$, $\delta_N = 0.3$ and $\delta_N = 0.5$). Vertical and horizontal axes represent anisotropy parameters of the background VTI medium.

6.3 Orthorhombic anisotropy parameter estimation: case studies

In this part, I will first perform an inversion on P-wave slownesses that are measured along various azimuthal directions of a synthetic pseudo 3D VSP experiment. To generate pseudo 3D VSP data, I will use 36 identical walkaway VSP models (rotated radially at every 5^o of azimuth) with horizontal layer geometry where only anisotropy parameters in the orthorhombic layer change as a function of azimuth. Next, I will apply slowness method to data measured in 3D VSP experiment at the location of well CRC-1 in the Otway geosequestration site.

6.3.1 Pseudo 3D synthetic VSP

To construct synthetic pseudo 3D VSP, 36 walkaway VSPs are positioned radially at every $\phi = 5^o$ azimuthal steps. Each 2D walkaway model is composed of 13 horizontal layers. The layer geometry and elastic parameters are identical among the models from various azimuths, except for the anisotropy parameters $\delta(\phi)$ and $\varepsilon(\phi)$ of the orthorhombic layer. Figure 15 shows the geometry of the earth model and parameters of the synthetic VSP survey that were used to construct the pseudo 3D VSP. In this figure, sources are positioned along a 6 km line on the surface and at every 20 m intervals. Borehole is located in the centre of the survey line. Receivers are positioned in the borehole from 0.5 to 2 km depth at every 10 m interval. Layer geometry is horizontal and velocity is adopted from the sonic log measured at CRC-1 well in the CO2CRC's Otway geosequestration site. Elastic parameters used in the model are summarized in table 1.

The orthorhombic layer here is defined as a combination of a VTI medium and a single system of vertical fractures with $\delta_N = 0.3$ and fracture normals rotated by 60^o from x_1 axis. VTI parameters ($V_{P0} = 3251$ m/s, $V_{S0} = 1779$ m/s, $\gamma = 0.07$, $\delta = -0.1$, $\varepsilon = 0.2$ and $\rho = 2420$ kg/m^3) are first resolved to derive the compliance matrix s_{VTI} of the background medium. Next, I will compute the compliance matrix of the rotationally invariant fracture set with $\delta_N = 0.3$ and fracture normals in the x_1 direction, s_f^{RI,x_1} using Equation 4. The assumption here is that the fractures are rotationally invariant ($K_{NV} = K_{NH} = K_{VH} = 0$ and $K_V = K_H = K_T$) and dry ($K_N = K_T$). Anisotropic parameters of the orthorhombic medium ($\delta^{(1)}$, $\delta^{(2)}$, $\delta^{(3)}$, $\varepsilon^{(1)}$, $\varepsilon^{(2)}$, $\gamma^{(1)}$ and $\gamma^{(2)}$) have to be

defined in its natural coordinates. Therefore, I will sum both compliances (s_{VTI} and s_f^{RI,x_1}) and then inverse the summation result to derive the stiffness matrix of the orthorhombic medium at its natural coordinates (Equations 9 and 10). I could also insert fracture weakness δ_N (δ_V and δ_H) and VTI stiffness coefficients into Equation 5 directly to derive the stiffness matrix of the orthorhombic medium. Now, anisotropic parameters of the orthorhombic medium can be computed as usual.

To derive the stiffness matrix of the orthorhombic medium that is generated by embedding a vertical fracture set rotated by 60^o from x_1 axis, I will first reorient the fracture compliance matrix s_f^{RI,x_1} to its new direction and derive $s_f^{RI,(\alpha,\beta)}$ and then add this to compliance matrix of the VTI medium s_{VTI} and invert the result. I will use Equations 6 to 8 to rotate s_f^{RI,x_1} to new direction defined by unit vector **n**, ($\alpha = 60^o$ and $\beta = 0^o$) and Equations 9 and 10 to derive the stiffness coefficients of the orthorhombic medium.

Equations 62 and 63 of Chapter 3 show that an orthorhombic medium can be modeled as VTI medium with azimuthally varying anisotropy parameters. To use Equations 62 and 63 of Chapter 3, ϕ has to be replaced by $\phi - 60^o$. Figure 16 displays values of $\delta(\phi)$ computed for the orthorhombic layer number 11. Figure 17 displays values of $\varepsilon(\phi)$ computed for the orthorhombic layer number 11. The elastic parameters of the background VTI rock, δ_b and ε_b, the embedding fracture weakness, δ_N, direction of the fracture normal, α and anisotropic parameters of the resultant orthorhombic medium are printed in the title of the Figure 16. Values of $\delta(\phi)$ and $\varepsilon(\phi)$ in this figure have been used to build 36 2D velocity models which are only different in $\delta(\phi)$ and $\varepsilon(\phi)$ used in the orthorhombic layer.

P-wave first arrival times are picked and used to estimate slownesses. Figure 18 displays an example of P-wave travel times recorded by the receiver positioned at depth 1500 m within the orthorhombic layer. Travel times are restricted to maximum source offset equal to 2000 m and plotted for the entire azimuthal range.

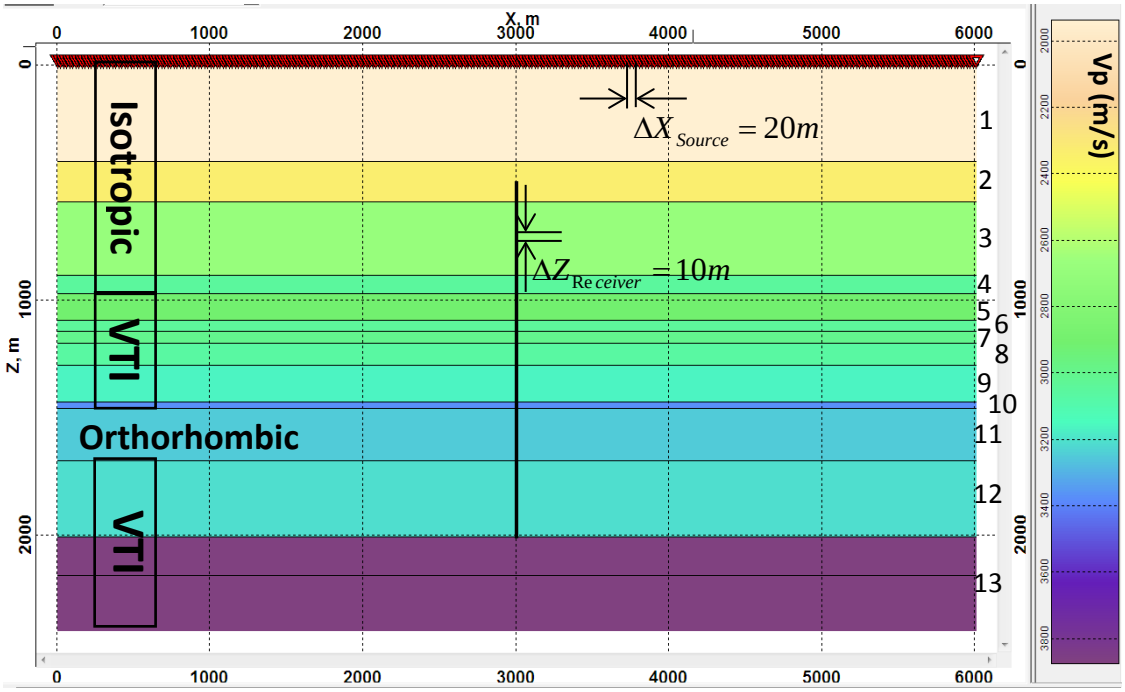

Figure 15, the geometry of the 2D model and parameters of the synthetic walkaway VSP survey.

Property / Layer	Vp_0 (m/s)	Vs_0 (m/s)	ρ (Kg/m^3)	δ	ε	γ
1	1937	760	2026	0	0	0
2	2329	1089	2141	0	0	0
3	2689	1279	2212	0	0	0
4	3051	1596	2287	0	0	0
5	2915	1514	2215	-0.14	0.08	0.07
6	3040	1595	2260	-0.14	0.08	0.07
7	3007	1618	2258	-0.14	0.08	0.07
8	3063	1657	2282	-0.14	0.08	0.07
9	3164	1735	2309	-0.14	0.08	0.07
10	3375	1801	2322	-0.14	0.08	0.07
11	3251	.....	2420	$\delta(\phi)$	$\varepsilon(\phi)$	.....
12	3214	1635	2358	-0.14	0.08	0.07
13	3878	2287	2491	-0.14	0.08	0.07

Table 1, elastic parameters of the 2D model displayed in Figure 15.

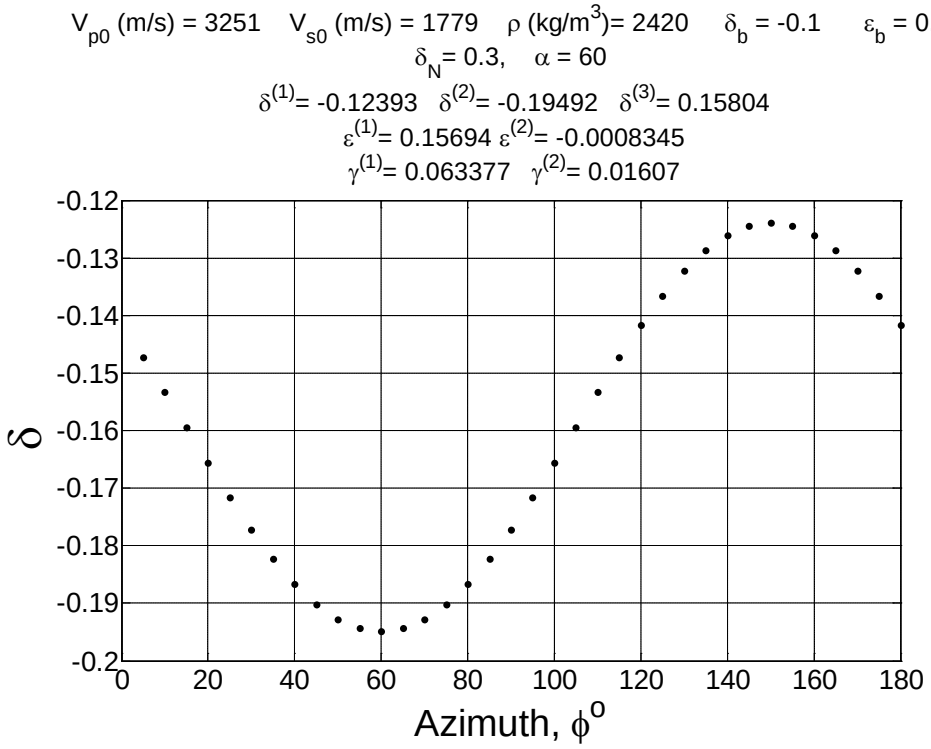

Figure 16, values of $\delta(\phi)$ computed for the orthorhombic layer number 11 using Equations 62 and 63 of Chapter 3.

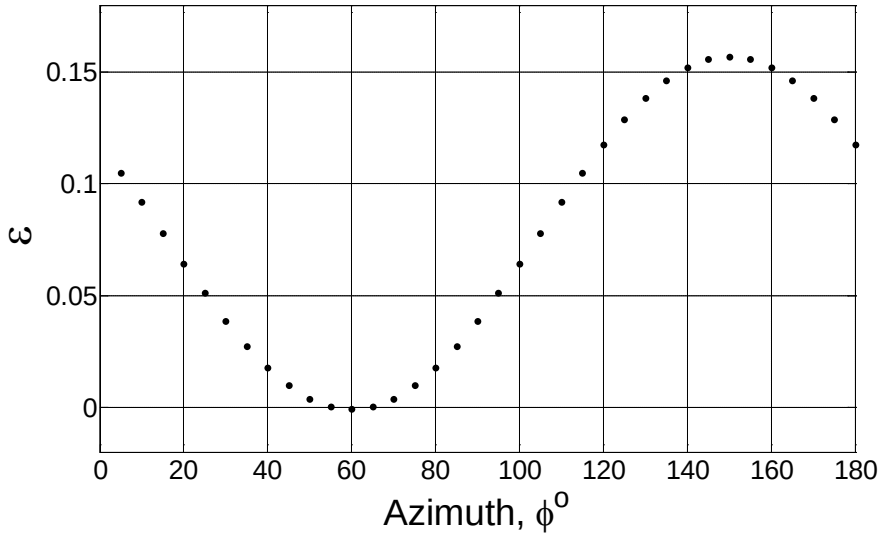

Figure 17, values of $\varepsilon(\phi)$ computed for the orthorhombic layer number 11 using Equations 62 and 63 of Chapter 3.

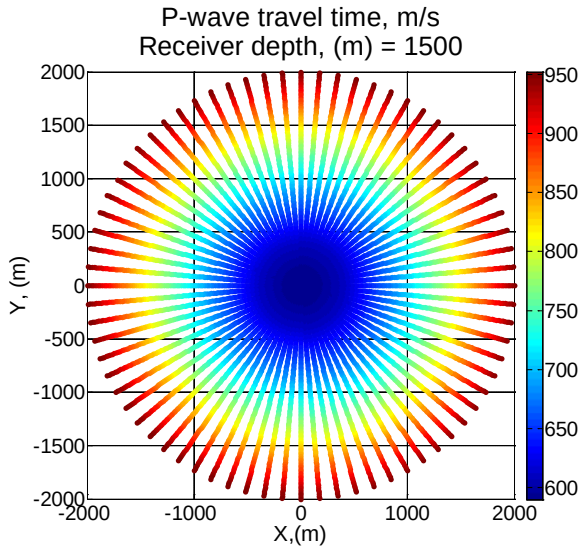

Figure 18, an example of P-wave travel times recorded by the receiver positioned at depth 1500 m within the orthorhombic layer.

For any given receiver that is used to estimate anisotropy parameters, slowness vector, **P** has to be estimated for all the sources on the surface. To compute vertical component, p_3 of the slowness vector (of a P-wave generated by a given source on the surface and recorded by the given receiver in the borehole), an array of five neighbouring receivers are selected where the given receiver is located in the centre of the array. The gradient of first arrival times recorded by the array is regarded as the vertical component of the slowness vector, $p_3 = dt/dx_3$. To compute horizontal components of the slowness vector, p_1 and p_2 a number of sources are selected within a radial distance (300 m here) to the given source. The rate of travel time change with respect to the distance between sources in x_1 and x_2 directions is regarded as horizontal component of the slowness vector, $p_1 = dt/dx_1$ and $p_2 = dt/dx_2$. The two components are measured on the surface and can be transferred to receiver depth by using the Snell's law, as long as the layer geometry is horizontal and there is small lateral velocity variation in the overburden layers. Vertical component of the slowness vector, p_3 and horizontal components of the slowness vector p_1 and p_2 can be estimated by solving (in a least-square sense) a system of equations $A * X = B$. An example of such a system of equations is given below where 3 receivers at depths x_3 , $x_3^{'}$ and $x_3^{''}$ have recorded first arrival times

$(t_{x_3},\ t'_{x_3},\ t''_{x_3}), (t_{x'_3},\ t'_{x'_3},\ t''_{x'_3})$ and $(t_{x''_3},\ t'_{x''_3},\ t''_{x''_3})$ of the P-waves generated by 3 sources at the coordinates $(x_1,\ x_2), (x'_1,\ x'_2)$ and $(x''_1,\ x''_2)$ on the earth surface:

$$A = \begin{bmatrix} x_1 & x_2 & x_3 & 1 \\ x'_1 & x'_2 & x_3 & 1 \\ x''_1 & x''_2 & x_3 & 1 \\ x_1 & x_2 & x'_3 & 1 \\ x'_1 & x'_2 & x'_3 & 1 \\ x''_1 & x''_2 & x'_3 & 1 \\ x_1 & x_2 & x''_3 & 1 \\ x'_1 & x'_2 & x''_3 & 1 \\ x''_1 & x''_2 & x''_3 & 1 \end{bmatrix},\ X = [p_1 \quad p_2 \quad p_3 \quad const],\ B = \begin{bmatrix} t_{x_3} \\ t'_{x_3} \\ t''_{x_3} \\ t_{x'_3} \\ t'_{x'_3} \\ t''_{x'_3} \\ t_{x''_3} \\ t'_{x''_3} \\ t''_{x''_3} \end{bmatrix} \qquad \textbf{(111)}$$

Components of the P-wave slowness vector, **P** (Figure 19) can now be used to compute P-wave slownesses (Figure 20, top left):

$$|P| = \sqrt{p_1^2 + p_2^2 + p_3^2}\ , \qquad \textbf{(12)}$$

and wavefront normal, **n** (Figure 20, top right):

$$n_1 = \frac{P_1}{|P|},\quad n_2 = \frac{P_2}{|P|}\ ,\quad n_3 = \frac{P_3}{|P|} \qquad \textbf{(13)}$$

P-wave phase (dip) angle can be computed from n_3 by (Figure 20, bottom):

$$\theta = \cos^{-1} n_3 \qquad \textbf{(14)}$$

P-wave phase velocity V_P is computed by inverting the slowness (Figure 21):

$$V_P = \frac{1}{|P|} \qquad \textbf{(15)}$$

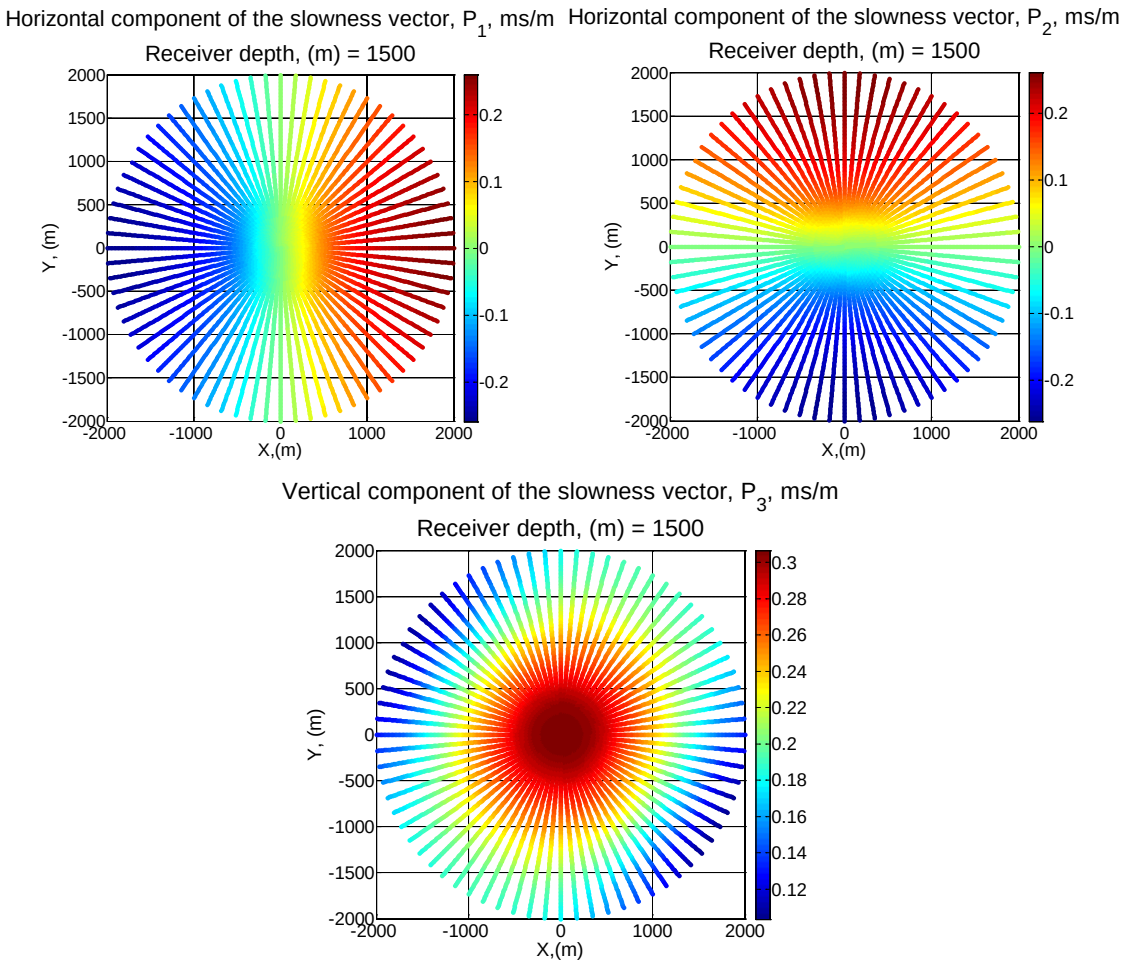

Figure 19, displays the values of the 3 components of the slowness vector computed from the travel times recorded by the receiver located at depth 1500 m within the orthorhombic layer.

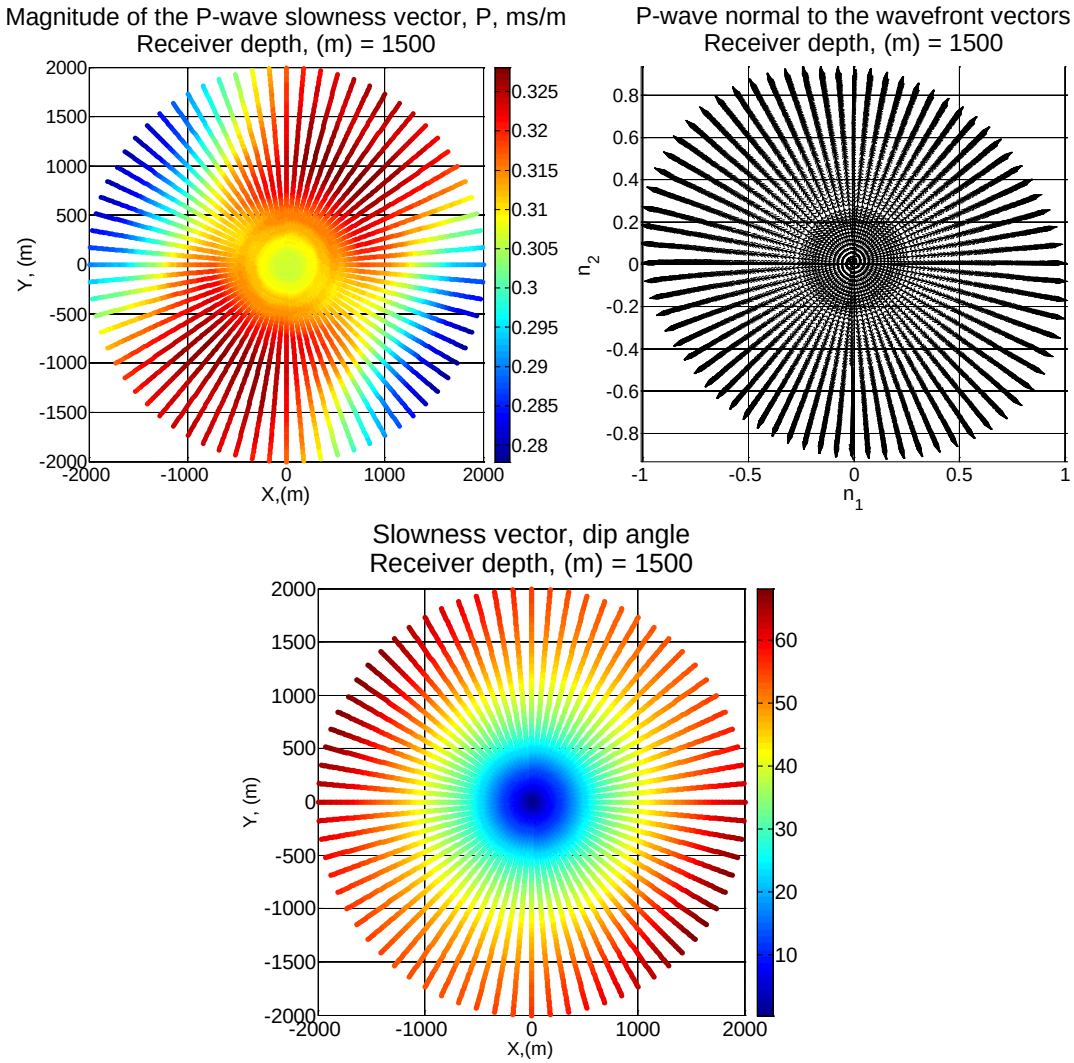

Figure 20, top left, magnitude of the P-wave slowness vector $|P|$ and top right, normal vectors to P-wave wavefront computed for the receiver located at depth 1500 m within the orthorhombic layer. Bottom figure displays values of P-wave (phase) dip angles for the corresponding slownesses in top figures.

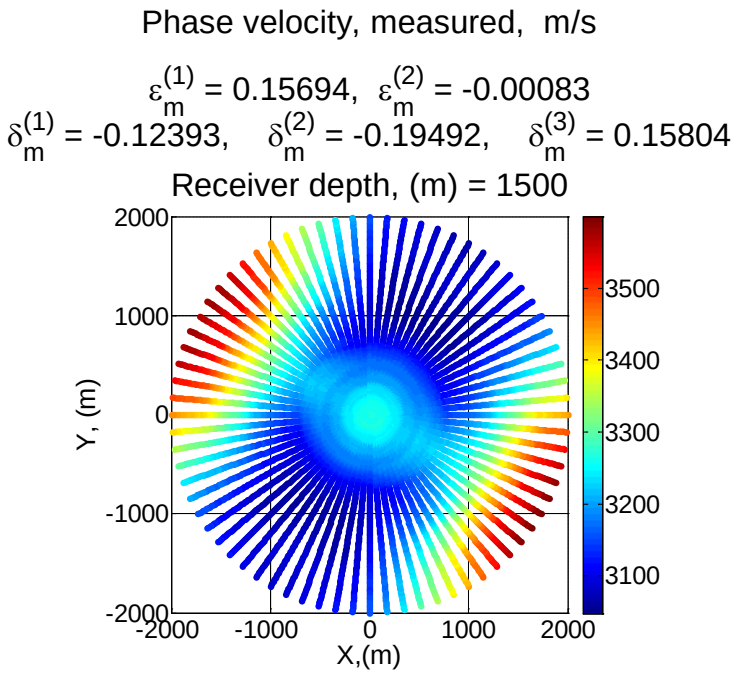

Figure 21, P-wave phase velocities computed for the receiver located at depth 1500 m within the orthorhombic layer.

P-wave velocities are calculated from the slownesses assuming X, Y and Z coordinates are equivalent to x_1, x_2 and x_3, respectively. In order to use exact relationship for the phase velocity in orthorhombic media as forward model in the inversion, measurement directions have to be rotated so that X axis lies in the direction of fracture normal x_1 (60^o rotated anti-clockwise from X direction). The rotation is performed on the matrix of wavefront normals by multiplying the so called Euler rotation matrix E. Matrix of wavefront normals is a $3\times m$ matrix for which the rows correspond to three components of the direction of the slowness vector and the columns correspond to m measurements directions. Euler rotation is usually performed through the three rotation angles (the χ convention): Φ about the Z axis that generates new intermediate coordinate system Z, X', Y', Θ about the X' axis that generates the second intermediate coordinate system Z', X', Y" and Ψ about Z' axis that will generate the final coordinate system Z', X", Y'". Components of the Euler rotation matrix in the χ convention are given as:

$$E = \begin{vmatrix} \cos\Psi\cos\Phi - \cos\Theta\sin\Phi\sin\Psi & \cos\Psi\sin\Phi + \cos\Theta\cos\Phi\sin\Psi & \sin\Psi\sin\Theta \\ -\sin\Psi\cos\Phi - \cos\Theta\sin\Phi\cos\Psi & -\sin\Psi\sin\Phi + \cos\Theta\cos\Phi\cos\Psi & \cos\Psi\sin\Theta \\ \sin\Theta\sin\Phi & -\sin\Theta\cos\Phi & \cos\Theta \end{vmatrix} \quad (16)$$

Here, matrix of wavefront normals is rotated by Euler angles: $\Phi = 60^o$, $\Theta = 0^o$ and $\Psi = 0^o$. Now that the measured velocities are oriented along the natural coordinates of the orthorhombic medium, the exact relationship described in Section 3.11 (Equations 35-52) can be used for the inversion.

In the inversion part, a least square objective function of velocity is minimized to estimate the stiffnesses of the orthorhombic medium. I assume that C_{33} and C_{55} are a priori known from the measurements of vertical P- and S-wave velocities. The S-wave has to be the one that is polarized in the x_1 direction. The orthorhombic parameters can now be computed from the estimated stiffness coefficients. The estimated parameters and the error in the inversion are shown in Figure 22.

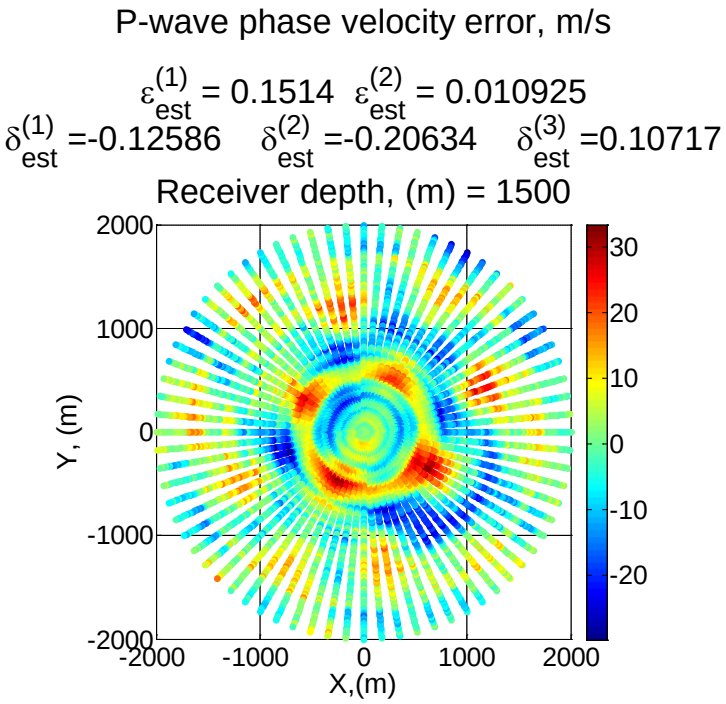

Figure 22, errors of the inversion in terms of the difference between the measured and modelled phase velocities for the receiver located at depth 1500 m. Estimated orthorhombic parameters are printed in the title and used to calculate the model velocities.

Low error values in Figure 22 and the similarity between the results of the inversion for orthorhombic parameters: $\delta_{est}^{(1)} \approx -0.126$, $\delta_{est}^{(2)} \approx -0.206$, $\delta_{est}^{(3)} \approx 0.107$, $\varepsilon_{est}^{(1)} \approx 0.151$ and $\varepsilon_{est}^{(2)} \approx 0.011$ and the corresponding model values ($\delta_{m}^{(1)} \approx -0.124$, $\delta_{m}^{(2)} \approx -0.195$, $\delta_{m}^{(3)} \approx 0.158$, $\varepsilon_{m}^{(1)} \approx 0.157$ and $\varepsilon_{m}^{(2)} \approx 0$) emphasis the applicability of the method for orthorhombic parameter estimation at Otway geosequestration site. Only accuracy of estimating $\delta_{est}^{(3)}$ appears to be less than the accuracy of estimating other parameters. This can be a result of short phase angle coverage, $\theta_{\max} \approx 65^{o}$ at the measurement interval (see Figure 20, bottom).

6.3.2 3D VSP example, CO2CRC's Otway project

CO2CRC has acquired 3 sets of VSP surveys, zero-offset VSP, offset VSP, and a 3D VSP at CRC-1 well location in 2010. CRC-1 is a vertical well and has been used by CO2CRC to inject CO_2 into the underground geological formations at Otway geosequestration site. 3D VSP data was acquired using 8 receiver (at 15.2 m intervals) downhole tool simultaneously with the acquisition of 3D surface seismic (Table 1 of Chapter 2). Receivers are positioned within the interval depth from 1500 to 1605.84 m MD. A mini Buggy vibrator was used as VSP source in 2010 3D VSP survey. Source positions were located by DGPS system.

Figure 23, displays source locations for 3D VSP surveys in 2008 and 2010. Position of wells CRC-1, Naylor-1 and source locations for zero-offset and offset VSPs are also shown in Figure 23.

Figure 24 top, shows values of seismic source elevation in the survey area. These values have been used to compute source elevation related statics (bottom). A replacement velocity, 1800 m/s has been applied to bring all the travel times to a constant datum, 30 m above the sea level. This velocity has been selected based on available near-surface velocity information in the area.

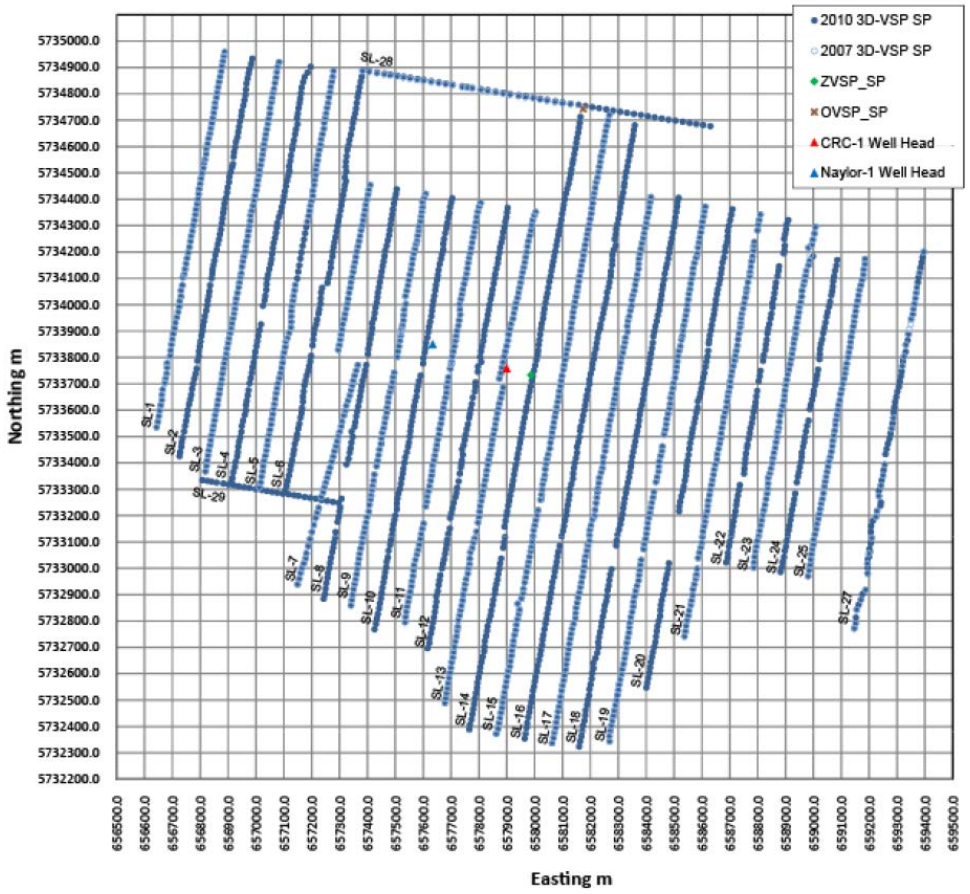

Figure 23, seismic source locations for zero-offset VSP (green dot), offset VSP (brown ×) and 3D VSP surveys acquired by CO2CRC Australia at Otway geosequestration site in 2008 and 2010. (Schlumberger 3D VSP QC report, 2010).

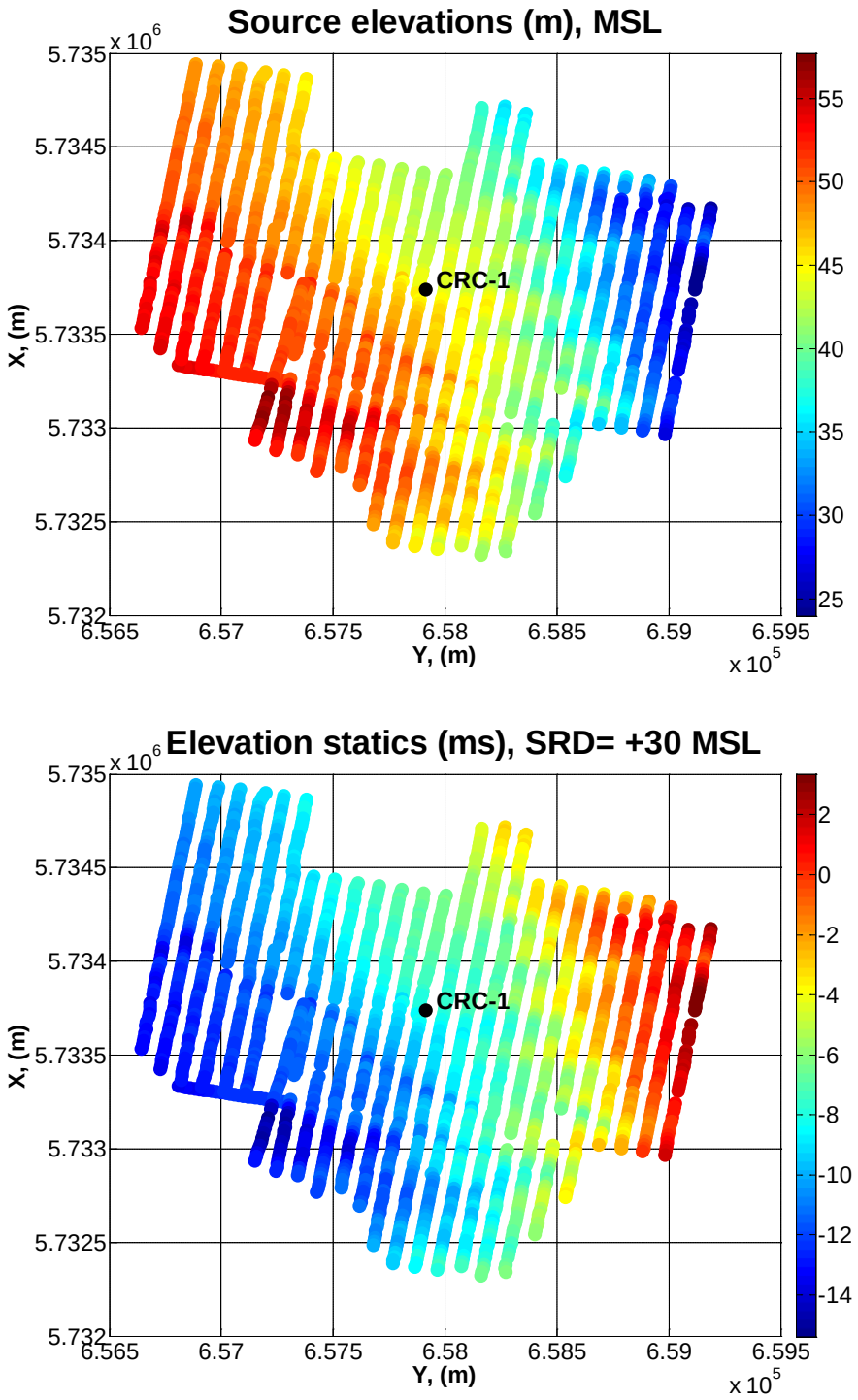

Figure 24, seismic source elevation in the 3D VSP survey area (top). A replacement velocity, 1800 m/s has been used to compute elevation related statics relative to a flat datum +30 m above MSL.

P-wave first arrival times, recorded by 8 receivers are picked and corrected for the source elevation statics. Figure 25 shows travel times recorded by a single receiver positioned at depth 1545 m (black dots) and corrected travel times for the elevation statics (red curve). Elevation related statics acquire greatest values from the sources located at the Eastern side of the survey where the source elevations are largest (Figure 24, top) and decrease by moving towards the Western side of the survey area. By applying this correction to measured travel times we have reduced the effect of source elevation variation on resulting horizontal components of P-wave slowness vector.

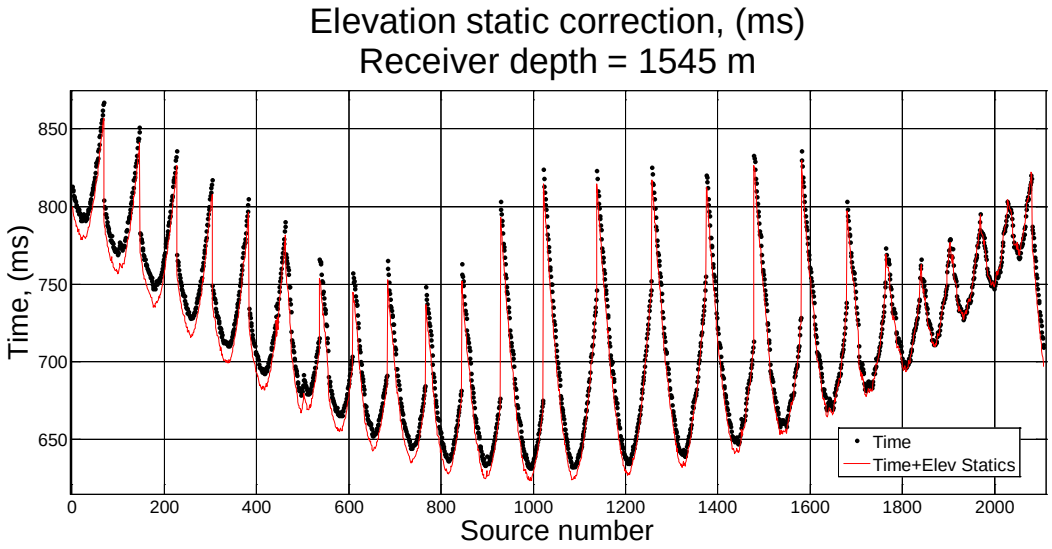

Figure 25, P-wave first arrivals recorded by the receiver positioned at depth 1545 m (black dots) and corrected for the elevation statics (red curve).

P-wave slownesses and velocities are computed exactly the same way as described for pseudo 3D VSP in Section 6.3.1. Emphasized by 3D seismic sections observed at the location of well CRC-1, overburden geometry above the receiver interval is composed of nearly horizontal and structurally simple formation layers (see Figure 3 of Chapter 2). The absence of large faults and other geometrical complexities in the overburden increases the lateral homogeneity in layer velocity at this location. Horizontal layer geometry and lateral homogeneity are two main assumptions that will allow us to apply Snell's law at CO2CRC's Otway geosequestration site. Based on Snell's law, horizontal

component of the slowness vector is preserved (remains constant) as the wave is traveling in the subsurface. As a result, this component can be measured on the surface and used in the receiver level. Figure 26 shows P-wave dip phase angle (top) and velocities (bottom) computed from 3D VSP slowness measurements in the survey area. As with pseudo 3D synthetic exercise, direction of P-wave phase velocity (direction of the vector **n** or the slowness vector) has to be referenced relative to the natural coordinates of the orthorhombic medium in order to use the velocity equation in the inversion. In the inversion, a least square objective function of velocity is minimized to estimate the stiffnesses of the orthorhombic medium. I assume that C_{33} and C_{55} are a priori known from the measurements of vertical P- and S-wave velocities. Vertical P-wave velocity can be estimated from first arrivals of zero-offset VSP and S-wave velocity from borehole log measurements. The S-wave has to be in the direction of the x_3 symmetry axis and polarized in the x_1 direction (normal to the fracture plane). However, the results of the inversion appear to be independent on the value of the S-wave velocity.

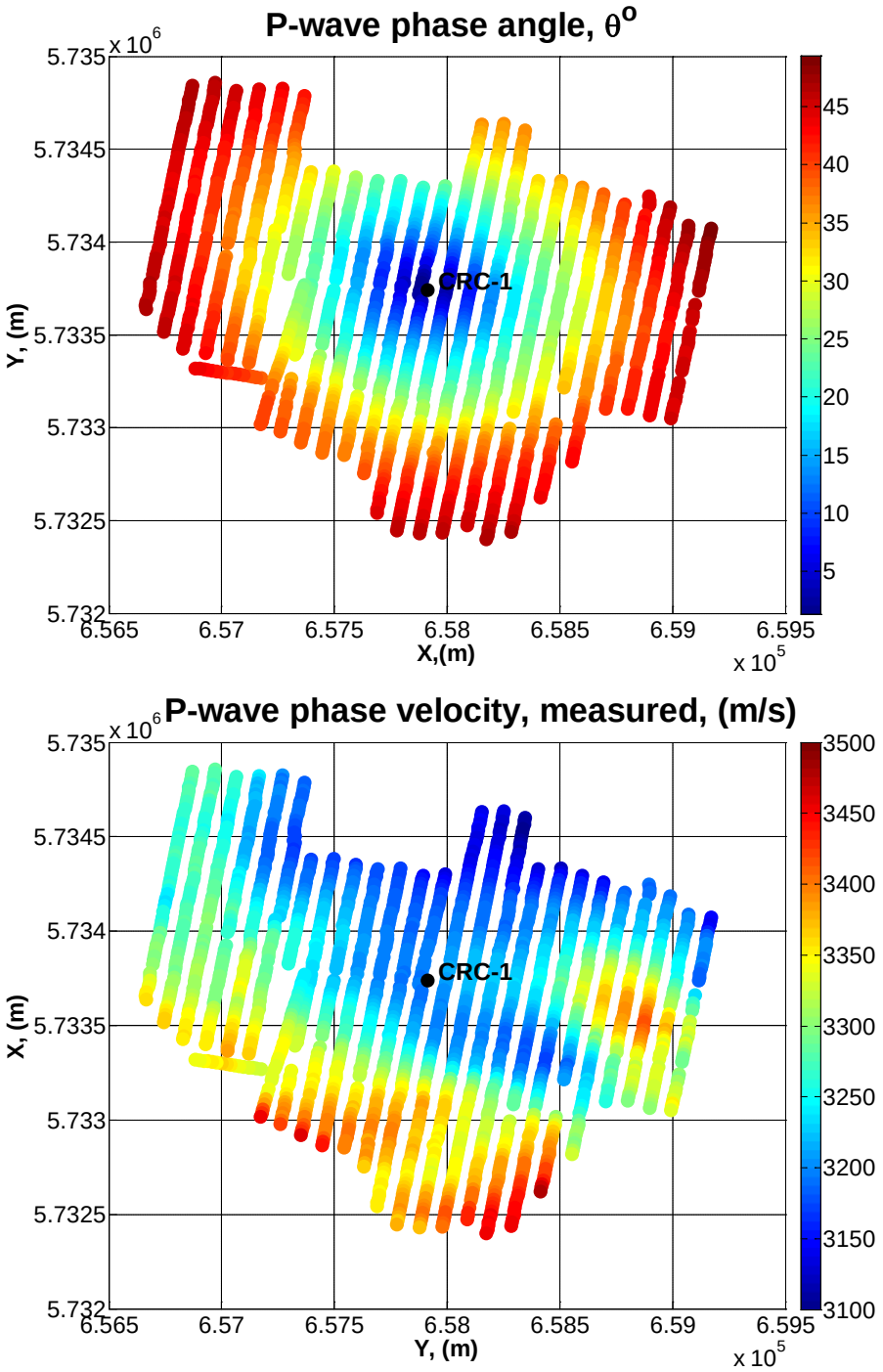

Figure 26, P-wave phase angles (top) and phase velocities (bottom) computed from 3D VSP first break times in the survey area.

One way to extract the direction of the natural coordinates of the orthorhombic medium is to rotate the data within a range of plausible angles, compute the difference between

the modelled and measured velocities and find the minimum in standard deviations. Figure 27 shows the standard deviation values as a function of the 3 Euler angles computed for the errors between the measured and modelled velocities. Maximum match between the modelled and the measured velocities appears at azimuth 150^o ($\Phi - \Psi = 170^o - 20^o$) and dip $\Theta = 8^o$. This direction is close to the direction of fast shear wave polarization (maximum horizontal stress direction) reported by Bóna et al. (2009) and Pevzner et al. (2010).

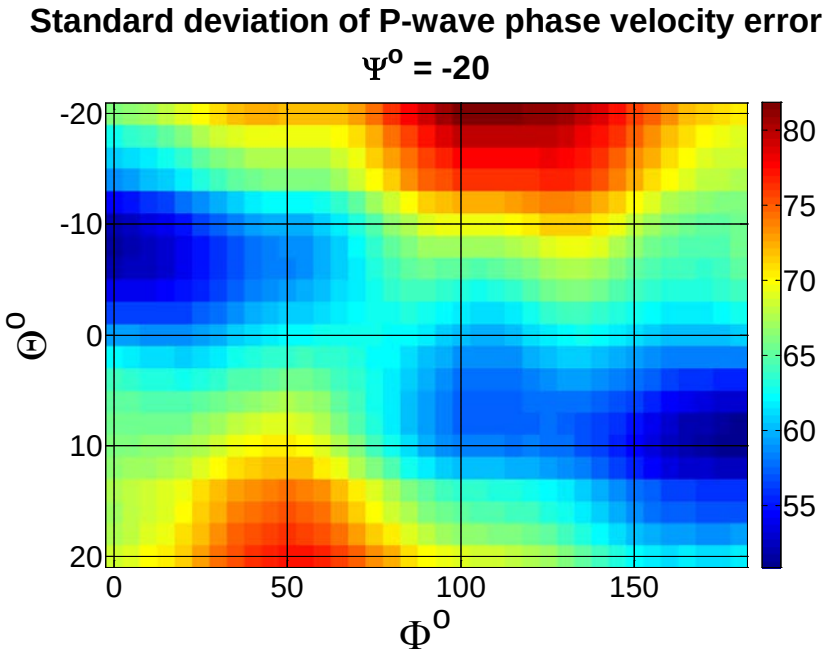

Figure 27, standard deviation of the errors in modeling measured velocities as a function of 3 Euler angles.

Anisotropy parameter estimates, $\delta_{est}^{(1)} \approx -0.026$, $\delta_{est}^{(2)} \approx -0.017$, $\delta_{est}^{(3)} \approx -0.027$, $\varepsilon_{est}^{(1)} \approx 0.145$ and $\varepsilon_{est}^{(2)} \approx 0.1$ are taken from the inversion with the smallest standard deviation in velocity mismatch (Figure 27). Figure 28 shows the modelled velocities with the estimated orthorhombic parameters printed on the map. There is a reasonable degree of resemblance between the measured velocities shown in Figure 26 (bottom) and the modelled values in Figure 27. Considering the results of uncertainty analysis for orthorhombic parameter estimation presented in Section 6.2, we can expect a reasonable degree of confidence (less than $\pm$ 5% estimation error) for anisotropy parameters

estimated at Otway geosequestration site. This conclusion is mainly based on the availability of adequate phase angle coverage ($\theta_{\max} \approx 50^o$) that was obtained from sufficient source offset to depth ratio in Otway geosequestration site as well as presence of weak to moderate anisotropy in the shale formation and absence of intensive fracturing for the depth interval corresponding to the shale formation where VSP measurements were recorded. This is close to the uncertainty conditions represented by the error plots in the left columns ($\delta_N = 0.1$) of Figures 5-9 for 1% random noise on the slowness vectors and $\theta_{\max} = 45^o$ and $\theta_{\max} = 60^o$.

Small negative values for delta ($\delta^{(1)}$ and $\delta^{(2)}$) are usually regarded as an indication of inter-bedding thin isotropic layers (Berryman et al., 1999). However, in CRC-1 well location receivers are surrounded by a shale formation with dominant intrinsic anisotropy. Values of epsilon are also close and the medium may be approximated by VTI anisotropy as well as orthorhombic.

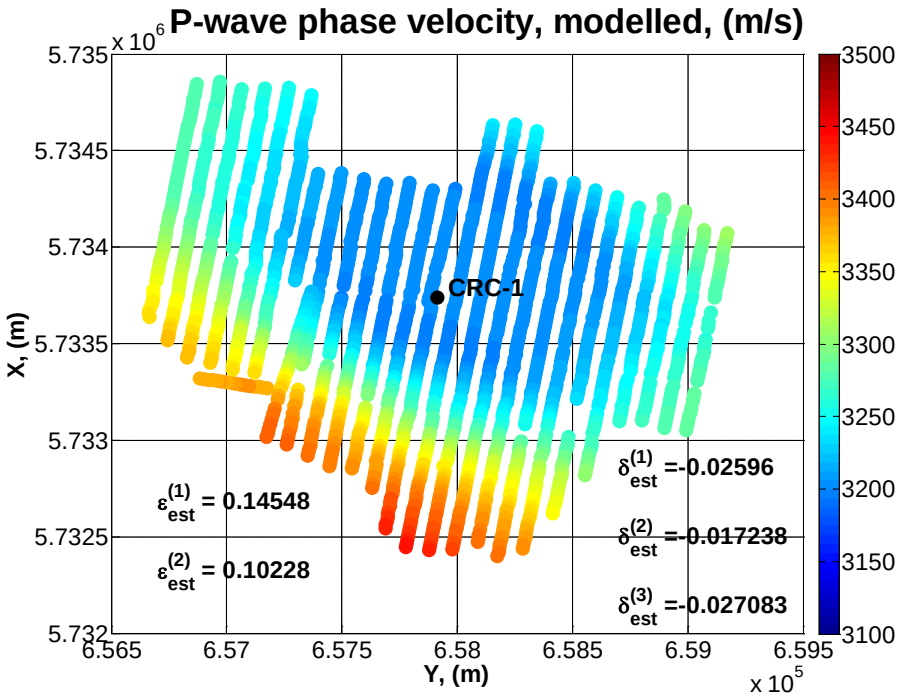

Figure 28, modelled velocities and corresponding orthorhombic parameters obtained from 3D VSP measurements at the location of well CRC-1 in Otway geosequestration site.

6.4 Remarks

When modeling orthorhombic medium with dry and rotationally invariant fractures, anisotropy parameters $\delta^{(1)}$ and $\varepsilon^{(1)}$ defined in the symmetry plane along with the fracture plane can be approximated by corresponding parameters in the background VTI medium if the intensity of the fracturing and the magnitude of the anisotropy in the VTI medium are small.

Approximate relationship is less accurate in estimating parameters $\delta^{(1)}$ and $\delta^{(2)}$ than estimating parameters $\delta^{(3)}$, $\varepsilon^{(1)}$ and $\varepsilon^{(2)}$. Estimation of parameters $\delta^{(1)}$ and $\delta^{(2)}$ using approximate relationship seems to be strongly influenced by the presence of the fractures. Estimation of parameters $\delta^{(3)}$, $\varepsilon^{(1)}$ and $\varepsilon^{(2)}$ is less sensitive to the fractures in the medium.

The exact method is capable of estimating anisotropy parameters $\delta^{(1)}$, $\delta^{(2)}$, $\delta^{(3)}$, $\varepsilon^{(1)}$ and $\varepsilon^{(2)}$ for the entire range of VTI anisotropy, embedded fracture intensity and measurement noise (up to 3%) if sufficient dip angle coverage is provided. Anisotropy parameters defined in the symmetry plane perpendicular to the fracture plane $\delta^{(2)}$ and $\varepsilon^{(2)}$ are more reliably estimated than the parameters defined in the fracture (symmetry) plane $\delta^{(1)}$ and $\varepsilon^{(1)}$.

In the synthetic Pseudo 3D VSP example, orthorhombic parameters have been accurately derived from the slowness measurements where P-wave phase angles cover up to about 70^{o}. Important assumption here is that the overburden homogeneity allows us to use horizontal slownesses (measured on the surface) to construct slowness vector at the receiver interval.

In the real 3D VSP example, horizontal layer geometry and absence of any major fault or structural complexity in the survey area have made it easy to compute horizontal component of the slowness vector. P-wave dip (phase) angles reach to more than 45^{0} degrees for the sources located in the edges of the survey and cause a reasonable level of confidence in the estimations. Minimum error in velocity modeling by orthorhombic anisotropy aligns in the direction of maximum horizontal stress reported previously in Otway area.

Chapter 7, Summary, conclusions and recommendations

In this chapter, I will first summarize most of the work presented in previous chapters and review the result of the analysis for each chapter. Then, I will shape my final conclusion that is based on an accuracy comparison between several parameter estimation methods and results of anisotropy analysis in CO2CRC's Otway geosequestration site. In the end, I will present some suggestions and recommendations with regards to the application of seismic anisotropy for the purposes of monitoring and verification of CO_2 geosequestration at Otway.

7.1 Summary of the chapters

In Chapter 1, I gave an introduction to why seismic exploration industry has decided to use multi-parameter and computationally intensive anisotropic earth models for seismic processing and interpretation instead of simple standard isotropic models. Application of VSP recordings in the form of wave slowness and polarization data for the estimation of medium anisotropy was then reviewed and the limitations and the assumptions related to available methods were discussed. The recent application of time-lapse seismic anisotropy in monitoring the changes in the state of subsurface stress as a result of CO_2 injection and linking the stress change to the development of new fracture systems trough building geomechanical earth models was then introduced as a motivation for this PhD research. Motivated by this idea, estimation of elastic (anisotropy) parameters of the medium surrounding VSP recording interval at CO2CRC's Otway geosequestration site was set as a priority for this PhD research through which the reliability of existing parameter estimation methods will be inspected and the results will be presented in a quantitative manner. In Chapter 1, I have also presented a summary of the previous anisotropy studies in the Otway geosequestration site which can be used to guide this research and verify the results of the current study. Research methodology and organization of the results were presented at the end of Chapter 1.

In Chapter 2, I introduced CO2CRC as the Australia's collaborative research organization in carbon capture and geosequestration. I also reviewed CO2CRC's objectives, activities and research program in carbon capture and storage. As a part of monitoring and verification (M&V) program for CO_2 storage, CO2CRC's Otway project in Victoria was introduced where 65000 tonnes of CO_2 rich gas has been injected into

Waarre C (a depleted gas reservoir) formation by the year 2010. To investigate the changes in the acoustic properties of Waarre C reservoir as a result of CO_2 injection, I presented an inversion exercise over three seismic surveys in the Otway geosequestration site using a model based algorithm. The results of the inversion showed that both the amplitude and the acoustic impedance responses of Waarre C reservoir to 65000 tonnes of CO_2 injection at the stage 1 of Otway program are subtle and cannot be used to detect CO_2 migration in the reservoir. However, seismic amplitudes at top Waarre C reservoir appear to be more responsive (and detectable) than the acoustic impedance attribute for the current amount of injected CO_2. The results of the inversion for both the amplitude changes (2-9%) and the acoustic impedance change (2%) were in full agreement with the results of modeling seismic response for Waarre C formation by Caspari et al. (2010). Considering the results of the acoustic impedance inversion and forward modeling presented above, application of the conventional time-lapse seismic signals (variation of top reservoir amplitudes and rock acoustic impedance) will not offer great help in achieving monitoring and verification objectives of the stage 1 of the CO2CRC's Otway geosequestration project. Because of this, I have turned my attention (in the later chapters) towards more complex anisotropy and elastic parameter estimation methods that can be ultimately used to estimate underground stress changes as a result of the elasticity change in the reservoir/overburden rock in a CO_2 geoequestration project. A coupled seismic-geomechanical model can then be built to infer whether the stress changes are large enough to develop new fracture systems or reactivate existing ones from which CO_2 can escape.

To understand seismic anisotropy in earth, in Chapter 3, I reviewed the definition of two mostly encountered anisotropic medium symmetries in sedimentary basins, transverse isotropy and orthorhombic and the characteristics (phase/group velocity and polarization) of seismic wave propagation in these media. A prior understanding of these characteristics of P-wave propagation in anisotropic media was necessary to understand the analysis that was presented in the later chapters. I have also described the parameterization suggested by Thomsen (1986) for TI media and Tsvankin (1997) for orthorhombic media and the range of these parameters in earth sedimentary basins. These parameterizations and range of anisotropy values were used in the uncertainty

analysis to define the anisotropy models. To facilitate understanding of important characteristics of P-wave propagation in TI and orthorhombic mediums, several example plots of phase/group velocities and polarization direction (dip) in these mediums were presented at the end of Chapter 3. In these examples, I observed that, in TI media with large positive ε and small positive δ (this can represent shale formations), P-wave polarization dips lay between the group angle and the phase angle (closer to group angle) for rays with group angles up to $\psi = 74^o$ ($\theta = 55^o$) from vertical. Weak anisotropy approximation in TI mediums works well for approximating polarization dips for rays with group angles of up to $\psi = 57^o$ ($\theta = 40^o$) and group angles are almost perfectly reproduced by weak anisotropy approximation for the entire range of ray propagation angles. In the case of moderate positive ε and small negative δ (this can be produced by inter-bedding of thin isotropic layers) the medium appears isotropic with respect to P-wave polarization dip, group and phase angles and group/phase velocities for propagation dips of up to around $\theta = \psi = 27^o$. In the orthorhombic medium produced by embedding a set of dry and vertical fractures into a VTI background, P-wave group velocity and polarization vectors deviate from the direction of the slowness vector in both the vertical and horizontal planes. However, this deviation appears to be similar for both the group velocity and polarization vectors in the vertical plane. In chapters 4, 5 and 6, numerical data (generated the same way as the examples) have been contaminated by noise and inverted to anisotropy parameters to quantify the uncertainties related to several VSP based anisotropy parameter estimation methods.

In Chapter 4, I first looked at the uncertainties of VTI parameter estimation from P-wave slownesses that can be computed from walkaway VSP travel-time measurements. Equation 1 of Chapter 4 produces reliable inversion results for δ and unreliable estimates of ε in the short offset range ($\theta_{\max} = 30^o$) and small noise level (1%). In this case, $\theta_{\max}$ has to increase to around 45^o in order to obtain a reliable estimate of ε. As the noise level increases (to 3%), $\theta_{\max}$ has to be increased to more than 60^o in order to acquire a reasonable accuracy for both ε and δ estimations. Equation 2 of Chapter 4 shows a better performance than Equation 1 in estimating ε from short offset data (

$\theta_{\max} = 30^o$) within mild anisotropy range and small slowness noise (1%). The accuracy of using Equation 2 of Chapter 4 for estimating parameter δ from short offset data is also good and increases with increasing $\theta_{\max}$. In Section 4.6, I have described the effect of maximum P-wave propagation angle, $\theta_{\max}$ on VTI parameter estimation at well CRC-1 in a synthetic walkaway VSP example. The accuracy of the estimations increases with source offset. However, the presence of head waves at two shallow intervals (approximately at 600 and 800 m) reduces the estimation accuracy. Synthetic Slownesses show no significant sign of noise interference at 3D VSP recording interval (1500 to 1600 m). This example also showed that the application of Snell's law to use surface calculated horizontal component of the P-wave slowness vector at the receiver level is valid at the location of well CRC-1 and that the geometry of 3D VSP survey is capable of producing sufficient slowness data range to constrain VTI parameters. On the other hand, slowness data obtained from 3D VSP measurements at well CRC-1 confirmed that the anisotropy of the shale formation (measurement interval) is azimuthal and may have lower symmetry than VTI. A limitation of P-wave slownesses only methods is that they rely on the measurements of the horizontal components of the slowness vector in parameter estimation and may not be applicable in the area with complex overburden geometry or strong lateral velocity variation. To overcome this issue, horizontal components of the slowness vector have been replaced by another local measurement, dip direction of the polarization vector, in the slowness-polarization methods.

In Chapter 5, I looked at the applicability and uncertainty of estimating VTI anisotropy parameters based on using only P-wave slowness-polarization data that can be measured in a walkaway VSP survey. Grechka and Mateeva (2007) relationship is valid only in a small range of medium anisotropy and cannot be used to estimate large VTI parameters. Increasing the range of P-wave propagation angles has little effect on improving the inversion results. On the other hand, the exact slowness-polarization relationship (Equations 2 to 4 of Chapter 5) can be used to estimate any VTI anisotropy in the medium if accurate polarization measurements exist. Restricting wave propagation angles (related to source offset) to less than the critical angle of the medium will

increase accuracy of polarization measurements in a VSP survey by avoiding head wave interferences at shallow intervals. Slowness-polarization method based on the exact Equations 2-4 of Chapter 5, is able to (within a reasonable accuracy) recover VTI anisotropy parameters ε and δ for the depth intervals below 1000 m of the well CRC-1 2D model. The large inversion accuracy of the deeper intervals is mainly because of the accuracy in P-wave polarizations that are not influenced by other wave types for up to $\nu_{\max} = 70^o$. On the other hand, shallow P-wave polarization measurements contain significant interference with head waves that are generated by sources positioned at large offsets in the model. This polarization noise has reduced the accuracy of parameter estimation for shallow intervals by reducing $\nu_{\max}$ to less than 50^o. Both the P-wave slowness and polarization measurements show that the anisotropy of the overburden shale in Otway geosequestration site changes with azimuth and may not be sufficiently constrained by TI models. An orthorhombic model would be the simplest anisotropy that can explain azimuthal anisotropy in the overburden shale (recording interval) at the Otway site.

In Chapter 6, I have looked at the possibility and the uncertainties of fitting an orthorhombic anisotropy model to velocity measurements at well CRC-1 3D VSP survey. For an orthorhombic model generated by embedding a set of vertical fractures into a VTI background medium, Tsvankin (1997) approximate relationship for P-wave phase velocity in orthorhombic media is less reliable in estimating parameters $\delta^{(1)}$ and $\delta^{(2)}$ than estimating parameters $\delta^{(3)}, \varepsilon^{(1)}$ and $\varepsilon^{(2)}$. Estimation of parameters $\delta^{(1)}$ and $\delta^{(2)}$ using approximate relationship seems to be strongly influenced by the presence of the fractures. On the other hand, estimation of parameters $\delta^{(3)}, \varepsilon^{(1)}$ and $\varepsilon^{(2)}$ is less sensitive to the fractures in the medium. The exact orthorhombic phase velocity relationship is capable of estimating anisotropy parameters $\delta^{(1)}, \delta^{(2)}, \delta^{(3)}, \varepsilon^{(1)}$ and $\varepsilon^{(2)}$ for the entire range of VTI anisotropy, strong fracture intensity and large measurement noise (up to 3%) if sufficient dip angle coverage is given. Anisotropy parameters defined in the symmetry plane perpendicular to the fracture plane $\delta^{(2)}$ and $\varepsilon^{(2)}$ are more reliably estimated than the parameters defined in the fracture (symmetry) plane $\delta^{(1)}$ and $\varepsilon^{(1)}$. In the synthetic Pseudo 3D VSP example for well CRC-1, orthorhombic parameters have

been accurately recovered from the slowness measurements where P-wave phase angles cover up to around 70^o. Overburden homogeneity allowed us to use horizontal slownesses (measured on the surface) to construct slowness vector in the receiver interval. This was verified to be valid assumption based on the analysis for 2D synthetic VSP data generated for well CRC-1. In the real 3D VSP example for well CRC-1, near horizontal layer geometry and absence of any major fault or structural complexity in the survey area have made it possible to use P-wave horizontal slowness (computed at the surface) at the receiver interval. P-wave phase angles reach to more than 45^o for the sources located at the edges of the survey and cause a reasonable level of confidence in the estimations. Orientation of symmetry planes for the best fitted orthorhombic model to velocity data measured from 3D VSP recordings of well CRC-1 in 2010 matches closely to the direction of fast and slow shear wave polarizations (159^o, 69^o , respectively) that were reported by Bóna et al., (2011). Symmetry axis, x_3 of the best fitted orthorhombic model at well CRC-1 location is deviating from vertical direction by about 8^o. Estimated anisotropy parameters for the orthorhombic model fitted to well CRC-1 3D VSP measurements are as the following: $\delta^{(1)} \approx -0.02$, $\delta^{(2)} \approx -0.01$, $\varepsilon^{(1)} \approx 0.14$ and $\varepsilon^{(2)} \approx 0.1$. Reliable estimation of $\delta^{(3)}$ would normally require velocity measurements along near horizontal phase directions which are absent for the depth interval where 3D VSP data at well CRC-1 were recorded. No attempt was made to conduct a similar analysis as in 2010 on VSP data recorded at well CRC-1 in 2008. The reason is the large distance (200 m) between source lines in 2008 survey which decreases the accuracy of parameter estimation by reducing the number of adjacent source points that are available for estimation of horizontal component of the slowness vector.

7.2 Conclusions

In this thesis, I have studied the reliability of several anisotropy parameter estimation methods that could be potentially utilized to estimate elasticity (anisotropy) coefficients of the overburden rock at Otway geosequestration site by using VSP measurements of well CRC-1. Quantifying the accuracy of each estimation method is an essential step before utilizing these parameters for the purposes of monitoring underground stress

change as a result of CO_2 injection and modeling development of new fracture conduits for CO_2 migration away from the reservoir. In general, VSP methods that include horizontal components of the slowness vector (Chapter 4 and 6) seem to produce more accurate estimations of the anisotropy parameters δ and ε than the methods that exclude this component. However, these methods have the disadvantage of being dependent on the overburden conditions. On the other hand, methods which use polarization measurements instead of horizontal components of the slowness vector (Chapter 5) have the advantage of being independent of the overburden condition but are strongly dependent on the accuracy in polarization measurements.

The results of this study indicate that the selection of a proper methodology for anisotropy parameter estimation based on only P-wave measurements in a VSP survey is mainly dependent on our ability to accurately estimate either horizontal components of the slowness vector or the polarization vector. If the overburden condition allows us to measure the horizontal component of the slowness vector on the surface and transfer it to the receiver level and there is enough phase slowness dip angle coverage, the methods based on slownesses only are the proper methods to choose. However, if there is a shortage of dip angle coverage, application of slownesses only methods for ε estimation is not recommended. Instead, depending on our ability to accurately estimate polarization vectors, the method based on weak anisotropy approximation of the phase velocities would be the proper method to choose. If the overburden conditions are such that we cannot transfer the horizontal slownesses to the receiver location, the only hope for accurate estimation of VTI parameters would be to use slowness-polarization methods. Here, the method that uses the exact relationship between vertical slownesses and polarization dips (Chapter 5) can be the proper candidate, provided we are able to accurately measure P-wave polarization vectors. This would be tedious in places where receivers are located close to the geological interfaces with high elastic contrast. Reflection and conversion of the original P-wave to other types of up- and down-going waves or wave interference phenomenon caused by the arrival of head waves at large offsets (required for higher accuracy) will significantly distort the particle displacements (polarizations) recorded by the receivers. Fortunately, the accuracy of the estimations based on the exact relationship between vertical slowness and polarization dip is not

strongly dependent on the use of large offsets and as a result, polarization related noise could be reduced by avoiding large offsets without sacrificing too much of the accuracy.

These results were applied to the CO2CRC Otway project. In particular increasing P-wave phase angles (source-receiver offset) will generally increase the accuracy of parameter estimation. However, generation of head waves by sources located at large offsets has contaminated both the slowness and polarization vectors that are measured in shallow depth intervals between 600 and 1000 m. Similar data measurements for deeper intervals (below 1000 m) appear to be less distorted by head waves or other type of waves than the shallow section. 3D VSP dataset acquired in 2010 has been capable of providing sufficient slowness data to constrain the anisotropy parameters at Otway geosequestration site. Shale formation in which downhole receivers at well CRC-1 are fixed exhibits azimuthal anisotropy that has symmetry lower than VTI. Inversion of pseudo-synthetic 3D VSP data generated by finite-difference modeling at well CRC-1 shows that orthorhombic anisotropy parameters can be accurately constrained within the available range of slowness measurements. The following anisotropy parameters of an orthorhombic anisotropy model have been estimated for the shale formation (measurements interval) at well CRC-1: $\delta^{(1)} \approx -0.02$, $\delta^{(2)} \approx -0.01$, $\varepsilon^{(1)} \approx 0.14$ and $\varepsilon^{(2)} \approx 0.1$. The best fitted orthorhombic model represents two azimuthal directions of 150^o and 60^o for its symmetry planes with x_3 axis dipping about 8^o from vertical direction. These azimuthal directions are supported by the results of the shear wave splitting analysis at well CRC-1 (Pevzner et al., 2010) and borehole breakout study by Hillis et al. (1995) that reports a nominal maximum horizontal stress azimuth of 125^o .

7.3 Recommendations and future work

Successful application of time-lapse seismic anisotropy in CO_2 monitoring and verification largely relies on the accuracy of estimated anisotropy (elastic) parameters of the fitted model. As a result, reliability of the selected parameter estimation method has to be first addressed with respect to variables such as the data type that is used in the inversion (P-/S-wave, slowness/polarization), data range (offset/depth, azimuth) and noise. All these aspects have been investigated in this research work with application to the CO2CRC Otway project. Nonetheless, important improvements in VSP anisotropy

parameter estimation at Otway geosequestratio site can still be achieved by increasing intrinsic VSP signal to noise ratio, for instance, through the application of stronger seismic sources on the surface. Stronger signals will help us to estimate polarization direction of both P- and S-waves more accurately and hence free the requirement of estimating horizontal component of the slowness vector through the application of slowness-polarization methods. For the slownesses only methods, decreasing receiver separation of the future 3D VSP surveys will help in a better estimation of horizontal component of the slowness vector and anisotropy parameters. Increasing source offset on the surface will increase the range of phase angles that are recorded by the receivers and results in a more confident estimation of anisotropy parameters. A larger measurement interval in the borehole will enable us to monitor anisotropy with respect to depth (and lithology) as well as time and azimuth. Ideally entire borehole interval should be populated with closely spaced receivers to stabilize and improve inversion results. With good data quality both the slowness and polarization vectors of P- and S-waves can be used to invert (through the application of Christoffel equation) for 21 elastic parameters of the most general anisotropy in the medium. Addition of cross-well measurements would have greatly improved the inversion accuracy, reduce the need for very long VSP offsets and hence large sources. Inclusion of shear waves into the computation would further improve the anisotropy estimates and in general characterisation of the rock structure. As a next step in monitoring CO_2 migration in the CO2CRC Otway project, my recommendation would be to build a 3D geomechanical earth model through the integration of surface seismic data (horizons/faults), laboratory core measurements (for static elastic parameters) and borehole measurements (pore pressure and principal vertical and horizontal stresses) that will help us to understand the link between the existing (or newly generated) fracture/fault networks and the change in the state of underground stress as a result of CO_2 injection into the reservoir rocks and ideally help us to detect the high risk areas from which CO_2 leakage can occur.

Refrences

Aki, K., and P.G., Richards, 1980, Quantitative seismology. Theory and methods: Vol. 1, W.N. Freeman & Co.

Alford, R. M., 1986, Shear data in the presence of azimuthal anisotropy: Dilley, Texas: 56th Annual International Meeting, SEG, Expanded Abstracts, 476-479.

Alkhalifah, T., and I. Tsvankin, 1995, Velocity analysis for transversely isotropic media: Geophysics, **60**, 1550-1566.

Alkhalifah, T., I. Tsvankin, K. Larner, and J. Toldi, 1996, Velocity analysis and imaging in transversely isotropic media: Methodology and a case study: The Leading Edge, **15**, 371–378.

Asgharzadeh, M., A. Bóna, R. Pevzner, M. Urosevic, and B. Gurevich, 2012, Uncertainties in local anisotropy estimation from multi-offset VSP data: 74th Conference and Exhibition incorporating SPE Europec, EAGE, Expanded Abstracts, A027.

Asgharzadeh, M., A. Bóna, R. Pevzner, M. Urosevic, and B. Gurevich, 2013, Reliability of the slowness and slowness-polarization methods for anisotropy estimation in VTI media from 3C walkaway VSP data: Geophysics, **78(5)**, C57–C66.

Auld, B. A., 1973, Acoustic fields and waves in solids: J. Wiley and Sons.

Backus, G. E., 1962, Long-wave elastic anisotropy produced by horizontal layering: Journal of Geophysical Research, **67**, 4427–4440.

Bakulin, A., C. Slater, H. Bunain, and V. Grechka, 2000 a, Estimation of azimuthal anisotropy and fracture parameters from multiazimuthal walkaway VSP in the presence of lateral heterogeneity: 70th Annual International Meeting, SEG, Expanded Abstracts, 1405-1408.

Bakulin, A., V. Grechka and I. Tsvankin, 2000 b, Estimation of fracture parameters from reflection seismic data - Part I: HTI model due to a single fracture set: Geophysics, **65**, 1788–1802.

Bakulin, A., V. Grechka and I. Tsvankin, 2000 c, Estimation of fracture parameters from reflection seismic data - Part II: Fractured models with orthorhombic symmetry: Geophysics, **65**, 1803–1817.

Banik, N. C., 1987, An effective anisotropic parameter in transversely isotropic media: Geophysics, **52**, 1654–1664.

Berryman, J. G., 1979, Long-wave elastic anisotropy in transversely isotropic media: Geophysics, **44**, 896–917.

Berryman, J. G., V. Grechka, and P. A. Berge, 1999, Analysis of Thomsen parameters for finely layered VTI media: Geophysical Prospecting, **47**, 959-978.

Bóna, A., and M. A. Slawinski, 2011, Wavefronts and rays as characteristics and asymptotics: World Scientific, ISBN: 978-981-4295-51-2.

Bóna, A., I. Bucataru, and M. A. Slawinski, 2008, Inversion of ray velocity and polarization for elasticity tensor: Journal of Applied Geophysics, **65**, 1-5.

Bóna, A., and M. A. Slawinski, 2008, Comparison of two inversions for elasticity tensor: Journal of Applied Geophysics, **65**, 6-9.

Slawinski, M. A., Lamoureux, M. P., Slawinski, R. A., & Brown, R. J., 2003, VSP traveltime inversion for anisotropy in a buried layer: Geophysical Prospecting, **51**, 131-140.

Caspari, E., J. Ennis-King, M. Asgharzadeh, D. Makarynska, B. Gurevich, and M. Urosevic, 2010, Prediction of time-lapse seismic response from simulations of CO2 flow in a depleted gas reservoir: Otway case study: Presented at CO2CRC Research Symposium.

Cooperative Research Centre for Greenhouse Gas Technologies (CO2CRC). 2013a. "About Us" Australian Government's Cooperative Research Centre programs. Accessed May 20, http://www.co2crc.com.au/about.

Cooperative Research Centre for Greenhouse Gas Technologies (CO2CRC). 2013b. "CO2CRC Research Management Structure" Australian Government's Cooperative Research Centre programs. Accessed May 20, http://www.co2crc.com.au/research.

Cooperative Research Centre for Greenhouse Gas Technologies (CO2CRC). 2013c. "CCS Project in Australia" Australian Government's Cooperative Research Centre programs. Accessed May 20, http://www.co2crc.com.au/research/ausprojects.html.

Cooperative Research Centre for Greenhouse Gas Technologies (CO2CRC). 2013d. "Overview" Australian Government's Cooperative Research Centre programs. Accessed May 20, http://www.co2crc.com.au/otway.

Cooperative Research Centre for Greenhouse Gas Technologies (CO2CRC). 2013e. "Operations" Australian Government's Cooperative Research Centre programs. Accessed May 20, http://www.co2crc.com.au/otway/operations.html.

Cooperative Research Centre for Greenhouse Gas Technologies (CO2CRC). 2013f. "Otway Project: Monitoring CO2" Australian Government's Cooperative Research Centre programs. Accessed May 20, http://www.co2crc.com.au/otway/monitoring.html.

Crampin, S., 1981, A review of wave motion in anisotropic and cracked elastic media: Wave Motion, **3**, 343–391.

Crampin, S., 1985, Evaluation of anisotropy by shear-wave splitting: Geophysics, **50**, 142–152.

Crampin, S., 1990, The potential of shear-wave VSPs for monitoring recovery: A letter to management: The Leading Edge, **9**(3), 50-52.

Dodds, K., T. Daley, B. Freifeld, M. Urosevic, A. Kepic, and S. Sharma, 2009, Developing a monitoring and verification plan with reference to the Australian Otway CO2 pilot project: The Leading Edge, **28**(7), 812-818.

De Parscau J., 1991, P- and SV-wave transversely isotropic phase velocities analysis from VSP data: Geophysical Journal International, **107**, 629-638.

Dewangan, P., and V. Grechka, 2003, Inversion of multicomponent, multiazimuth, walkaway VSP data for the stiffness tensor: Geophysics, **68**, 1022—1031.

Esmersoy, C., 1990, Split-shear wave inversion for fracture evaluation: 60th Annual International Meeting, SEG, Expanded Abstracts, SN1.6.

Fuck, R. F., A. Bakulin, and I. Tsvankin, 2009, Theory of travel-time shifts around compacting reservoirs: 3D solutions for heterogeneous anisotropic media: Geophysics, **74**(1), D25–D36.

Gaiser, J. E., 1990, Transversely isotropic phase velocity analysis from slowness estimates: Journal of Geophysical Research, **95**, 11241-11254.

Galperin, E. I., 1974, Vertical seismic profiling and its exploration potential: SEG Special Publication, Tulsa, OK, USA

Gomez, E., X. Zheng, I. Pšenčík, S. Horne, and S. Leaney, 2004, Local determination of weak anisotropy parameters from a walkaway VSP qP-wave data in the Java Sea region: Studia Geophysica Geodaetica, **48**, 215-230.

Grechka, V., A. Mateeva, G. Franco, C. Gentry, P. Jorgensen, and J. Lopez, 2007, Estimation of seismic anisotropy from P-wave VSP data: The Leading Edge, **26**, 756–759.

Grechka, V., and A. Mateeva, 2007, Inversion of P-wave VSP data for local anisotropy: Theory and case study: Geophysics, **72**(4), D69-D79.

Grechka V., and I. Tsvankin, 2003. Feasibility of seismic characterization of multiple fracture sets: Geophysics **68**, 1399-1407.

Grechka, V., P. Contreras and I. Tsvankin, 2000, Inversion of normal moveout for monoclinic media: Geophysical Prospecting, **48**, 577–602.

Grechka, V., P. Jorgensen, and J.L. Lopez, 2006, Anisotropy estimation from marine 3D VSP data: Offshore Technology Conference, 17866-PP.

Hatchell, P., and S. Bourne, 2005, Rocks under strain: Strain-induced time-lapse time shifts are observed for depleting reservoirs: The Leading Edge, **24**, 1222–1225.

Helbig, K., 1956, Die Ausbreitung elastischer Wellen in anisotropen Medien: Geophysical Prospecting, **4**, 70–104.

Helbig, K., 1994, Foundations of elastic anisotropy for exploration seismics: Pergamon Press.

Helbig, K., and L. Thomsen, 2005, 75–plus years of anisotropy in exploration and reservoir seismics: A historical review of concepts and methods: Geophysics, **70**(6), 9nd–23nd.

Herwanger, J. V., and S. A. Horne, 2005, Linking geomechanics and seismics: Stress effects on time-lapse multi-component seismic data: 67th Conference and Exhibition, EAGE, Extended Abstracts, C011.

Herwanger, J.V. and S. Horne, 2009, Linking reservoir geomechanics and time-lapse seismics: Predicting anisotropic velocity changes and seismic attributes: Geophysics, **74**(4), W13–W33.

Hillis, R. R., S. A. Monte, C. P. Tan and D. R. Willoughby, 1995, The contemporary stress field of the Otway Basin, South Australia: Implications for hydrocarbon exploration and production: Australian Petroleum Exploration Association Journal, **35**, 494-506.

Horne, S., and S. Leaney, 2000, Short note: Polarization and slowness component inversion for TI anisotropy: Geophysical Prospecting, **48**, 779-788.

Hsu, C.-J., and Schoenberg, M., 1993, Elastic waves through a simulated fractured medium: Geophysics, **58**, 964–977.

Hsu, K., M. Schoenberg, and J. Walsh, 1991, Anisotropy from polarization and moveout: 61st Annual International Meeting, SEG, Expanded Abstracts, 1526-1529.

Jaeger, J. C., N. G.W. Cook, and R.W. Zimmerman, 2007, Fundamentals of rock mechanics, 4th edit, Blackwell Publishing.

Jílek, P., B. Hornby, and A. Ray, 2003, Inversion of 3D VSP P-wave data for local anisotropy: A case study: 73rd Annual International Meeting, SEG, Expanded Abstracts, 1322-1325.

Kochetov, M., and M. A. Slawinski, 2009, Estimating effective elasticity tensors from Christoffel equations: Geophysics, **74**(5), WB67-WB73.

Korn, G., and T. Korn, 1968, Mathematical handbook for scientists and engineers: McGraw-Hill Book Co.

Lagarias, J.C., J. A. Reeds, M. H. Wright, and P. E. Wright, 1998, Convergence Properties of the Nelder-Mead simplex method in low dimensions: SIAM Journal of Optimization, **9**(1), 112-147.

Li, R., K. Dodds, A. Siggins, and M. Urosevic, 2006, A rock-physics simulator and its application for CO2 sequestration process: Exploration Geophysics, **37**(1), 67-72.

Lynn, H. B., and L. Thomsen, 1986, Shear wave exploration along the principal axis: 56th Annual International Meeting, SEG, Expanded Abstracts, 474-476.

Lynn, H., W. Beckham, K. Simon, C. Bates, M. Layman, and M. Jones, 1999, P-wave and S-wave azimuthal anisotropy at a naturally fractured gas reservoir, Bluebell-Altamont Field, Utah: Geophysics, **64**, 1312–1328.

Macbeth, C., 2002, Multicomponent VSP analysis for applied seismic anisotropy: Handbook of Geophysical Exploration, **26**, Pergamon, Elsevier Science.

Mallick, S., K. Craft, L. Meister and R. Chambers, 1998, Determination of the principal directions of azimuthal anisotropy from P-wave seismic data: Geophysics, **63**(2), 692–706.

Markovsky, I., and S. Van Huffel, 2007, Overview of total least-square methods: Signal Processing, **87**, 2283-2302.

Martin, M. A., and T. L. Davis, 1987, Shear-wave birefringence: A new tool for evaluating fractured reservoirs: The Leading Edge, **6**, 22–28.

Mavko, G., T. Mukerji, and N. Godfrey, 1995, Predicting stress-induced velocity anisotropy in rocks: Geophysics, **60**, 1081–1087.

Mensch, T., and P. Rasolofosaon, 1997, Elastic-wave velocities in anisotropic media of arbitrary symmetry — generalization of Thomsen's parameters ε , δ , and γ: Geophysical Journal International,**128**, 43–64.

Miller, D. E., and C. Spencer, 1994, An exact inversion for anisotropic moduli from phase slowness data: Journal of Geophysical Research, **99**, 21651-21657.

Naville, C., 1986, Detection of anisotropy using shear-wave splitting in VSP surveys: Requirements and Applications: 56th Annual International Meeting, SEG, Expanded Abstracts, 391-394.

Nichols, D., F. Muir, and M. Schoenberg, 1989, Elastic properties of rocks with multiple sets of fractures: 59th Annual International Meeting. SEG, Expanded Abstracts, 471–474.

Nicoletis, L., C. Client, and F. Lefeuvre, 1988, Shear-wave splitting measurements from multishot VSP data: 56th Annual International Meeting, SEG, Expanded Abstracts, 527-530.

Owusu, J. C., S. Horne, and A. Shabbir, 2011, Slowness surface construction and inversion from 3D VSP data: First Break, **29**(2), 45-50.

Pevzner, R., B. Gurevich, and G. Duncan, 2009, Estimation of Azimuthal Anisotropy from VSP Data Using Multicomponent Velocity Analysis: 71st Conference and Exhibition incorporating SPE Europec, EAGE, Expanded Abstracts, P-182.

Pevzner, R., M. Urosevic, B. Gurevich, V. Shulakova, A. Bóna, E. Caspari, F. Alonaizi and A. Kepic, 2012, Seismic monitoring of CO2 geosequestration: CO2CRC Otway project experience: 1th Joint International Workshop for the Earth's Surface and Subsurface 4D Monitoring, Saudi Arabia.

Postma, G. W., 1955, Wave propagation in a stratified medium: Geophysics, **20**, 780-806.

Rommel, B.E., 1994, Approximate polarization of plane waves in a medium having weak transverse isotropy: Geophysics, **59**, 1605-1612.

Rudzki, M. P., 1898, Uber die Gestalt elastischer Wellen in Gesteinen, IV Studie aus der Theorie der Erdbebenwellen: Bulletin of the Academy of Sciences Cracow, 373–384.

Rueger, A., 1996, Reflection coefficients and azimuthal AVO analysis in anisotropic media: PhD. Thesis Colorado Scholl of Mines.

Sarout, J., L. Molez,Y. Guéguen, and N. Hoteit, 2007, Shale dynamic properties and anisotropy under tri-axial loading: Experimental and theoretical investigations: Physics and Chemistry of the Earth, Parts A/B/C, **32**(8–14), 896–906.

Sayers, C. M., 2002, Stress-dependent elastic anisotropy of sandstones: Geophysical Prospecting, **50**, 85–95.

Sayers, C., 2004, Monitoring production-induced stress changes using seismicwaves: 74th Annual International Meeting, SEG, Expanded Abstracts, 2287–2290.

Schoenberg, M., 1980, Elastic wave behavior across linear slip interfaces: Journal of the Acoustical Society of America, **68**, 1516-1521.

Schoenberg, M., 1983, Reflection of elastic waves from periodically stratified media with interfacial slip: Geophysical Prospecting, **31**, 265–292.

Schoenberg, M., and C. Sayers, 1995, Seismic anisotropy of fractured rock: Geophysics, **60**, 204–211.

Schoenberg, M., and F. Muir, 1989, A calculus for finely layered anisotropic media: Geophysics, **54**, 581–589.

Schoenberg M., and K. Helbig, 1997, Orthorhombic media: Modeling elastic wave behavior in a vertically fractured earth: Geophysics **62**, 1954-1974.

Shaiban, A., A. Bóna, R. Pevzner, M. Urosevic, 2012, Time-lapse seismic anisotropy analysis for CO2 geosequestration using 3D 3C VSP data: 73th Conference and Exhibition, EAGE, Expanded Abstracts, F048.

Shapiro, S. A., and A. Kaselow, 2005, Porosity and elastic anisotropy of rocks under tectonic stress and pore-pressure changes: Geophysics, **70**(5), N27–N38.

Slawinski, M., 2009, Waves and rays in elastic continua: World Scientific, ISBN: 978-981-4289-00-9.

Staples, R., J. Ita, R. Burrell, and R. Nash, 2007, Monitoring pressure depletion and improving geomechanical models of the Shearwater field using 4D seismic: The Leading Edge, **26**, 636–642.

Thomsen, L., 1986, Weak elastic anisotropy: Geophysics, **51**, 1954-1966.

Thomsen, L., 2002, Understanding seismic anisotropy in exploration and exploitation: Distinguished Instructor Series, Society of Exploration Geophysicists.

Tsvankin, I., 1996, P-wave signatures and notation for transversely isotropic media: An overview: Geophysics, 61,467-483.

Tsvankin, I., 1997, Anisotropic parameters and P-wave velocity for orthorhombic media: Geophysics, **62**, 1292–1309.

Tsvankin, I., 2001, Seismic signatures and analysis of reflection data in anisotropic media: Handbook of Geophysical Exploration, **29**, Pergamon, Elsevier Science.

Tsvankin, I., J. Gaiser, V. Grechka, M. Van der Baan, and L. Thomsen, 2010, Seismic anisotropy in exploration and reservoir characterization: An overview: Geophysics, **75**(5), 75A15–75A29.

Turner, B. and S. Hearn, 1995, Shear-wave splitting analysis using a single-source, dynamite VSP in the Otway basin: Exploration Geophysics, **26(4)**, 519–526.

Verdon, J. P., D. A. Angus, J. M. Kendall, and S. A. Hall, 2008, The effect of microstructure and nonlinear stress on anisotropic seismic velocities: Geophysics, **73**(4), D41–D51.

Wang, Z., 2002, Seismic anisotropy in sedimentary rocks, part 2: Laboratory data: Geophysics, **67**, 1423–1440.

White, J. E., L. Martineau-Nicoletis, and C. Monash, 1983, Measured anisotropy in Pierre shale: Geophysical Prospecting, **31**, 709-725.

White, R., and R. Simm, 2003, Tutorial: Good practice in well ties: First Break, **21**, 75-83.

Williamson, P. and E. Maocec, 2000, Estimation of local anisotropy using polarizations and travel times from the Oseberg 3D VSP: 9th International Workshop on Seismic Anisotropy.

Willis, H., G. Rethford, and E. Bielanski, 1986, Azimuthal anisotropy: The occurrence and effect on shear wave data quality: 56th Annual International Meeting, SEG, Expanded Abstracts, 479–481.

Winterstein, D. F., 1990, Velocity anisotropy terminology for geophysicists: Geophysics, **55**, 1070–1088.

Zatsepin, S. V., and S. Crampin, 1997, Modeling the compliance of crustal rock: I. - Response of shear-wave splitting to differential stress: Geophysical Journal International, **129**, 477–494.

Zheng, X. and I. Pšenčík, 2002, Local determination of weak anisotropy parameters from qP-wave slowness and particle motion measurements: Pure and Applied Geophysics, **159**, 1881-1905.